Greenhouse Gas Emissions from Inland Waters in the Conterminous United States: a Process-based Modeling Study

by

Yuanzhi Yao

A dissertation submitted to the Graduate Faculty of
Auburn University
in partial fulfillment of the
requirements for the Degree of
Doctor of Philosophy

Auburn, Alabama
December 14, 2019

Keywords: Inland water, Greenhouse gas,
Land-use change, Climate change, Hydrological modeling.

Approved by

Hanqin Tian, Chair, Solon & Martha Dixon Professor of School of Forestry and Wildlife Sciences
Xing Fang, Arthur H. Feagin Chair Professor of Civil Engineering
Latif Kalin, Professor of School of Forestry and Wildlife Sciences
Ming-Kuo Lee, Robert B. Cook Professor of Geosciences
Shufen Pan, Assistant Professor of School of Forestry and Wildlife Sciences

Abstract

The growing awareness of global warming promotes great interest in investigating the magnitude, spatial, and temporal patterns of the major greenhouse gas (CO_2, CH_4, and N_2O) emissions in the earth systems. The Greenhous Gas (GHG) emissions from inland waters, including rivers, lakes, and reservoirs, remain largely uncertain at the global and continental scales. Empirical-based approaches are widely used to assess the inland water CO_2, CH_4, and N_2O emissions. However, the accuracy of the empirical approaches would substantially decrease with the environmental condition changes mainly due to the inherent weakness in explaining the mechanisms of carbon and nitrogen dynamics in the terrestrial and aquatic systems. Inspired by the improved understanding of the mechanisms controlling carbon and nitrogen dynamics at the terrestrial-aquatic interface, a newly developed scale adaptive water transport model was coupled with the Dynamic Land Ecosystem Model (DLEM) to construct a submodule called – DLEM Terrestrial Aquatic Interface Model (DLEM-TAIM) to better represent the river routing and associated physical and biogeochemical processes. To the best of our knowledge, the DLEM-TAIM is the first process-based model that is capable of concurrently estimating CO_2, CH_4, and N_2O emissions from inland waters. First, we used Chesapeake Bay watershed as a testbed for testing the performance of the coupled model in simulating hydrological processes, river temperature and carbon dynamics at the land-aquatic continuum. Then we nested the inland water GHG model into the DLEM-TAIM modeling framework and applied the coupled model to the Conterminous United States (CONUS). Driven by a gridded dataset at a spatial resolution of 5 arc-minutes, we examined how multiple changes in climate, land use/land cover, elevated CO_2,

nitrogen deposition and nitrogen fertilizer use affected the GHG emissions from inland water and the relative role of high-order streams and headwater streams in the continental carbon budget for the time period from 1860 to 2018. Our simulation results show that the emissions of CO_2, CH_4, and N_2O from inland waters in the recent decade (2009-2018) were 201.73 ± 30.0 Tg C/year, 7.8 ± 0.6 Tg CH_4-C/year , 60.53 ± 8.7 Gg N_2O-N/year, which increased by 29.7%, 33.26%, and 58.2% since the 1900s, respectively. The Global Warming Potential (GWP) at the 100-year time horizon (GWP-100 years) for CO_2, CH_4, N_2O from inland waters are 0.73 ± 0.11, 0.04 ± 0.01, 0.29 ± 0.02 Pg CO_2 equiv. yr^{-1}, respectively. The total of GWP of the three GHG emissions from inland waters over the CONUS was 1.06 ± 0.13 Pg CO_2 equiv. yr^{-1}, which is comparable to terrestrial carbon sink over CONUS. Thus, the continental carbon and GHG budget need to consider emissions from inland waters.

Acknowledgments

I would like to express my greatest thanks for the guidance of my major advisor, Dr. Hanqin Tian, and his sustainable encouragement during the past five years. Without his patience, this dissertation would never be accomplished. I appreciate the continuous supports from my committee members: Dr. Xing Fang, Dr. Kalin Latif, Dr. Ming-kuo Lee, and Dr. Susan Pan.

I would like to thank our project collaborators: Dr. Marjy Friedrichs, Dr. Raymond Najjar, Dr. Eileen Hofmann, without the funding support from NASA projects (NNX11AD47G and NNX14AF93G) and NOAA projects (NA16NOS4780207, NA16NOS4780204)), I could not accomplish my research. I also would like to express thanks to my university reader Dr. Di Tian who help me with the dissertation.

I would like to thank our current group members: Dr. Hao Shi, Dr. Tina Xu, Mr. Naiqing Pan, Mr. Zihao Bian, Mrs. Jing Wang, Mr. Boyuan Wang, Mr. Zhuonan Wang, Mr. Yongfa You, Mr. Dr. Xing Wu, Dr. Chengcheng Gang, Dr. Fangjie Mao, Mr. Hang Song, Mrs. Liangyu Huang. They give me so much help.

I am also grateful to our previous group members: Dr. Jia Yang, Dr. Shree Dangal, Dr. Kamaljit Banger, Dr. Guangsheng Chen, Dr. Wei Ren, Dr. Bo Tao, Dr. Liang Xue, Dr. Yi Zhou, Dr. Peipei Pan, Dr. Dan Liu, Dr. Zhihua Pan, Dr. Chaoqun Lu, Dr. Bowen Zhang, Dr. Qichun Yang, Dr. Nan lv, Mr. Jingwei Wu, Dr. Qinfeng Gao, Dr. Shulan Cheng.

I want to thank my friends: Dr. Xin Fan, Dr. Yecheng Xu, Dr. Haoran Zhang, Dr. Shaoyang Yang, Dr. Tao Jiang, Dr. Zekun Wang, Dr. Fuxi Zhang, Mr. Penghui Gao, Dr.Rui

Yang, Mr. Dongji Feng, Mrs. Jingjing Li, Dr. Xinquan Cheng, Dr. Xin Fan. I received many bits of help from my friends here for the past five years.

Finally, I would like to thank my beloved wife, Ran Zhang, my parents, Mr. Ke Yao and Mrs. Suying Guo, and my wife's parents Yinyan Kong and Zhiyong Zhang, for all their supports, encouragement and companionship. Their guidance and encouragement inspire me in my whole life. And also, I would like to thank my beloved sons: Peter Yao and Lucas Yao, who give me so much happiness.

Table of Contents

List of Tables

List of Figures

List of Abbreviations

GHG	Greenhouse Gas
IPCC	Intergovernmental Panel on Climate Change
CONUS	Contiguous United States or Conterminous United States
DLEM	Dynamic Land Ecosystem Model
MOSART	Model of Scale Adaptive River Transport
TAIM	Terrestrial Aquatic Interface Model
MAR	Mid-Atlantic Region
CBW	Chesapeake Bay Watershed
DOC	Dissolved Organic Carbon
POC	Particulate Organic Carbon
DIC	Dissolved Inorganic Carbon
DON	Dissolved Organic Nitrogen
PON	Particulate Organic Carbon
GDP	Gross Domestic Product
GWP	Global Warming Potential
USGS	United States Geological Survey
DEM	Digital Elevation Model

SWAT Soil & Water Assessment Tool

Global NEWS model Global Nutrient Export from Watersheds (NEWS) model

CBW Chesapeake Bay Watershed

DBW Delaware Bay Watershed

Chapter 1: Introduction

1.1 Background

The concentration of atmospheric greenhouse gases (GHGs), including CO_2, CH_4, and N_2O, increased by 40%, 150%, and 20%, respectively, during the past century (Ciais et al., 2014, 2008; Montzka et al., 2011). The growing awareness of the negative impact induced by global warming prompted great interests of the scientific communities to understand the inherent mechanisms controlling the CO_2, CH_4, and N_2O dynamics in the earth systems. Inland waters, among the major component of the earth's surface, play active roles in the global or regional carbon cycle and GHG emissions (Raymond et al., 2013). The estimated global inland water CO_2 degassing reached 2.1 Pg C yr^{-1}, which is comparable to the land carbon sink with the estimated ranges from 1.2 to 3.8 Pg C yr^{-1} (Regnier et al., 2014). It has been suggested that inland water releases significant CO_2 with the fluxes rate much higher than that of the land surface (Butman and Raymond, 2011). Not only CO_2 emission, significant CH_4 and N_2O emissions have been observed from inland waters worldwide (Bastviken et al., 2004; Kroeze et al., 2005; Stanley et al., 2016). The greenhouse gas effect of CH_4 and N_2O are much higher than that of the CO_2, with the Global Warming Potential (GWP) of 28-32 and 298 times of CO_2, respectively (Ciais et al., 2014). Therefore, concurrently estimating the contribution of inland water CO_2, CH_4 and N_2O emissions became a critical issue to close the global or regional GHG budget.

Inland water GHG emissions were poorly constrained at the global and continental scales. The global estimates of the riverine CO_2 emissions range from 540 Tg C/yr to 1.7 Pg C /yr (Lauerwald et al., 2015; Raymond et al., 2013). The riverine CH_4 emission remains highly

uncertain with the magnitude ranges from 1.1 to 20.1 CH_4-Tg C/year. Little is known about the N_2O emission from rivers, with the magnitude ranges from 0.03 Tg N_2O-N / year to 2.1 Tg N_2O -N/ year globally (Beaulieu et al., 2011; Hu et al., 2016; Kroeze et al., 2005; Maavara et al., 2018). The budget of lake N_2O is still in the debate regarding the role of lakes as N_2O sink or sources at large scale (Mengis et al., 1996; Webb et al., 2019). More reliable modeling tools are needed to reduce uncertainties.

Most of the previous researches used empirical-based approaches to estimate the CO_2, CH_4, and N_2O emissions from lakes, reservoirs, and rivers, respectively. Raymond et al. (2013) used water quality data, including the concentration of inorganic carbon, alkalinity, water temperature, to quantify the pressure of carbon dioxide (pCO_2) and the associated CO_2 evasions. They directly multiplied the estimated fluxes rates with the surface area of the water body to assess the total emissions, which was unable to quantify the temporal pattern of the CO_2 emissions over time. A similar approach named emission factor (EF) has been widely deployed to quantify CH_4, and N_2O emissions from inland waters in Intergovernmental Panel on Climate Change (IPCC) reports and research articles (Metz et al., 2005; Beaulieu et al., 2011; Gardner et al., 2016). However, the current empirical-based approaches established on statistical regression cannot reveal the mechanisms responsible for CO_2, CH_4 and N_2O fluxes in the aquatic systems. The accuracy of the empirical equation or data-based analysis would decrease when the environmental condition changes, which undermine its application in long-term assessment and future projection under the context of aggravated climate change and intensive human disturbances.

Inland water emissions strongly regulated by climate change and human disturbances. The CO_2 emission is closely relevant to the hydraulics loading, which is positively correlated

with precipitation (Liu and Raymond, 2018). The raised temperature directly influences the equilibrium concentration of CO_2, CH_4 and N_2O dissolved in water, which in turn moderates the gas exchange rate between the air-water interfaces (Sander, 2015). Human activities, such as forest clear-cutting, induced large carbon loading from land to river, which largely increased riverine CO_2 and CH_4 evasions (Noacco et al., 2017). On the other hand, agriculture activities increased the alkalinity of the rivers which significantly inhibit the CO_2 emissions from waters (Raymond and Cole, 2003).

Motivated by the increased understanding of the production and consumption of CO_2, CH_4 and N_2O in waters through field experiments (Beaulieu et al., 2011, 2010; Houghton, 2010; Quick et al., 2019; Stanley et al., 2016), process-based models or semi-empirical models have been developed to estimate the magnitude and spatio-temporal patterns of GHG emissions. Laruelle et al. (2015) developed a process-based model that decoupled with the earth system models to simulate the CO_2 evasion along the land-aquatic continuum over the north-eastern region of the Conterminous United States (CONUS). Similarly, the semi-processed based riverine model has been proposed and decoupled with the GlobalNEWs model to estimate N2O emissions from rivers at the global level (Maavara et al., 2018). Thus, the hydrological models are the key component of the inland water GHG modeling.

It should be noted that rivers not only bridge up the terrestrial and oceanographic ecosystems but also link the inland waters (rivers, lakes, and reservoirs). Thus, large scale river routing models with lakes mixing are of great importance to represent the lateral transport of carbon and nitrogen constitutes and the associated GHG emissions from inland waters. Wollheim et al. (2008) used a semi-empirical large scale hydrological model to estimate lateral nitrogen transport from land to ocean, and the nitrogen loading products of this study have been applied to

estimate the riverine N_2O emissions (Beaulieu et al., 2011). The riverine carbon and nitrogen fluxes estimated by Global-News model have been applied extensively to assess the CO_2 and N_2O emissions globally (Kroeze et al., 2005; Kroeze and Seitzinger, 1998; Raymond et al., 2013; Seitzinger and Kroeze, 2000). Therefore, accurately modeling the riverine processes is critical to understand the carbon and nitrogen balance of the land-aquatic system.

Since most previous riverine studies only focus on high-order stream, recent studies suggest that headwater streams play important roles in global carbon and nitrogen cycles, and GHG budgets: (1) Headwater streams are hotspots of carbon dioxide emissions, which account for 70% of total emissions from global rivers (Raymond et al., 2013). (2) Headwater streams also strongly regulate the nitrogen removal of the river basin (Grant et al., 2018). (3) Recent studies investigated the N_2O emission along with different stream orders and found that the 1^{st} order streams released a large proportion of the N_2O gas in the corn-belt located at the central region of the CONUS (Garnier et al., 2009; Turner et al., 2015). (4) Headwater streams are located at the interface between the land and aquatic systems, thus they are very sensitive to climate change and human disturbances (Isaak et al., 2016a). All these confirm that understanding the physical and biogeochemical processes within headwater streams is critical to estimate the inland water GHG emissions. However, conventional large-scale river routing models were conducted at coarse spatial resolutions due to the limited computational resources, which could not well capture the processes within small headwater streams (1^{st} – 3^{rd} order streams). Therefore, representing the processes within headwater streams river remain a challenge, which substantially hampers the performance of the current large-scale hydrological models in estimating GHG emissions.

To better understand the dynamics of CO_2, CH_4, and N_2O fluxes in inland waters and the consequential GHG emissions at the continental scale, we improved the hydrological model and the associated biogeochemical component within the terrestrial ecosystem modeling framework – DLEM (Dynamic land ecosystem model) (Tian et al., 2016). We applied the coupled model to the Contiguous United States (CONUS) to estimate the GHG emissions and the relative role in the continental carbon budget.

1.2 Study area

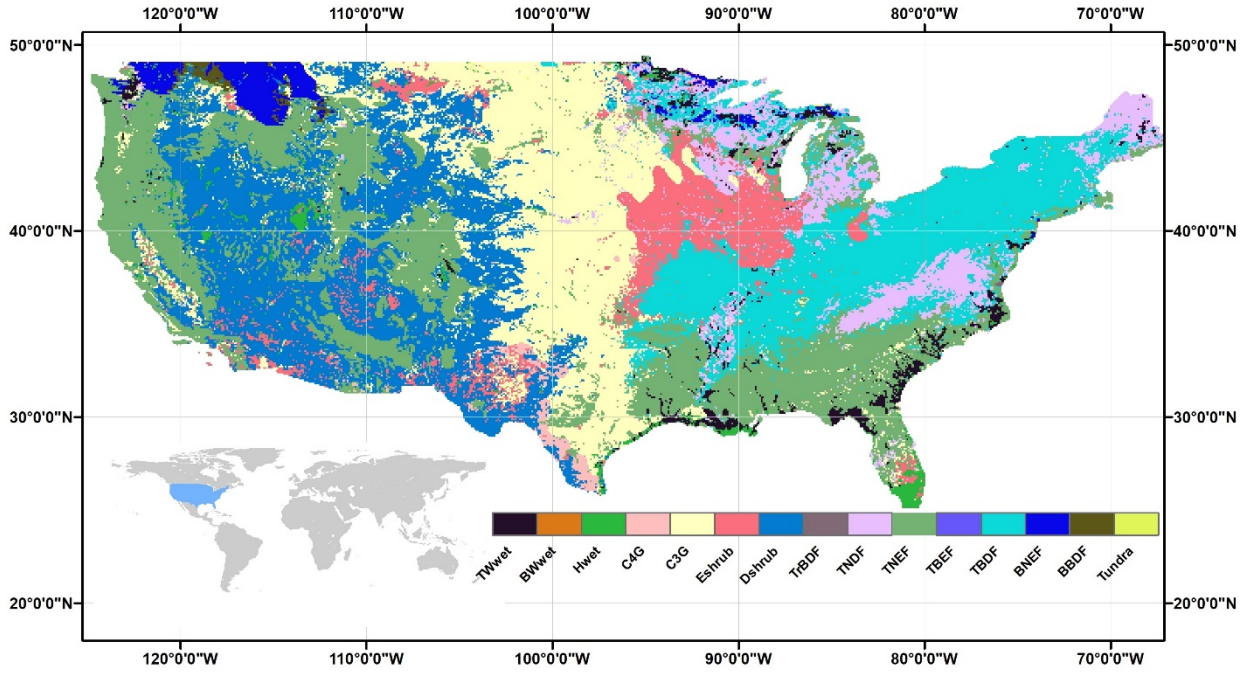

Figure 1-1. The major plant function types over the Contiguous U.S.

(BBDF: Boreal Broadleaf Deciduous Forest, BNDF: Boreal Needleleaf Deciduous Forest, TBDF: Temperate Broadleaf Deciduous Forest, TBEF: Temperate Broadleaf Evergreen Forest, TNEF: Temperate Needleleaf Evergreen Forest, TrBDF: Tropical Broadleaf Deciduous Forest, TrBEF: Tropical Broadleaf Evergreen Forest, Eshrub: Evergreen Shrub, Dshrub: Deciduous

Shrub, C3G: C3 Grassland, C4G C4 Grassland, Hwet: Herbaceous Wetland, BWwet: Boreal Woody Wetland, TWwet: Tropical Woody Wetland)

This study focusses on the Conterminous United States (CONUS) (Figure 1-1), which is located at the center of the North America continent. The region spans 4,509 km from Florida (east) to the State of Washington (West) and extends 2,660 km from the Northern border to the South. As the major land of the world's most powerful country, this region covers 8,080,464 km^2 and sustains 327.2 million people based on the census 2018. The overall climate condition is temperate but becomes subtropical in the south. The dominant plant function types in the eastern CONUS are temperate evergreen needle leaf and deciduous broadleaf. The evergreen shrubland and C3 grassland are the major natural vegetation types over the center of the CONUS. In the western region, the temperate needle leaf forest and deciduous shrubland cover most of the spaces.

1.3. Research objectives

The overarching goal of this study is to predict the GHG emissions from inland waters of the CONUS and understand the inherent mechanism underneath the simulated results. The attribution analysis would be helpful to evaluate the contribution of each environmental factor to the GHG emission from inland water, which would have explicit implications for land management.

We raise three essential research questions:

Question 1: What is the impact of climate change or anthropogenic disturbances on the spatial and temporal patterns of run-off and water temperature?

Hypothesis: Significant climate change and extensive human activities have substantially altered the land processes during the last century. The in-stream processes would follow the changes in land processes.

Question2: What is the magnitude of CO_2, CH_4, and N_2O emissions from inland waters? How did the GHG emissions from inland waters change in the past century?

Hypothesis: The magnitude of CO_2, CH_4, and N_2O emissions from inland waters can be better estimated by the improved riverine biogeochemistry model. The changes in land carbon and nitrogen loading to rivers would influence the GHG balance in inland waters.

Question 3: How much do climate and human activities affect the inland water GHG budget?

Hypothesis: Climate change and hydraulic loading increased carbon and nitrogen loading from land to rivers, which in turn increased GHG emission from inland waters. Human activities induced more N loading to contribute to the increase in GHG emissions.

Our strategies to answer these questions include the following tasks:

Task 1: Examine the changes in water temperature induced by climate change or land-use conversion.

Task 2: Investigate the CO_2, CH_4, and N_2O emissions from inland waters.

Task 3: Conduct factorial experiments to quantify the contribution of environmental factors, including elevated atmospheric CO_2 concentration, climate inputs, land-use conversions, and nitrogen fertilizer/manure application, nitrogen deposition, to the inland water GHG emissions.

1.4 Research methods

1.4.1. The Dynamic Land Ecosystem Model (DLEM model)

Dynamic Land Ecosystem Model 2.0 (DLEM 2.0) (Figure 1-2 a) is a fully distributed land biosphere model that explicitly simulates the vegetation dynamics, soil biogeochemistry, and the

associate land carbon cycle, nitrogen cycle, and fluxes of water and nutrients. The land model of DLEM quantifies runoff, carbon, and nitrogen loading as the initial condition of the aquatic module. Recently, DLEM has been extensively used in the eastern coast and Mississippi river basin to estimate the carbon and nitrogen fluxes at the terrestrial-aquatic interface.

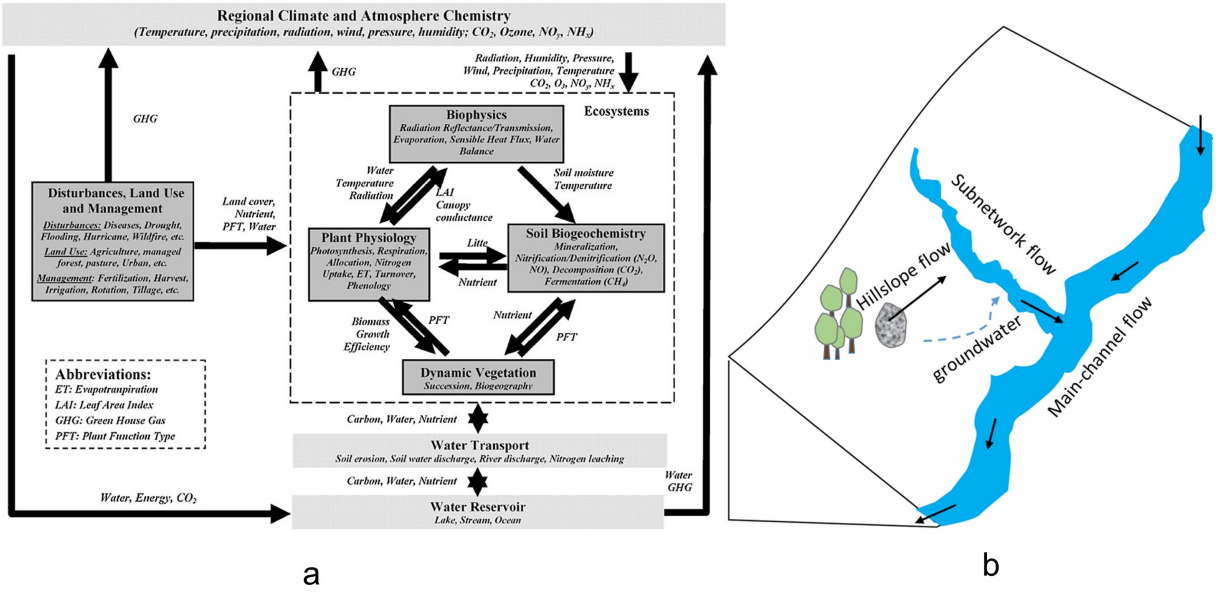

Figure 1-2 The general Framework of Dynamic Land Ecosystem Model - Terrestrial Aquatic Interface Model (DLEM –TAIM). (a). The concept model of DLEM. (b). The concept model of scale adaptive water transport scheme.

1.4.2. Scale adaptive water transport scheme

To better represent the riverine processes, a scale adaptive and fully physical-based scheme named Model Of Scale Adaptive River Transport (MOSART) (Figure 1-2 b) was incorporated into DLEMframework (Li, 2013, 2015). We named this couple modeling system as DLEM – TAIM. The MOSART model helps to reduce both spatial and temporal scale effects by considering the sub-grid routing processes. MOSART model separates the water transport within the grid cells into three components: hillslope flow, subnetwork flow, and main channel flow.

DLEM land model provides surface runoff and drainage runoff to the riverine model, and hillslope flow represents the merging of surface runoff. The water of hillslope flow would contribute to the subnetwork flow combined with groundwater discharge. There is a groundwater pool nested into the grid unit, which receives water from drainage runoff and flows out with parameterized residence time. The main channel flow combines inflow water from upstream grid cells and local subnetworks, and routes to the downstream grid cell. All the channel routing processes used a hydraulic-based river routing method (kinematic wave methods).

1.4.3. Coupling water temperature with the DLEM-TAIM

Inspired by the newly developed hydrological framework, we developed a fully physical-based water temperature model. We improved the soil temperature component in the DLEM land model to represent the effect of the Leaf Area Index (LAI) and litter equivalent LAI to the soil temperature. We linked the soil water temperature to the groundwater heat input. The temperature of both groundwater and surface water function as boundary conditions, forcing the water temperature in each river segment along the streamline.

1.3.4. Riverine biogeochemistry and GHG dynamics

Align with the new feature of the water transport model; we extended the biogeochemical processes from the main channels to the subnetworks within a grid unit. We developed a process-based riverine CH_4 and N_2O model and incorporated it into the DLEM C-N coupled modeling framework. The production of CH_4 is from the decomposition of organic carbon in the water column and bottom sediment. The oxidation of CH_4 is associated with the denitrification of NO_3^- within waters. Both nitrification and denitrification would contribute to the production of N_2O in waters.

1.5 Simulation protocol

We set-up an equilibrium run for all the grid units with all the model driving forces keep consistent with the year 1860. When the carbon, nitrogen and water pool of one grid unit reaches steady-state, the equilibrium run finishes. To smooth the jumping effect of fluxes from equilibrium run to the transient run, we conducted a spin-up run with climate inputs selected randomly during 1860-1890. After the spin-up run, we conducted the transient run from the year 1860 to 2018 with all the climate forcing, land-use change, CO_2 concentration, N deposition, and N fertilizer application changed year-by-year). We calibrated and validated the model performance against observations from the major rivers across the contiguous U.S.

To attribute the contribution of environmental factors to the riverine fluxes and GHG degassing, we designed factorial experiments with each of the driving forces keep consistent with the year 1860. We considered the simulation with all the driving forces changed over time as all-combine run. The contribution of environmental factors to the changes in GHG emissions was derived from the comparison between factorial experiments with all-combine run.

1.6 Organization of dissertation

The dissertation is organized into six standalone chapters. Chapters two to five are organized in the format of journal articles and will be submitted to different professional journals.

Chapter 2: Coupling DLEM with a scale adaptive water transport model.

In chapter two, we coupled a scale adaptive water transport scheme with our land biosphere model (DLEM) and named it as DLEM –TAIM. We described detailed information of the hydrological model structure, input data processing, model parameters, and validate the modeled water discharge against observations.

Chapter 3: Assessing impacts of global change on the water temperature of headwater and high-order streams across the Mid-Atlantic region of the U.S. by using a coupled modeling framework

In chapter three, we developed a fully physical-based water temperature model within the DLEM- TAIM framework, which links the thermal energy balance of land and aquatic systems together. Therefore, we can better understand how land processes affect water discharge and water temperature, which is essential to the riverine biogeochemistry. This study used the Mid-Atlantic Region of the U.S. as the testbed.

Chapter 4: Modeling carbon export and CO_2 evasion from river network: Application to Chesapeake Bay Watershed and Delaware River Basin.

In chapter four, we mostly focus on riverine carbon dynamics. We developed the riverine CO_2 evasion model under the DLEM- TAIM modeling framework. We used the Chesapeake Bay and Delaware Bay region of the U.S. to test our model. We validated the riverine carbon exports and compared our estimated CO_2 degassing with previous studies. We highlighted the importance of 1^{st} order stream (or refers to as small steams) in riverine CO_2 emissions, which can be well captured by our scale adaptive riverine model.

Chapter 5: Assessing the spatial and temporal variations in CO_2 and CH_4 emissions from inland waters over the Conterminous U.S.

In chapter five, we developed a process-based riverine CH_4 model based on the riverine carbon model described in chapter 4 and incorporated it into the DLEM- TAIM modeling framework. We applied the riverine carbon model across the contiguous U.S. and validated the riverine carbon fluxes of major rivers in the CONUS, and finally predicted the spatial and temporal patterns of riverine CH_4 concentration and emissions across the CONUS.

Chapter 6: Increased Riverine N_2O emission across the continental U.S.

In chapter six, we develop a process-based riverine N_2O model within the DLEM- TAIM framework. We validated the exports of nitrogen species of the major rivers in the CONUS. We also validated the performance of the newly developed model in predicting the spatial and temporal patterns of riverine N_2O emissions across the CONUS through observations collected from the literature review.

Chapter 7: Summarizing GHG emissions from the inland water systems across the CONUS. We discussed the nexus between the triple GHGs within aquatic systems. We quantified the CO_2 equivalent emissions of the triple GHGs and compared them with the U.S. land carbon sink to highlight the importance of the inland water GHG emissions.

Chapter 2. Coupling DLEM with a scale adaptive water transport model

2.1. Introduction

Rivers, as referred to as the land-aquatic continuum, bring carbon, nutrient, sediment, and thermal energy into the coastal ocean, and play essential roles in the regional carbon and nutrient cycles (Regnier et al., 2013). Changes in patterns of flow regimes led to profound physical and ecological impacts on the lower reaches of the rivers and the coastal estuaries (Palmer and Ruhi, 2019). Climate change and human activities substantially influenced the spatial and temporal patterns of surface runoff and streamflow (Raymond and Hamilton, 2018).

To better understand to what extent the changes in environmental conditions would affect the flow regimes, we proposed a coupled hydrological modeling framework in this chapter. We incorporated a newly developed water transport scheme known as Scale Adaptive Water Transport Model (MOSART) (Li et al., 2013) into the framework of the process-based ecosystem model -- Dynamic Land Ecosystem Model (DLEM) (Tian et al., 2012; Liu et al., 2013), aiming to improve the representation of daily freshwater discharge. This newly developed modeling framework was named as the Dynamic Land Ecosystem Model- Terrestrial Aquatic Interface Model (DLEM-TAIM). The Chesapeake Bay Watershed and Delaware Bay Watershed (Figure 2-1), which located in the northeastern of CONUS, experienced significant land-use and climatic changes since the beginning of the 20th century (Walsh et al., 2013). The ubiquitous data available, including observations of water discharge, water quality filed measurement, land management as well as climate inputs, make this region a suitable place as a testing bed of the DLEM-TAIM.

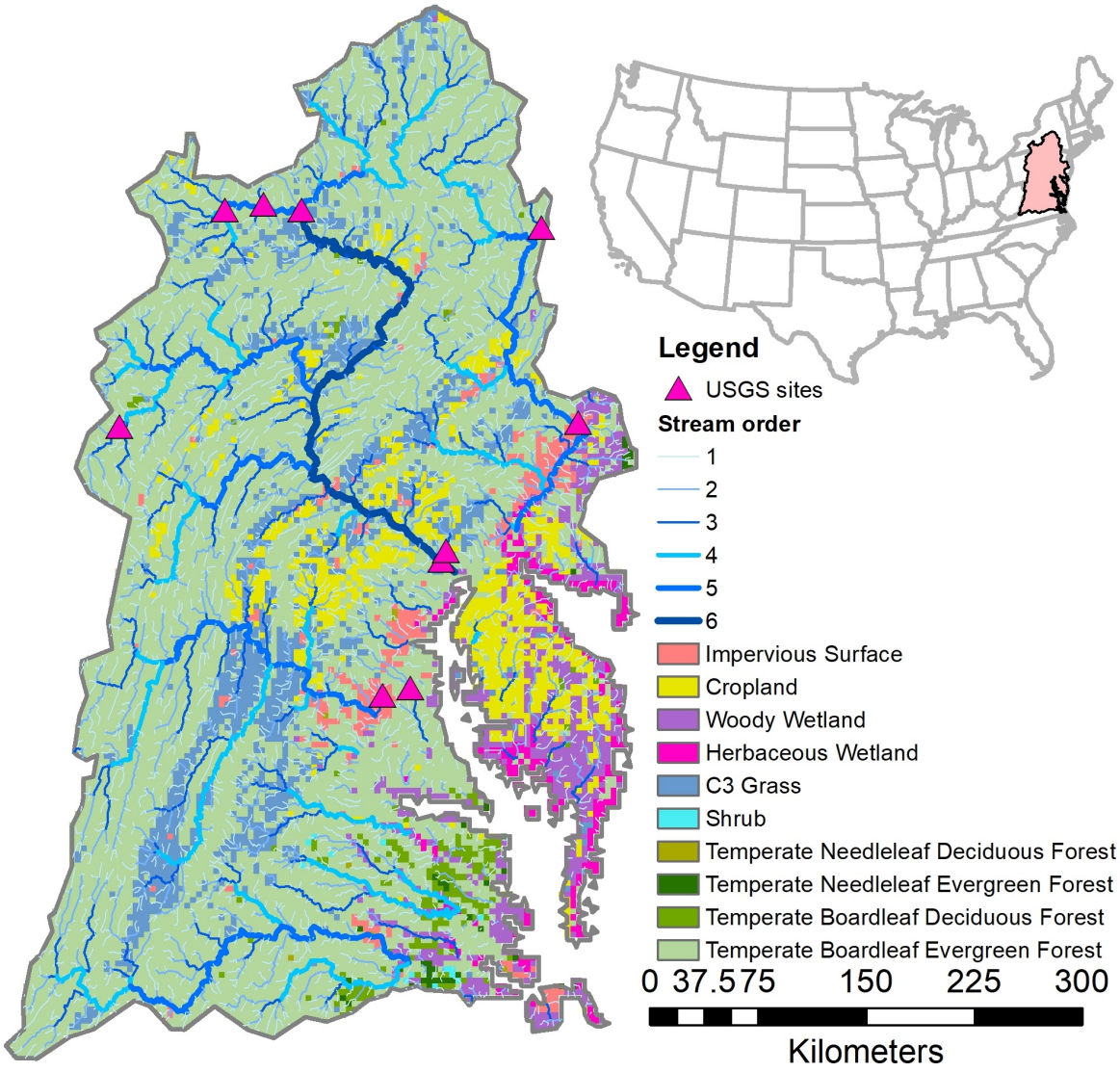

Figure 2-1. The major plant function types and land-use in Chesapeake Bay Watershed and Delaware Bay Watershed.

2.2. The development of the hydrological model DLEM - TAIM

2.2.1. The Dynamic Land Ecosystem Model (DLEM model)

The Dynamic Land Ecosystem Model 2.0 (DLEM 2.0) (Figure 2-2. A) is a fully distributed land model, which explicitly predict carbon-nitrogen coupled vegetation dynamics (Tian et al., 2012;

Chen et al., 2013) and terrestrial water cycle (Liu et al., 2013). This model simulates plant growth, soil biogeochemistry, and the associated water fluxes on land driven by the forces include climate variables, CO_2 concentration, N deposition, and N applications.

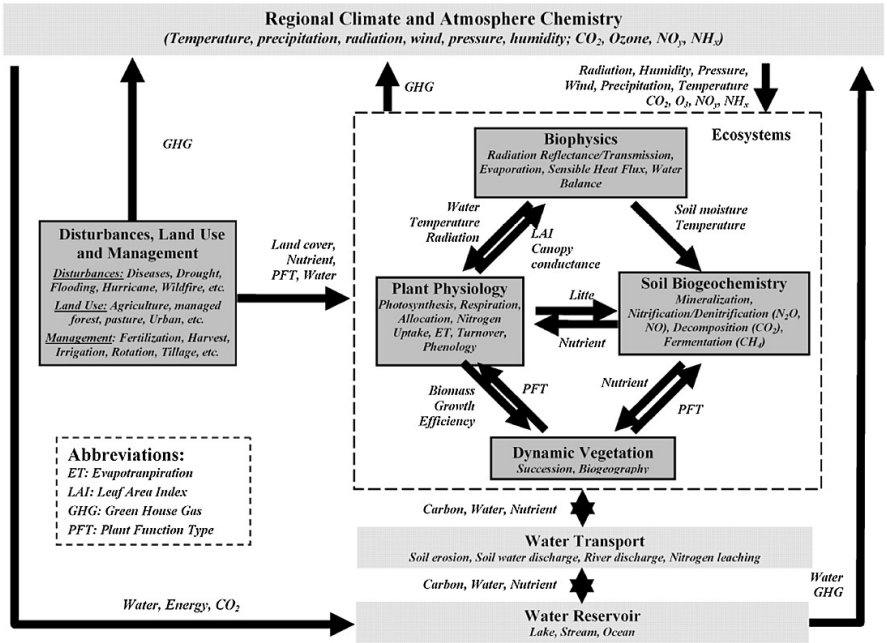

(A)

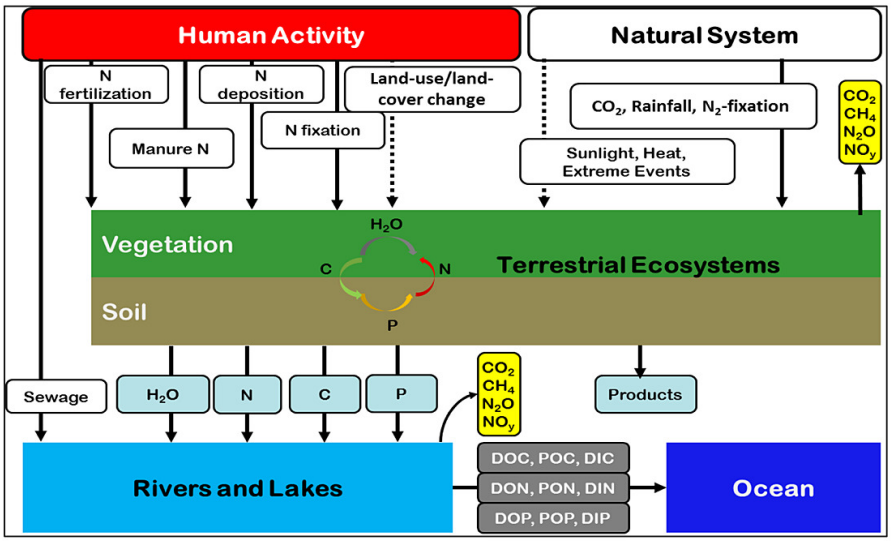

(B)

Figure 2-2. The general framework of the Dynamic Land Ecosystem Model (A) and Terrestrial Aquatic Interface Model (B) (Tian et al., 2015c).

The previous DLEM version used Linear Reservoir routing (LRR) method (Coe, 1998; Costa and Foley, 1997), which deploys simple empirical linear equations to represent the residence time, and outflow rate of the local stream and lake pool which are nested into a grid unit. The model has been applied to estimate the fluxes of water, carbon (Tian et al., 2015c), and nitrogen (Yang et al., 2015b) from land to the oceans across the CONUS (Figure 2-2. B).

2.2.2. Hydraulic methods

Linear Reservoir Routing (LRR) method calculates flow velocity solely based on channel slope, which misses critical physical parameters in water transport processes such as roughness, water depth, flow distances, etc. (Chow, 1964a). Thus, the hydraulics methods were introduced in our model, which solved Saint-Venant equations (SVE) to calculate outflow rates from the current grid cell to the downstream grid cell. Conventionally, there are three ways to solve the SVE. The full SVE equation, or named as dynamic wave method, contains all the physical variables and solving it requires enormous computational resources. Thus, one of its simplified versions, the Kinematic Wave Method was introduced in the model (Chow, 1964). Here, the SVE is given as:

$$\frac{\partial Q}{\partial x} + L\frac{\partial h}{\partial t} = q \tag{1}$$

$$S_f - S_0 = 0 \tag{2}$$

Where Q is outflow rate; h is the depth of runoff; q is lateral inflow from subnetworks; S_f is friction gradient; S_0 is longitudinal slope of the channel bottom, L is the length of the river channel.

$$v = \frac{1}{n}h^{\frac{2}{3}}S_0^{\frac{1}{2}} \tag{3}$$

where v is the flow velocity, and n is the Manning's roughness coefficient.

$$\mathrm{Q} = vhL = \frac{L}{n}h^{\frac{5}{3}}S_0^{\frac{1}{2}} \tag{4}$$

The equation can be converted as:

$$\mathrm{h} = \left(\frac{n}{L} S_0^{-\frac{1}{2}}\right)^{\frac{3}{5}} Q^{\frac{3}{5}} \tag{5}$$

here we assume:

$$a = \left(\frac{n}{L} S_0^{-\frac{1}{2}}\right)^{\frac{3}{5}} \tag{6}$$

$$b = \frac{3}{5} \tag{7}$$

then:

$$h = aQ^b \tag{8}$$

and equation 1.1 can be modified to:

$$\frac{\partial Q}{\partial x} + L\frac{\partial}{\partial t}(aQ^b) - q = 0 \tag{9}$$

We applied the finite difference method to estimate the outflow as:

$$\frac{\Delta t}{\Delta x} Q_{i+1}^{t+1} + La(Q_{i+1}^{t+1})^b = \frac{\Delta t}{\Delta x} Q_i^{t+1} + La(Q_{i+1}^{t})^b + q_{i+1}^{t+1}\Delta t \tag{10}$$

where, Q_i^{t+1} is the discharge of the unit catchment i at period t+1, while Q_{i+1}^{t+1} is the discharge of the last adjacent unit catchment of catchment i at period t+1.

The equation was solved by using Newton-Raphson method:

$$[Q_{i+1}^{t+1}]^{k+1} = [Q_{i+1}^{t+1}]^k - \frac{\frac{\Delta t}{\Delta x}[Q_{i+1}^{t+1}]^k + La\left([Q_{i+1}^{t+1}]^k\right)^b - \frac{\Delta t}{\Delta x} - La(Q_{i+1}^{t})^b - q_{i+1}^{t+1}\Delta t}{\frac{\Delta t}{\Delta x} + Lab\left([Q_{i+1}^{t+1}]^k\right)^{b-1}} \tag{11}$$

2.2.3. Scale adaptive water transport model

A scale adaptive and fully physical-based model named Model for Scale Adaptive River Transport (MOSART) has been incorporated into DLEM (Li et al., 2013), aiming to reduce the scale effect in both spatial and temporal levels. The MOSART model separates the water

transport within the computational units into hillslope flow, subnetwork flow, and main channel flow. The water from surface runoff (calculated in DLEM land model) merges as hillslope flow first. The subnetwork flow, or small headwater streams, receive water from hillslope flow and groundwater and flows into the main channel of the local grid unit. All the three river routing processes of the MOSART model used kinematic wave methods because it is accurate in predicting overland flow and channel flow. The diffusive wave method was not used at this level because we do not consider the backwater effect in a coarse spatial resolution in this study. The concept model of the MOSART was shown in figure 2-3.

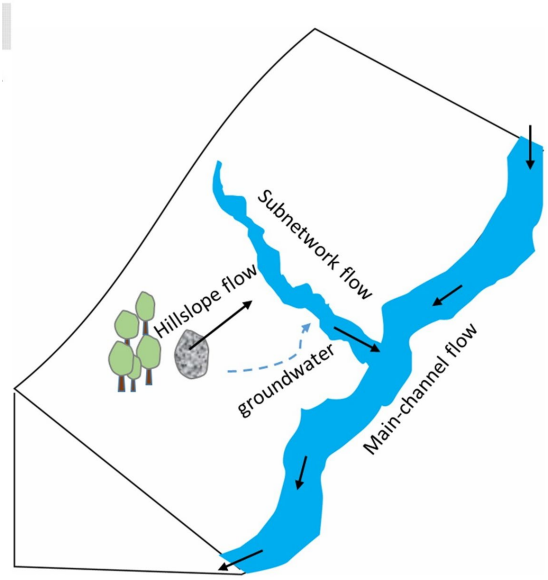

Figure 2-3. The general framework of the scale adaptive water transport module.

To attain scale adaptive, the length of the main channel, subnetworks, and hillslope flow changes align with the changes in spatial resolution:

$$L_h = \frac{A_{local}}{2L_{total}} \tag{12}$$

$$L_s = \frac{A_{local}}{2L_{main}} - L_h \quad (13)$$

Where L_h and L_t represent the length of the hillslope flow and subnetwork flow, A_{local} is the surface area of a grid cell; L_{main} is the length of the main channel; L_{total} denotes the total length of the rivers or streams within a grid unit. Here, the L_{total} and L_{main} are generated from fine resolution (30-m) hydrological corrected topographic data National Hydrography Dataset Plus V2 (NHD plus V2, available at: http://www.horizon-systems.com/NHDPlus), and aggregated into the coarse resolutions grid cell (4-km) for our model simulation.

Table 2-1 The Manning's roughness coefficient of different land-cover types.

	Land cover types	**Manning roughness coefficient**
1	Bare land	0.01
2	glacier	0.035
3	Deciduous forest	0.36
4	Evergreen forest	0.32
5	Shrubland	0.4
6	Cropland	0.32
7	Grassland	0.37
8	Impervious surface	0.04
9	Woody wetland	0.086
10	Herbaceous wetland	0.1825

Note: The parameters were primarily brought from Kalyanapu et al. (2010) and adjusted to match the data.

To obtain the channel slope of the subnetwork and main channel, we first quantified the stream order for each of the NHD streamlines. Then we defined the channel slope of the highest stream orders of the NHD 30-m data within the 4-km grid as the slope of the main channel of the grid unit. Other than the highest stream order within the grid cell, the average slope of the low-order streams is defined as the slope of the subnetwork.

Tabel 2- 2 The calibrated Manning's roughness coefficient of stream orders.

Stream order	Manning roughness coefficient
Subnetworks	0.06
1	0.05
2	0.055
3	0.05
4	0.045
5	0.04
6 or higher	0.03

In the current modeling framework, we do not explicitly simulate the lateral groundwater transport from the plant's root zone to the headwater streams. The groundwater process is a lumped groundwater pool with the outflow rates calculated from a predefined residence time (Coe, 1998; Costa and Foley, 1997).

Manning's roughness coefficient of land surface and river channels are parameterized in this study. For overland flow, the surface roughness of that grid cell is calculated from historical land-cover types. The roughness for each land-cover type is given in (Kalyanapu et al., 2010)

(Table 2-1). Similar to other distributed hydrological models, we divide the stream network into different segments based on stream orders and calibrate the parameters (Table 2-2) for each stream order (Chen et al., 2017). We define the subnetwork within the grid cell as 0 stream order. We calibrated the Manning's roughness to each stream order.

2.2.4. Watershed delineation and river network input dataset

In this study, we obtained the 4-km resolution climate variables from the PRISM dataset (available at: http://www.prism.oregonstate.edu/). To match the spatial resolution of the climate data, we developed a 4-km resolution hydrography dataset, including flow direction, flow accumulation, and flow distance (Yao et al., 2012; Yao and Shi, 2015). The 4-km resolution hydrography data was generated from the Digital Elevation Model (DEM) from the hydrological corrected hydrography dataset HYDRO1K in 1-km resolution. Directly resample the original 1-km resolution DEM data to 4 km would substantially alter the byproduct of the hydrological analysis based on the DEM data including the flow direction, streamline and watershed boundary. We, therefore, conditioned the topographic data using the following three steps. (1) Export the stream-lines and watershed boundaries generated from the fine resolution HYDRO1K dataset as vector format. (2). Build walls for each watershed (Vincent and Soille, 1991) on the 4-km resolution DEM, which means increasing the elevation around the vectorized watershed boundaries. The walls help to control the position of the boundary line during the flow direction calculation. (3)Agree-method, an improved version of the stream burning algorithm, which decreases the elevation value of the streamline and the associated flood plain area, helps to confine the position of streamlines (Lindsay, 2016).

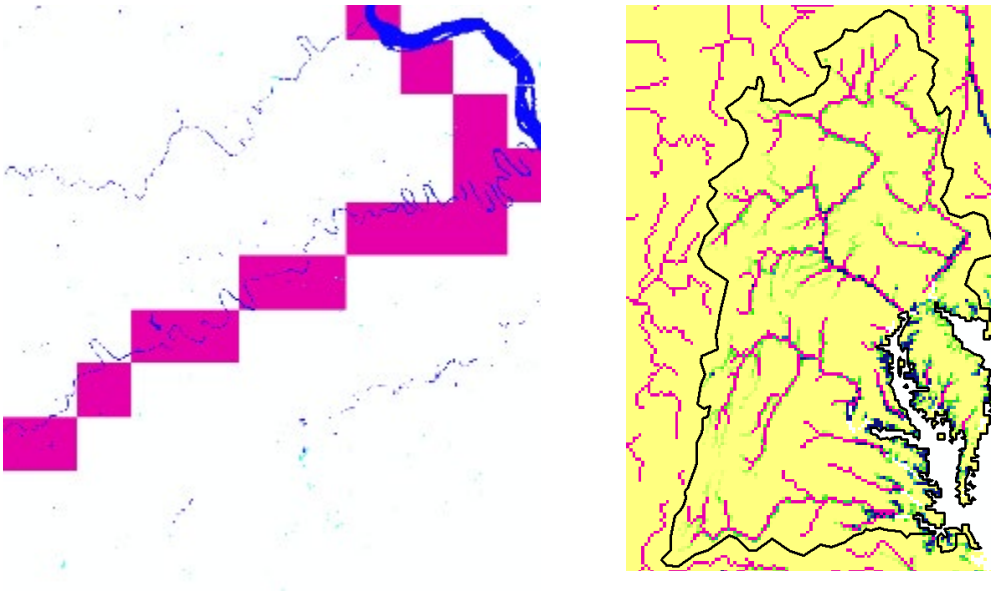

Figure 2-4. The mismatch between the hydrography dataset and the remote sensing-based surface water body.

2.2.5. River surface area

We estimate the water surface area (A_s) of both headwater streams and high-order streams as:

$$A_s = \begin{cases} A_{RS,water} & high\ order\ streams \\ W \times L, & headwater\ streams \end{cases} \quad (14)$$

where $A_{RS,water}$ is the remote-sensing data-based water surface area; W and L are the channel width and flow distance (m), respectively; the channel width of headwater stream is estimated through an empirical equation (Allen et al., 2018):

$$W = Q^{\frac{3}{5r+3}} \times (0.5\,A^{0.42})_i^{\frac{r-1}{r+0.6}} \times \left(8.1(9.8\,S)^{0.5}k^{-\frac{1}{6}}14^{-\frac{5}{3}}(1-\frac{1}{r+1})\right)^{-\frac{3}{5r+3}} \quad (15)$$

where A is the upstream area of the local subnetwork (m), Q is flow discharge (m/s); r is the shape parameter (Allen et al., 2018), k is a bed roughness length scale:

$$k = (8.1\,g^{0.5}n)^6 \quad (16)$$

where g is gravitational acceleration, and n is the Manning's friction coefficient (was set as 0.04 in this study).

In this study, we manually characterized the water body of streams and lakes based on the National Land Cover Database (NLCD 2011) (Homer et al., 2015a). However, the flow direction and streamline derived from topographic data were used as the input of the hydrological model to determine the flow path of the main channel flow cell-to-cell. The obvious mismatch has been detected between the stream-line of the hydrograph data and the remote sensing-based surface water body data (Figure 2-4). To correct the mismatch, we conducted a moving window algorithm tracing back from the end of the river reach to the most upstream and merging the stream surface area into the hydrography-based streamline. The Pseudocode of the stream surface merging algorithm can be found in Algorithm 2-1.

Algorithm 2-1. The Pseudocode (C++ format) of the stream surface merging procedure.

```
# Put all the index of the river outlets (obtained in hydrography data) into the list: list_stream
# streamline is the array of the hydrography data, 1 in the array means streams and 0 denote the land
# stream_RS is the remote sensing-based waterbody area data aggregated from NLCD
# stream_merge is the merged stream surface area of a grid cell
# fdr is the flow direction data

do while (list_stream is not empty)
{
      i  =  list_stream.pop();

      // mergying stream surface area
      stream_merge[i] += stream_RS[i];
      for (int j = all the neighbour cells around i)
          stream_merge[i] += stream_RS[j];

      m = upstream grid cell of i   ;  // obtained from fdr data
      list_stream.pop(m);
}
```

2.2.6. Lake model

Following the advanced feature of the MOSART model, which characterized the streams into small streams and large rivers, we characterize lakes into small lakes and large lakes as well. The

lake input data was obtained from the HydroLakes dataset (available at: https://www.hydrosheds.org). We defined the lakes with the upstream area (attribute in the Hydrolakes dataset) smaller than the area of the 4-km grid cell as small lakes. On the other hand, the lake with an upstream area larger than the area of the grid cell is registered as large lakes. The small and large lakes were coupled with the routing of subnetworks and main channels, respectively. In our model, the incoming flow of subnetwork flow and main channel flow would flow into the pools of small lakes and large lakes first. Moreover, the outflow rate of the lakes pools is quantified through residence time given in the Hydrolakes dataset (Messager et al., 2016).

2.2.7. Reservoir operation model

In this study, a reservoir routing model has been incorporated into DLEM-TAIM (Hanasaki et al., 2006; Biemans et al., 2011; Haddeland et al., 2006). This model requires one standalone run without dam operation in the model as natural flow and then used natural flow as input to conduct another simulation with dam operation. The predicted flow with dam impact is known as management flow. During the management flow simulation, the model first calculates the target dam release through natural flow and local water demand, followed by the prediction of actual dam operation rules based on the storage of the reservoirs. Here, the target release can be given as:

$$r'_{m,yr} = i_{mean} \tag{17}$$

$$\begin{cases} r'_{m,yr} = \dfrac{i_{mean,m}}{10} + \dfrac{9}{10} \cdot i_{mean,m} \cdot \dfrac{d_{mean,m}}{d_{mean}} & if \quad d_{mean,m} > 0.5 \cdot i_{mean,m} \\ r'_{m,yr} = i_{mean} + d_{mean,m} - d_{mean} & if \quad d_{mean,m} < 0.5 \cdot i_{mean,m} \end{cases} \tag{18}$$

where i_{mean} represents annual mean natural flow (flow without dam), $r'_{m,yr}$ represents target outflow of dams, *m*, and *yr* denote monthly or annually, respectively. d_{mean} and $d_{mean,m}$ denote

annual and monthly water demand locally. Here, the ratio k_{rls} represents the reservoir storage (S) over the dam storage capacity (C).

$$k_{rls} = \frac{S}{0.85\ C} \tag{19}$$

Thus, the actual reservoir water release can be expressed as:

$$\begin{cases} r_{m,yr} = k_{rls} \cdot r'_{m,yr} & (c \geq 0.5) \\ r_{m,yr} = (\frac{c}{0.5})^2\ k_{rls} \cdot r'_{m,yr} + \left(1 - \left(\frac{c}{0.5}\right)^2\right) \cdot i_{mean,m} & (0 \leq c \leq 0.5) \end{cases} \tag{20}$$

$$c = {}^{C}/_{i_{mean}} \tag{21}$$

Following the same procedure described in the lake model (section 2.2.5), we characterized the dams into small dams and large dams and coupled with subnetworks and main channels, respectively. We obtained the reservoirs information from Global Reservoir and Dam (GRanD) database (Lehner et al., 2011a) and National Inventory of Dams (NID, available at: https://nid.sec.usace.army.mil).

2.2.8. Parallelization of the hydrological model

Algorithm 2-2. Pseudocode (C++ format) of the parallelization for channel routing processes

```
// nlayers is the number of layers sorted based on the accumulation value

for (int i = 0; i < nlayers ; i ++ ){
    // nCells is the number of grid cells of a defined layer
    int nCells = numCells r(i);

    //parallelization of the river routing
    # pragma omp parallel for
   for (int j = 0; j < nCells; j ++)
      // conduct channel routing of the current cell, cell index is the position of the grid cell
       routing (cell_index)
}
```

The hydraulics method is computationally intensive. Thus, parallelization is required to enhance the performance of the hydrological model. Here, we used a layered parallelization method deploying the OPENMP library to accelerate the computational speed (Liu et al., 2014). This algorithm assumes no water exchange among the pixels with the same flow-accumulation value (define as the same layer). The Pseudocode of the parallelization algorithm is shown in Algorithm 2-2.

2.2.9. Parameterization at the sub-basin level

DLEM- TAIM is not only a fully grid-based model but also hybrid with a sub-basin level parameterization to mitigate the intrinsic weakness of the grid-based model (Tesfa et al., 2014). We developed a software system by C# language in Microsoft Visual Studio IDE. In this software system, we divided the study region into several sub-basins and calibrated the parameter for each stream order and river basins (Figure 2-5).

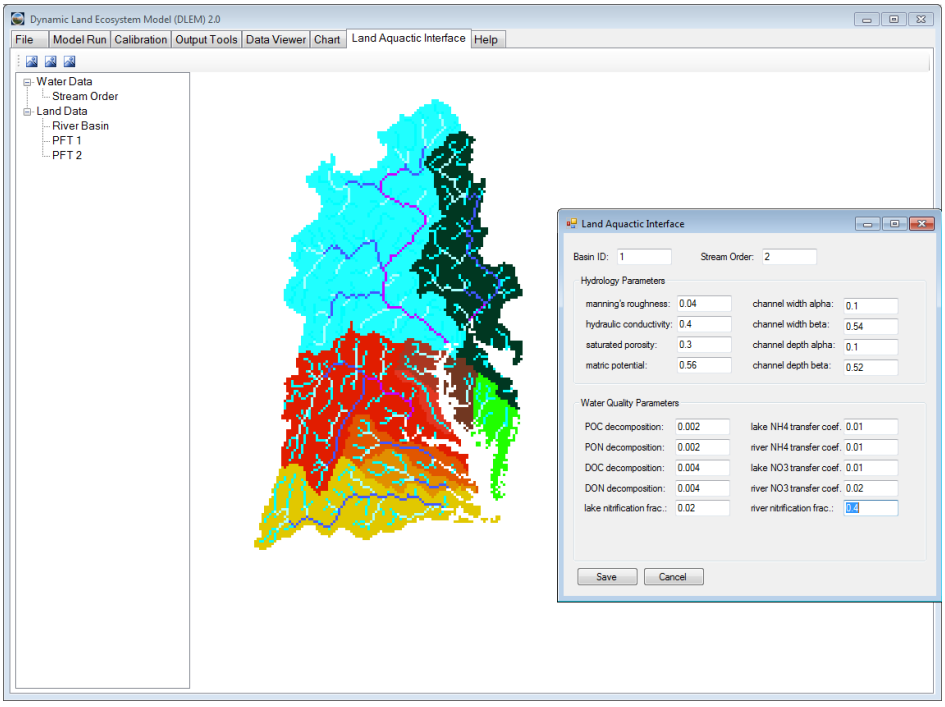

Figure 2-5. The DLEM-TAIM model user interface and parameterization at the basin level.

2.3. Model evaluation and simulation

2.3.1. Model inputs

We developed a 4-km resolution input dataset to conduct DLEM including climate variables, land-use, nitrogen inputs, and atmospheric CO_2 concentration. We reconstruct historical land-use by assembling the National Land Cover Database (NLCD) (Homer et al., 2015b), county-level inventory data of cropland (Waisanen and Bliss, 2002), North American Land Cover (http://landcover.usgs.gov/nalcms.php), and HYDE land-use data (Goldewijk, 2001). The spatial and temporal pattern of land-use change could be found in figure 2-6. The daily climate variables were obtained from the PRISM climate (Daly et al., 2008). Here, precipitation and temperature show a large increase from 1960 to 2015 over the CBW and DBW.

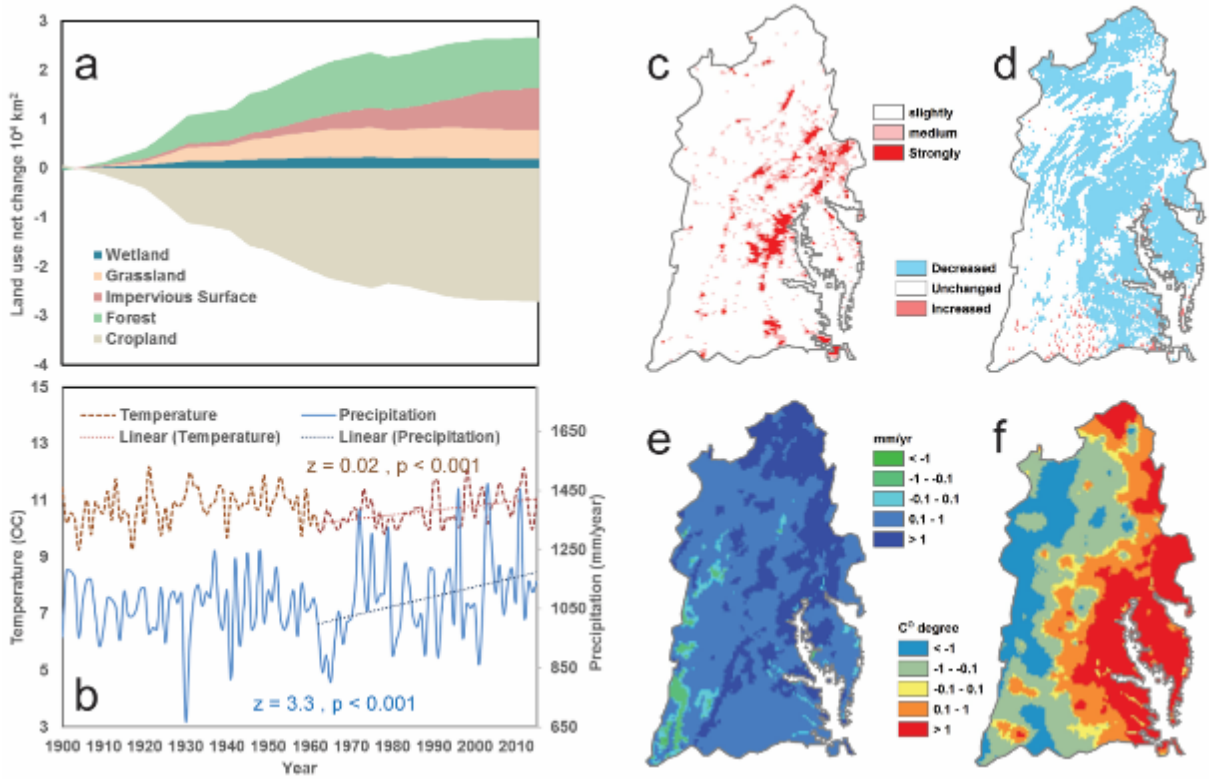

Figure 2-6. The model input of Chesapeake Bay Watershed and Delaware Bay Watershed. (a). The net land-use change from 1900 to 2015, (b). Temporal patterns of climate variables from 1900 to 2015, (c). Changes in urban impervious surface. (d). Changes in cropland fraction. (e). Changes in annual precipitation. (f). Changes in air temperature

2.3.2. Model validation in different land-use types and stream orders

To evaluate the accuracy of DLEM-TAIM in predicting daily water discharge, we compared DLEM-TAIM simulated results against United States Geological Survey (USGS) observations (Figure 2-1, Figure 2-7). The comparison results indicated that the model simulations agreed well with observations. The model behaves well in predicting the magnitude and temporal variability of flow discharges. Precisely, the newly developed hydrological model could well capture the temporal pattern of streamflow in different land-cover types and stream orders.

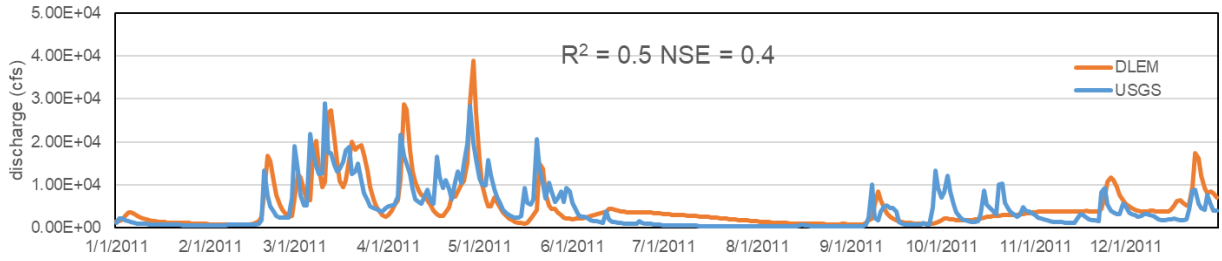

USGS Site No. 01530332, Susquehanna river stream order 3

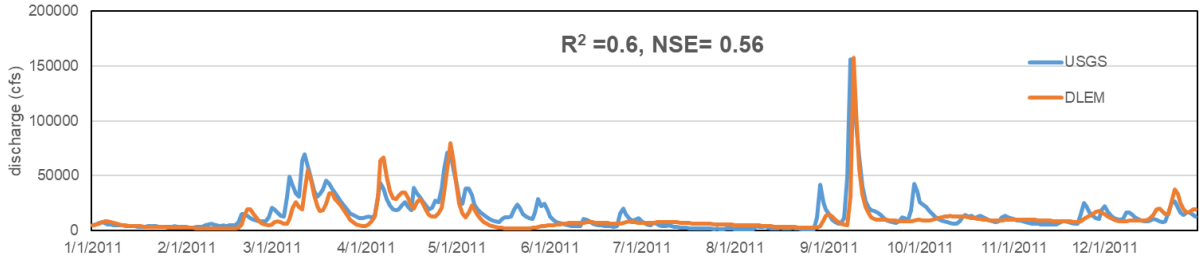

USGS Site No. 01515000, Susquehanna river stream order 4

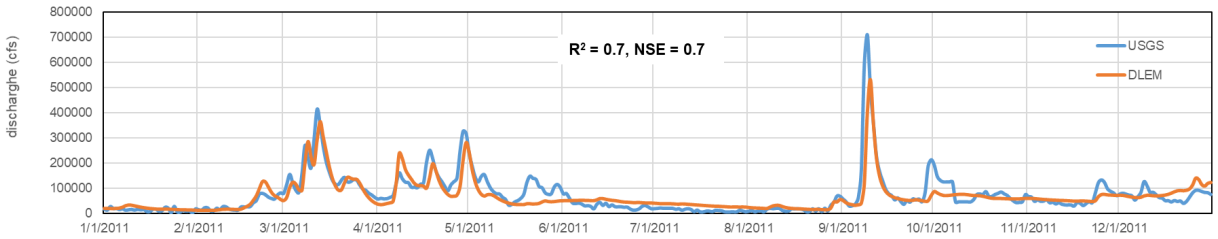

USGS Site No. 01578310, Susquehanna river stream order 4

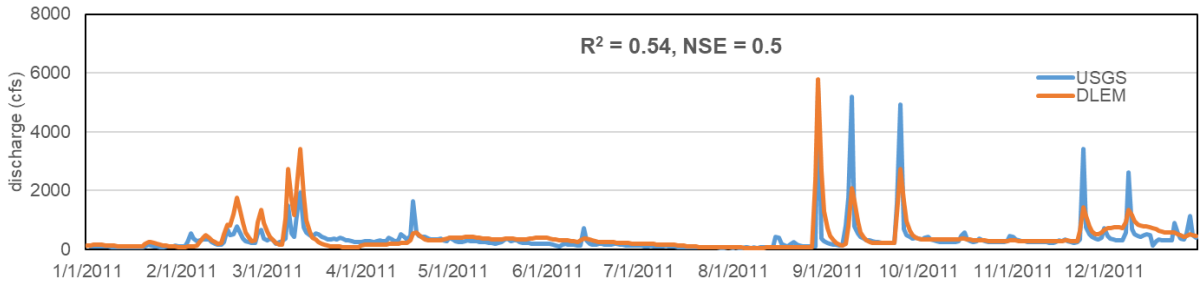

USGS Site No. 01578475, stream order 2, dominant land-use: Cropland

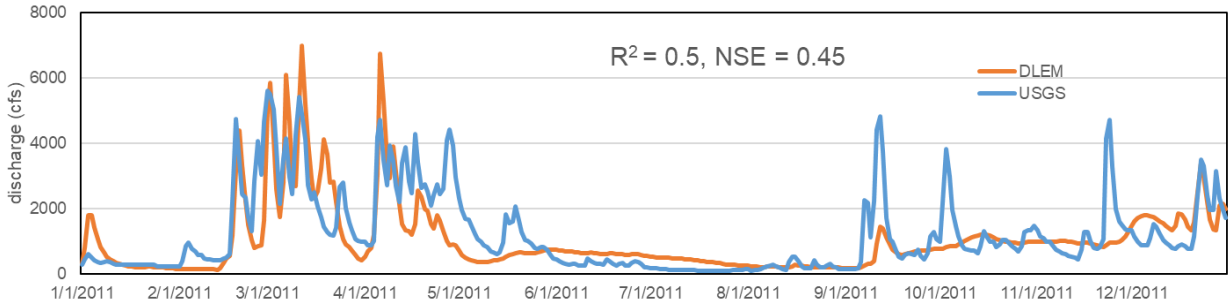

USGS Site No. 01541303, Susquehanna river, stream order 2, dominant land-use: Forest

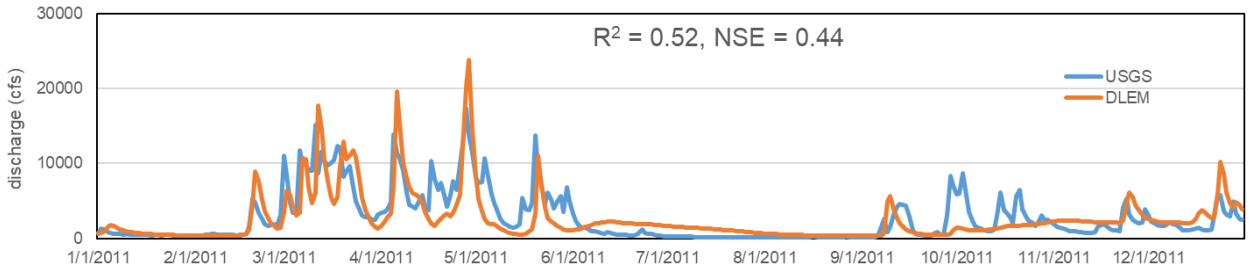

USGS Site No. 01526500, Susquehanna river, stream order 2, dominant land-use: Forest

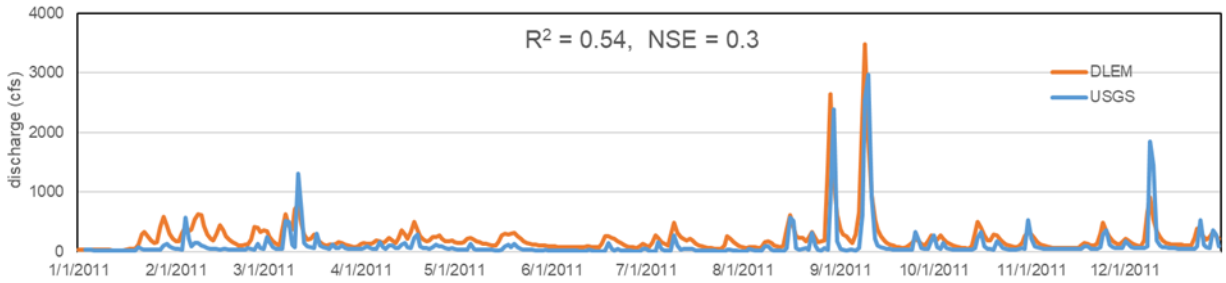

USGS Site No. 01649500, Susquehanna river, stream order 2, dominant land-use: impervious surface

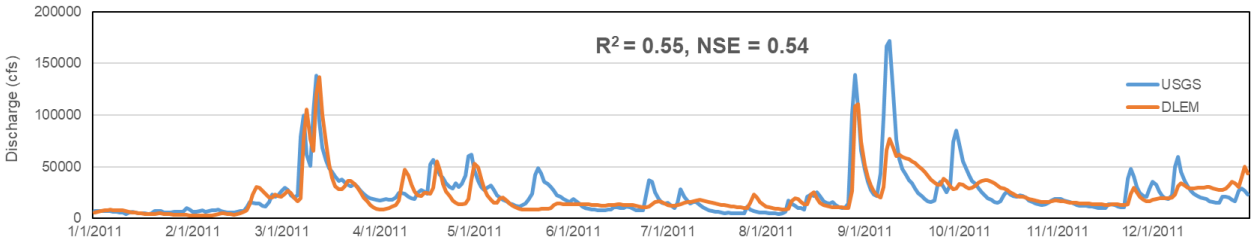

USGS Site No. 01463500 Delaware river at Trenton NJ, stream order 4

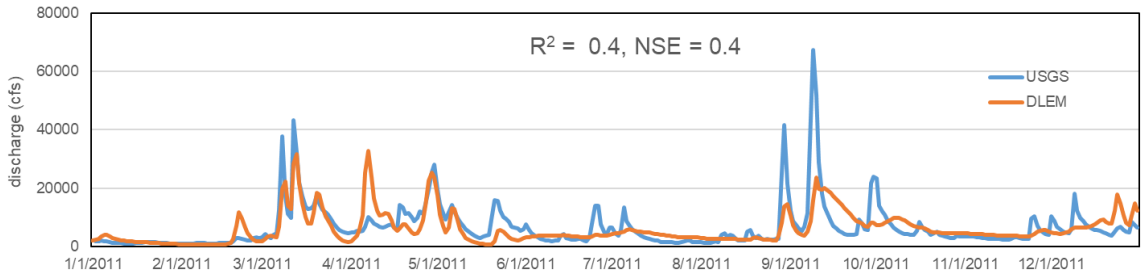

Site No. 01437500, Delaware River, stream order 3

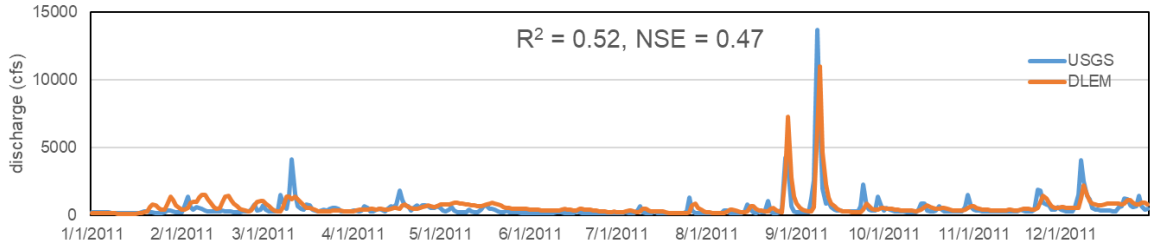

Site No. 01594440, Patuxent River, stream order 2

Figure 2-7. The comparison of DLEM-TAIM simulated daily water discharge against observations from the United States Geological Survey (USGS) in different stream orders or sub-regions with different land-use types.

2.3.3. Factorial experiments

To quantify the contribution of environmental factors to the long-term changes in discharge, we conducted several factorial experiments. The simulation with all the driving forces changed over time was considered as all-combine simulation, and the simulations with each of the factors remain unchanged since 1900 were considered as factorial experiments (Table 1-1). By comparing the estimated discharge of factorial simulations with that of all-combine simulation, the magnitude of changes in flow discharge induced by each environmental factor was attributed.

Table 1-1. The design of factorial experiments for attributing the changes in water discharge to environmental factors including climate, atmospheric carbon dioxide (CO_2), nitrogen deposition (NDEP), nitrogen management (NMAN).

	Factors				
	Climate	***CO_2***	***Land-use***	***NDEP***	***NMAN***
Simulation 1	1900-2015	1900-2015	1900-2015	1900-2015	1900-2015
Simulation 2	1900-2015	1900-2015	1900-2015	1900-2015	1900
Simulation 3	1900-2015	1900-2015	1900-2015	1900	1900-2015
Simulation 4	1900-2015	1900-2015	1900	1900-2015	1900-2015
Simulation 5	1900-2015	1900	1900-2015	1900-2015	1900-2015
Simulation 6	1900	1900-2015	1900-2015	1900-2015	1900-2015

2.3.4. Results

The annual mean water discharge from land to the Chesapeake Bay is 68.92 ±16.21 (km^3/yr) from 1895 to 2015. The annual mean discharge to Delaware Bay is 19.7±4.5 (km^3/yr) during the same period (Figure 2-8). Total water discharge increased significantly in Chesapeake Bay

Watershed and Delaware Bay Watershed (*p*-value less than 0.05) from 1962 to 2015 with the increasing rates of 0.34 (km^3/yr) and 0.12 (km^3/yr), respectively. The significant increasing trend could be explained by a significant increase in precipitation since the 1960s.

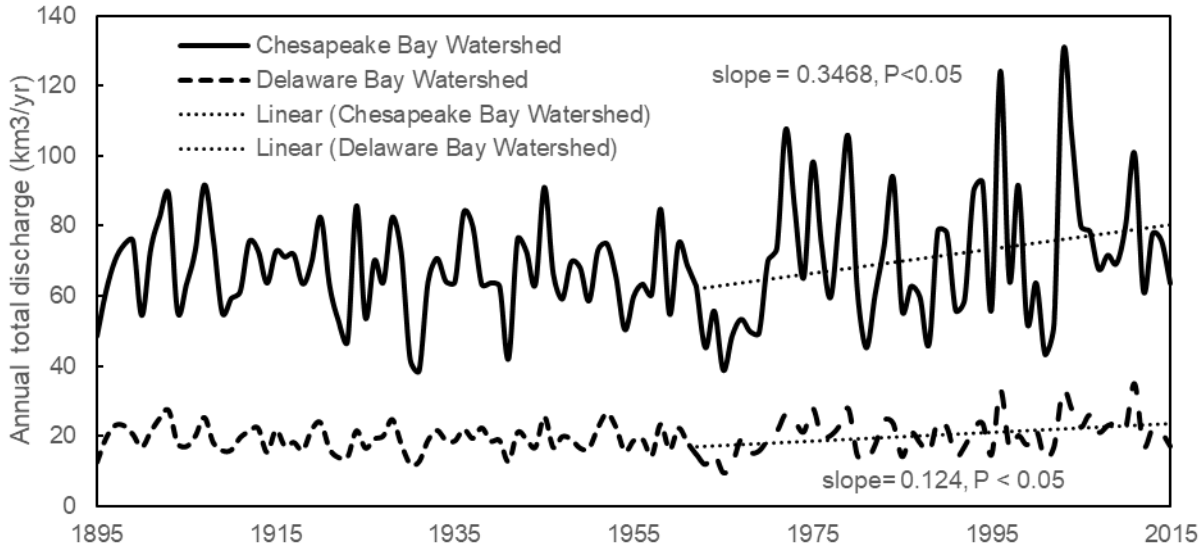

Figure 2-8. Total water discharge from land to the Chesapeake Bay and Delaware Bay from 1895 to 2015.

Flood peak (maximum value of the day in that year) does not show a significant increasing trend from 1930 to 2015 in Chesapeake Bay Watershed. However, the peak flow of Delaware Bay Watershed increased significantly ($p < 0.05$) with an increasing trend of 0.0015 (km^3/yr) (Figure 2-8), indicating an increasing flood risk in this region.

In Chesapeake Bay Watershed, climate change play as the dominant role to explain 63% of the increase in discharge, followed by land-use change (21.9%), and N deposition (8.6%) elevated CO_2 (5.5%) (Figure 2-10. a). Climate impact explained more than 87% of the interannual variations in discharge from the 1900s to 2006 - 2105 in the Delaware Bay Watershed, followed

by land-use conversion (7.8%), N deposition (3%), and elevated CO_2 concentration (1.8%) (Figure 2-10. b).

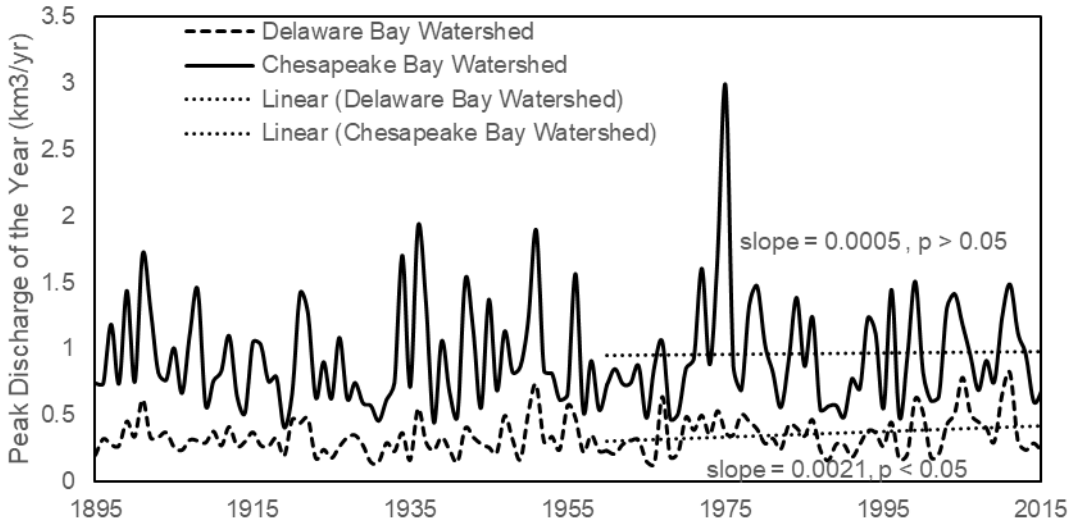

Figure 2-9. Annual peak discharge (maximum daily discharge in the year) of the Chesapeake Bay and Delaware Bay Watershed from 1895 to 2015.

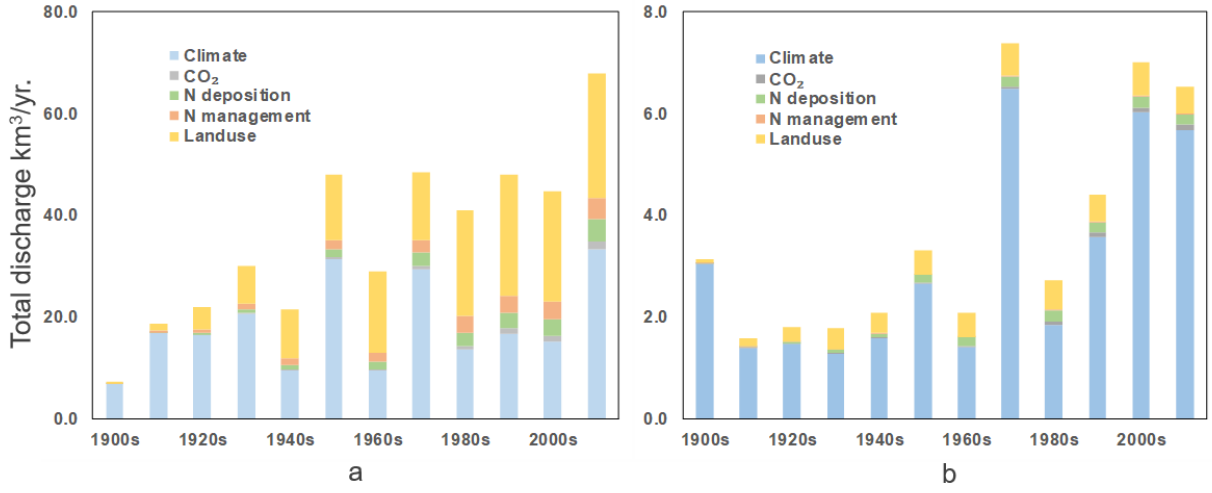

Figure 2-10. The factorial analysis of water discharge (unit: km^3/yr) of the Chesapeake Bay (a) and Delaware Bay (b) Watersheds in response to the changes in environmental conditions.

We conducted linear regression on each grid cell to quantify the increasing/decreasing rate of runoff from 1900-205. In general, the spatial pattern of the changes in runoff aligns with precipitation and land-use change (Figure 2-1, Figure 2-11). The surface runoff increased significantly in the megacities, supported by the finding that urbanization could induce more precipitation in megacities (Zhang et al., 2018). It should be noted that the surface runoff decreased in the cropland area (Figure 2-1, 2-11). The decreased water available for crops may indicate the water security problem for agriculture activities in this region.

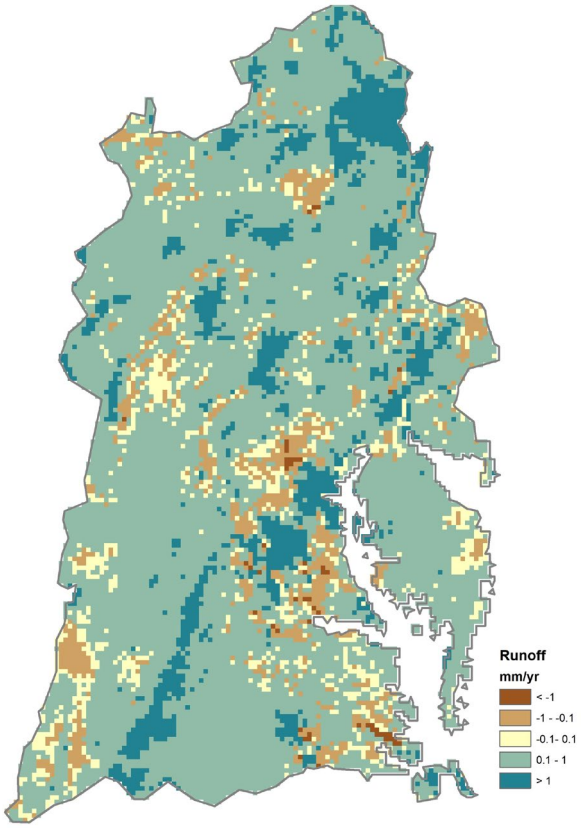

Figure 2-11. Changes in runoff over the Chesapeake Bay Watershed and Delaware Bay Watersheds during 1900-2015.

2.4. Conclusion

In this chapter, we incorporated a scale adaptive water transport scheme into DLEM to simulate the spatial and temporal patterns of water fluxes from land to the Chesapeake Bay and Delaware Bay during the past 110 years. We found a significant trend of increasing discharge from 1962 - 2015 that is aligned with climate change. The flood peak value increase from 1930 to 2015 in the Delaware Bay Watershed mainly owing to land-use change, but the peak flow does not show a significant increasing trend in Chesapeake Bay Watershed. Development and improvement of the representation of the associated water temperature and biogeochemical processes in small streams and large rivers in this proposed coupling framework will be discussed in the following chapters.

Chapter 3: Assessing impacts of global change on the water temperature of headwater and high-order streams across the Mid-Atlantic region of the U.S. by using a coupled modeling framework

Abstract: Stream water temperature substantially regulates the structure and functioning of the aquatic ecosystems, and thereby accurately estimating its spatial and temporal pattern is an essential task for ecological studies. Empirical equations, which are derived from the relationship between air temperature and water temperature, have been extensively applied in past studies. However, empirical equations cannot explain the mechanism of the drivers that contribute to changes in water temperature, which leads to decreased reliability when the environmental condition changes. Meanwhile, few studies tried to couple soil temperature with stream water temperature to capture the synergy of thermal balances between the terrestrial and riverine systems. Here, we incorporated a new water transport scheme into the Dynamic Land ecosystem model (DLEM) to predict water temperature in higher-order streams (> 1st order) and headwater streams (1st order). Driven by a 4-km geo-referenced dataset, our new water temperature model was utilized to predict the spatiotemporal variations of water temperature in the Mid-Atlantic Region of the U.S. (MAR, including Chesapeake Bay Watershed and Delaware Bay River Basin) for the period 1900-2015. Results revealed that water temperature during 1970-2016 increased significantly in the higher-order and headwater streams at a rate of ~0.028 ºC/year and 0.031 ºC/year, respectively. The buffering effect of groundwater on the water temperature in headwater streams diminished under the context of global warming. The factorial analysis showed that climate change and variability explain most of (~80%) the variations in stream water temperature from 1900 to 2015. However, land-use conversions (from cropland to forest mostly), CO_2

fertilization, and land nitrogen management contributed more than 70% of the changes in stream water temperature during the 1970s.

3.1. Introduction

Stream water temperature is a fundamental physical variable reflecting the balance of thermal energy in aquatic systems (Chapra, 2008). It has been well documented that stream water temperature could substantially affect the solubility of oxygen and gases (Sander, 2015), govern the decomposition or mineralization rate of organic matters (Pastor et al., 2003), and regulate the nitrogen (Harrison et al., 2009) and phosphorus dynamics (McQueen and Lean, 1987), which in turn moderate the metabolic rate (Claireaux et al., 2000) of microorganism and shape the spatial distribution of habitats supporting aquatic species (Isaak et al., 2010). Given the importance of water temperature to the aquatic biogeochemistry and biodiversity, significant efforts have been invested in monitoring and estimation of stream water temperature (Van Vliet et al., 2013).

Although ubiquitous water discharge monitoring sites have been established worldwide, the observations of water temperature are still lacking (Wanders et al., 2019). A modeling approach is needed to construct the spatial and temporal patterns of stream water temperature across large regions. Empirical relationships, which are derived from the regression analysis of observed water temperature and air temperature, are commonly deployed in water quality models due to their low computational complexity (Leach and Moore, 2019). The empirical equation-based approach provides reliable estimates of water temperature for regional studies because the parameters or the regression equation was calibrated to match the data. Thus, the empirical models implicitly contain the mechanisms, including the hydrological or thermal response of the watershed to climate conditions, which control the spatial-temporal pattern of stream water temperature. Therefore, the performance of the empirically-based approach strongly relies on the data availability of the study region due to the spatial heterogeneity of hydrological conditions among different watersheds. However, the statistical correlations might fail if the environmental

conditions change (Arismendi et al., 2014), which implies its limitation in long-term water temperature prediction. The reason for this is that the empirical relationships cannot represent the mechanisms of how environmental factors contribute to the changes in stream water temperature. This inherent weakness hampered its applications in decision support relevant studies.

Stream water temperature is prone to climate change and anthropogenic disturbances. Significant stream water temperature rising was found in the Chesapeake Bay Watershed, which is aligned with the increase of air temperature in the region (Rice and Jastram, 2015). Land management, such as clear-cutting, can also bring a significant impact on water temperature (Brown and Krygier, 1970; D. Chen et al., 2016). The impacts of water resource management, such as dam construction, reservoir operation on water temperature are still in debatable (Buccola et al., 2016), due to the trade-off between the increase in both water surface area and the thermal energy leaking from the bottom of the reservoirs (Chen & Fang, 2015b).

Promoted by a better understanding of the energy balance within river waters from field works, physically-based approaches, which incorporate climate and hydraulic variables into the energy balance equations, have been developed and widely used worldwide. The computational units of stream water temperature models include irregular triangle grids (G. Chen et al., 2016), sub-catchments (Ficklin et al., 2012), and regular grid meshes (Yearsley, 2012). And the study area extends from basin (Wu et al., 2012a) or regional levels (Buccola et al., 2016; Isaak et al., 2017) to continental (Li et al., 2015b) or global scales (Van Vliet et al., 2013; Wanders et al., 2019). Physical-based models could well capture the changes in environmental conditions and provide reliable results for historical data reconstruction (Wanders et al., 2019) and future projections (Ficklin et al., 2014; Wu et al., 2012a). Therefore, a combined approach was proposed (Ficklin et al., 2012) by introducing hydrological inputs into the empirical-based

equation of the Soil & Water Assessment Tool (SWAT) model (Arnold et al., 2012). The hydrological inputs, including hydraulic loading, snowmelt, groundwater, surface runoff, and lateral soil flow, substantially improved the performance in representing the stream temperature of the mountainous regions. However, the application of a physical-based model still faces challenges, such as the high computational complexity and massive data requirement. On the other hand, both the physical-based model and empirical approaches are established under certain assumptions. Thus, current physical-based models still need to incorporate empirical equations to represent or simplify the mechanism, which has not been fully understood. For instance, most of the models used empirical equations to quantify the water temperature of headwater streams as the boundary condition (Haag and Luce, 2008; Van Vliet et al., 2012).

Except for the semi-empirical approached proposed by Ficklin et al. (2012), none of the studies presents the spatial distribution of stream temperature in upstream areas. The headwater zone, known as the terrestrial- aquatic interface, was recognized as the hotspots of greenhouse gas (GHGs) emissions (Butman and Raymond, 2011), and prompted great interest to both filed work and the modeling community. A recent study suggested that headwater streams play as the refuge of climate change (Isaak et al., 2016b) that help to preserve the endangered cold-water species under the context of global temperature increase. Although this study suggests that the headwater zones can buffer the impact of climate (headwater small streams have cooler water temperature in summer and warmer water temperature in winter than that of high-order streams), they are vulnerable to climate change and human activities as well when the changes of environmental conditions are reaching to the tipping point (Nepstad et al., 2008). Without surprise, the headwater zones themselves are subject to a heavy impact from human or natural disturbances (Isaak et al., 2010; Cover et al., 2010) during the past century. It has been noted that

water temperature within the headwater streams increased ~5 ºC after a fire disturbance (Isaak et al., 2010; Koontz et al., 2018). Hence, detecting the changes in land surface processes is essential in predicting the water temperature within the streams.

In this study, we coupled a new water transport scheme named Model for Scale Adaptive River Transport (MOSART) (Li et al., 2013, 2015b) within the Dynamic Land Ecosystem Model- Terrestrial Aquatic Interface Model (DLEM-TAIM) framework (Tian et al., 2015c). Under this newly developed modeling framework, we developed a physical-based water temperature model with the new water transport scheme. We explicitly link the groundwater temperature to the stream water as boundary conditions and improve the model representation of the groundwater fed, sub-grid routing thermal energy exchanges within the headwater streams. The major objectives of this study are (1) to describe the coupling framework of a water temperature model with DLEM land model; (2) to construct the spatial and temporal pattern of water temperature of head water streams and high order streams from 1900 to 2016; (3) to attribute the contribution of environmental factors to the stream water temperature across the Mid-Atlantic Region (MAR).

3.2. Methods and input data

3.2.1. The Dynamic Land Ecosystem Model (DLEM model)

The terrestrial processes were simulated by the Dynamic Land Ecosystem Model 2.0 (DLEM 2.0) (Figure 3-1. a), which couples major terrestrial water cycle (Liu et al., 2013), carbon-nitrogen coupled vegetation dynamics (Tian et al., 2012; Chen et al., 2013) to explicitly estimate plant growth, soil biogeochemistry, and the associated water fluxes, greenhouse gas emissions in terrestrial ecosystems driven by the climate forcing and the anthropogenic disturbances. The model has been extensively applied at the relatively coarse resolutions such as 0.5 degrees

(global level) or five arc-minutes (regional level) (Tian et al., 2015c). Therefore, to reduce the scaling effect, sub-grid processes were introduced into the terrestrial simulations by utilizing a cohort unit. The land-use cohort divides each grid cell into five normalized vegetation coverages, including the fraction of cropland and four primary natural vegetation covers prescribed by cropland, and six non-vegetation types including urban impervious surface, glacier, lake, stream, ocean water, and bare-ground. DLEM model has been extended to represent the riverine transport, known as the terrestrial-aquatic interface, and thus is well suited for quantifying the lateral or vertical fluxes of water, carbon (Tian et al., 2015c) and nitrogen (Yang et al., 2015b) from land to the oceans (Figure 3-1. b).

3.2.2. Soil temperature module in DLEM

In the DLEM model, the soil column was divided into 10 layers, and the thickness of each layer was defined as 0.05 m, 0.05 m, 0.1 m, 0.2 m, 0.2 m, 0.3 m, 0.3 m, 0.5 m, 0.8 m, 1.0 m respectively. DLEM simulated the thermal energy exchange between the layers, more details about the numerical methods could be found in the technical description of the Community Land Model (Bonan et al., 2013). In the DLEM model, we did not explicitly quantify the temperature of the vegetation canopy and the heat fluxes between the canopy and the soil surface. Thus, we quantify the surface soil temperature by using a semi-empirical method as the upper boundary condition of the soil layers, which considers the effect of Leaf Area Index (LAI) and litter on soil temperature (Kang et al., 2000):

$$\begin{cases} T_j - T_{j-1} = \left[\mathrm{A} - T_{j-1}\right]\exp\left[-z\left(\frac{\pi}{k_s * 86400}\right)^{0.5}\right]\exp[-k_t \times (LAI + Litter)], \text{when A} > T_{j-1} \\ T_j - T_{j-1} = \left[\mathrm{A} - T_{j-1}\right]\exp\left[-z\left(\frac{\pi}{k_s * 86400}\right)^{0.5}\right]\exp[-k_t \times (LAI)], \text{when A} < T_{j-1} \end{cases} \quad (1)$$

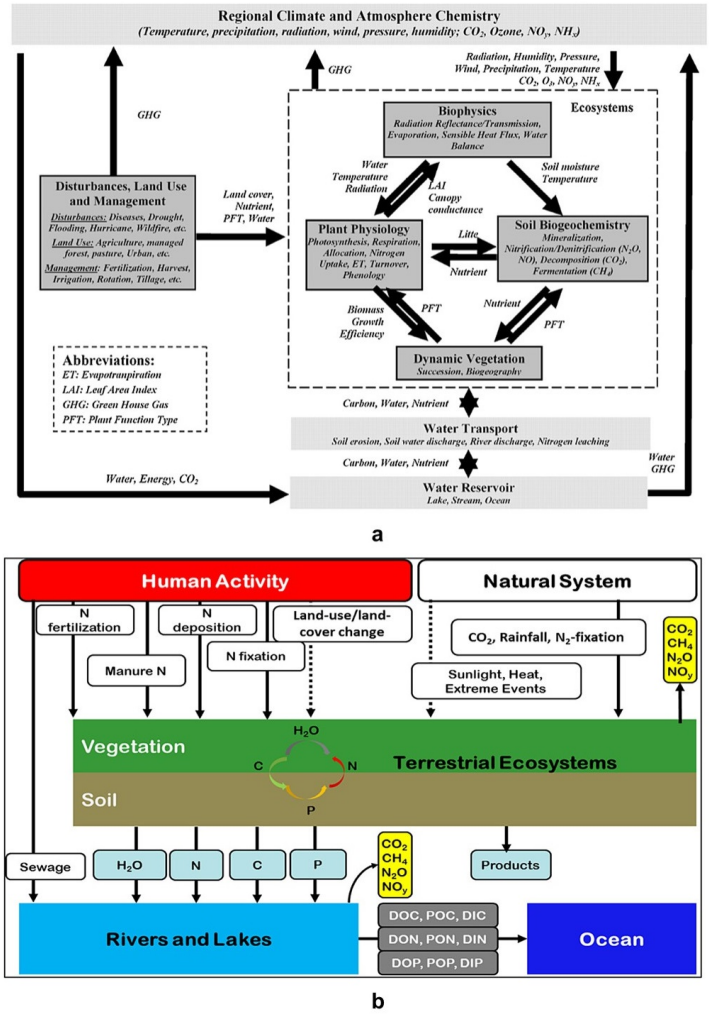

Figure 3-1. The general framework of the DLEM land-ocean aquatic continuum.

Where A is the 11-day mean daily air temperature, T_j , T_{j-1} is the surface soil surface temperature of the current day and the previous day, κs the thermal diffusivity (which is set as 0.004 cm^2s^{-1}), LAI is leaf area index, $Litter$ is LAI equivalent of ground litter, k_t is a calibration parameter.

3.2.3. Scale adaptive river routing processes

Figure 3-2 The general framework of the scale adaptive water transport module.

A scale adaptive water transport scheme, known as Model for Scale Adaptive River Transport (MOSART), was incorporated into the DLEM aquatic module. The new scheme separates the water transport process within a grid unit into hillslope flow, subnetwork flow, and main channel flow (Figure 3-2). Hillslope flow is the water routing process that merges surface runoff and flows to subnetworks. A groundwater pool receives water from subsurface runoff (shallow groundwater flow) and contributes to subnetworks with outflow rates derived from a fixed residence time. The subnetwork flow represents the routing process of *headwater streams* (or 1st order streams defined in this study) that receives the outflow from the hillslope flow and groundwater pool and then flows into the main channel. Both hillslope and subnetwork flow are sub-grid routing processes within a grid cell. The main channel flow represents the routing process of *high-order streams* (higher than 2nd order streams in a 4-km resolution grid cell for

this study) receiving flow from subnetworks and upstream grid cells and flows to a downstream grid cell.

In the water temperature module of DLEM, we simulated the thermal energy dynamics of headwater streams (subnetworks in MOSART framework) and high-order streams (main channel flow in the MOSART framework) separately. Thus, we need to estimate the water surface area of both types of streams. We obtained the surface area data (Allen and Pavelsky, 2018) from remote sensing products for the high order streams, and quantified the water surface area (A_s) of headwater streams through a relationship proposed by Allen et al., 2018:

$$A_s = \begin{cases} A_{RS,water} & high\ order\ streams \\ W \times L, & headwater\ streams \end{cases} \quad (2)$$

$$W = Q^{\frac{3}{5r+3}} \times (0.5\,A^{0.42})_i^{\frac{r-1}{r+0.6}} \times \left(8.1(9.8\,S)^{0.5}k^{-\frac{1}{6}}14^{-\frac{5}{3}}(1-\frac{1}{r+1})\right)^{-\frac{3}{5r+3}} \quad (3)$$

where $A_{RS,water}$ denotes the surface area obtained from remote sensing data; W and L represent the channel width and flow distance of the rivers in the given pixel respectively; A is the drainage area here we define it as the area of one grid cell, Q is water discharge in the current time (m/s); r represents the shape parameter (which was set to 1.5) (Allen et al., 2018). k is a bed roughness length scale:

$$k = (8.1\,g^{0.5}n)^6 \quad (4)$$

Where n is the Manning friction coefficient which was set as 0.04, and g is gravitational acceleration (m/s^2).

3.2.4. Water temperature module

We developed a riverine water temperature model within the scale adaptive water transport module and fully coupled it with the soil water temperature model of DLEM (Figure 3-3).

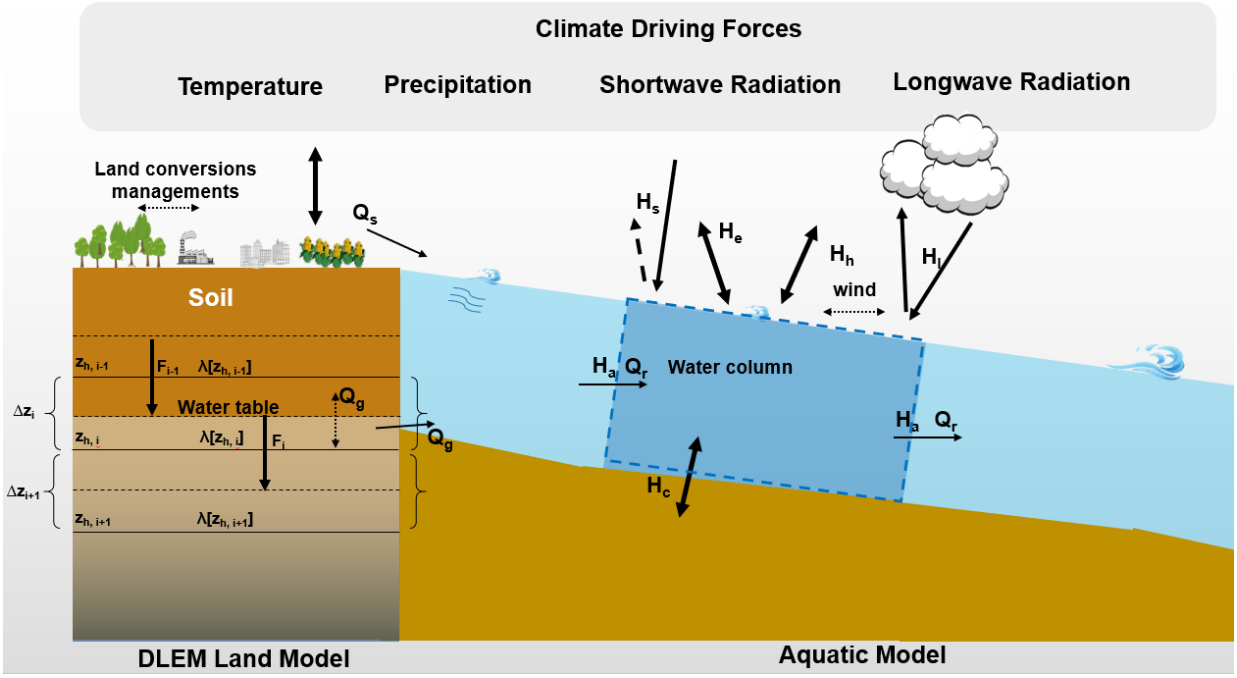

Figure 3-3. The framework of DLEM couple with the water temperature model

The energy balance within the river channels can be given as:

$$\frac{\Delta T}{\Delta t} = \frac{H_a + \left(1 - C_{ef}\right) A_s \times (H_s + H_l + H_e + H_c + H_h)}{C_w \times M} \quad (5)$$

Where C_w represents the specific heat of water, (which is set to 4.186 J/g°C), M is the total mass of water stored in the river channel (kg), C_{ef} is the ratio of water surface area shaded by plant canopies (we only consider the shading effect on headwater streams); H_a (W) is the sum of lateral heat fluxes, including thermal inputs from upstream grid cells, local subnetworks, and downstream thermal energy loss. In this model, we simulated the lateral heat transport within subnetworks ($H_{a,sub}$) and main channels ($H_{a,main}$) separately:

$$H_{a,sub} = \rho_w C_w \times \left(Q_{hil}\left(T_{w,hil} - T_{w,sub}\right) + Q_g\left(T_{w,g} - T_{w,sub}\right)\right) \quad (6)$$

Where ρ_w represents the water density (kg m^{-3}), $Q_{hil}$and Q_g represent the flow discharge of hillslope flow and subsurface flow (shallow groundwater), respectively. $T_{w,hil}$, $T_{w,g}$ and $T_{w,sub}$ represent the water temperature of hillslope flow, groundwater, and subnetworks, respectively. We assume the water temperature of the hillslope flow equals to surface soil temperature. We quantify the average soil temperature from surface to a given depth of the soil column as the temperature of the groundwater, and the depth is calibrated as 0.5 in this study. The lateral heat flux of the main channel is given as:

$$H_{a,main} = \rho_w C_w \times \left(\sum_{i}^{Nup} Q_{up,i}(T_{w,up,i} - T_{w,main}) + Q_{sub}(T_{w,sub} - T_{w,main}) \right) \quad (5)$$

Where $Q_{up,i}$ is the inflow from up-stream grid cells, $T_{w,main}$ and $T_{w,up,i}$ are the water temperature of upstream inflow and main channel flow, respectively.

Hs is the net short-wave radiation and (Wm^{-2}) which is set as 97% of the incoming shortwave radiation (H_{s-in}) (Wu et al., 2012a), H_l is the net long-wave radiation which is calculated as the difference between incoming longwave radiation (H_{lw-in}) of atmosphere and longwave energy emission from a water body (H_{lw}) (Thornton and Running, 1999), here H_{s-in} and H_{lw-in} were obtained from climate data, H_{lw} is given as:

$$H_{lw} = 0.97 \times \sigma \times (T_w + 273.15)^4 \quad (6)$$

σ is the Stefan-Boltzmann constant (set as 5.67×10-8W m^{-2}K^{-4}). H_c represents the riverbed-water specific conductive heat exchange flux (Wm^{-2}), which is set to 5% of the net solar radiative flux (Wu et al., 2012a). H_e is are the specific latent flux (Wm^{-2}) which is estimated as：

$$H_e = -\rho_w \times E \times \lambda_e / (86.40 \times 10^6) \quad (7)$$

E represents the evaporation rate of water (mm d^{-1}), λ_e denotes the latent heat fluxes through vaporization (J kg^{-1}), Here, the evaporation rate is estimated as:

$$E = K_l \times (e_{sat} - e) \quad (8)$$

e_{sat} denotes the saturation vapor pressure (hPa), and e represents the actual vapor pressure (hPa) which are calculated in DLEM land model (Thornton and Running, 1999), we quantify K_l as:

$$K_l = 0.211 + 0.103 \times V_{wind} \times F_{wind} \quad (9)$$

where V_{wind} is wind speed of 3-meters above the ground/water surface (m s^{-1}), F_{wind} is the dimensionless factor, which is set as 0.8 (Haag and Luce, 2008), λ_e is given as:

$$\lambda_e = 2499.64 - 2.51 \times T_w \quad (10)$$

H_h is the sensible heat fluxes (Wm^{-2}) and can be expressed as:

$$H_h = -\gamma \times \frac{P}{1013} \times K_l \times \lambda_e \times \frac{T_w - T_{air}}{86.40 \times 10^6} \times \rho_w \quad (11)$$

Where γ represents the psychrometric constant at the standard air pressure, which is set as 0.655 (hPa/°C), P denotes the actual air pressure (hPa).

3.2.5. Study area and model driving forces

The model was applied to the Chesapeake Bay Watershed and Delaware River Basin (Figure 3-4), both of which are located within the Mid-Atlantic Region (MAR) of northeast US. MAR is the most urbanized region of the country and sustains more than 25.5 million people. The region covers more than 16,6533 square kilometers of the land surface and experienced large land conversions due to reforestation and water conservations during the last century (Hassett et al., 2005).

In this study, we developed a 4-km resolution dataset of this region as model input to run the DLEM model with climate, land conversion, and land management driving forces from 1900 to 2015. The potential vegetation map was reconstructed for MAR which combines land-use data obtained from National Land Cover Database (NLCD, Jin et al., 2013), North American Land

Cover (http://landcover.usgs.gov/nalcms.php), Global C4 vegetation map (Still, 2003). We used the county-level inventory data of cropland area and urban area to prescribe the land-use change of natural vegetation (Waisanen and Bliss, 2002). The flow chart which describes the generation procedure of land-use data was shown in Figure 3-11. As shown in Figure 3-5, the cropland area decreased by 57.3% (Figure 3-5. d) during the past 100 years. This is primarily due to the 9.1% increase in forest area and the 507.5% increase in urban impervious surface. Most of the urban expansion occurred surrounding the megacities, including Washington DC., Baltimore, and Philadelphia (Figure 3-5. c).

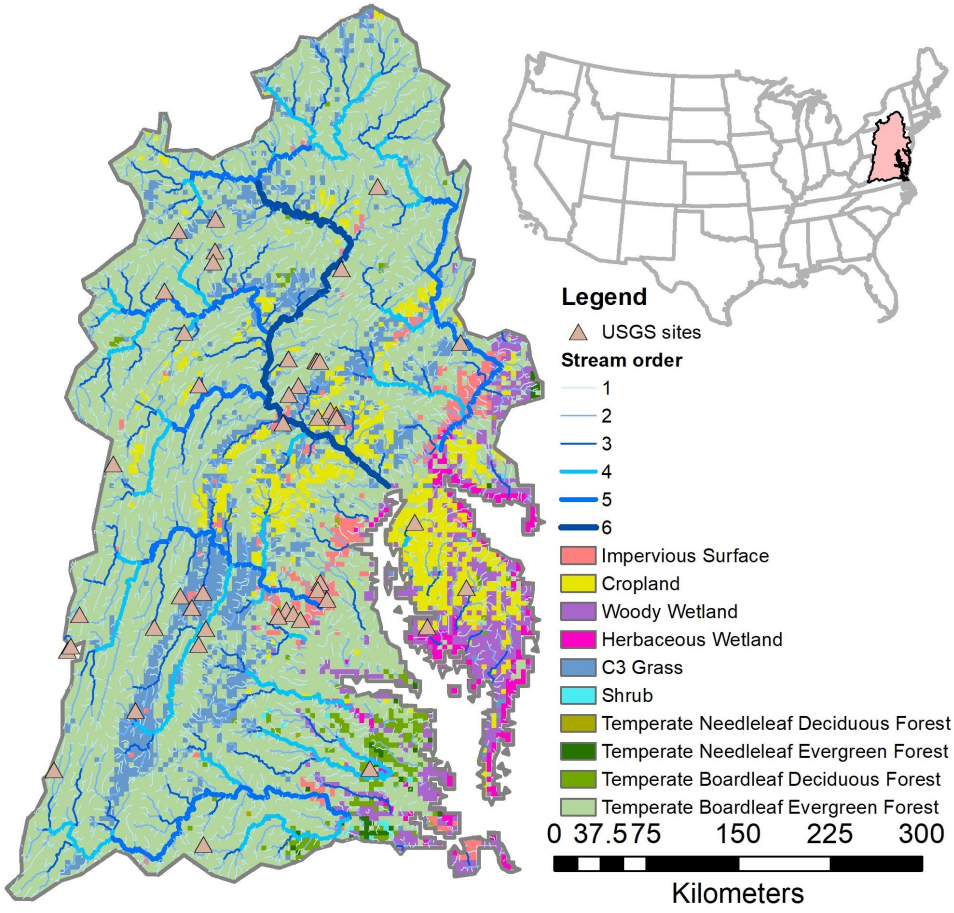

Figure 3-4. The major plant function types and land-use in the Mid-Atlantic Region.

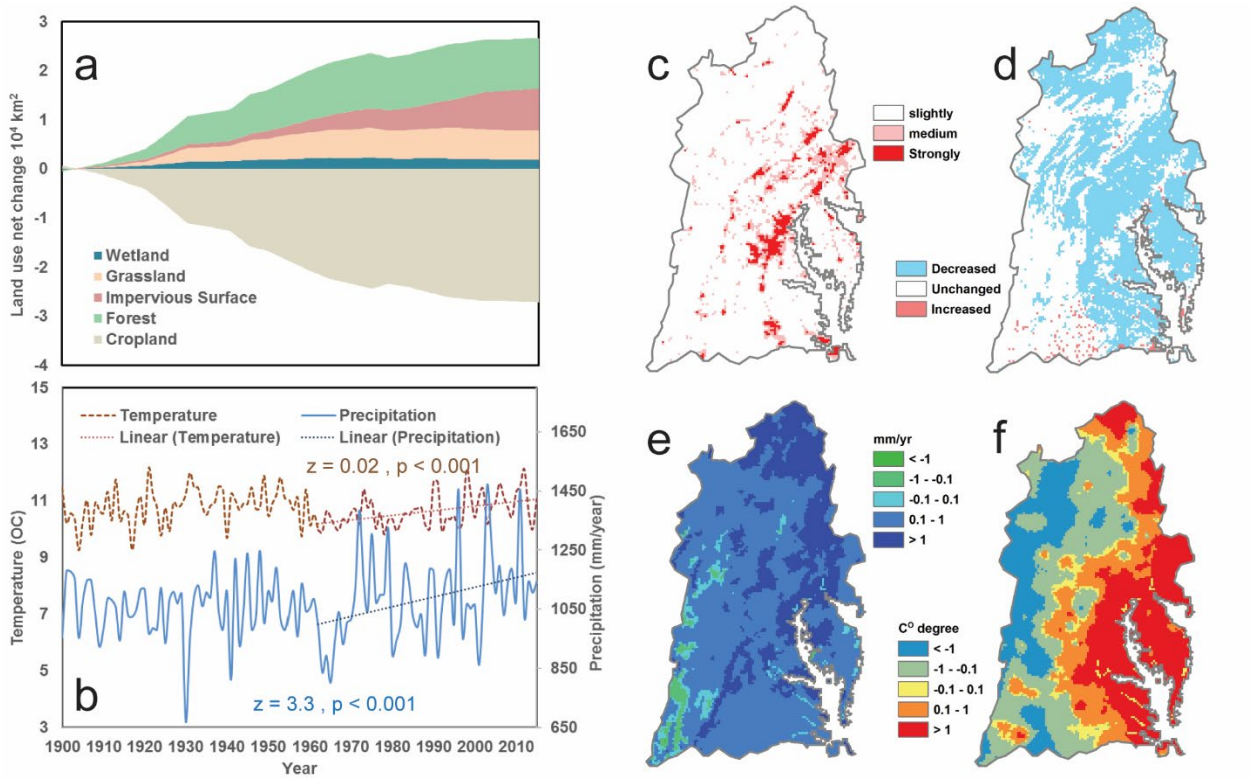

Figure 3-5. The spatial-temporal pattern of land conversion and long-term climate change over the Mid-Atlantic Region from 1900-2015. a. Temporal pattern of net land-use change from 1900 to 2015, b. Temporal pattern of annual mean precipitation and air temperature from 1900 to 2015, c. Changes in urban impervious surface. d. Changes in cropland. e. Changes in annual total precipitation. f. Changes in annual mean air temperature.

We obtained daily climate variables from Parameter-elevation Relationships on Independent Slopes Model (PRISM) climate dataset (available at: http://www.prism.oregonstate.edu/). Which included 4-km resolution historical daily minimum, mean and maximum temperature, precipitation. The mean annual precipitation was 1080.0±131.7 mm year^{-1}, and the annual mean temperature was 11.6±0.2°C during 1895-2014, respectively. Both precipitation and air temperature show significant increases ($p < 0.001$) from 1960 to 2014 with the increasing rates of 3.28 mm/yr and 0.016 ºC/yr, respectively.

3.3. Simulation experiments, statistical analyses, and data for model performance evaluation

3.3.1. Simulation experiments

Before the year-to-year simulation from 1895 to 2016, we first set-up an equilibrium run for all grid units. The simulation is forced by the land-use data of the year 1895, and the 30-year mean (1895-1924) climate data to represent the pre-industry environmental condition. The equilibrium ran finishes when carbon, nitrogen and water pools reached the steady-state (Thornton and Rosenbloom, 2005). Other driving forces including the atmospheric CO_2 concentration, land-use change, and nitrogen inputs, are kept at the pre-industry level (1895) as well, to excludes human disturbance. After the equilibrium run, we conduct a 30-year spinning-up run with randomly selected climate variables from 1900 and 1929. The spinning up run functions as a buffer to smooth the carbon and nitrogen fluxes between the equilibrium run and the year-to-year transient run (Tian et al., 2012). Finally, we conducted the transient run from the year 1895 to 2015 with all the driving forces change over time. We calibrated parameters and validated the simulated water temperature with field observations; the parameter set with the best performance was considered as the best estimator to be used for further experimental analysis.

To assess the contribution of environmental factors to the changes in water temperature, we set-up six simulations with each of the environmental factors keeps consistent with the level in 1900 (Table 3-1). The simulation with all the driving forces change year-by-year is recognized as the all-combine run, and the contribution of each environmental factor was calculated by comparing the simulated water temperature of each run with the all-combine run. It should be noted that all the simulations used the same parameter set.

Table 3-1. The experimental design for attributing changes in water temperature to natural and anthropogenic factors including precipitation, temperature, climate, atmospheric carbon dioxide (CO_2), land-use and nitrogen inputs (including N deposition, N fertilizer, and N manure)

	Factors					
	Precipitation	*Temperature*	***Climate***	***CO_2***	***Land-use***	***N**-inputs*
Simulation 1	1900-2015	1900-2015	1900-2015	1900-2015	1900-2015	1900-2015
Simulation 2	1900-2015	1900-2015	1900-2015	1900-2015	1900-2015	1900
Simulation 3	1900-2015	1900-2015	1900-2015	1900-2015	1900	1900-2015
Simulation 4	1900-2015	1900-2015	1900	1900	1900-2015	1900-2015
Simulation 5	1900-2015	1900	1900-2015	1900-2015	1900-2015	1900-2015
Simulation 6	1900	1900-2015	1900-2015	1900-2015	1900-2015	1900-2015

3.3.2. Statistical methods

We calculated Root-Mean-Square Deviation (RMSD), Nash-Sutcliffe coefficient (NSE) (Nash and Sutcliffe, 1970), and Coefficient of Determination (R^2) to validate the model performance in predicting the water temperature of headwater streams and high-order streams (Table 3-2, Figure 3-12). Mann-Kendal trend test and Theil Sen linear regression were used to examine the increasing or decreasing trend of annual mean air temperature and annual mean precipitation (Figure 3-5). To validate the long-term changes in water temperature spatially, we deployed the Mann-Kendal trend test (p-value less than 0.05) (Figure 3-7 c) on the time series data of each grid unit from 1900 to 2015. The increasing or decreasing rate (slope) was quantified by Theil Sen linear regression conducted on each grid cell (Figure 3-7 a, b).

3.3.3. Model validation

Table 3-2. The summary of matrices of model performance.

			Physical based model			***Empirical model***		
USGS site No.	***start year***	***end year***	***R^2***	***NSE***	***RMSD***	***R^2***	***NSE***	***RMSD***
large river channel								
01428750	1989	2004	0.82	0.46	5.40	0.92	0.54	5.00
01460300	1998	1999	0.90	0.62	5.32	0.91	0.85	3.79
01490120	2006	2009	0.81	0.57	6.32	0.93	0.73	5.01
01493112	2012	2015	0.90	0.10	5.61	0.95	0.30	5.36
01673638	2007	2009	0.88	0.48	7.16	0.89	0.48	7.15
02011490	1984	1995	0.89	0.60	4.50	0.83	0.64	4.29
headwater streams								
before 1980								
01516500	1959	1959	0.88	0.74	6.07	0.80	0.67	6.86
01549100	1973	1977	0.86	0.51	5.18	0.79	0.34	6.02
01549300	1973	1977	0.86	0.63	4.71	0.77	0.54	5.30
01547700	1956	1966	0.79	0.05	8.66	0.75	0.12	8.33
01568700	1974	1976	0.77	0.63	4.27	0.70	0.56	4.63
01568750	1974	1976	0.77	0.43	5.14	0.73	0.23	6.00
01575730	1978	1979	0.81	0.44	6.93	0.82	0.33	7.62
01575741	1978	1979	0.82	0.77	4.38	0.83	0.84	3.60
01575746	1978	1979	0.78	0.61	5.21	0.80	0.70	4.52
after 1980								
01571490	1993	1995	0.88	0.01	5.05	0.93	0.46	3.58
01559795	1993	2000	0.87	0.33	6.29	0.91	0.08	7.35
01555400	1999	2000	0.78	0.32	6.54	0.94	0.90	2.50
01571820	1996	2007	0.76	0.41	4.71	0.71	0.40	4.71
01564997	1994	1995	0.85	0.61	5.31	0.93	0.73	4.43
01537524	2001	2002	0.93	0.10	7.34	0.94	0.01	7.81
01548303	2012	2015	0.88	0.74	2.85	0.89	0.70	3.06
01573695	2012	2015	0.91	0.76	4.02	0.96	0.91	2.43
01610400	2002	2003	0.86	0.52	5.12	0.87	0.47	5.35
01613900	2007	2008	0.64	0.32	6.14	0.69	0.51	5.17
01614830	2006	2009	0.91	0.28	5.33	0.92	0.37	4.81
01621050	2002	2004	0.88	0.20	6.48	0.91	0.43	5.50
01630700	2006	2009	0.92	0.81	3.22	0.92	0.89	2.40
01645704	2007	2014	0.95	0.70	4.11	0.95	0.78	3.53
01645762	2007	2017	0.95	0.64	4.44	0.94	0.70	4.07
01649190	2007	2014	0.88	0.55	5.29	0.95	0.71	4.24
01650800	2012	2013	0.88	0.50	5.64	0.96	0.91	2.36
01651800	2012	2013	0.87	0.76	3.93	0.94	0.87	2.88
01654500	2013	2015	0.94	0.78	3.63	0.94	0.86	2.91
01656903	2007	2015	0.82	0.56	4.68	0.91	0.80	3.16
163626650	2007	2009	0.87	0.09	7.39	0.64	0.36	6.22
165389205	2011	2014	0.95	0.91	4.38	0.94	0.95	3.28

To validate the performance of the modeled water temperature within the headwater stream and high-order streams, we compared our model simulation results against the daily water temperature measurements from United States Geological Survey (USGS) website (available at: https://waterdata.usgs.gov/nwis). The sites are well distributed in the sub-basins across the region, and mostly located at the headwater zones. The site's information and the summary of NSE, R^2, and RSMD for the validation could be found in Table 3-2. Overall, the model simulated water temperature agrees well with the observed water temperature with most of the R^2 values are higher than 0.9.

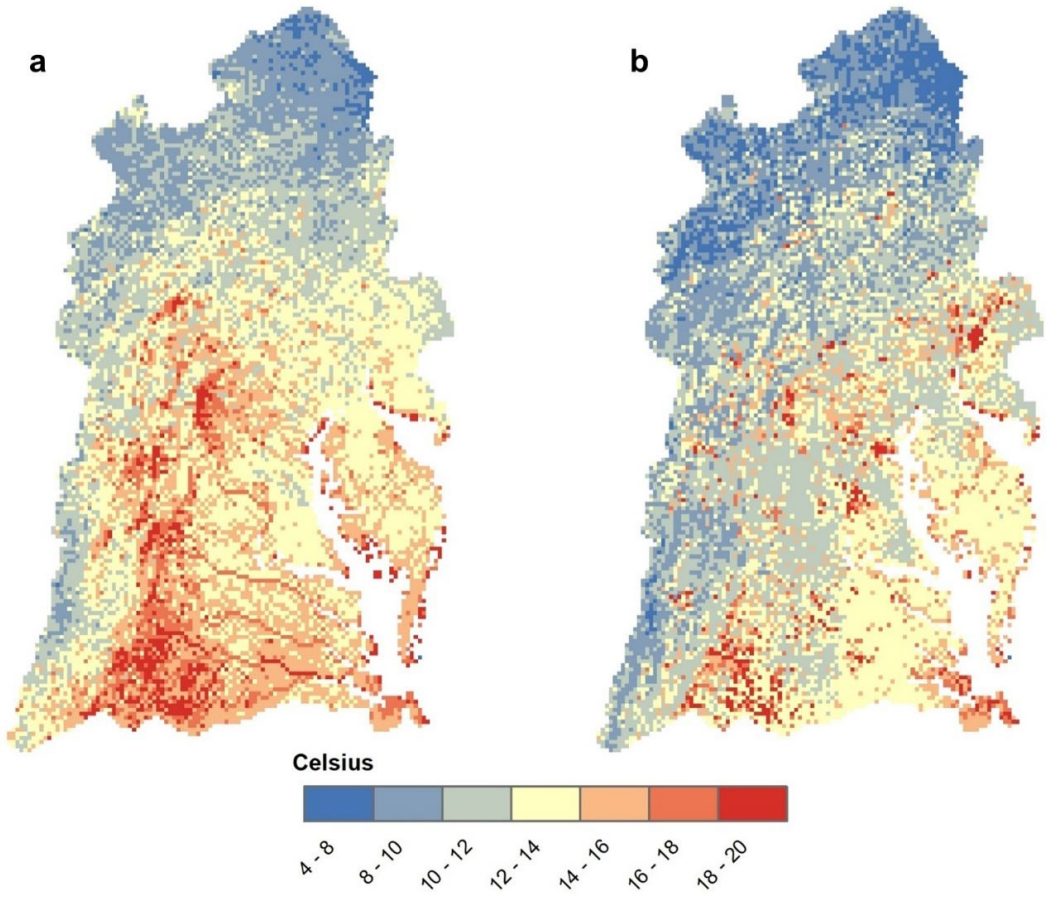

Figure 3-6. Spatial pattern of annual average water temperature within rivers (a) and small streams (b) of the year 2015.

3.4. Results

3.4.1. Spatial and temporal patterns of water temperature

The spatial pattern of the water temperature generally follows the latitudinal distribution, with most of the southern rivers have higher annual mean water temperature (16 ºC - 20 ºC) than that in the northern rivers (8 ºC - 14 ºC) (Figure 3-6). Topography helps to shape the spatial pattern of water temperature. The southern-ward of the Appalachian mountain has relatively lower water temperatures (4 ºC - 12 ºC). However, the eastern-ward of the mountain has much higher water temperature (12 ºC - 20 ºC). On the other hand, the coastal regions have much higher water temperature (12 ºC - 20 ºC) than that of the inland regions (4 ºC - 16 ºC) (Figure 3-6).

In this study, we plotted and analyzed the spatial and temporal pattern of water temperature within the high-order streams (higher than 1st stream order, Figure 3-6. a) and headwater streams (1st order streams, Figure 3-6. b) separately across the MAR of the year 2015. In general, the annual mean water temperature in the headwater streams is cooler than that in the high-order streams. In most of the regions, the annual mean water temperature of headwater streams is lower than 12 ºC. However, the annual mean water temperature in high-order streams is mostly above 12 ºC.

In the megacities (Figure 3-4, Figure 3-5 c), such as Washington DC., Baltimore and Philadelphia, the annual mean water temperature reached to 18 ºC - 20 ºC in headwater streams (Figure 3-6 b), but stream water temperature dropped quickly to 12 ºC - 14 ºC when the water transport to the 2nd stream order (Figure 3-6 a). In the south part of the study region, the annual

mean water temperature is mostly about 10 ºC – 14 ºC, the water temperature of the high-order streams reached to 16 ºC - 20 ºC at the high steam orders.

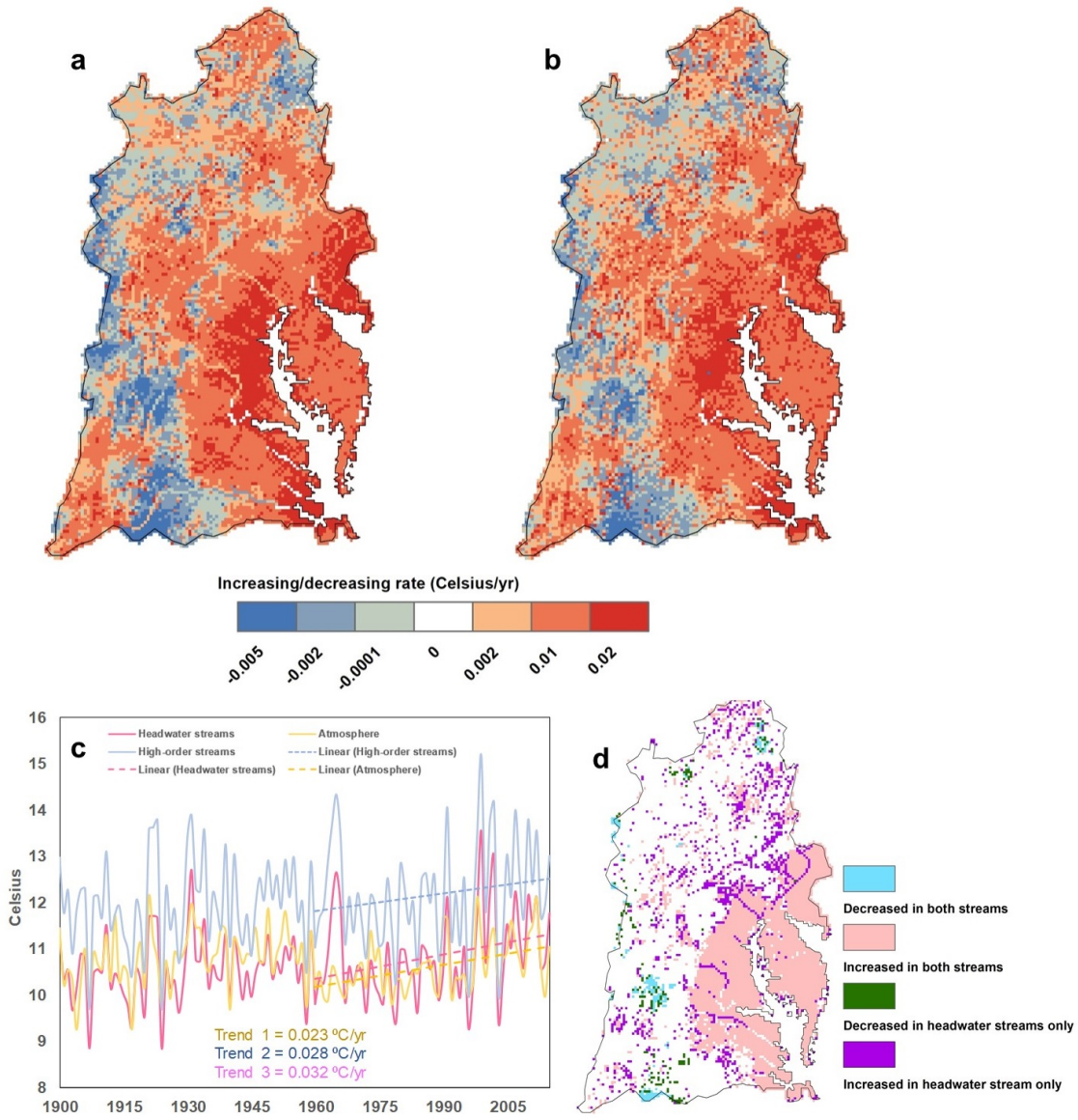

Figure 3-7. Changes in annual average water temperature within rivers (a) and small streams (b) across the Mid-Atlantic Region from 1900 to 2016 (c). Significance of long-term changes in water temperature of small streams and rivers (d). Note: The trends in (c) are the increasing rates of air temperature (trend 1), and water temperatures in high-order streams (trend 2) and headwater streams (trend 3) from 1960 to 2015.

3.4.2. The long-term changes in water temperature in headwater streams and high-order streams

The overall water temperature in high-order streams increased significantly from 1900 to 2016, with an increasing rate of 0.0047 ºC / year. Specifically, the increasing rate elevated to 0.028 ºC / year from 1970 -2016 (Figure 3-7. c). The water temperature in headwater streams increased significantly during 1900 to 2016 with an increasing rate of 0.0065 ºC / year, and the increasing rate reached to 0.031 ºC / year from 1970 -2016 (Figure 3-7. c).

In coastal regions or downstream regions, the water temperature of lower-order streams (lower than 5^{th} stream order) shows a significant increasing trend (Figure 3-7. c) from 1900 to 2015. However, the increasing trend of headwater streams is lower than that in high-order streams (Figure 3-7. a, b). It should be noted that the increasing trend of water temperatures in high order streams (higher than 5^{th} stream order, Figure 3-4, 3-7. a) is not statistically significant, and the increasing trend is less than 0.002 ºC / year from 1900 to 2015.

In the inland-ward of the MAR, stream water temperatures remaining relatively steady, with most of the grid points do not show statistically significant trends during the past 100 years (Figure 3-7. c). However, there still are many 1^{st} order headwater streams show a century-long increasing trend. Only seldom points show a significant decreasing trend of water temperature in both high-order streams and headwater streams. The stream water temperature of the northern regions has a slight increasing or decreasing trend, with the rate ranges from -0.0001 ºC / year to 0.002 ºC / year. Surprisingly, nearly half of the southern streams have a slight decreasing rate of steam-water temperature with a value of about -0.005 ºC / year.

3.4.3. Attribution the contribution of environmental factors to changes in stream water temperature

According to our factorial analysis, climate factors explain more than 90% of the changes in streams water temperature across the MAR since the 1900s (Figure 3-8). Around the 1970s, climate impact to water temperature in high-order streams and headwater streams diminished to 30.3% and 4.4%, respectively (Figure 3-8). Land-use conversion accounts for 37.4% and 61.4% of the changes in water temperature in high-order streams and headwater streams during this time period (Figure 3-8). Nitrogen inputs and CO_2 fertilization effect contribute more than 30% of the increased in water temperature with high-order streams and headwater streams in the 1970s. After the 1970s, the contribution of land-use, CO_2, and N inputs to the changes in high-order streams water temperature damped to ~10%, but still, account for ~20% of the changes in headwater stream water temperature (Figure 3-8).

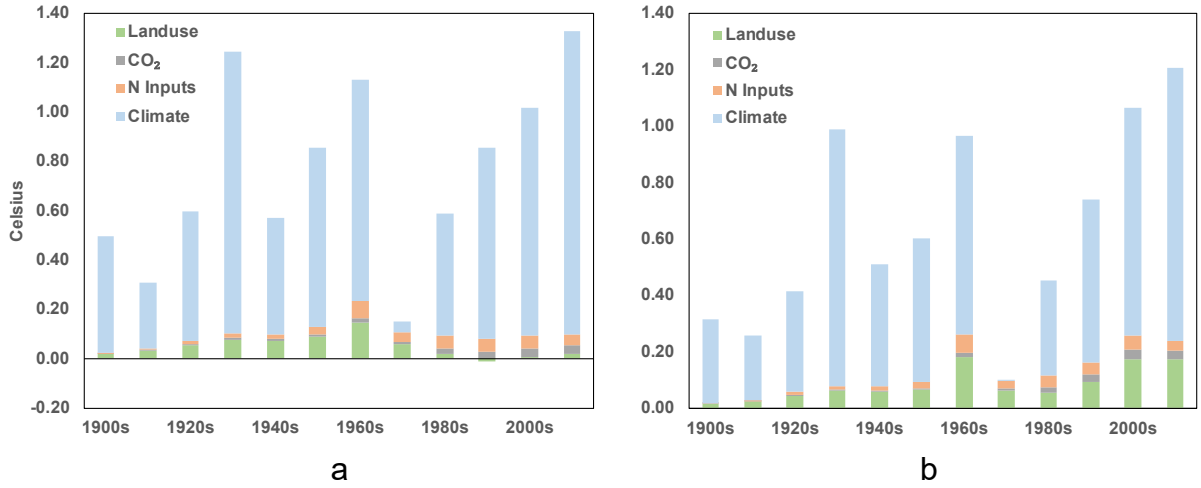

Figure 3-8. Contribution of environmental factors to the changes in water temperature in large rivers (a) and small streams (b).

3.5. Discussions

3.5.1. The impact of climate on the water temperature of high-order streams and headwater streams

Air temperature is still the dominant driver of the increasing or variations in water temperature. The spatial pattern of the increasing trend in water temperature (Figure 7.d) follows that of air temperature (Figure 3-5.f), with both water temperature and air temperature increased in coastal regions and decreased in the mountain regions. Air temperature primarily influences water temperature in two pathways: (1) Thermal energy exchanges between air and water interface (Arismendi et al., 2014). (2). Rising air temperature influences land surface temperature, and indirectly changes the temperature of shallow groundwater and the adjacent headwater streams (Kurylyk et al., 2015; Menberg et al., 2014).

It has been revealed by the statistical analysis of 129 USGS site measurements (Rice and Jastram, 2015) that, the stream water temperature and air temperature across the Chesapeake Bay Watershed show significant increasing trend since the 1970s with the increasing rate of 0.028 ºC / year and 0.023 ºC / year, respectively. The magnitude of the increasing trend in this statistical-based study (Rice and Jastram, 2015) is consistent with the DLEM predicted increasing rate (0.028 ºC / year) of water temperature in high-order streams (larger than 1st streams) from 1970 to 2015 across the whole MAR. However, this DLEM-based modeling study suggested a higher increasing rate of water temperature (0.031 ºC / year) in 1st order headwater streams, which been underestimated by the data analysis-based study.

Overall, the contribution of air temperature to the changes in water temperature in high-order streams is consistent with that of headwater streams in our factorial analysis (Figure 3-9. a). Thus, the higher increasing rate of water temperature in headwater streams indeed sourced

from other environmental factors. Precipitation is another dominant climate variable that significantly influences the stream water temperature. A higher precipitation rate would enlarge the water surface area in the headwater zone, which accelerates the thermal energy exchange between air and water (equation 5). On the other hand, the increase in precipitation resulted in more cooling groundwater discharge in summer and warming groundwater flow in winter (Briggs et al., 2018), which substantially buffers the seasonal variations of water temperature in both headwater streams and high-order streams (Burns et al., 2017; Snyder et al., 2015). Additionally, the increased precipitation cools the land surface even though evaporative energy release also contribute to the changes in water temperature (Trenberth and Shea, 2005)

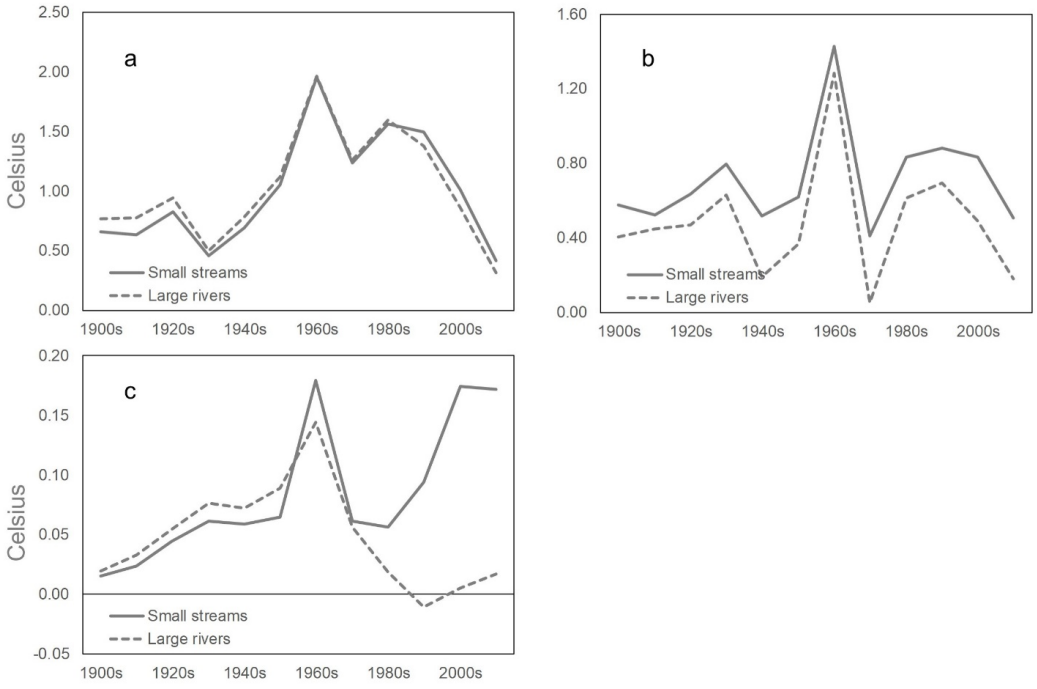

Figure 3-9. Changes in water temperature of rivers and small streams across the Mid-Atlantic Region in response to the atmosphere temperature (a), precipitation (b), and land-use change (c).

.

Our factorial experiments suggested that the contribution of precipitation to headwater steams temperature is larger than that of high-order streams (Figure 3-9. b). Here we only consider the absolute value of the contribution of air temperature and precipitation because of the variations in climate conditions which do not account for the long-term change. That is because the increased precipitation substantially increased groundwater discharge. Headwater streams, which experienced heavy groundwater and surface water exchanges, show less seasonal variation than that in the main river channel. Thus, headwater streams are conventionally thought as the refugia of the climate change due to the cooling effect of groundwater discharge during the summer season (Ficklin et al., 2014; Isaak et al., 2016b; Snyder et al., 2015)

A recent study found that the thermal energy of water seepage from shallow groundwater increased significantly with the rising land-surface temperature in the Blue Ridge Mountains of the U.S. (Briggs et al., 2018). The refugia of cold water species would disappear soon under the context of the global warming (Leach and Moore, 2019). Similarly, we found a faster increasing rate of temperature in groundwater-fed headwater streams across the MAR (Figure 3-7.c), which is supporting by the findings at the site or catchment level (Leach and Moore, 2019).

3.5.2. Land conversions on water temperature

Land-use change shows a tremendous impact on the water temperature in high-order streams and streams. As predicted by DLEM, water temperature in urban regions reached to 18 ºC -20 ºC in 2015, which is higher than the water temperature of the sub-urban regions (Figure 3-6. b). The model simulation results suggest that the water temperature in headwater streams is susceptible to urbanization, which is supported by the catchment level study conducted at the north of Washington D.C. (Nelson and Palmer, 2007). However, the effect of land-use changes on water temperatures quickly damped while water flows into 2nd stream orders or higher (Figure 3-6. a)

because solar radiation and sensible heat fluxes exchange dominate the water temperature with the water surface area increased to a certain level.

This study region experienced a large fraction of cropland conversion to forest land during the last century (Figure 3-5.a), and the land-use conversions could contribute to the changes in water temperature (Yearsley et al., 2019). The changes in plant canopies and associated net water surface area receiving solar radiation could directly influence water temperature. Thus, the term *effective water surface area* (Li et al., 2015b) was introduced into the model with a fixed value (0.875) to represent the shading effect of the plants. In this study, we calibrated the shading effect of different plant function types on headwater streams (equation 5) to match the observed water temperature of headwater streams. Such as forest land has a higher shading effect, but less in grasslands or shrublands. On the other hand, the changes in vegetation types resulted in different ground litter depth and surface albedo which directly link to the soil evaporative energy release. In DLEM simulations (Figure 3-6), water temperature in forests or grassland is much lower than that in regions with high fractions of the urban impervious surface due to the higher evapotranspiration rates (Trenberth and Shea, 2005).

3.5.3. The sensitivity of groundwater effects on water temperature

Earth system models and hydrological models do not explicitly simulate the lateral transport of groundwater from the soil root zone to the tributary streams. Thus, simplification is needed by defining the headwater streams temperature or seepage groundwater temperature. Most of the previous modeling studies used empirical-based models to represent the water temperature of the headwater zone. This empirical-based headwater temperature was given as the boundary condition to force the water temperature models (Brown, 1969; Van Vliet et al., 2013, 2012; Van Wijk and De Vries, 1963; Wanders et al., 2019; Wu et al., 2012a, 2012a). Thus, the sensitivity of

water temperature in response to the boundary condition has not been thoroughly investigated. Especially for the outlet of the rivers, climatic and hydraulics variables including surface area, air temperature, radiations were conventionally considered as the dominant drivers (Li et al., 2015b; Wu et al., 2012a).

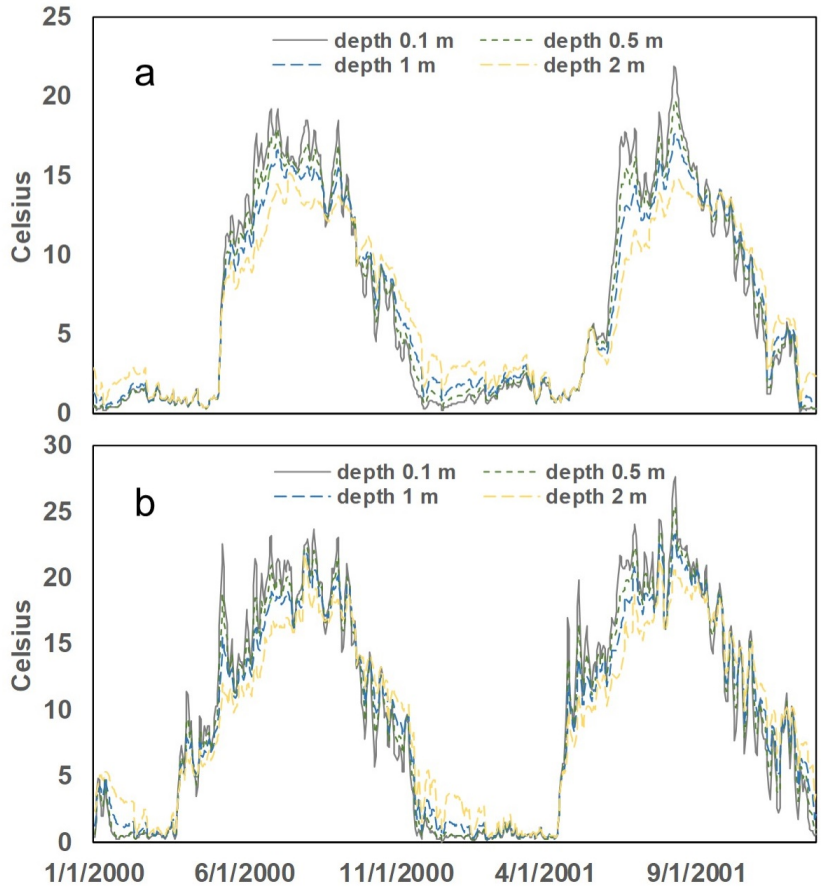

Figure 3-10. Simulated water temperature at the outlet of the Delaware River (a) and Susquehanna river (b) in response to the setting of groundwater boundary conditions.

Here, we investigated the sensitivities of the water temperature at the high-order streams of the Delaware River (Figure 3-10. a) and Susquehanna River (Figure 3-10. b) in response to the

setting of groundwater temperature. In this model, we defined the temperature of seepage groundwater flows as equals to the mean soil temperature from the surface to a calibrated soil depth (0.5m). We plotted the simulated daily water temperature from 2000 to 2001 at two USGS sites, which are located at the 3rd (site number: 01428750) and 5th (site number: 01460300) order of the Delaware River with the calibrated depth given as 0.1 m, 0.5 m, 1 m, and 2 m, respectively. The sensitivity analysis suggested that water temperature continuously drops with the increases of calibrated soil depth increased from 0.1m to 2m. A noticeable time lag was detected in both sites when the depth was set as 0.1 m and 2 m, respectively. Therefore, correctly defining the seepage groundwater temperature to couple the land model with riverine transport is of great importance to improve the model performance. Li et al. (2015) suggested the boundary condition of seepage groundwater temperature is from the water table to the bottom of the root zone (5 m depth in the Community Land Model (Oleson et al., 2010)), which is much deeper than that in this study. However, the apparent time lag between their simulation and observations suggest a modification of their settings.

3.5.4. Limitation of the empirical-based model

Air temperature has been widely applied as a sole indicator to predict water temperature in empirical models (Brown, 1969; Chen and Fang, 2015b; Mohseni et al., 1998; Segura et al., 2014; Wehrly et al., 2009). The regression equation was established by statistical methods with most of the water temperature observations obtained from the high-order streams. Due to the lack of observations available in the headwater streams, the empirical methods may not have enough support to estimate the water temperature in the headwater zones accurately. There is a growing debate on if air temperature could be used as the sole indicator of water temperature (Arismendi et al., 2014); the reliability of regression equations would be hampered with the

changes in climate and hydrological condition (Arismendi et al., 2014). Our results suggested that using the empirical model may largely underestimate the increasing rate of water temperature within the headwater streams (Figure 3-7. c), which is supporting by the site level study within the Columbia river basin (Leach and Moore, 2019).

Our factorial analysis suggests that climate variables cannot explain the changes in water temperature during the 1970s (Figure 3-8, Figure 3-9). However, the contribution of climate to the stream water temperature reached more than 80% from 1980 to 2015. That suggests a high accuracy of empirical equations in predicting water temperature from 1980 to 2015, but a relatively lower value during the 1970s. To confirm this assumption, we compare the accuracy of the process-based model and empirical-based model. We found that the accuracy of the empirical model is equivalent to that of the physical-based model from 1980 to 2015, but the physical-based model is more accurate before the 1970s (Table 3-2).

3.5.5. Uncertainties

Although this model is process-based, we still used several semi-empirical equations to represent the physical processes. For instance, we conducted a semi-empirical based method to estimate the water surface area (Allen et al., 2018). Additionally, the model parameters may induce large uncertainties as well but have not been well investigated in this study.

Human activities, such as water extraction, were not considered in the model. Water extraction from groundwater and stream water are ubiquitous agricultural activities, which would significantly affect soil evaporation, groundwater outflow and even soil properties (Keery et al., 2007). In this study, we investigated the effect of CO_2 and nitrogen inputs to the stream water temperature (primarily through the effect of plant growth). Although these factors only provide minor contributions to the increase of water temperature and the function of the CO_2 fertilization

effect is still in debate, those human-induced effects would propagate shortly (Terrer et al., 2016). Furthermore, the hot water release from industry has already been considered as the thermal pollutant which strongly affects the health of the aquatic ecosystems (Webb et al., 2008). However, it is not realistic to incorporate this part into the model due to a lack of inventory data as model inputs. In this model, we only considered the mixture of water with dams and lakes, but do not include dam and lake routing and stratifications. Although the cooling effect of dams has been well documented in observations and modeling studies (Chen and Fang, 2015a; King et al., 1998), the effect of dams on water temperature is still in the debate which will be a great uncertainty source of the modeling results (Chen and Fang, 2015a).

3.5. Conclusion and future research

In this study, we investigated the water temperature by developing a water temperature module within the DLEM -TAIM modeling framework. This model linked the thermal energy balance of land and aquatic systems together, which can well address how land processes would affect the water discharge and water temperature. We deployed and validated this model on MAR of the U.S and filled the knowledge gaps of water temperature within headwater streams. Since this work mostly focuses on impacts of climate and human disturbances on the temperature in headwater streams, our future research would investigate how the improved water temperature module would influence aquatic biogeochemistry. Since this study region does not have large lakes and reservoirs, the missing component to represent the dam and lake routing and stratification would not influence the reliability of the model. With the improved technology and data source available, remote sensing-based methods prompted a new direction to estimate water temperature (Martí-Cardona et al., 2019). Therefore, better data-model integrations are needed to

enhancing model capability in predicting headwater stream and high-order stream water temperature and the associated biogeochemical cycles.

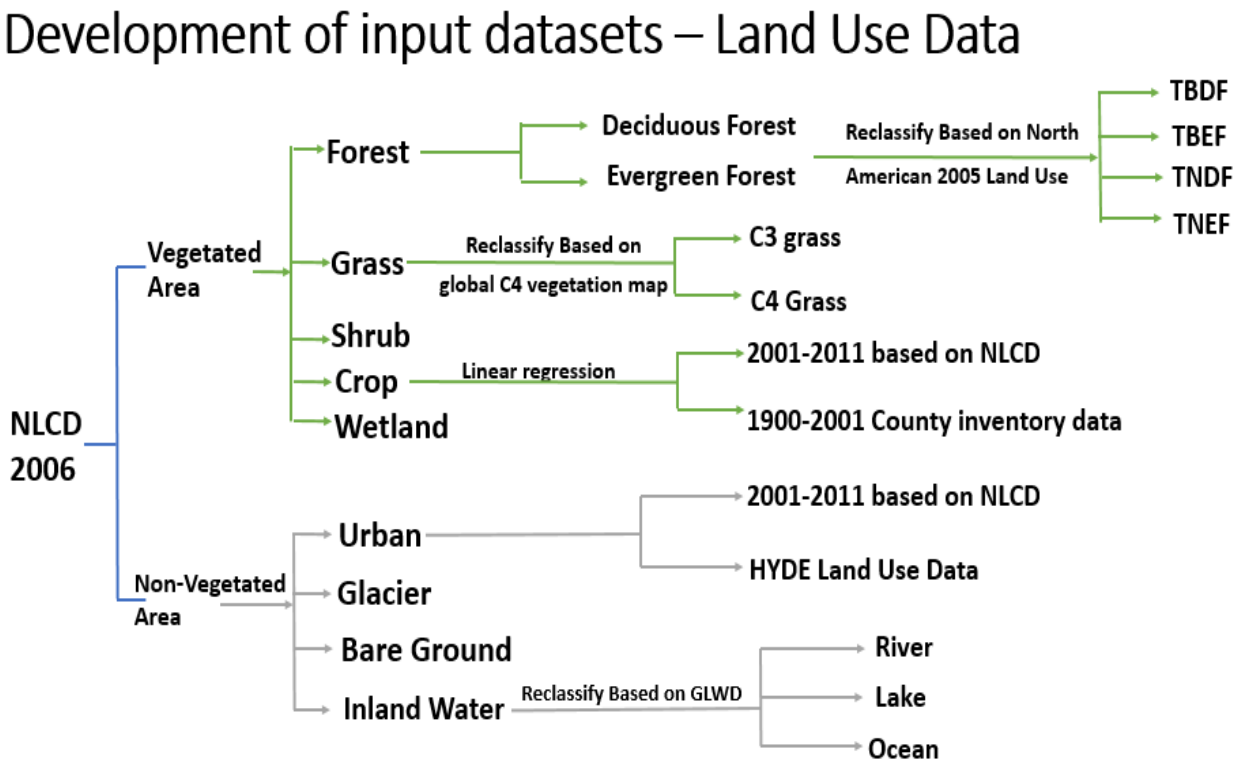

Figure 3-11. The flowchart to describe the development of historical land-use cohort

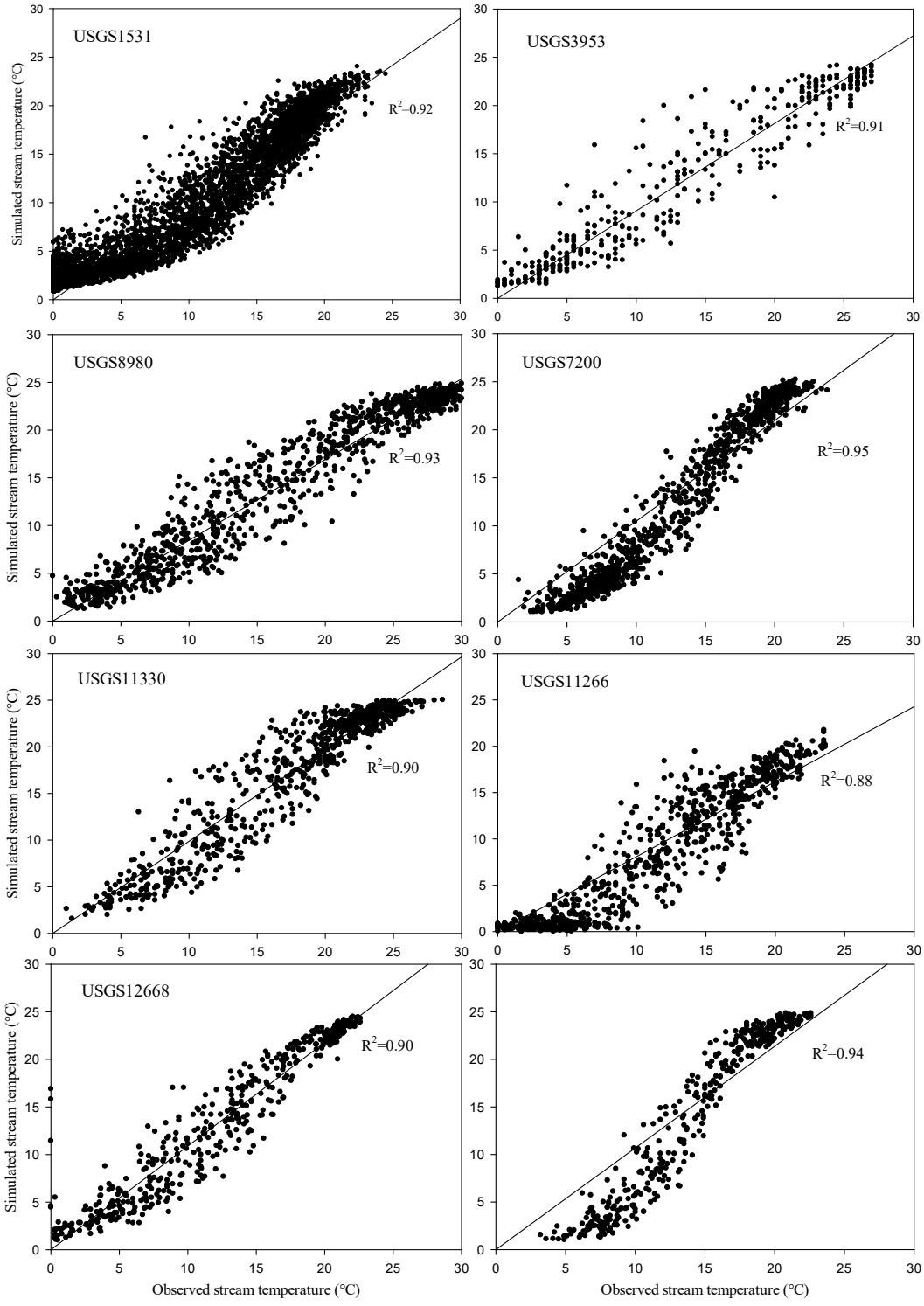
USGS1531
R2=0.92
USGS3953
R2=0.91
USGS8980
R2=0.93
USGS7200
R2=0.95
USGS11330
R2=0.90
USGS11266
R2=0.88
USGS12668
R2=0.90
R2=0.94
Simulated stream temperature (°C)
Observed stream temperature (°C)

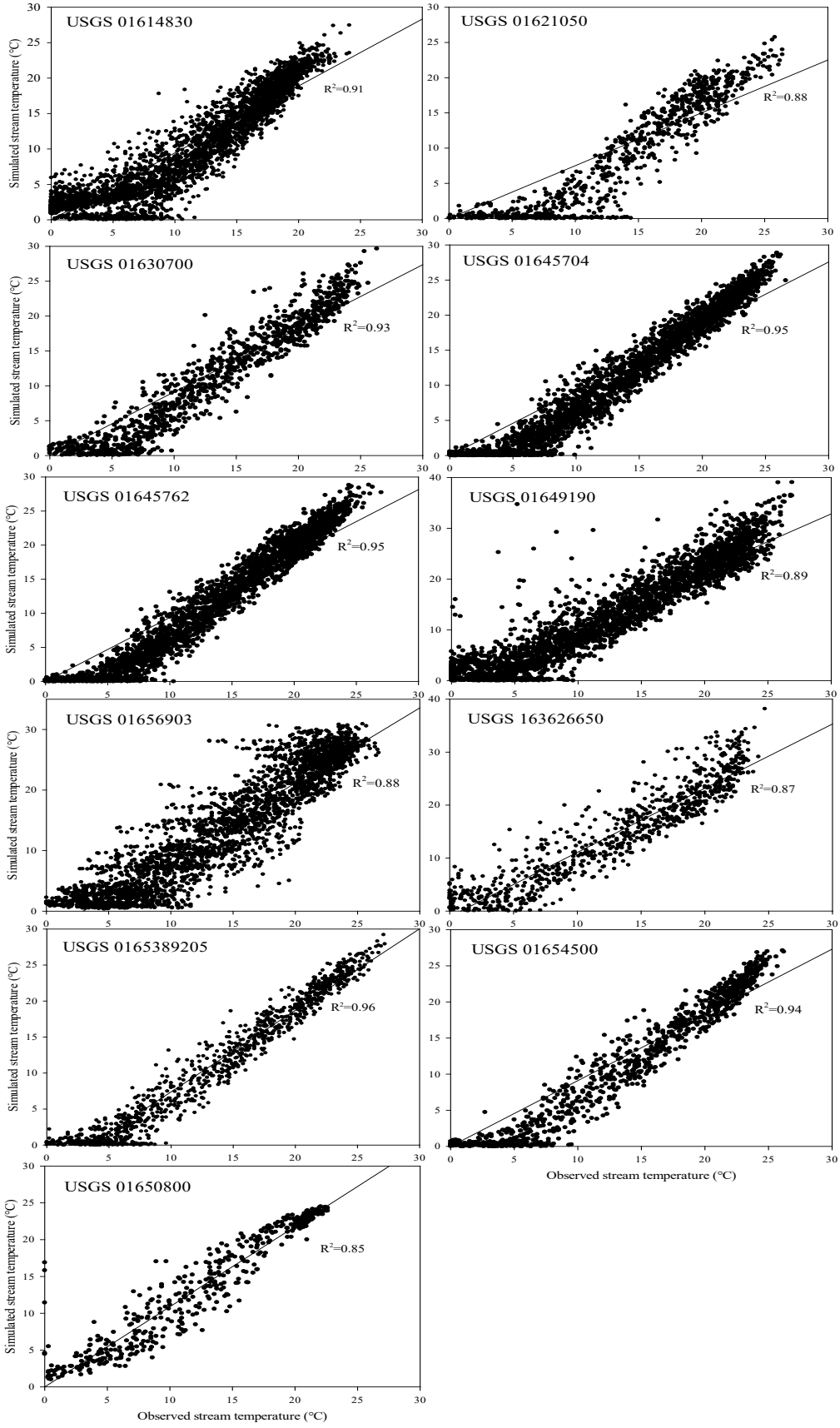
USGS 01614830
R²=0.91
USGS 01621050
R²=0.88
USGS 01630700
R²=0.93
USGS 01645704
R²=0.95
USGS 01645762
R²=0.95
USGS_01649190
R²=0.89
USGS 01656903
R²=0.88
USGS 163626650
R²=0.87
USGS 0165389205
R²=0.96
USGS 01654500
R²=0.94
USGS 01650800
R²=0.85
Simulated stream temperature (°C)
Observed stream temperature (°C)

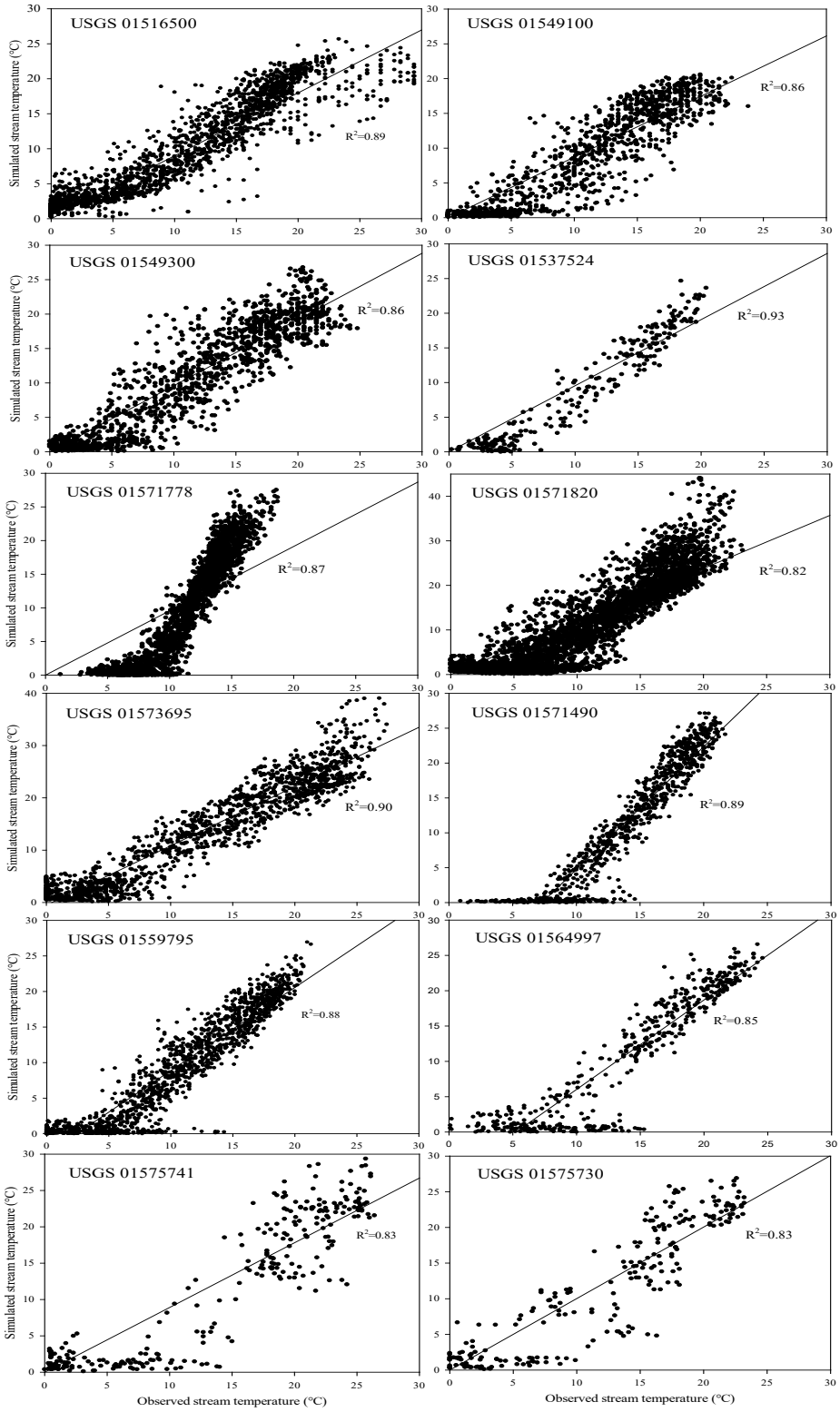

Figure 3-12. Compare stream water temperature again USGS observations across the CBW and DRB.

Chapter 4: Modeling carbon export and CO_2 evasion from river network: application to Chesapeake Bay Watershed and Delaware Bay Watershed

Abstract: Riverine carbon fluxes have been recognized as an essential part of the global/regional carbon cycle. However, accurate estimation of the carbon fluxes at a large spatial scale, such as in large basins, has not been fully constrained due to the lack of modeling tools and data-model integrations. Here, we coupled the Dynamic Land Ecosystem Model (DLEM) with a scale-adaptive hydrological model to simulate the carbon exports, CO_2 degassing, and carbon burial in the riverine ecosystems. This coupled model can well address CO_2 emissions from the small headwater streams through the incorporation of sub-grid routing, and more importantly, this model can quantify the impacts of climate change and anthropogenic activities on terrestrial ecosystems and consequently GHG emissions of riverine ecosystems. Taking advantage of the new model, we investigated riverine carbon fluxes across the Chesapeake Bay Watershed (CBW) and Delaware Bay Watershed (DBW) from 1900 to 2015. Driven by a 4-km spatial resolution input dataset, the model was calibrated and validated using reported daily discharge and water quality data from United States Geological Survey (USGS). Our results suggested that riverine CO_2 degassing (886.25 ± 177.1 Gg C/yr, ±1 standard deviation) account for most of the carbon fluxes across the study region followed by Dissolved Inorganic Carbon (DIC) fluxes (883.26 ±268.58 Gg C/yr), Dissolved Organic Carbon (DOC) fluxes (293.27 ± 81.55 Gg C/yr), carbon deposition (118.19 ± 32.27 Gg C/yr), and Particulate Organic Carbon (POC) fluxes (105.4±35.41 Gg C/yr). The headwater zone (1st to 3rd stream order) contributes more than 73% of the riverine CO_2 emissions. The long-term changes in Riverine CO_2 degassing, DOC, and DIC

exports show a significant increasing trend after the 1960s with the increasing trend of 2.74 Gg CO_2-C/yr, 2.01 Gg DOC-C/yr, and 5.83 Gg DIC-C/yr, respectively. Climate variability explains 57.5% of the increased in carbon fluxes, followed by land-use/land-cover change (24.92%), N deposition (7.54%), N applications (5.86%) and CO_2 effect (4.18%). Here, re-forestation indirectly decreased the riverine export of all carbon species, while increased temperature and precipitation, extensive nitrogen fertilizer use, CO_2 fertilization effect, and N deposition all contribute to the increase of riverine DOC, POC, and DIC fluxes.

Keywords: Chesapeake Bay Watershed, Delaware River Basin, Carbon export, CO_2 degassing, Dynamic Land Ecosystem Model (DLEM).

Key points: 1, Riverine Carbon fluxes from Chesapeake Bay Watershed and Delaware River Basin from 1900 to 2015

2, Modeling carbon dioxide degassing from small rivers

Introduction

Rivers and streams, namely as the terrestrial-aquatic ocean continuum (Regnier et al., 2013), bridge up the two largest carbon reservoirs: terrestrial and marine ecosystems. Longitudinal carbon fluxes through river channels to the ocean or CO_2(s) release to the atmosphere from rivers are much larger than our previous thoughts (Regnier et al., 2014). Therefore, riverine carbon fluxes have been suggested to revise carbon accounting of the conterminous U.S. and Amazon river basin (Butman et al., 2016; Hastie et al., 2019). It has been noted that the terrestrial carbon loss into rivers, also referred to as terrestrial carbon loading, is the dominant component of the carbon fluxes of inland waters (McDonald et al., 2013). However, the terrestrial carbon loading is a poorly constrained term (Drake et al., 2018). Thus, developing tools to accurately quantify the magnitude and spatial and temporal patterns of the carbon loading, lateral carbon fluxes, and riverine CO_2 degassing along the land-ocean continuum is of great importance to the regional carbon cycles (Regnier et al., 2013).

Data-based analyses have been conducted at regional and continental levels to quantify the carbon exports and CO_2 emissions. However, none of these studies quantify the temporal variability of carbon fluxes across large spatial scales (Butman et al., 2016; Butman and Raymond, 2011; Raymond et al., 2013). Although regression-based tools, for instance, Load Estimator LOADEST (Runkel et al., 2004a), SPAtially Referenced Regression On Watershed attributes (SPARROW) (Georghiades, 2003), has been widely deployed to reconstruct the continuous temporal patterns of carbon fluxes at the site level, none of these models extend the model performance to predict the spatial patterns of carbon fluxes along stream networks. Additionally, the regression-based methods cannot attribute the impacts of environmental factors

on the terrestrial-aquatic carbon dynamics due to their intrinsic weakness, which limits the applications to policy-relevant studies.

After a long time miss-understanding of riverine carbon budget as a fixed term in the science community, the impacts of climate change and human disturbances on riverine carbon dynamics became apparent during the past twenty years (Regnier et al., 2013). Thus, understanding the impacts of changes in environmental conditions on the land and aquatic carbon cycle through field experiments or data analysis are of great importance to the further investigation of the inherent mechanism of the carbon cycle. Enhanced exports of Dissolved Organic Carbon (DOC) and Dissolved Inorganic Carbon (DIC) has been found primarily due to the long term increase in air temperature (Laudon et al., 2012; Pastor et al., 2003). Precipitation and the associated hydrological response of the watershed play critical roles in regulating carbon fluxes (Raymond and Oh, 2007). Further human activities have substantially influenced the terrestrial carbon cycle, resulting in significant impacts on the aquatic carbon cycle (Raymond and Hamilton, 2018). A recent data analysis study revealed that land conversion from organic-rich soils during World War II substantially increased soil carbon loss into rivers (Noacco et al., 2017). Unexpected anthropogenic effects, including the CO_2 fertilization effect and enhanced nitrogen deposition, led to an increase in carbon loading to rivers (Findlay, 2005; Houghton, 2010). Not only terrestrial carbon inputs to rivers determine the riverine carbon fluxes, fluvial conditions, including hydraulic loading and water temperature, also help to regulate the riverine carbon dynamics (Chapra, 2008; Harrison et al., 2009; Isaak et al., 2016b).

The precise understanding of the intrinsic mechanism of the terrestrial or aquatic carbon dynamics from fieldwork spurred substantial progress in establishing process-based models (Dick et al., 2015; Tian et al., 2015c; Laruelle et al., 2017; Seitzinger et al., 2005). Process-based

models help fill the data gaps across spatial and temporal scales. However, Earth system models (ESMs) are limited by their lack of integration between land and ocean systems through riverine carbon flow along the land-ocean continuum (Bauer et al., 2013). In recent decades, model complexity increased significantly with the representation of microorganism activities coupled with carbon and nutrient dynamics, which result in considerable uncertainty (Chapra, 2008; Hofmann et al., 2008). Additionally, most ESMs are applied at the coarse spatial resolutions, and thus the surface and subsurface hydrodynamics are overly simplified. Notably, the headwater streams (1^{st}-3^{rd} stream-order) are excluded in the ESMs due to their small area (McClain et al., 2003) and the structural complexity, such as the complex topography, subsurface hydraulics and microbial activities (Battin et al., 2009).

There is increasing recognition of headwater streams as the hotspots (McClain et al., 2003) of riverine CO_2 degassing (Battin et al., 2009). Recent studies indicate that most of the riverine carbon is degassed from headwater streams (Butman et al., 2016; Butman and Raymond, 2011; Raymond et al., 2013), and the dominant source of running water CO_2 and dissolved organic carbon in groundwater input (Corson-Rikert et al., 2016; Findlay et al., 1993; Hotchkiss et al., 2015). Additionally, the headwater streams and floodplains are found to store most of the riverine carbon, which is far beyond previous thoughts (Beckman and Wohl, 2014; Wohl et al., 2012). Despite increasing recognition of the role of headwaters in the carbon export and degassing to the overall riverine fluxes (Holgerson & Raymond, 2016), physical sampling programs in small rivers are limited and have not been incorporated into ESMs.

To better understand the role of riverine CO_2 emissions and lateral carbon fluxes in the regional carbon cycle, we coupled a scale adaptive river routing scheme (MOSART, Li et al. 2013) with a dynamic land ecosystem model (DLEM, Tian et al. 2015). To test the performance

of our newly improved terrestrial-aquatic interface module within the DLEM framework (DLEM-TAIM), we applied the model to the Chesapeake Bay and Delaware Bay watersheds located in the Northeast of the U.S (Figure 4-1), the two largest bays of the Atlantic Seaboard. Major rivers draining into the Chesapeake Bay include Susquehanna River, Potomac River, James River, Rappahannock River, York River, etc. The Chesapeake Bay Watershed (CBW) spans more than 64,299 square miles. The Delaware Bay Watershed (DBW) covers 12,800 square miles. These two regions, as the most urbanized area of the U.S., have been subject to massive land conversion during the last century and sustained more than 25.5 million people.

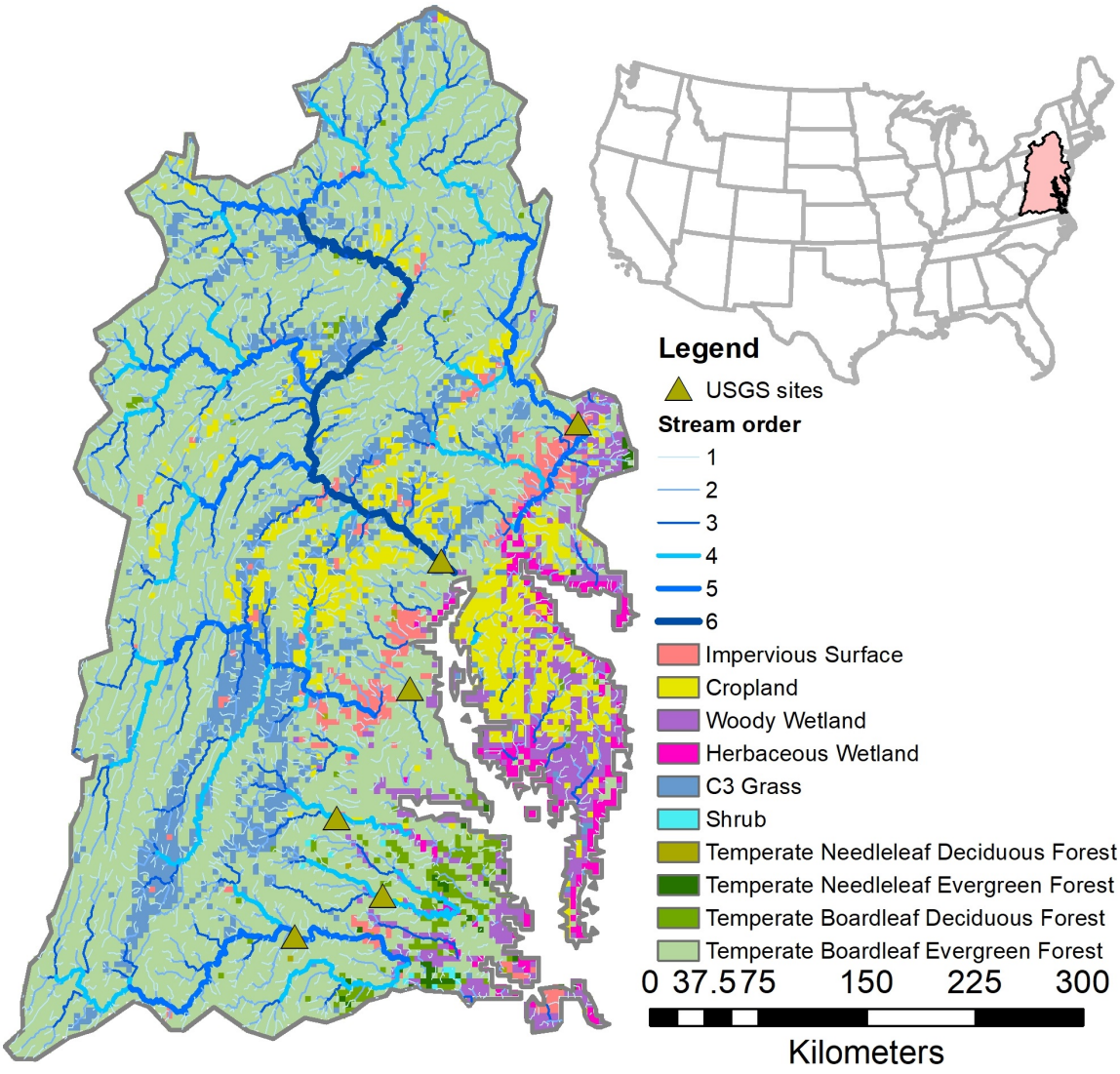

Figure 4-1. The major plant function types and land-use in Chesapeake Bay Watershed (CBW) and Delaware Bay Watershed (DBW)

In this study, we quantified the magnitude and spatial patterns of riverine CO_2 degassing and lateral fluxes of carbon species: Particulate Organic Carbon (POC), DOC, and DIC from Chesapeake Bay Watershed (CBW) and Delaware Bay Watershed (DBW) to the ocean water

from 1900 to 2015. Furthermore, we attributed the contribution of each environmental control to riverine C fluxes in the study region.

4.2 Methodology: model improvement

4.2.1. Improvement of DLEM-Terrestrial/Aquatic Interface Module (TAIM)

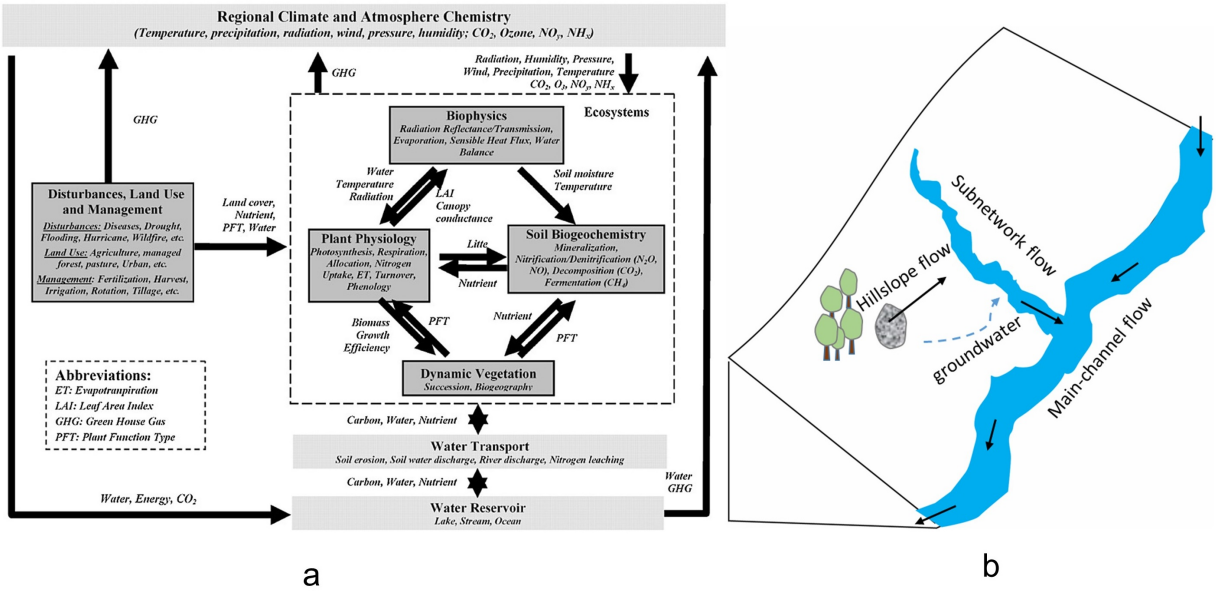

Figure 4-2. The general framework of the DLEM Terrestrial Aquatic Interface Model. (a). The concept model of DLEM. (b). The concept model of Model for Scale Adaptive River Transport (MOSART)

Building upon the Dynamic Land Ecosystem Model 2.0 (DLEM 2.0) (Tian et al. 2015) and the MOdel for Scale Adaptive River Transport (MOSART) (Li et al., 2013), in this study, we have developed and improved the Terrestrial-Aquatic Interface Module (TAIM) (Figure 4-2) for simulating dynamics of coupled hydrological and biogeochemical processes along the land-ocean aquatic continuum (LOAC).

DLEM2.0: A process-based terrestrial ecosystem model that couples carbon and nitrogen dynamics between plants and soil, and river routing to simulate water, carbon and

nitrogen fluxes, and GHGs emissions in terrestrial ecosystems (Figure 4-2. a). To address the sub-grid terrestrial processes, DLEM utilized a land-use cohort structure as the basic unit, which aggregated four natural plant function types, one cropland type, and urban impervious into one grid cell. The model simulated land carbon dynamics, including plant photosynthesis, soil biogeochemistry forced by the climate variables, and land-use changes. The outputs of land carbon and nutrients loading from the DLEM land module are utilized as the boundary condition to force the riverine biogeochemistry module (Tian et al. 2015).

In our previous studies, DLEM has been well validated against observational data and then applied to quantify water discharge (Liu et al., 2013; Tao et al., 2014; Yang et al., 2015d), and riverine exports of carbon (Ren et al., 2015; Tian et al., 2015c), and nitrogen (Yang et al., 2015a).

The previous DLEM version used the Linear Reservoir Routing (LLR) method (Coe, 1998) to calculate river routing at the continental scale. However, the inherent weakness of LLR method, which used constant variables to calculate flow velocity at each grid (an empirical equation based on channel slope) limiting its ability in predicting the temporal pattern (monthly and daily level in this study) of water discharge (Li et al., 2013; Yamazaki et al., 2011).

MOSART: In this study, A scale adaptive and fully physical-based model named Model MOSART (Li et al., 2013) (Figure 4-2. b) was incorporated into DLEM. The MOSART model separates the water transport within the grid cells into three sub-grid processes: hillslope flow, subnetwork flow, and main channel flow. The water from surface runoff will contribute to hillslope flow first. The subnetwork flow receives the water from hillslope flow, groundwater discharge, and flows into the main channel. The main channel flow merges water from upstream

grid cells and local subnetworks, and flow to the downstream grid cell. All three river- routing processes used kinematic wave methods (Chow, 1964a) to calculate the channel routing, which requires several physical parameters (channel length, bank-full depth, channel slope, and channel roughness) aggregated from the fine resolution

hydrography dataset. Similar to most land surface model, DLEM only consider vertical movements of subsurface soil moisture and lumped the lateral groundwater transport with parameterized outflow rates from a groundwater pool to the local subnetworks.

The apparent benefits gained from the scale adaptive water transport module are: while shifting the grid size in simulating, the length of the hillslope flow, and subnetwork flow shifting together according to the generalized hydrograph dataset (processed from high-resolution river network data (Figure 4-10). In other words, the length of small streams (subnetworks) within a grid cell would get longer (or shorter) when the grid size grows larger (smaller). Therefore, the parameters of the new water transport module only require minor re-calibration during scale shifting.

Here, we used remote sensing-based river surface area data (Allen and Pavelsky, 2018) as input for the large river channels. However, the water surface area of small rivers could not be detected by remote sensing data, and the small rivers are so dynamic. Hence, the water surface area of the small rivers is calculated from a statistical-based method (Allen et al., 2018) as shown in eq (1) (2):

$$A_s = \begin{cases} A_{RS,water} & Large\ river\ channel \\ W \times L, & small\ rivers \end{cases} \quad (1)$$

$$W = Q^{\frac{3}{5r+3}} \times (0.5\,A^{0.42})_i^{\frac{r-1}{r+0.6}} \times \left(8.1(9.8\,S)^{0.5}k^{-\frac{1}{6}}14^{-\frac{5}{3}}(1-\frac{1}{r+1})\right)^{-\frac{3}{5r+3}} \quad (2)$$

Where A_s is the surface area of the water body, $A_{RS,water}$ is the surface area derived from remote sensing data, W and L are the width and length of the rivers channel respectively, Q is water discharge (m/s), A is upstream area (ha), k is a bed roughness length scale, and r is shape parameter and was set at 1.5 in this study.

4.2.2. Riverine biogeochemical processes

The primary in-stream processes of carbon species include lateral transportation, decomposition of organic matter, particle organic matter deposition, and CO_2 degassing. These physical and biogeochemical processes have been adopted into the scale adaptive water transport scheme. Specifically, this module could address the processes within small-river align with a sub-grid routing of the water transport module. The net fluxes of carbon species in the main channel and subnetwork are given by:

$$\frac{\Delta M_{POC}}{\Delta t} = F_{a,POC} - v_s A_s c_{POC} - R_{POC} M_{POC} \quad (3)$$

$$\frac{\Delta M_{DOC}}{\Delta t} = F_{a,DOC} - R_{DOC} M_{DOC} \quad (4)$$

$$\frac{\Delta M_{DIC}}{\Delta t} = F_{a,DIC} + R_{POC} M_{POC} + R_{DOC} M_{DOC} - E_{CO2} \quad (5)$$

where M_{POC}, M_{DOC}, M_{DIC}, are the total mass of POC, DOC, and DIC respectively, in the main channel or subnetworks (gC), Δt is the time step, F_a is net advective transportation fluxes of carbon species ($gC \cdot d^{-1}$) (including inflow and outflow), R is the respiration rate of the organic carbon species, v_s is the settling velocity of particulate organic matters. Here, the hillslope flow receives carbon species from the land surface (with surface runoff) and contribute to subnetwork flow (Figure 4-2. b). The biogeochemical process within the hillslope flow was not considered in this study.

The advective fluxes of carbon through subnetwork combines carbon inputs from both hillslope flow and drainage runoff that are expressed as:

$$F_{a,sub} = F_{h/c} + F_{g/c} - Q_{sub}C_{sub} \quad (6)$$

where $F_{h/c}$ is the carbon flux (DIC, DOC or POC) of hillslope flow, $F_{g/c}$ is the carbon flux from the groundwater pool to the subnetworks. Here, the hillslope flow and groundwater pool received carbon loadings from surface runoff and subsurface runoff, respectively, which were estimated by DLEM land model. More detail about the calculation of carbon loadings could be found in Tian et al. (2015c). DLEM land model explicitly estimated the carbon loadings, more detail could be found in Tian et al. (2015c). Q_{sub} is flow rates of and subnetwork flow ($m^3 \cdot s^{-1}$), C_{sub} is the concentration (mg/L) of all three carbon species in hillslope flow, groundwater, and subnetworks, respectively.

The advective carbon fluxes through the main-channel was described as:

$$F_{a,main} = \sum_{i=1}^{n} Q_{up,i}C_{up,i} + Q_{sub}C_{sub} - Q_{main}C_{main} \quad (7)$$

where Q_{up} and Q_{main} are the flow rates of upstream grid cells and the main channel in the current grid cell ($m^3 \cdot s^{-1}$), respectively. C_{up} and C_{main} are the associate concentration (mg/L) of carbon species, respectively.

The settling velocity of the particle is estimated by a simplified Stokes' law (Thomann and Mueller, 1987), and is given by:

$$v_s = 0.033634 \times \alpha \times (\rho_s - \rho_w)\, d^2 \quad (8)$$

Where ρ_s and ρ_w are the density of particle and water, respectively, d is the diameter of the particle.

The respiration of organic carbon in rivers is computed according to a first-order kinetics equation:

$$R_{DOC,POC} = M_{DOC,POC} \times K_{res} \times (Q_{10})^{\frac{T_W - T_S}{10}} \quad (9)$$

where K_{res} is the reduction rate(m·d^{-1}), and M_{CO2} is the total mass of dissolved CO_2 (gC) in the river channel. T_w is the water temperature (^{o} C), and T_s is the reference temperature (20^{o} C). DLEM explicitly quantify the CO_2 emission from saturated water bodies, the major controlling factor of CO_2 degassing is temperature, water pH, flow velocity, and air CO_2 concentration. Here, the CO_2 degassing E_{CO2} is estimated as:

$$E_{CO2} = K_{CO2} \times \left(C_{CO2} - C_{CO2eq}\right) \times A_s \quad (10)$$

C_{CO2} is the dissolved CO_2 concentration (mg/L), which is estimated as a fraction of DIC concentration (C_{DIC}). In our model, the ($\frac{C_{CO2}}{C_{DIC}}$) ratio is controlled by water pH and water temperature (Chapra, 2008). The C_{CO2eq} represent the equilibrium CO_2 concentration (mg/L) which calculated based on Henry's law (Sander, 2015),:

$$C_{CO2eq} = -2400 \times EXP(\frac{1}{273+T_w} - \frac{1}{298}) \quad (11)$$

Where T_w (Celsius Degree) is water temperature. The gas exchange rate K_{CO2} (m·d^{-1}) is estimated as:

$$K_{CO2} = K_{600} \times (\frac{Sc_{CO2}}{600})^{-0.5} \quad (12)$$

where Sc_{CO2} is the Schmidt Number for CO_2 (He et al., 2017), and K_{600} is the gas exchange coefficient (Raymond et al., 2012). The term Sc_{CO2} is calculated as:

$$K_{600} = SI \times V \times 2841.6 + 2.03 \quad (13)$$

$$Sc_{CO2} = 1911.1 - 118.11 \times T_w + 3.4527 \times {T_w}^2 - 0.04132 \times {T_w}^3 \quad (14)$$

Where SI is the channel slope, V is flow velocity.

4.2.3. Statistical method

We conducted the Mann-Kendal trend test and Theil Sen linear regression to examine the increasing trend of time series data, including air temperature and precipitation (Figure 4-3, d, e,

f) and carbon fluxes (Figure 4-6). The same approach was applied to each grid cell within the CBW and DBE regions from 1900 to 2016 (Figure 4-7). The change rate (slope) and trend (p-value less than 0.05 means the trend is statistically significant. When the trend is significant, we use the slope to predict whether the trend is decreasing or increasing) were given in Figure 4-7. We calculated the Nash-Sutcliffe coefficient (NSE) (Nash and Sutcliffe, 1970) and coefficient of determination (R^2) to validate the model performance in predicting the DOC, DIC, and POC fluxes of each river respectively (Figure 4-4).

4.3. Simulation protocol and input data

4.3.1. Simulation experiments

The DLEM simulation follows three major steps: (1) We conducted equilibrium run driven by the potential natural vegetation map, 30-year average daily climate forcing, and other forcing including CO_2 concentration, land-use, nitrogen management at the level of 1900. The iteration finished until all the carbon, nitrogen, and water pools reach the equilibrium state. (2) To smooth the simulation results between the equilibrium run and transient run, we conduct a 30-year spinning-up run (Thornton and Rosenbloom, 2005; Tian et al., 2012), which randomly selected the driving forces between 1900 and 1929. (3). After the spinning-up run, the program reset to the year 1900 and run sequentially from the year 1900 to 2015, with all the forcing changes year-by-year.

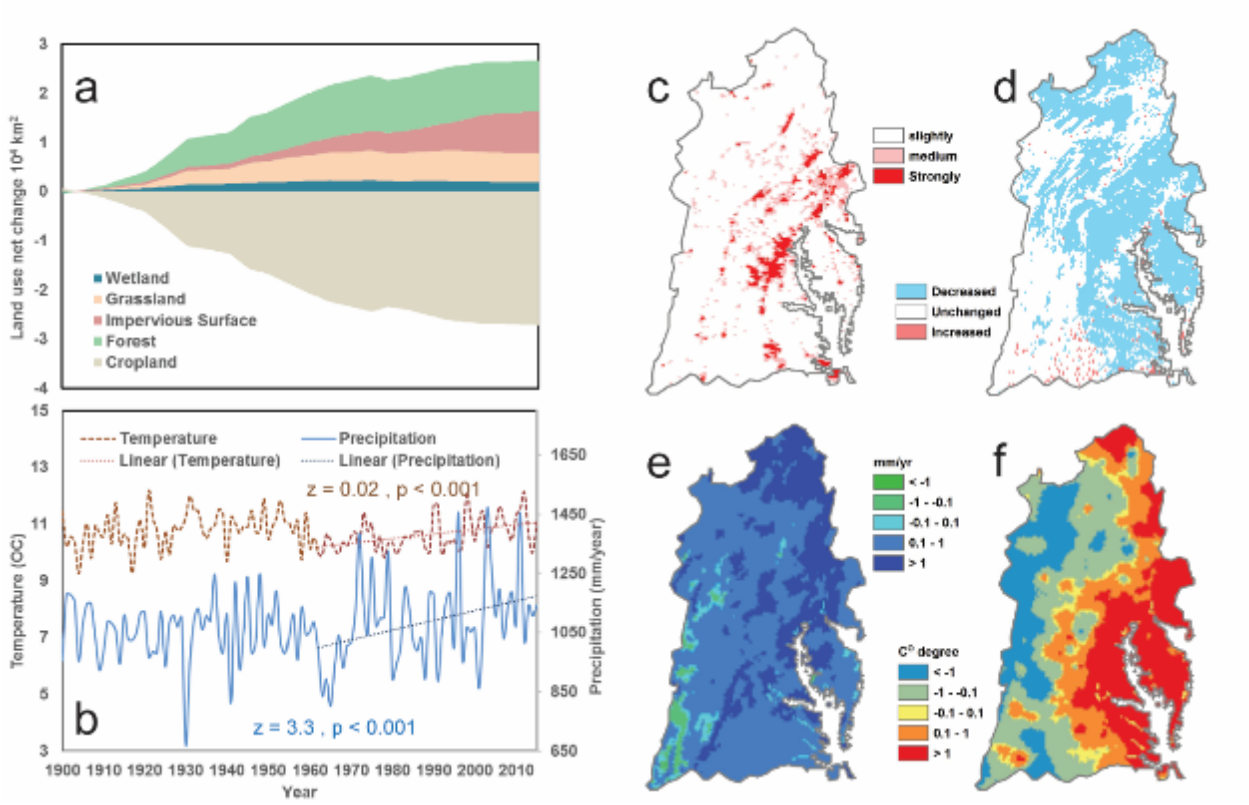

Figure 4-3. The land-use change and climate variability in CBW and DBW. (a). Temporal patterns of net land-use change from 1900 to 2015, (b). Temporal patterns of annual mean precipitation and air temperature from 1900 to 2015, (c). Changes in urban impervious surface. (d). Changes in cropland. (e). The change rate of annual precipitation. (f). The change rate of air mean temperature

To attribute the contribution of climate change, land-use change, nitrogen deposition, nitrogen management, and atmospheric CO_2 concentration (Tian et al., 2015c; Xu et al., 2010) to the riverine carbon fluxes, we first ran the all-combined simulation as the reference simulation with calibrated parameters. And then, we conducted a series of factorial experiments (Table 4-1) by keeping each driving factor at their level in 1900: In Simulation 2, nitrogen fertilizer use and manure nitrogen usage were continuously kept at the level in 1900. In simulation 3, NO_y and NH_x depositions were held constant at the level of the year 1900. In simulation 4, the land-use

cohort of the year 1900 was set-up to represent the constant land-use condition. In simulation 5, the atmospheric CO_2 concentration was not elevated since 1900. In simulation 6, the 30-year (1900-1929) average daily climate driving forces were used to represent the climate of the year 1900 and were continuously kept in the simulation. The contribution of each factor to the carbon fluxes was quantified from the subtraction with the carbon fluxes of the reference simulation.

Table 4-1. The experimental design for attributing riverine carbon fluxes to natural and anthropogenic factors including climate, atmospheric carbon dioxide (CO_2), nitrogen deposition (NDEP), nitrogen management (NMAN).

	Factors				
	Climate	***CO_2***	***Land-use***	***NDEP***	***NMAN***
Simulation 1	1900-2015	1900-2015	1900-2015	1900-2015	1900-2015
Simulation 2	1900-2015	1900-2015	1900-2015	1900-2015	1900
Simulation 3	1900-2015	1900-2015	1900-2015	1900	1900-2015
Simulation 4	1900-2015	1900-2015	1900	1900-2015	1900-2015
Simulation 5	1900-2015	1900	1900-2015	1900-2015	1900-2015
Simulation 6	1900	1900-2015	1900-2015	1900-2015	1900-2015

4.3.2. Input data

In this study, a 4-km resolution model input has been developing to drive DLEM to include climate driving force, historical land-use cohort, nitrogen inputs, and atmospheric CO_2 concentration.

To reconstruct historical land-use/land-cover data for the study area, we combined data from multiple sources (Figure 4-11), including the National Land Cover Database (NLCD) (Homer et

al., 2015b) , North American Land Cover (http://landcover.usgs.gov/nalcms.php), Global C4 vegetation map (Still et al., 2003), county-level land use inventories (Waisanen and Bliss, 2002), and the Global Lakes and Wetlands Database (http://www.worldwildlife.org/pages/global-lakes-and-wetlands-database). Due to the massive urbanization trend during the last century, the cropland area decreased by 53%, while the urban area increased by 497%, respectively. Constrained by the cropland conversion and urban expansion, the forest coverage, which is the dominant natural vegetation in the study area, increased by 10% from1900 to 2015 (Figures 4-3, a, c, d) followed by grassland increased by 21%.

The daily climate dataset was obtained from PRISM (Daly et al., 2008) climate dataset. (available at: http://www.prism.oregonstate.edu/). This dataset provides the gridded estimates of four essential climate variables, including daily minimum, mean and maximum temperature, and precipitation. Over the study area, precipitation and temperature demonstrated significant spatial and temporal variability during 1895 – 2015 (Figure 4-3, b, e, f). The average annual precipitation was 1080.0 ± 131.7 mm yr^{-1} with the maximum and minimum precipitation that occurred in 2003 (1506 mm) and 1930 (658mm), respectively. Temperature demonstrated significant inter-annual variability. The annual mean temperature in this area was 11.6 ± 0.2°C during 1895-2015. The annual mean temperature showed a considerable fluctuation, with a significant increasing trend from 1960 to 2014.

The scale adaptive water transport module requires several hydrograph data as model inputs. Here the flow direction, bank-full width, and bank-full depth are obtained from the HYDRO1K database (Earth Resources Observation And Science Center, 2017), which was derived from hydrological corrected topographic data (Tarboton, 1997). The channel density was used to quantify the length of hillslope flow and subnetwork flow, derived from National Hydrography

Dataset plus v2 data (available at: http://www.horizon-systems.com/NHDPlus/index.php). The manning's roughness of each grid cell was calculated from land cover and water depth. More detail about how to calculate bank-full depth, band-full width, and manning roughness can be found in Getirana et al. (2012). The major dam information of this study region was derived from Global Reservoir and Dam (GRanD) database (Lehner et al., 2011b), and it was nested into the 4-km grid level and used to quantify the damming effect on POC deposition (Vörösmarty et al., 2003).

4.3.3. Model validation

To assess the performance of carbon exports predicted by DLEM, we compared the carbon fluxes of the major rivers in the study region predict by DLEM during 1979-2015 against the statistical estimations by Load Estimator (LOADEST) (Runkel et al., 2004b) derived from USGS water quality observations (Figure 4-4). For each river, the USGS sites were select based on the data availability and the location, which is closest to each river outlet among all the sites. The detailed information about the USGS sites for validation can be found in Table 4-2. Most of the riverine carbon export predicted by DLEM agreed well with the LOADEST estimations (The R^2 values are higher than 0.7 and NSE values are higher than 0.5 in most of the sites).

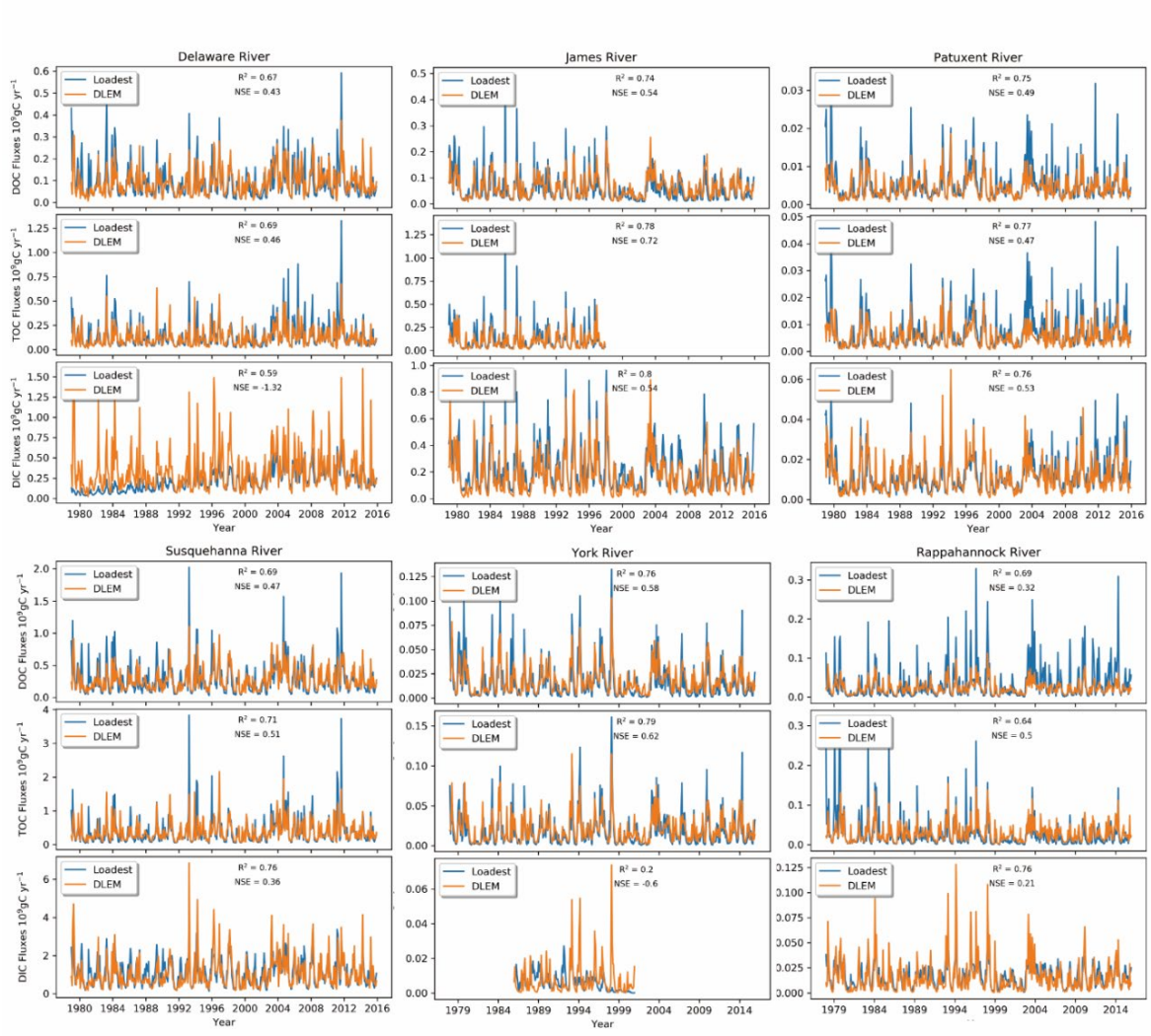

Figure 4-4. Comparing DLEM simulated carbon fluxes with LOADEST estimations derived from USGS observations

4.4. Results

4.4.1. Temporal patterns of riverine carbon exports across CBW and DBW

Simulated results show consistent temporal patterns of riverine C fluxes in the two river basins. In CBW, land carbon loading decreased by 27% from 1943.5 ± 353.3 Gg C yr^{-1} in the 1900s to 1424.3 ± 256.3 Gg C yr^{-1} in the 1960s. Riverine carbon exports, CO_2 degassing, carbon burial, and carbon pool decreased substantially by 25%, 30%, 6%, 13%, respectively. After the 1960s,

riverine carbon exports, CO_2 degassing, carbon burial, and carbon pool increased substantially by 56%, 36%, 3%, and 33%, respectively, associated with a 42% increase in total land carbon loading (Figure 4-5. a). In the DBW region, land carbon loading decreased by 29% from 479.3 ± 100.6 Gg C yr-1 in the 1900s to 338.7 ± 85.9 Gg C yr-1 in the 1960s. The associate riverine CO_2 degassing, carbon burial and carbon pool decreased substantially by 28%, 29%, 16%, 6%, respectively. After the 1960s, the total land carbon loading increased by 45%, leading to the riverine carbon exports, CO_2 degassing, carbon burial and carbon pool increased significantly by 60%, 32%, 26%, and 26% respectively (Figure 4-5. b)

In the CBW region, DOC and DIC and POC exports contributed to 24%, 67%, and 9% of the riverine carbon exports on average from 1900 to 2016, respectively. No significant decreasing trend was found for any riverine carbon species from 1900 to 1960. The simulated DOC and DIC export increased significantly ($p<0.05$) from 1960 to 2016, with the average increasing trend of 1.6 Gg C/yr and 4.8 Gg C/yr, respectively (Figure 4-6. a). In the DBW region, riverine carbon export explained 52% of the riverine carbon fluxes (1900 – 2016 average). The total carbon exports decreased from 282.8 ± 65.9 Gg C yr^{-1} in the 1900s to 204.2 ± 55.1 Gg C yr^{-1} in the 1960s and increased to 327.2 ± 94.9 Gg C yr^{-1} in the 2000s (Figure 4-5. b). The DOC, DIC, and POC exports explained 19%, 75%, and 6% of the riverine carbon exports respectively. The exports of all three carbon species showed a significant increased increasing trend (DOC: 0.4 Gg C/yr, DIC:1.3 Gg C/yr and POC: 0.1 Gg C/yr) (Figure 4-6. b).

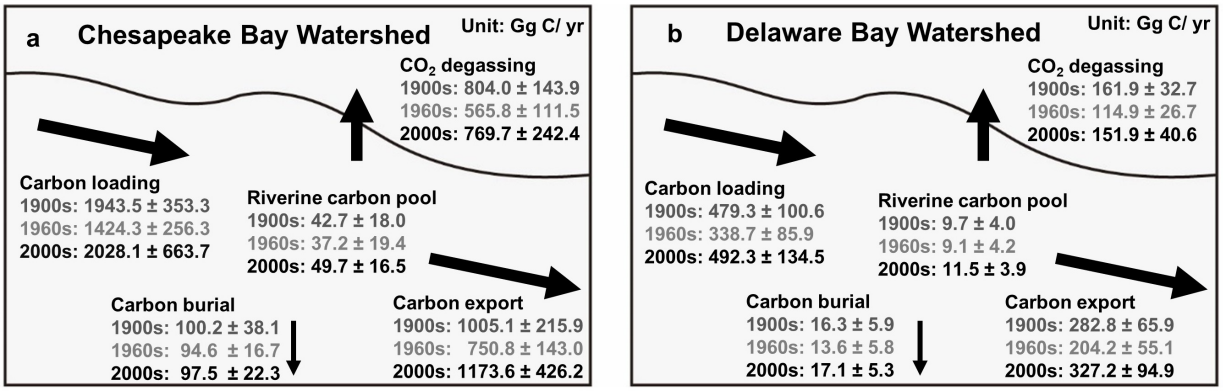

Figure 4-5. Carbon balance in CBW and DBW river networks simulated by DLEM. (a). Riverine carbon budget of CBW in the 1900s, 1960s, and 2000s. (b). Riverine carbon budget of DBW in the 1900s, 1960s, and 2000s.

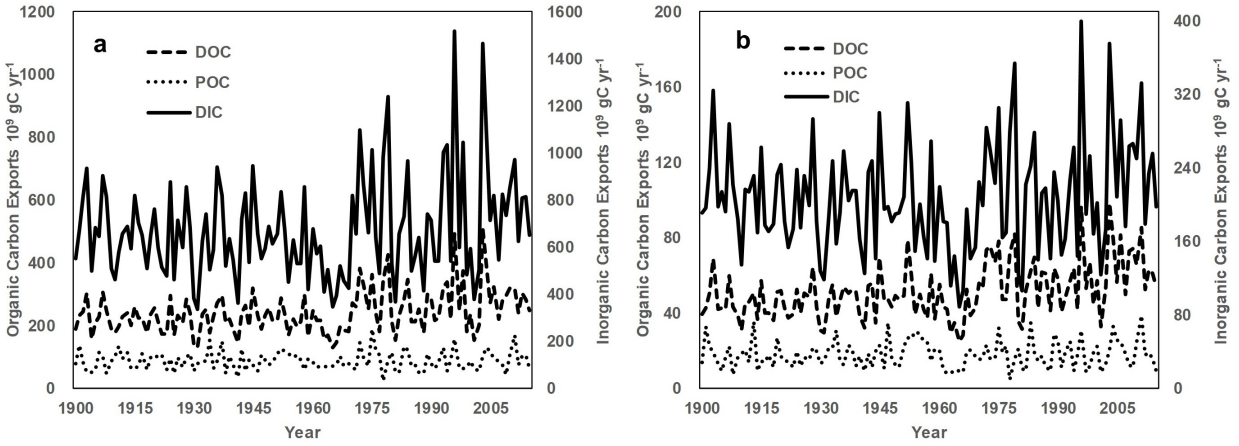

Figure 4-6. DLEM simulated riverine carbon fluxes from 1900 to 2016. (a). Temporal patterns of carbon exports from CBW from 1900 to 2016. (b). Temporal patterns of carbon exports from DBW from 1900 to 2016.

4.4.2. Spatial and temporal patterns of carbon loading from land

As shown in Figure 4-7 a, DOC loading increased significantly in most of the regions. In the eastern and northern parts of the CBW, DOC loading increased significantly (Figure 4-7 a), with an increasing rate of 0.002 – 0.004 gC m^2/yr^2. Across the southern part of the CBW and most of

the regions in DBW, the DOC loading rate increased significantly, with an average increasing rate of 0.004 – 0.008 gC m^2/yr^2. Land POC loading does not exhibit a significantly increasing or decreasing trend in the inland region of the study area. The changes of POC loading in coastal zones showed considerable inconsistency: decreased significantly with a rate of -0.003 gC m^2/yr^2 or increased significantly with a rate of 0.003 gC m^2/yr^2 (Figure 4-7. b).

The northern part of the DBW shows large increasing trend in DIC loading with an increasing rate of 0.02- 0.05 gC m^2/yr^2. The southern part of the study region represents a significant increasing trend of DIC loading with an increasing rate of 0.01 – 0.02 gC m^2/yr^2. Besides that, most of the regions do not have a significant increasing or decreasing trend or and show a decreasing trend of -0.05 gC m^2/yr^2 (Figure 4-7. c).

The CO_2 degassing directly correlates to the riverine DIC concentration and land DIC loading. The northern part of the DBW shows large increasing trend with an increasing rate of 0.1-0.2 10^6gC /yr^2 per 4-km grid cell. However, riverine CO_2 degassing in most of the regions show a significant decreasing trend with a rate of about -0.1 10^6gC /yr^2 of each grid cell.

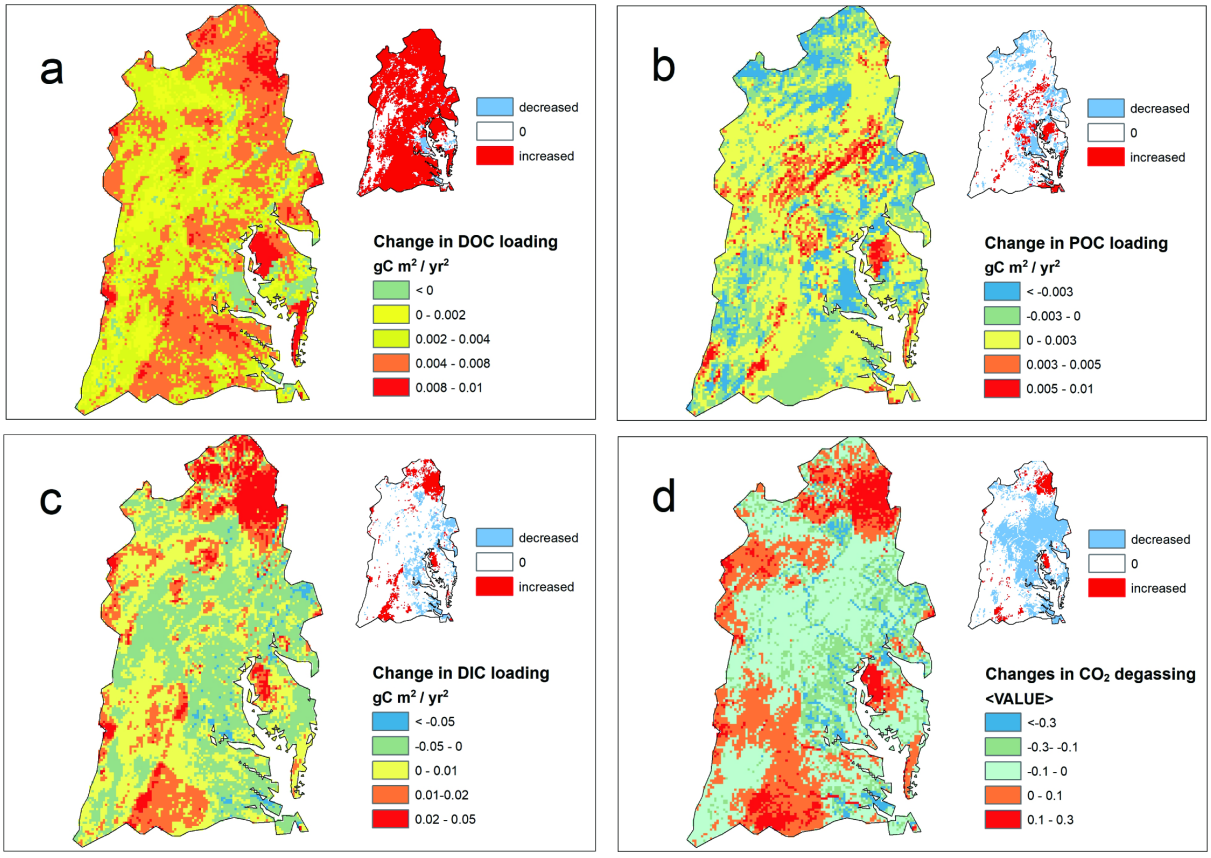

Figure 4-7. Spatiotemporal patterns of changes in terrestrial carbon loading and riverine CO_2 degassing from 1900 to 2015. (a). Changes in DOC loading, (b). Changes in POC loading. (c). Changes in DIC loading. (d). Changes in Riverine CO_2 degassing

4.4.3. Factorial contributions to the riverine carbon fluxes over CBW and DBW.

The factorial experiments revealed the contribution of each factor to riverine carbon exports in both CBW and DBW from the 1900s to 2006-2015 (Figure 4-8). For all the three riverine carbon species, climate plays the most important role in explaining the inter-annual variations of carbon exports. On the other hand, the contiguous long-term changes in carbon fluxes explained by elevated CO_2 concentration, long-term climate change (rising temperature and increasing

precipitation), increased nitrogen deposition and nitrogen applications, and land-use change (Figure 4-8).

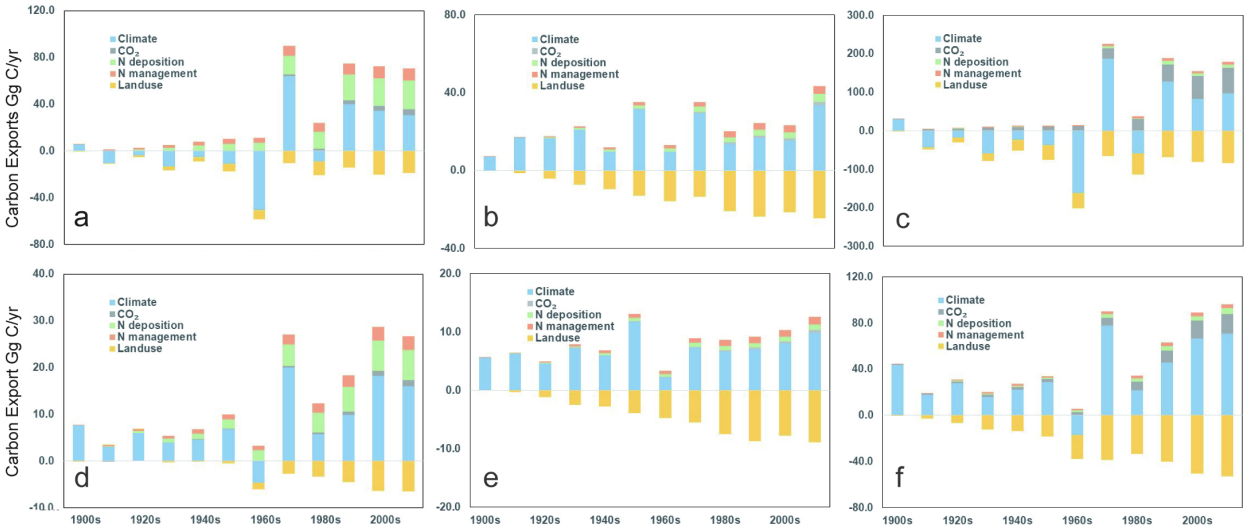

Figure 4- 8. Contribution of climate, CO_2, N deposition, N management (N fertilizer + N manure), and land-use change to riverine DOC exports in CBW (a) and DBW (d), POC exports in CBW (b), and DBW (e), DIC exports in CBW (c) and DBW (f).

Before the 1960s, climate change explains most of the changes in DOC for both CBW and DBW. After the 1960s, the impact of other factors on DOC fluxes increased substantially: In CBW, climate change increased DOC export by 30.6 Gg C/yr in the most recent 10-years, followed by N deposition 24.4 Gg C/yr), N management (10.4 Gg C/yr) and CO_2 (5.2 Gg C/yr) respectively, while land-use change plays a negative role which decreased DOC export by 19.2 Gg C/yr (Figure 4-8.a). Furthermore, in DBW, climate change increased DOC export by 9.9 Gg C/yr, followed by N deposition (6.6 Gg C/yr N management (2.9 Gg C/yr) and CO_2 (1.2 Gg C/yr), while land-use decreased DOC exports by 6.5 Gg C/yr (Figure 4-8. d).

Unlike the long-term changes in DOC exports, which was strongly regulated by multiple factors, the determinative factors of the changes in POC export are limited to climate change and land

conversion. Here, climate change explained most of the variations in POC export of both CBW and DBW from the 1900s to the 1920s (Figure 4-8. e). The contribution of land conversion increased to -9.0 Gg C/yr in DBW in the 2000s, the magnitude of land-conversion impact is comparable to that of the climate change (9.9 Gg C/yr) during the 2000s. Moreover, the impact of land conversion on POC exports reached -21.6 Gg C/yr, which substitutes climate change impact (15.2 Gg C/yr) to explain most of the changes in POC exports during the 2000s in CBW (Figure 4-8. b).

DIC exports were strongly affected by climate change as well; however, the impact of land-use change and atmospheric CO_2 concentration increased significantly since the 1920s. Climate change increased DIC exports by 97.4 Gg C/yr (Figure 4-8. c) in CBW followed by CO_2 effect (66.4 Gg C/yr), and land-use change decreased DIC exports by -83.6 Gg C/yr. Similar findings have been suggested for DBW, climate change increased DIC exports by 70.8 Gg C/yr, followed by CO_2 effect (17.1), and land-use change decreased DIC exports by -52.7 Gg C/yr. Nitrogen inputs have a slight impact on DIC exports in both regions (Figure 4-8. f).

4.5. Discussion

4.5.1. Riverine CO_2 degassing of CBW and DBW

One of the major contributions of this study is that we improved the model representation of the riverine CO_2 degassing. Specifically, we utilized a new statistical-based method (Allen et al., 2018) to estimate the surface area of the headwater streams within the sub-grid river routing scheme (Li et al., 2013). The DLEM model, therefore, can well capture the magnitude and spatial pattern of CO_2 degassing from small streams, which has been ignored in the previous modeling studies (Tian et al., 2015a, 2015c). The physical and biogeochemical module of the headwater streams and high-order streams in DLEM are fully process-based. Although the model

parameters associated with CO_2 degassing are consistent for both headwater streams and high-order streams, our model can well represent the relatively high gas emission rate in low order streams (Raymond et al., 2013).

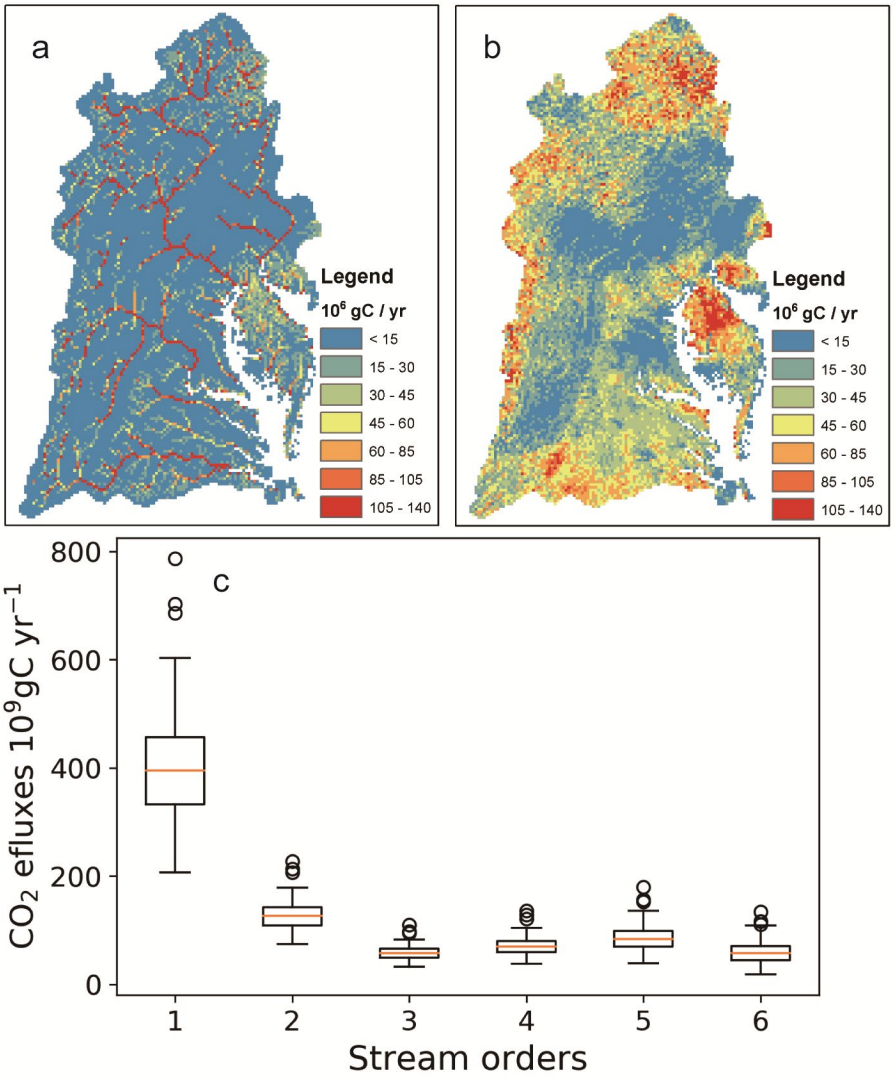

Figure 4-9. The CO_2 emissions from high-order streams (a) and headwater streams (c) of the year 2015. Simulated CO_2 emission along with stream orders (c) across the Chesapeake Bay Watershed and Delaware Bay Watershed.

The riverine CO_2 outgassing of CBW and DBW predicted by DLEM is about 886.25 ± 207.49 Gg C/yr, which accounts for 39% of the riverine fluxes in the 2000s. Although small

streams (1st order – the subnetworks of each 4-km grid cell in this study) only covers a small fraction of the water surface area in the study region (Allen and Pavelsky, 2018), they account for a large fraction of (50% in this study) of the total riverine CO_2 effluxes. The statistics of total CO_2 degassing along with stream orders (1st order to the 6th order) (Figure 4-9. c) predicted by DLEM follows a similar pattern of the inventory based data analysis across the conterminous U.S. (Butman and Raymond, 2011). Besides, the 1st-3rd order streams, which are characterized as the headwater streams, account for 73% of the total riverine CO_2 outgassing. This finding is supported by the previous experimental analysis (Argerich et al., 2016) and global inventory-based analysis (Raymond et al., 2013), suggesting that the headwater streams account for 70% CO_2 outgassing.

It has been noted that large area of urban and cropland is distributed in the central regions of the study area (Figure 4-2), the release of urban sewage wastewater and extensive liming of cropland increased water pH substantially (Asabere et al., 2018; Naylor and Schmidt, 1986). The low emission rates mainly due to their relative high-water pH value obtained from USGS observation, which has been utilized as the model input of DLEM (Figure 4-12). Water pH value plays an essential role in regulating the fraction of dissolved CO_2 concentration among the three DIC species (H_2CO_3, HCO_3^-, CO_3^{2-}), as described in the Bjerrum plot (Andersen, 2002). Additionally, the forest coverage is relatively low in the central region. Forest land is the largest reservoir of vegetation carbon, and soil litter carbon (Dixon et al., 1994), the high soil respiration rate of soil litters result in a high DIC concentration in the adjacent headwater stream (Corson & Rikert et al., 2016; Rasilo et al., 2017; Schindler & Krabbenhoft, 1998; Triska et al., 1993) and hence high CO_2 degassing rate.

The importance of small rivers on regional biogeochemical cycles and greenhouse gas emission has been well documented in previous studies ((Beckman and Wohl, 2014). The high rate of CO_2 effluxes are mainly due to high DIC or DOC concentrations: Although the magnitude of DOC decomposition in headwater zone is much lower than that of the large river channels (Varol and Li, 2017), the source of CO_2 outgassing are mainly from terrestrial/groundwater inputs (Argerich et al., 2016). Moreover, the gas exchange rate between the air-water interface of headwater streams is higher than that in large river channels due to the higher channel slope of the headwater streams.

Our simulation results suggested that land carbon loading decreased by about 26% from the 1900s to 1960s in both CBW and DBW, riverine CO_2 degassing, and total carbon export decreased by 30% and 25%, respectively. However, when the land carbon loading increased by 42% in the 2000s, the magnitude of increase in riverine CO_2 (35%) is much lower than that of riverine carbon exports (57%). The atmospheric CO_2 concentration increased significantly since the 1960s (Manabe and Wetherald, 1975), resulting in a higher equilibrium CO_2 concentration (Sander, 2015) in the air-water interface. Thus, the elevated atmospheric CO_2 concentration dampens the difference between equilibrium CO_2 concentration and dissolved CO_2 concentration in river waters, which in turn decreased riverine CO_2 emission. This phenomenon has important implication for the coupled land-aquatic ecosystems: since riverine carbon fluxes explain most of carbon variation in ecosystems (Hastie et al., 2019), the relative role of riverine CO_2 degassing and carbon exports to carbon fluxes at the land-aquatic interface shifts due to the climate change and human activities (Regnier et al., 2013).

4.5.2. Underlying controls on the riverine carbon exports

It has been noted that anthropogenic effects substantially changes the magnitude and spatial pattern of carbon fluxes at the global level (Regnier et al., 2013). In this study, the long-term changes in climate explain most of the inter-annual variability in riverine carbon fluxes (Figure 4-6 and 4-8). Changes in net primary productivity of plants in response to the elevated air temperature and precipitation, in turn, affect the plant carbon pools and soil carbon pools (Pan et al., 2015, 2014; Tian et al., 2012, 2011). The variations of organic carbon pool in the soil directly affect the terrestrial carbon loading rate (Figure 4-7), and associated doc fluxes as well. Similar to the climate impact, the increased N inputs, including deposition, N fertilizer, and Manure N, which alleviate the vegetation N limitation (Vitousek and Howarth, 1991), all contribute to the increased primary production and soil carbon pools (Figure 4-5). However, the land conversion from forest to cropland significantly decreased the soil carbon pool and the associated carbon fluxes of all species (Figure 4-5).

The trend of DIC fluxes predicted by DLEM decreased from the 1900s to the 1960s, but the DIC exports of the 2000s return to the level of 1900, which is supported by a recent review suggesting the DIC fluxes returned to the pre-industry level (Raymond and Hamilton, 2018). However, this review could not attribute the contribution of the environmental factors to the variability of DIC fluxes. Changes in organic matter or litter carbon pool induced the variations of respiration rate, which directly affect the DIC concentration in the soil water. The soil DIC concentration functions as the boundary condition of the riverine biogeochemical module, which is used to constrain mass balance in solving the riverine DIC concentration of each cell with time variables.

The lateral POC fluxes did not increase significantly in this study under the context of substantial changes in climate and land-use. The POC erosion from land strongly correlated to

soil erosion, which was calculated by the Modified Universal Soil Loss Equation (MUSLE) model (Williams and Berndt, 1977). In theory, the increased precipitation would result in a significant increase in POC erosion. However, several factors offset the precipitation effect. One is the large area of land conversion from cropland to forests. Cropland is recognized as the hotspot of soil erosion, while the soil erosion of natural forest is much lower than that in cropland. Additionally, the increase in organic matter content only slightly increased the POC loading rate. Although the percentage of organic matter per eroded soil increased, the high organic matter content inhibits the erodibility of soils by decreasing the K value in the MUSLE model (Williams and Berndt, 1977).

4.5.3. Uncertainty and future research

The substantial uncertainties in previous processed-based modeling studies suggested several improvements are needed for accurately quantifying lateral carbon exports and greenhouse gas emissions from the headwater zones (Aufdenkampe et al., 2011). First, the ability of the current model in simulating water pH dynamically is limited due to the lack of observational data, especially in the headwater streams. It is also unclear that the boundary conditions of river water pH (pH of Groundwater or surface runoff) and the mechanisms controlling water pH. Second, the traditional way to calculate pCO_2 largely overestimate CO_2 degassing in organic-rich freshwaters (Abril et al., 2015). More systematic observations and experimental analysis about the gas exchange rate and the processes within hyporheic zones need to be conducted in the future (Corson & Rikert et al., 2016; Findlay et al., 1993; Schindler & Krabbenhoft, 1998; Triska et al., 1993). Third, we do not consider river CO_2 uptake by algae, the food chain in the riverine system, POC consumption by aquatic species, and organic matter resuspension from bottom sediment. Although these processes are specifically important in the lentic aquatic system

(Maavara et al., 2017), it still would bring in large uncertainties in the estimation of carbon fluxes. Finally, this modeling study simplifies the river routing algorithm without considering the processes within small lakes or reservoirs. Small lakes or ponds do not clearly show the obvious linkage to the river networks, and the residence time of the small pond is hard to obtain on a large scale. Constraining the fate of lateral carbon exports and GHG emissions at the headwater streams has been challenging and is so far incomplete. It is critical to develop parameterizations to scale up small rivers into regional and global levels. Carbon dynamics at the riparian and hyporheic zone are determined by complex biophysical and biogeochemical processes with substantial spatial and temporal variations, such as physical erosion, river stage and flow velocity, water temperature, oxygen concentration, and microbial types (Battin et al., 2007; Butman et al., 2016). Improved understanding and quantification of the progression from subsurface carbon stores into lateral carbon transport and the biogeochemical processes by coupling land ecosystem model and hydrodynamic models are essential to improve the model performance. Lastly, our future research may consider how to couple lake or reservoir routing into the water transport model with improved lake/reservoir input dataset.

4.6. Conclusion

In this study, we coupled a scale adaptive water transport module with DLEM to address the biogeochemical processes within small streams. We investigated the lateral DOC, POC, and DIC fluxes of the river outlets and the CO_2 degassing from both small rivers and large rivers. The results of this study indicated that DOC exports of both CBW and DBW showed a large increasing trend after the 1960s due to climate change and increased nitrogen inputs, whereas the land-use conversion from cropland to natural vegetation dampen the increasing trend. The export of DIC showed a similar temporal pattern, mainly due to climate change and CO_2 concentration

increase. The export of POC does not show a significant increasing trend and is largely influenced by land conversion. The riverine CO_2 degassing account for 40% of the riverine carbon fluxes and did not show a significant increasing trend from 1900 - 2016. Although enhanced plant productivity increased the soil organic carbon content and the associated DIC fluxes in rivers, the elevated atmospheric CO_2 concentration dampens the variability of CO_2 effluxes in rivers. It should be noted that, although our model provides well-validated results to estimate riverine carbon budget, the magnitude, human footprint, spatial and temporal patterns of vertical carbon fluxes and lateral carbon exports remain highly uncertain due to uncertainties in model structure and parametrization. More advanced tools and well data-model integrations would be our future research goal to help people understanding and predicting the global/regional carbon cycle and its feedback to climate change (Ciais et al., 2008).

Table 4-2. USGS sites for the model selected for model validation

Rivers	*USGS Gauge Stations*
Delaware River	01463500
Susquehanna River	01578310
Potomac River	01646580
Patuxent River	01594440
York River	01673000
Rappahannock River	01668000
James River	02035000

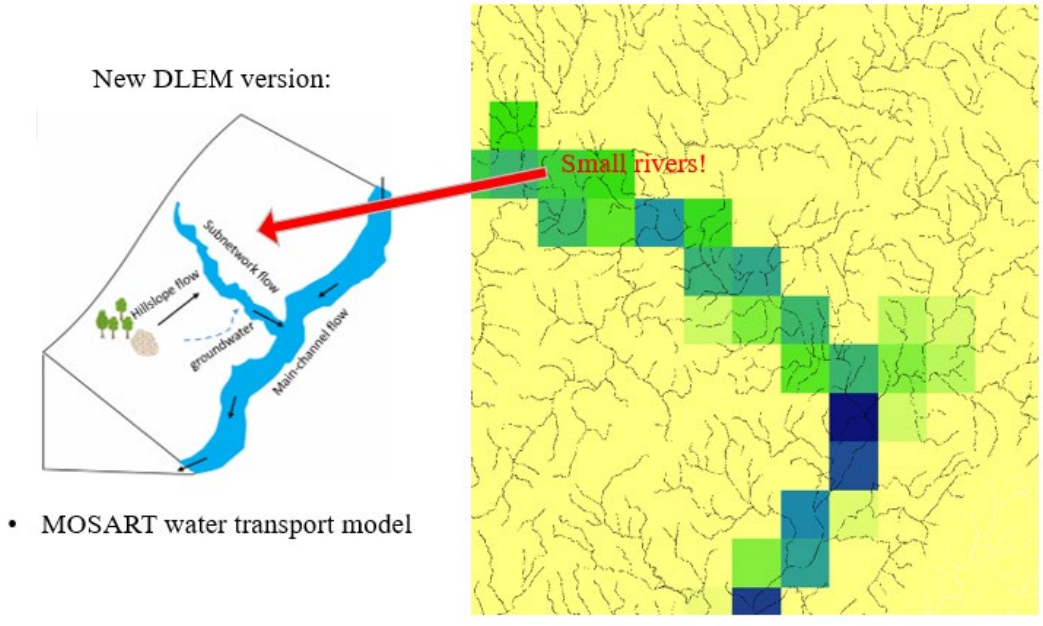

Figure 4-10. The concept model of the scale adaptive water transport model and the representation of small rivers in within water transport framework

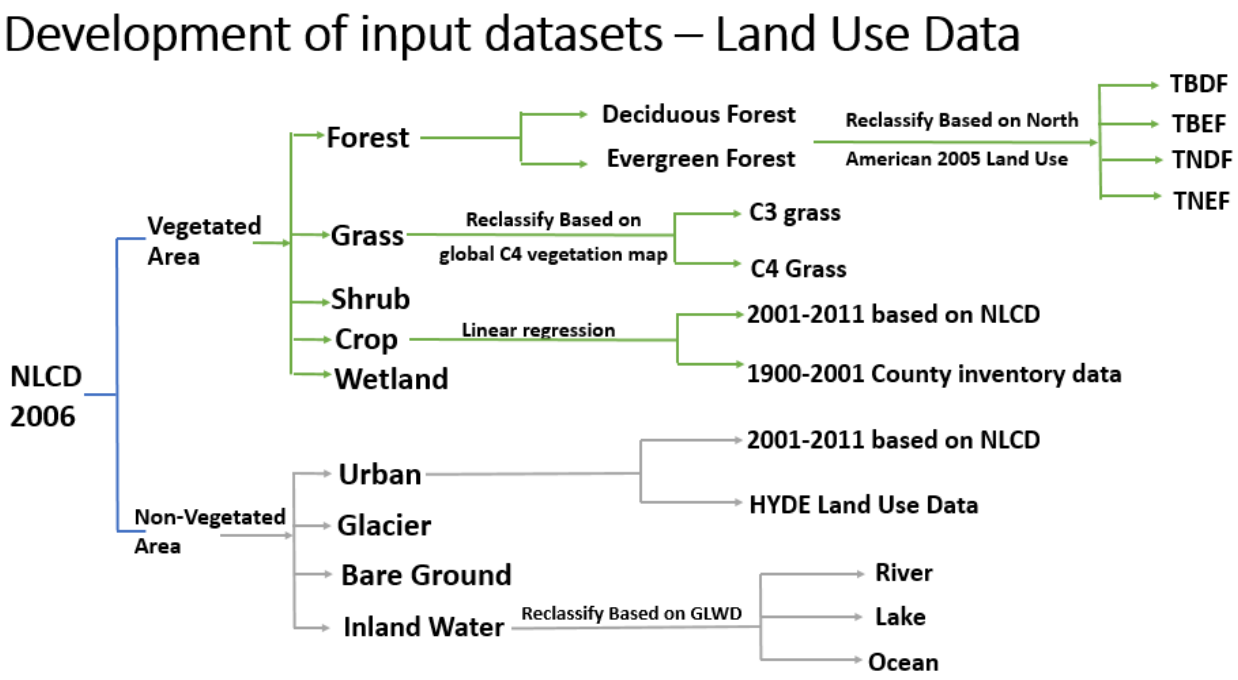

Figure 4-11. The flowchart to describe the development of historical land-use cohort

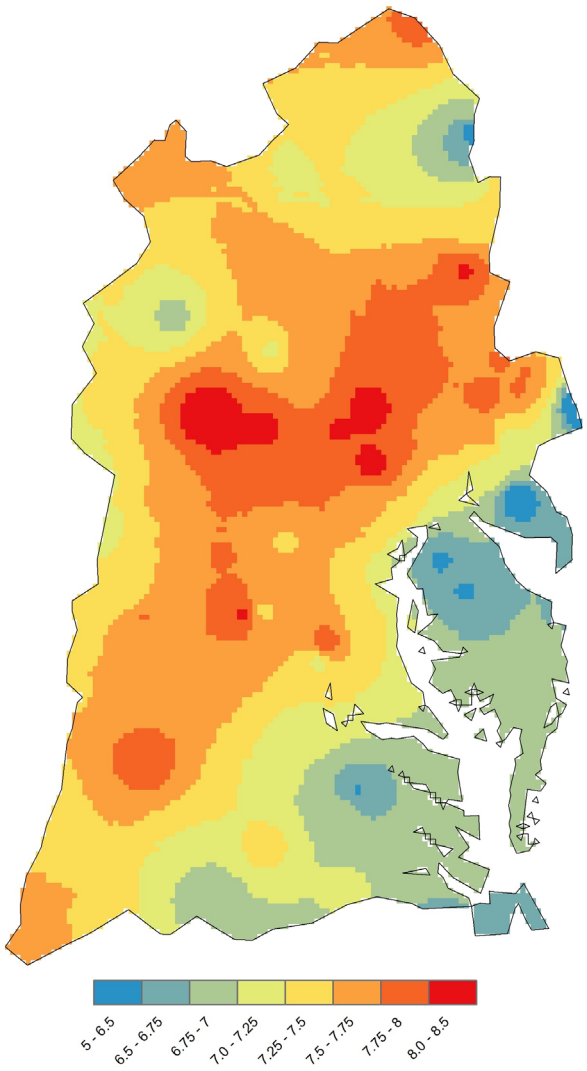

Figure 4-12. The spatial map of water pH interpolated based on long-term observations obtained from USGS.

Chapter 5. Assessing the spatial and temporal variations in CO_2 and CH_4 emissions from inland waters over the Conterminous U.S.

Abstract: Emissions of CO_2 and CH_4 from inland waters have been increasingly recognized as an essential portion to close the global or regional Greenhouse Gas (GHG) budget. However, accurate estimation of the riverine CH_4 emissions at a large spatial scale remains uncertain due to the lack of direct measurements and modeling tools. Here we developed a riverine CH_4 model based on the Dynamic Land Ecosystem Model and coupled it with a scale-adaptive hydrological model to simulate carbon exports and riverine CH_4 emissions. This model is the first process-based coupled biogeochemistry-biophysics-hydrology model, which can simultaneously estimate the source, production, and removal of dissolved CH_4 in the riverine ecosystems. This model can well address emissions from the small headwater streams through the incorporation of sub-grid routing, which is essential for a comprehensive evaluation of emissions from inland waters. Moreover, DLEM- CH_4 can quantify the impacts of climate change and anthropogenic activities on terrestrial ecosystems and consequently on CH_4 emissions of riverine ecosystems. Taking advantage of the new model, we investigated CH_4 emissions from the inland waters of the Conterminous United Stated during the period from 1900 to 2016. The model simulation was conducted at a spatial resolution of 5 arc-min and was calibrated and validated against observations from the United States Geological Survey (USGS). Our results suggested that the modeled CO_2 emission from streams is 113.6 Tg C/yr from 2009 – 2018. The headwater stream released 88% of the riverine CO_2 emissions. During the period from 1900 to 2018, the diffusive CH_4 emissions from rivers and lakes increased by 24.5% and 30.8%, respectively. The ebullitive CH_4 emissions from rivers and lakes increased by 35.8% and 37.9%, respectively. Small streams

(1^{st} –3^{rd} order streams within the 5 arc-min resolution grid cell) explain 48.0% of the diffusive CH_4 emissions, while large lakes account for 32.3% of the diffusive CH_4 emissions. Large lakes account for 82.7% of ebullitive CH_4 emissions, followed by small streams (11.6%). The estimation of ebullitive emissions has significant uncertainties due to the lack of observations and data model integrations. Therefore, more accurate observation is needed to improve the model performance in the future.

5.1. Introduction

Growing awareness of the aggravated environmental condition aligns with elevated temperature since the industrial era promoted new research directions, which aim to understand the responses and feedbacks of the terrestrial and aquatic ecosystems to climate change (Montzka et al., 2011). The major drivers of the greenhouse effect and the associated climate change are Greenhous Gases (GHGs). Carbon dioxide, as the most important GHG, has been received much attention. The CO_2 emission from inland waters was considered as a neglectable source (Cole et al., 2007). However, a large number of recent field studies observed significant CO_2 emissions from rivers and ponds (Butman et al., 2016; Holgerson and Raymond, 2016). Butman et al. (2016) analyzed the inland water carbon fluxes over the Conterminous United States and suggested that 70% of the carbon loading from land to river released to the atmosphere as CO_2 gas. While comparing the magnitude of the aquatic carbon fluxes with the terrestrial Net Primary Production (NPP), Butman et al. (2016) suggested that the introduction of carbon loading to the rivers could substantially revise the regional carbon budget. Thus, accurately simulating the aquatic CO_2 releasing is of great importance to close the continental carbon budget.

Methane gas(CH_4), the second important greenhouse gas whose Global Warming Potential (GWP) is 28–36 times larger than that of CO_2 for a 100-yr time horizon, increased by 150% during the last century (Ciais et al., 2014). With much of the attention being paid to the terrestrial CH_4 emissions (Xu et al., 2010), the contribution from inland waters was highlighted to the scientific community in the recent decade (Ciais et al., 2014). The estimated magnitude of CH_4 emissions from rivers, lakes, and reservoirs reached 1.1 - 20.1 Tg CH_4-C/year, 53.7 Tg CH_4-C/year, and 13.3 Tg CH_4-C/year, respectively (Deemer et al., 2016). However, those estimates are poorly constrained due to the lack of observations and reliable modeling approaches (Trimmer et al., 2012).

Riverine CO_2 and CH_4 emissions are strictly relevant to the riverine carbon export (Battin et al., 2008). There is a growing understanding of the sensitivity of riverine carbon fluxes to climate change (Regnier et al., 2014). Inland water CO_2 and CH_4 emissions, which are the primary feedback of the aquatic system to the climate system, are sensitive to the climate change and human disturbances under the context of changing carbon fluxes during the Anthropocene (Battin et al., 2009; Bauer et al., 2013; Maavara et al., 2017; Regnier et al., 2013). The dissolved CO_2 is one of the three dissolved inorganic carbon (DIC) species in waters. Thus the hydraulic loading and the pH of water could significantly regulate the magnitude of CO_2 emissions (Liu and Raymond, 2018). The production of dissolved and bubble CH_4 is primarily from organic matter. Recent studies suggested a positive relationship between Dissolved Organic Carbon (DOC) and CH_4 production in bottom sediment and water bodies (Wu et al., 2007; Baulch et al., 2011). Since most of the DOC comes from land carbon loading, understanding the controlling factors of land carbon loading is critical to estimating the CH_4 production and emissions in the aquatic system.

Empirical approaches and data-based analyses are the most popular methods to estimate CO_2 and CH_4 emissions. Water quality variables including river water temperature, alkalinity, as well as the concentration of inorganic carbon, have been used to quantify the pCO_2 of rivers and lakes (Butman and Raymond, 2011). The estimated CO_2 flux rate was quantified from pCO_2, equilibrium CO_2 concentration and piston velocity (Raymond et al., 2012). The total fluxes were estimated directly by multiplying with water surface areas (Raymond et al., 2012), which ignores the temporal variations of the gas exchange rate, concentrations of carbon substance, and water temperature. The water quality data-based study is considered as the reference to the modeling studies mainly due to a large number of variables listed for predicting CO_2 emission. However, water quality variables could not be directly used as indicators to quantify dissolved CH_4 concentrations. A most recent meta-data based analysis quantified the diffusive and ebullitive CH_4 fluxes by synthesizing data collected from a literature survey (Stanley et al., 2016). Due to the sparse data availability, this approach could not well represent the spatial heterogeneity of CH_4 emissions along with river orders, which has been observed and suggested in the counterpart CO_2 and N_2O studies (Butman and Raymond, 2011; Garnier et al., 2009; Turner et al., 2015). The seasonal or diurnal variations of riverine CH_4 fluxes may also raise large uncertainties. Thus, a more reliable tool is required to capture the spatial and temporal variations of riverine CH_4 fluxes.

Based on the understanding of the mechanism of CH_4 production and consumption in waters, several process-based models have been developed to simulate the CH_4 dynamics in the lake water body and bottom sediments (Fung et al., 1991; Van Huissteden et al., 2011). However, those site-level lake models or wetland models require flow-in discharge as model input (Fang and Stefan, 1998, 1995; Sharifi et al., 2016), that means it needs to be coupled with a

hydrological modeling framework, such as SWAT model or VIC model (Arnold et al., 2012; Guo et al., 2009). Rivers are recognized as the aquatic-ocean continuum linking land, lakes, reservoirs, and ocean, as a whole system. River water mixing in lakes and lateral carbon transport affects the carbon concentration in lakes. Thus more and more biogeochemical modeling research consider to couple with the river routing model (Lu et al., 2016). The process-based model was conducted to quantify the CO_2 emissions at the global or site level (Laruelle et al., 2015). However, none of the studies tried to couple the riverine carbon dynamics with the land ecosystem models. Since most of the carbon is originated from land carbon loading, a reliable tool is needed to give a comprehensive understanding of the nexus between the land and aquatic process.

Inspired by the knowledge gaps that existed in the previous studies, we developed a riverine CH_4 module under the framework of DLEM-TAIM to quantify the inland water carbon dynamics, and the resulting CO_2 and CH_4 emissions. We conducted the attribution experiments to quantify the contribution of each environmental factor to the changes in inland water CO_2 and CH_4 emissions.

5.2. Methods and model inputs

5.2.1 Study region

The Contiguous United States (CONUS) (Figure 5-1) refers to the region expanding southward from the north latitude (48º) to the Mexico boundary(32º). As the major land of the United States, the area of CONUS is 8,080,464 km^2 and supports 306 million people based on population census 2010. Topography helps to shape the climate condition and the vegetation distribution across the CONUS. The dominant plant function type is temperate evergreen needle-leaf forest in the southward of the Appalachian mountain, while the temperate deciduous

broadleaf forest is the dominant natural vegetation of the north of the Appalachian Mountains. Between the Appalachian Mountains and Rocky Mountains of CONUS, the dominant plant types are evergreen shrubland and C3 grassland. In regions west of the Rocky mountain, the climate is dry, thus temperate needle-leaf forest and deciduous shrubland are distributed across the whole region (Figure 5-1).

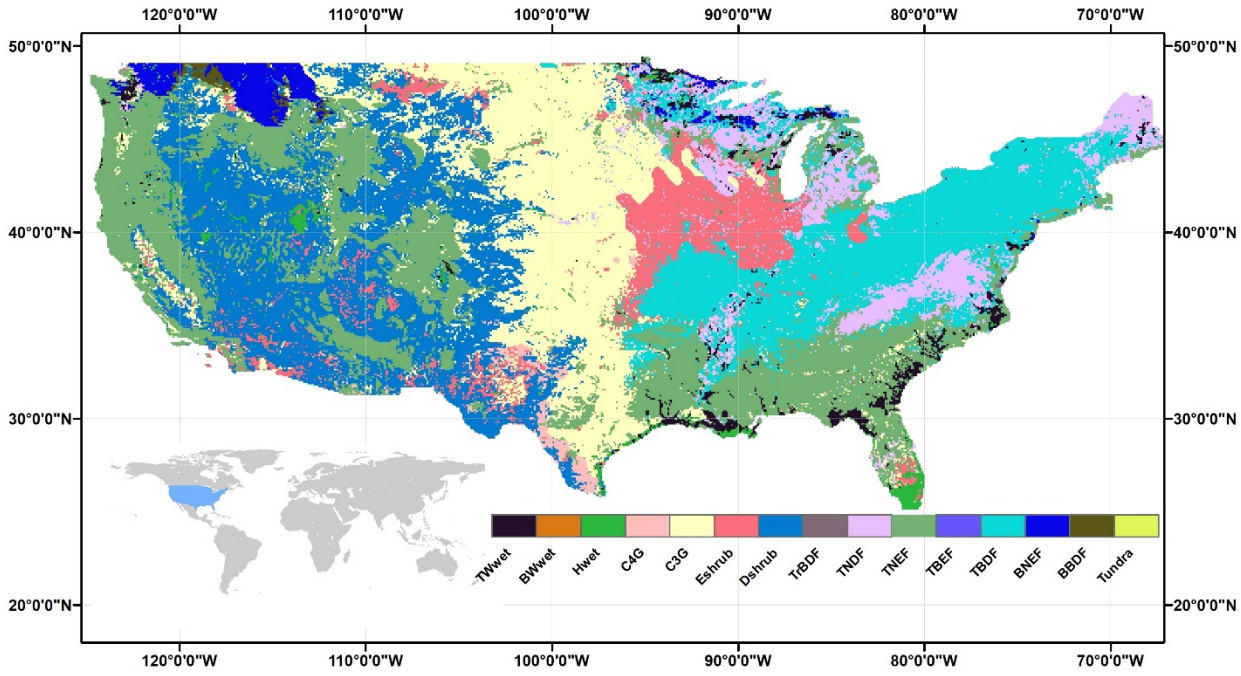

Figure 5-1. Major plant function types across the Contiguous United States (CONUS).

5.2.2 Dynamic land Ecosystem Model (DLEM)

In this study, we used a coupled modeling framework that combines the terrestrial ecosystem model with riverine transport to simulate the carbon and nitrogen fluxes. The Dynamic Land Ecosystem Model (Tian et al., 2015b, 2016, 2018a) is a process-based terrestrial ecosystem model (Figure 5-2.a) that explicitly predicts the land carbon, nitrogen, and water cycles. DLEM simulates the plant physiology, soil biogeochemistry and the associated terrestrial hydrological

processes, and riverine routing processes driven by climate forcing, land-use change, nitrogen deposition, fertilizer applications, and other environmental variables. The plant physiology component in DLEM modeled photosynthesis, respiration, and carbon, nitrogen allocations among root, stem, and leaf. Seven litter carbon pools are defined in DLEM to represent carbon dynamics within soil layers. The carbon and nutrients fluxes among soil pools are controlled by soil moisture and temperature with well-calibrated parameters. The land component of DLEM quantifies carbon loading from soil carbon pools including dissolved inorganic carbon (DIC), dissolved organic nitrogen (DOC) and particulate organic nitrogen (POC). These carbon loading functions as the major source of riverine carbon to drive the aquatic model.

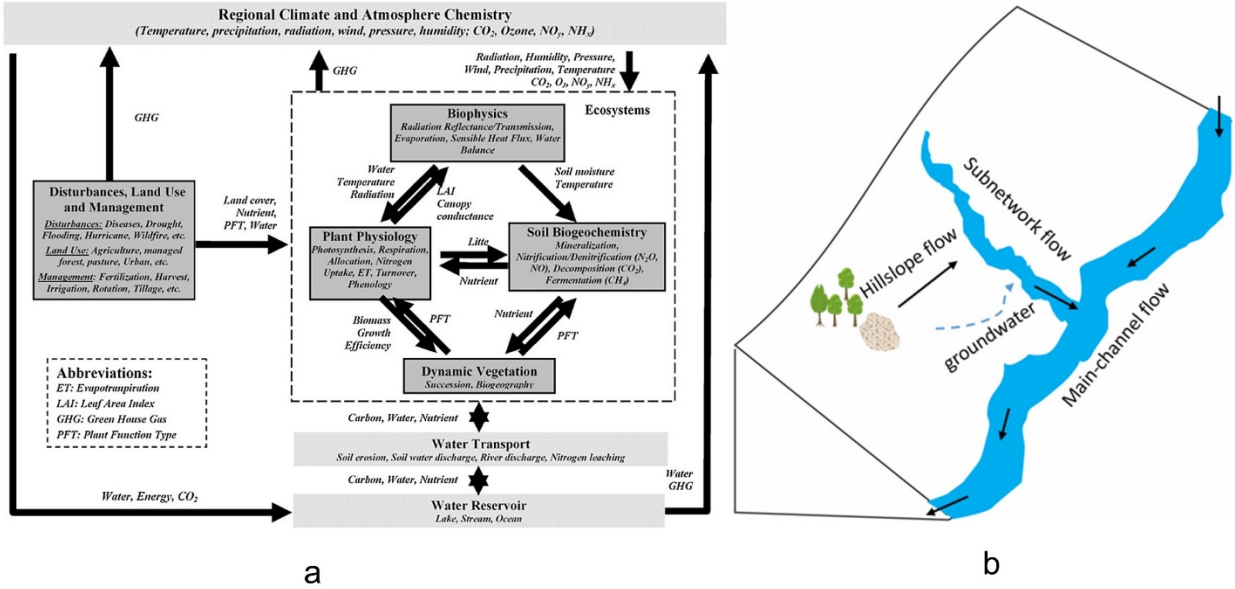

Figure 5-2. The general framework of the DLEM land-ocean interface. (a). The concept model of DLEM. (b). The concept model of Model for Scale Adaptive River Transport (MOSART)

5.2.3 Scale adaptive channel routing scheme.

In this study, a new water transport scheme named Model of Scale Adaptive (MOSART) (Figure 5-2.b) was coupled with DLEM. Aiming to reduce the scale effect, MOSART introduces two

local sub-grid processes, including hillslope flow and subnetwork flow, before the cell-to-cell channel routing. Here, hillslope flow begins with water merging from surface runoff and ends in the subnetworks. The subsurface flow from the root zone to the headwater stream was lump as a groundwater pool, with the outflow rate derived from a calibrated residence time. The subnetworks receive water from hillslope flow and lumped groundwater seepage. The main channel flow receives water from local subnetworks and upstream grid units. The cell-to-cell channel routing follows the predefined flow direction obtained from the Dominant River Tracing (DRT) hydrograph database (Wu et al., 2012b).In MOSART, the subnetwork flow represents the routing process of small streams (1st – 3rd stream order) within the 5 arc-min spatial resolution grid unit. The routing processes within the MOSART model are hydraulics based, which solved the Saint-Venant equations by using the kinematic wave method (Chow, 1964b).

2.1 Riverine CH_4 sub-model

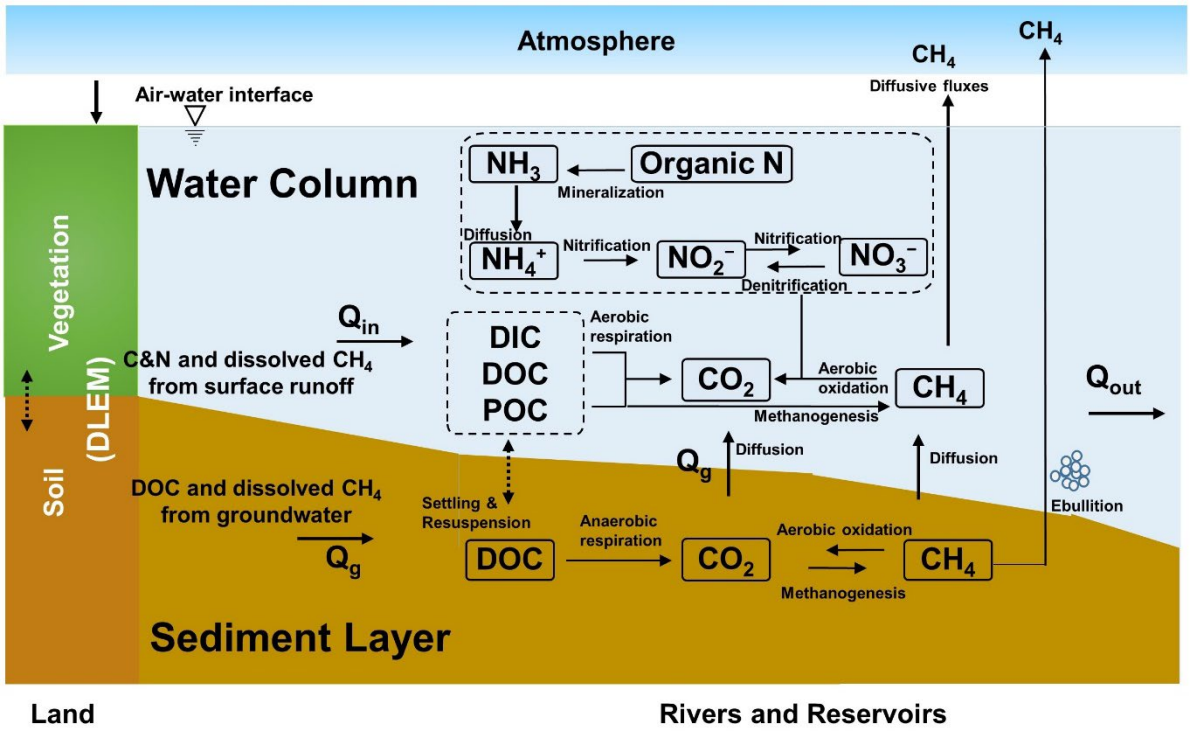

Figure 5-3. The general framework of the riverine CH_4 model.

A riverine CH_4 model (Figure 5-3) was developed following the advanced feature of the scale adaptive water transport scheme. Hillslope flow receives dissolved CH_4 from the land surface (with surface runoff) and contributes to subnetwork flow. Here, we assume CH_4 concentration in the surface runoff equals to the air equilibrium CH_4 concentration. We did not consider the biogeochemical processes in hillslope flow in this study, because we assume the hillslope flow belongs to the terrestrial process. The mass balance of CH_4 (include physical and biogeochemical processes) in the main channel and subnetwork are given by:

$$\frac{\Delta M_{diffusive-CH4}}{\Delta t} = F_a + Y_{water} + D - R - E \quad (1)$$

where M_{CH4} is the total mass of dissolved CH_4 is the main channel or subnetworks (g C), Δt is the time step (d), F_a is advective CH_4 fluxes ($gC \cdot d^{-1}$), Y_{water} is the CH_4 production within the water column ($gC \cdot d^{-1}$), D is the dissolved CH_4 from rainfall to rivers ($g\ C \cdot d^{-1}$), with an initial concentration equals to the air equilibrium concentration, R represents the CH_4 reduction ($gC \cdot d^{-1}$) to nitrogen gas, and E is riverine CH_4 effluxes ($g\ C \cdot d^{-1}$) between the air-water interface.

The advective CH_4 fluxes through subnetwork consider the contribution from both surface runoff and drainage that are expressed as:

$$F_{a,sub} = Q_{hill}C_{hill} + Y_{g/h} - Q_{sub}C_{sub} \quad (2)$$

where Q_{hill}, Q_{ground}, and Q_{sub} are flow rates of hillslope flow, ground water, and subnetwork flow ($m^3 \cdot s^{-1}$), respectively. C_{hill} , C_{ground} and C_{sub} are concentrations (mg/L) of dissolved CH_4 in hillslope flow (C_{hill} equals to the air equilibrium concentration), groundwater, and subnetworks, respectively. We assumed dissolved CH_4 yield in groundwater pool is linearly related to the land DOC leaching rate (Gardner et al., 2016) as:

$$Y_{g/h} = \sum K_{g/h} \times Leach_{DOC} \times Area_{veg} \quad (3)$$

where $Y_{g/h}$ is the dissolved CH_4 production (g/d) in groundwater lateral transport and production within the hyporheic zone, $K_{g/h}$ is the calibrated parameter ($m \cdot d^{-1}$), $Leach_{DOC}$ is the land DOC leaching rate (g C $m^{-2} \cdot d^{-1}$, and $Area_{veg}$ is the vegetation area (m^2).[0]

The advective CH_4 fluxes through the main channel were described as:

$$F_{a,main} = \sum_{i=1}^{n} Q_{up,i} C_{up,i} + Q_{sub} C_{sub} - Q_{main} C_{main} \quad (4)$$

where Q_{up} and Q_{main} are the flow rates of upstream grid cells and the main channel in the current grid cell ($m^3 \cdot s^{-1}$), respectively. C_{up} and C_{main} are the associate CH_4 concentration (mg-C/L), respectively.

The dissolved CH_4 production in the water column is partially from the decomposition of organic matters (DOC and POC):

$$Y_{water} = R_{DOC} \times r_{DOC} + R_{POC} \times r_{POC} \quad (5)$$

where r_{DOC} and r_{POC} are the organic carbon decomposition rate ($gC \cdot d^{-1}$). R_{DOC} and R_{POC} are the associate ratios of CH_4 production over the organic decomposition (Goñi and Thomas, 2000; McGinnis et al., 2015). The oxidation rate of CH_4 is correlated to the NO_3^- denitrification rate:

$$CH_4 + 4NO_3^- \rightarrow CO_2 + 4NO_2^- + 2H_2O \quad (5)$$

The oxidation rate of CH_4 in rivers is computed according to a first-order kinetics equation:

$$R = R_{oxidize} \times k_{denitrif} \times r_{NO3-CH4} \quad (6)$$

where $R_{oxidize}$ is the ratio oxidized ($m \cdot d^{-1}$), in this study we set the ratio as 0.1 (Deutzmann et al., 2014), and $k_{denitrif}$ is the denitrification rate of NO_3^- in the river channel, $r_{NO3-CH4}$ is the stoichiometric conversions from nitrate to CH_4. The CH_4 emission or sink was estimated as:

$$E = K_{CH4} \times (C_{CH4} - C_{CH4eq}) \times Area_{water} \quad (7)$$

where $Area_{water}$ is the water surface area (m^2) of rivers within each grid cell, which was calculated based on channel geometry (Getirana et al., 2012; Li et al., 2015a; Raymond et al., 2013). C_{N2O} and C_{N2Oeq} are the dissolved CH_4 concentration (mg-C/L) and equilibrium CH_4 concentration (mg-C/L), respectively. Equilibrium CH_4 concentration was calculated based on Henry's law(Sander, 2015):

$$C_{CH4eq} = 0.0025 \times Exp\left(-2600 \times \left(\frac{1}{273+T} - \frac{1}{298}\right)\right) \times p(CH_4) \times 12 \quad (8)$$

Where T (ºC) is water temperature. The gas exchange rate K_{CH4} ($m \cdot d^{-1}$) is estimated as:

$$K_{CH4} = K_{600} \times \left(\frac{Sc_{CH4}}{600}\right)^{-0.5} \quad (9)$$

where Sc_{CH4} is the Schmidt Number for CH_4, and K_{600} is the gas exchange coefficient; The term Sc_{CH4} is calculated as:

$$Sc_{CH4} = 2301.1 - 151.1 \times T + 4.7364 \times T^2 - 0.059431 \times T^3 \quad (10)$$

The net fluxes of dissolved CH_4 (include physical and biogeochemical processes) in the main channel and subnetwork are given by:

$$\frac{\Delta M_{ebullitive-CH4}}{\Delta t} = R_{sed-POC} \times M_{sed-POC} \quad (11)$$

Where $R_{sed-POC}$ is the ratio of CH_4 production align with the organic matter decomposition, $M_{sed-POC}$ is the organic matter of the bottom sediment. Here, the decomposition of the sediment POC governs the bubble methane production. To simplify the mechanism of CH_4 dynamics in water, we assume the transporting time of fluvial water in 5 arc-min degree cell is long enough for bubble floating from the bottom to the water surface. Thus, we do not consider the vertical transportation of ebullitive CH_4 in the model. The CH_4 production from bottom sediment was directly quantified as ebullitive emissions.

5.3. Simulation protocol and input data

5.3.1 Model driving forces

In this study, a 5 arc-min resolution model input dataset was developed to drive the DLEM model, including climate variables, historical land-use cohort, nitrogen fertilizer, nitrogen deposition, fertilizer, and manure nitrogen application, atmospheric CO_2 concentration.

We have created the potential vegetation map following the procedure of our previous study as base-map of the land-use cohort data (Liu et al., 2013), which combines vegetation information primarily from National Land Cover Database (NLCD) (Homer et al., 2015b) , North American Land Cover (Colditz et al., 2012), Global C4 vegetation map (Still et al., 2003). Four major plant function types were extracted for each grid cell and normalized to the areal fraction of the grid cell. To reconstruct the historical land-use cohort of the CONUS, 1-km resolution cropland data from 1850 to 2016, which combined from multiple data sources, was used to prescribed the fraction of the natural vegetation during the same period (Yu and Lu, 2018). Due to the growing food demand, cropland expanded west-wards (Figure 5-4) during the last century and encroached large areas of grassland and forest.

The 5 arc-min resolution climate datasets, including daily precipitation minimum, mean and maximum temperature, shortwave radiation, and wind speed from 1979 to 2018, were obtained from Metdata (GRIDMET) (available at: http://www.climatologylab.org/). To extend our simulation to pre-industry period, we obtained the historical climate variables from the dataset of Climatic Research Unit and National Centers for Environmental Prediction (CRUNCEP) during 1901 to 1979 (available at: https://rda.ucar.edu/datasets/ds314.3/) and Institute Pierre Simon Laplace (IPSL) simulation from 1850 to 1900 (available at: https://www.isimip.org/). We used GRIDMET data of the year 1979 as base-map and

reconstructed historical climate variables by using the trend of CRUNCP from 1901 to 1978 and IPSL from 1860 to 1900 at the grid level (Figure 5-5).

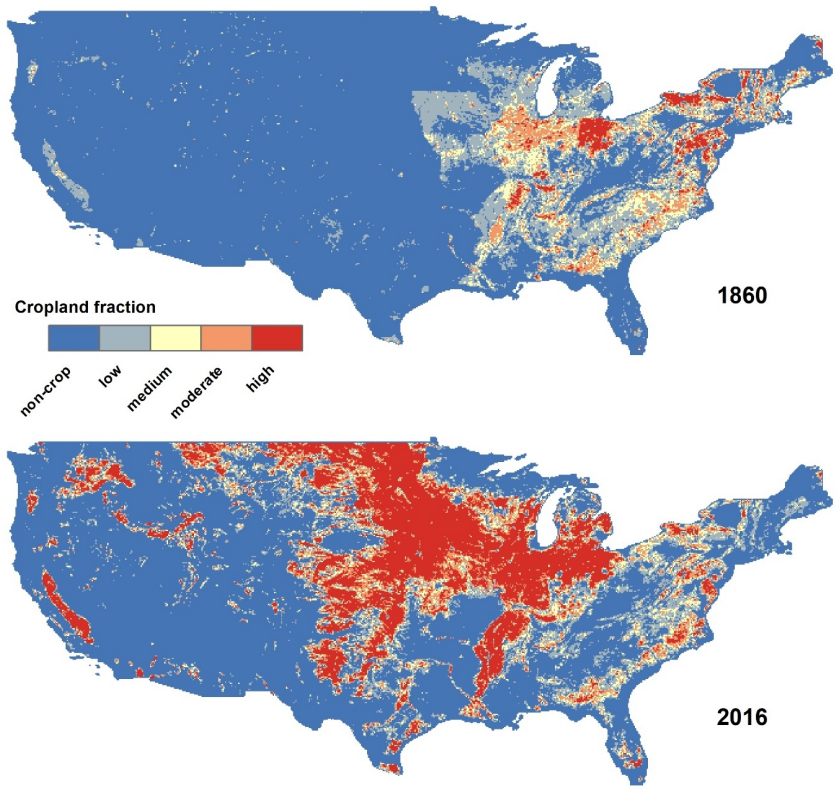

Figure 5-4. Cropland conversion of the U.S. from 1860 to 2016.

The mean annual precipitation of the CONUS since 1860 was 758.7 ± 54.2 mm yr^{-1} with the maximum, and minimum precipitation that occurred in 2018 (914.8 mm) and 1910 (626.9 mm), respectively. The annual precipitation increased significantly since the 1960s, with a rate of 0.99 mm/year. The annual mean temperature in this area was 10.8 ± 0.6°C since 1860, with the maximum and minimum precipitation occurred in 2012 (13.0°C) and 1884 (9.2°C), respectively. Temperature showed a significant increasing trend with a rate of 0.72 °C /100- year (Figure 5-5). Annually atmospheric CO_2 concentrations from 1900 to 2015 were obtained from the NOAA GLOBAL VIEW-CO2 dataset (https://www.esrl.noaa.gov). Long-term atmospheric CH_4

concentration data were obtained from the Advanced Global Atmospheric Gases Experiment (AGAGE) dataset (available at: https://agage.mit.edu/data/agage-data). N deposition dataset was obtained from Chemistry-Climate Model Initiative (CCMI) database (Figure 5-6). N fertilizer data was obtained from Cao, Lu, & Yu (2018). The manure N data was obtained from Zhang et al. (2017) (Figure 5-6).

The scale adaptive water transport module requires a hydrograph dataset as model inputs including flow direction, bank-full width and bank-full depth, which strictly from the Dominant River Tracing (DRT) hydrograph database (Getirana et al., 2012; Wu et al., 2012b). The channel density and channel slopes of small streams and rivers, which were used to quantify the length and slopes of hillslope flow, subnetwork flow, and main channel flow, were derived from National Hydrography Dataset plus v2 data (available at: http://www.horizon-systems.com/NHDPlus/index.php). The lake and reservoirs information of CONUS were derived from Hydrolakes dataset (Messager et al., 2016), and National Dam Inventory (NID) database (available at: https://nid.sec.usace.army.mil/), and was aggregated into the 5 arc-min spatial resolution grid cell.

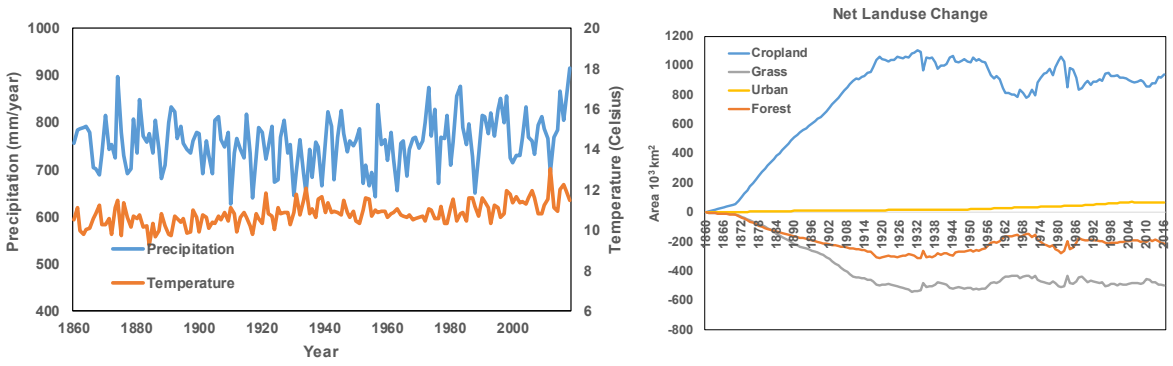

Figure 5-5. The temporal patterns of climate condition and land use change from 1860 to 2018.

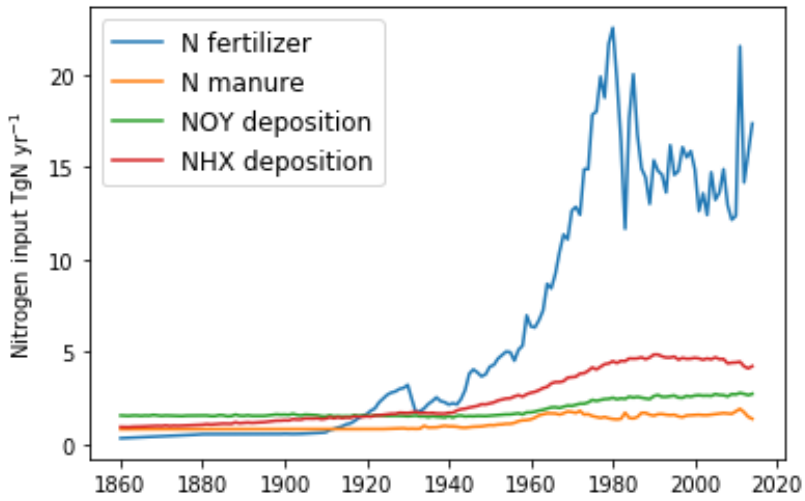

Figure 5-6. The temporal patterns of nitrogen inputs to the terrestrial ecosystem across the contiguous U.S from 1860 to 2018.

5.3.2 Simulation experiments

The DLEM simulation encompassed the CONUS primarily following three steps: (1) To eliminate the human disturbances to the terrestrial ecosystems, we conducted the equilibrium run for each grid cell driven by climate forcing of the pre-industry period and keeps the land-use, CO_2 concentration, nitrogen inputs consistent to the year of 1860. The equilibrium run finishes when the carbon, nitrogen and water pools within each grid reach remain steady. (2) To smooth the carbon, nitrogen, and water fluxes between the equilibrium run and transient run, a 30-year spinning-up run was set-up by randomly using climate forces between 1860 to 1870 (Thornton and Rosenbloom, 2005; Tian et al., 2012). (3). After the spinning-up run, we set up a transient run, with all the forcing changing over time.

To attribute the contributions of environmental factors, including climate change, land-use change, nitrogen deposition, nitrogen management, and atmosphere CO_2 concentration to the CH_4 emissions (Tian et al., 2015c; Xu et al., 2010), we conducted factorial experiments (as shown in Table 5-1) by keeping each driving factor consistent with that of the year 1860.

Simulation 1 is an all-combined simulation with all the driving forces changes over time. In simulation 2, climate driving forces were continuously kept at the level in 1860. In simulation 3, NO_y and NH_x depositions were continuously kept at the level of the year 1860. In simulation 4, the N fertilization and manure N application rates were kept unchanged since 1860. In simulation5, land-use conversion remained unchanged since 1860. By comparing the estimated CH_4 fluxes of simulation 2-6 with that of simulation 1 (all combine run), we obtained the contribution of each environmental factor to the inland water CO_2 and CH_4 emissions.

Table 5-1. The experimental design for inland water CH_4 emission driven by natural and anthropogenic factors including climate, atmospheric carbon dioxide (CO_2), nitrogen deposition (NDEP), nitrogen management (N management): N fertilizer and manure.

	Climate	**CO_2**	**NDEP**	**N management**	**Land-use**
Simulation 1	1860-2016	1860-2016	1860-2005	1860-2013	1860-2016
Simulation 2	1860-2016	1860-2016	1860-2005	1860-2013	1860
Simulation 3	1860-2016	1860-2016	1860-2005	1860	1860-2016
Simulation 4	1860-2016	1860-2016	1860	1860-2013	1860-2016
Simulation 5	1860-2016	1860	1860-2005	1860-2013	1860-2016
Simulation 6	1860	1860-2016	1860-2005	1860-2013	1860-2016

To attribute the contributions of each factors to the inland water CH_4 emissions, we designed a series of factorial experiments: **Simulation 1**: all-combined; **Simulation 2**: without land-use change; **Simulation 3**: without N management; **Simulation 4**: without N deposition**; Simulation 5**: without CO_2, and **Simulation 6**: without climate.

5.3.3 Statistical method

The Mann-Kendal trend test and Theil Sen linear regression method are used to determine the trend of the time series data. We quantified the coefficient of determination (R^2) to validate the performance in predicting methane emissions.

5.3.4 Model validation

To validate the performance of DLEM predicting carbon fluxes and the associated CH_4 emissions, the DLEM-simulated carbon concentrations were compared to the long-term carbon concentrations obtained from USGS. Our results showed that the simulated riverine carbon concentrations agreed well with most of the observations (Figure 5-7). We compared the model-estimated CH_4 fluxes against the observations collected from Stanley et al. (2016) (Figure 5-8). The validation results ($R^2 > 0.6$) suggested that DLEM could well capture the spatial pattern of riverine CH_4 emissions across the CONUS. (more information regarding model validation please refer to Figure 5-8).

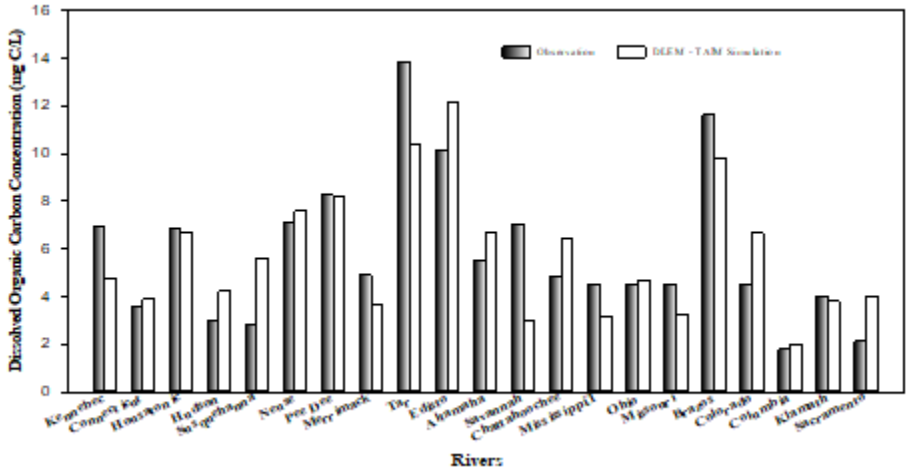

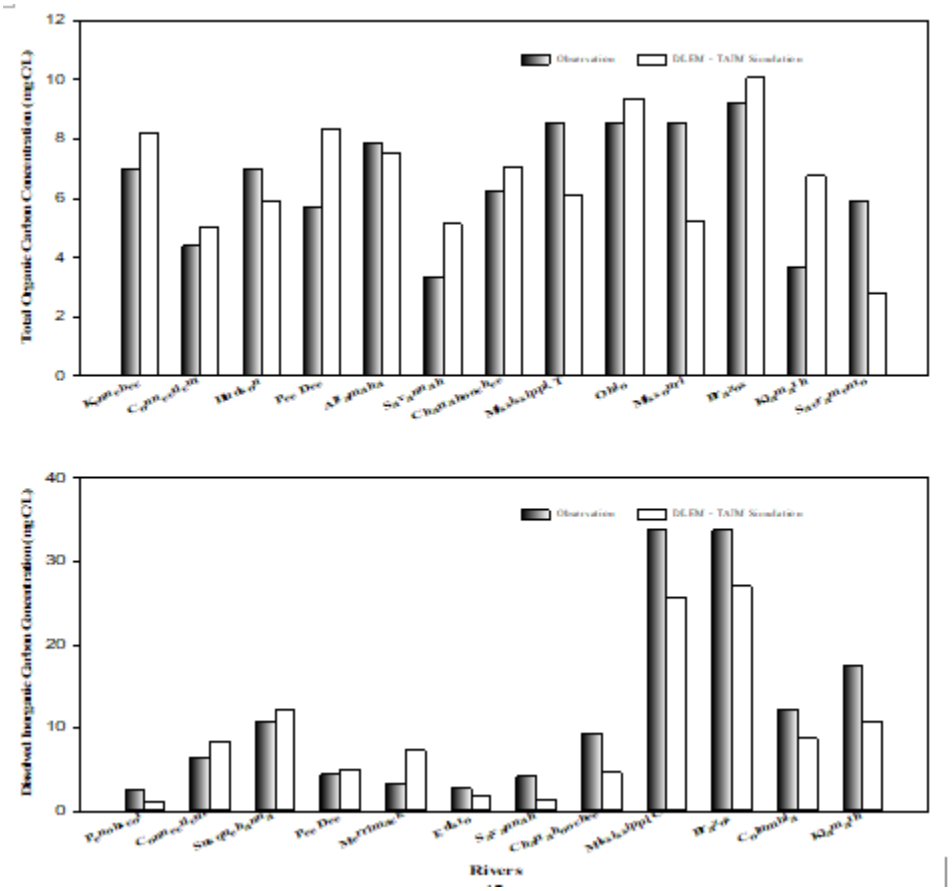

Figure 5-7. Validation of DLEM simulated carbon fluxes against USGS observations.

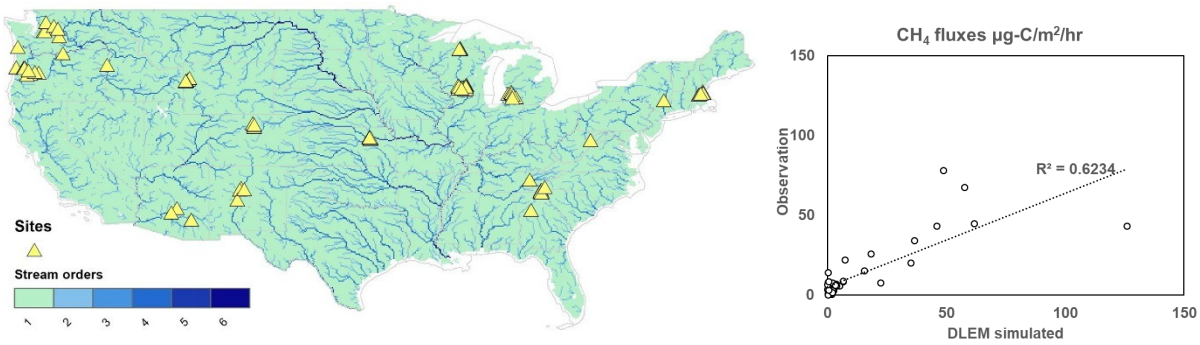

Figure 5-8. Validations of DLEM simulated CH_4 fluxes against observations.

5.4. Results

5.4.1 Spatio-temporal patterns of inland water CO_2 emission across the CONUS

The overall inland water CO_2 emissions increased significantly from 1900 to 2018, with an increasing rate of 0.22 Tg C/yr for both rivers and lakes (Figure 5-9 a). The decadal average

riverine CO_2 emission increased from 90.6 Tg C/yr in the 1900s to 113.6 Tg C/yr in 2009-2018. The decadal average lake CO_2 emission increased from 64.9 Tg C/yr in the1900s to 88.13 Tg C/yr in 2009-2018. Specifically, from 1960 to 2018, the increasing rate of streams and lakes reached 0.56 Tg C/yr and 0.62 Tg C/yr, respectively.

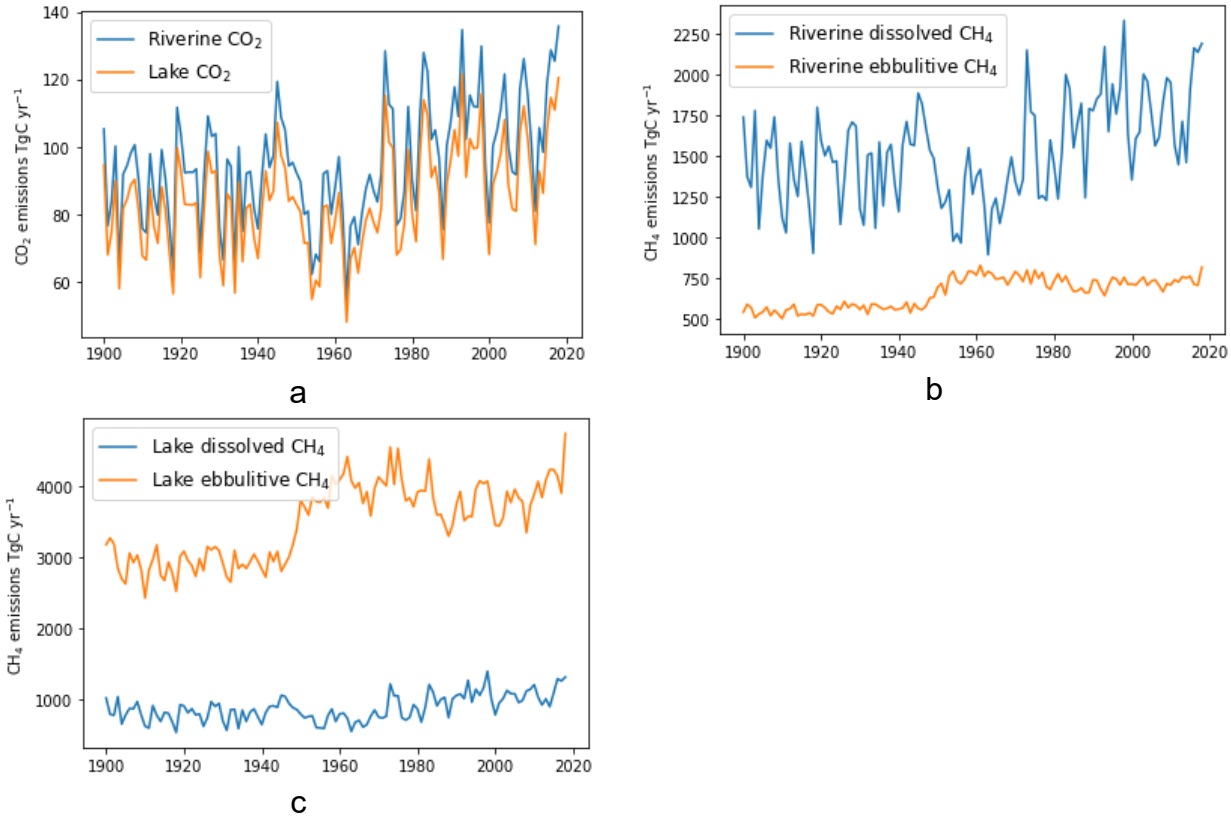

Figure 5-9. The temporal patterns of inland water CO_2 emissions (a), riverine CH_4 emissions (b), and lake CH_4 emissions (c) across the Conterminous U.S from 1900 to 2018.

The spatial pattern of CO_2 emission follows the distribution of vegetations with the eastern regions has much higher CO_2 emission rates than that of the western regions (Figure 5-10). The CO_2 emissions from small streams (1^{st} – 3^{rd} order streams within the 5 arc-min resolution grid

cell) account for more than 80% of the total riverine CO_2 emissions. The riverine CO2 emissions increased significantly in the southeast regions from the 1900s to 2009-2018 (Figure 5-11).

5.4.2 Spatio-temporal patterns of inland water CH_4 emission across the CONUS

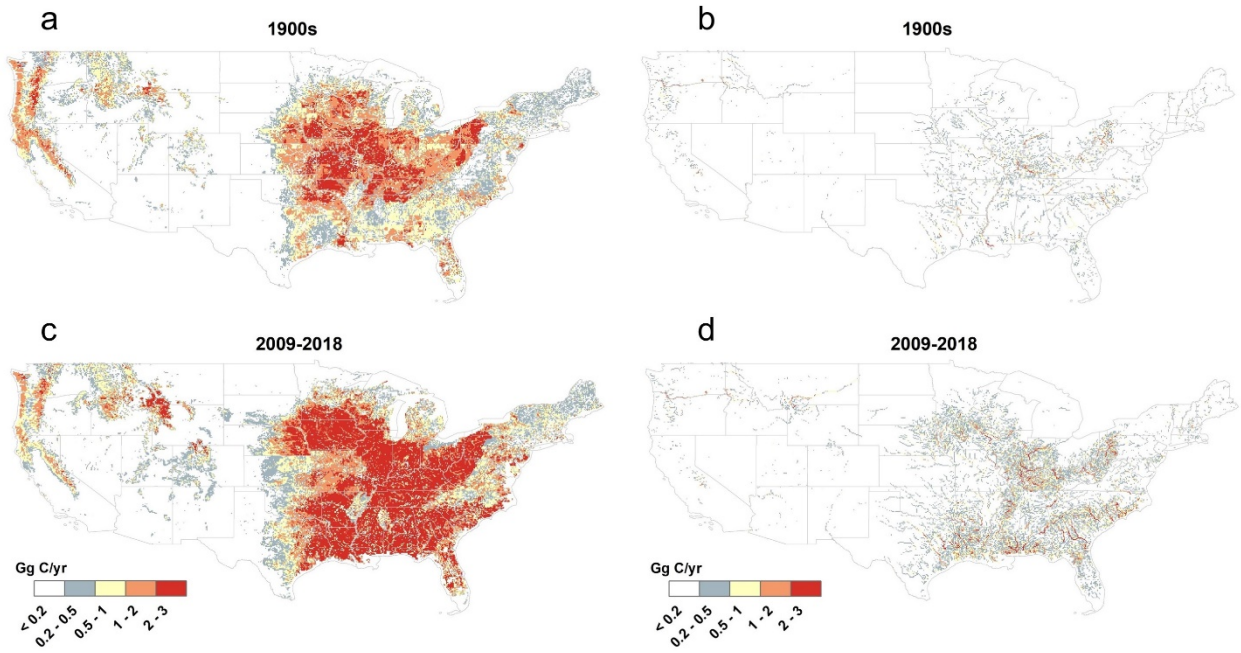

Figure 5-10. The spatial patterns of stream CO_2 emissions. a,b. emission from small streams and rivers during the 1900s. c,d. emission from small streams and rivers during 2009-2018.

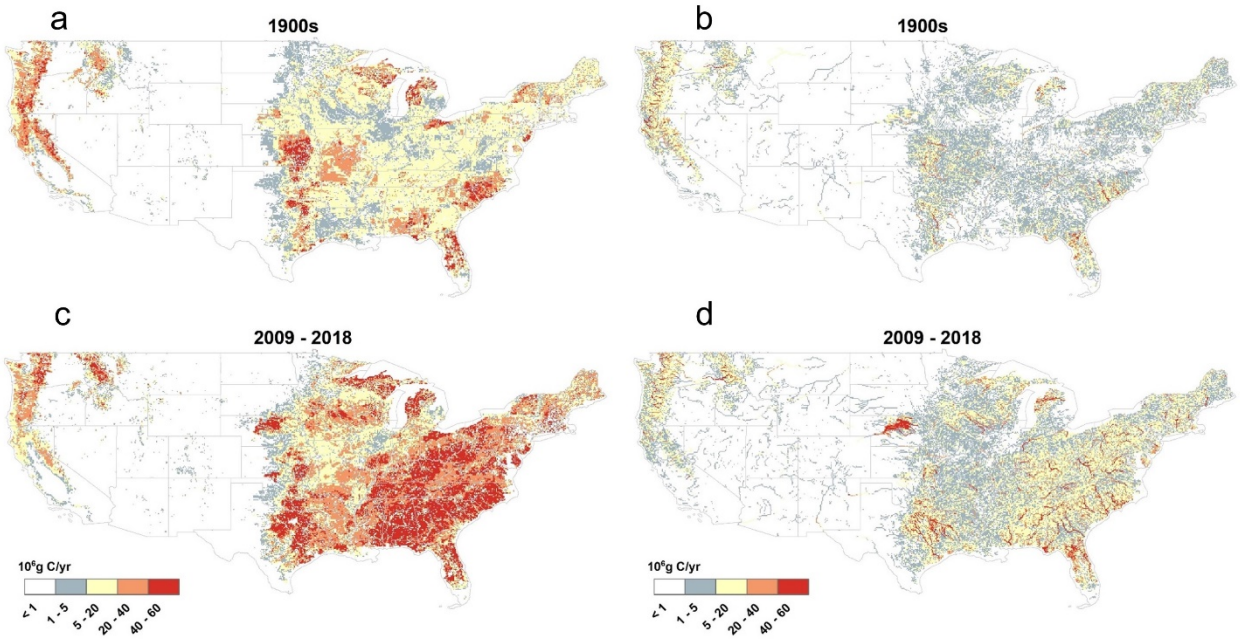

Figure 5-11. The spatial patterns of diffusive CH_4 emissions. a,b. emission from small streams and rivers during the 1900s. c,d. emission from small streams and rivers during 2009-2018.

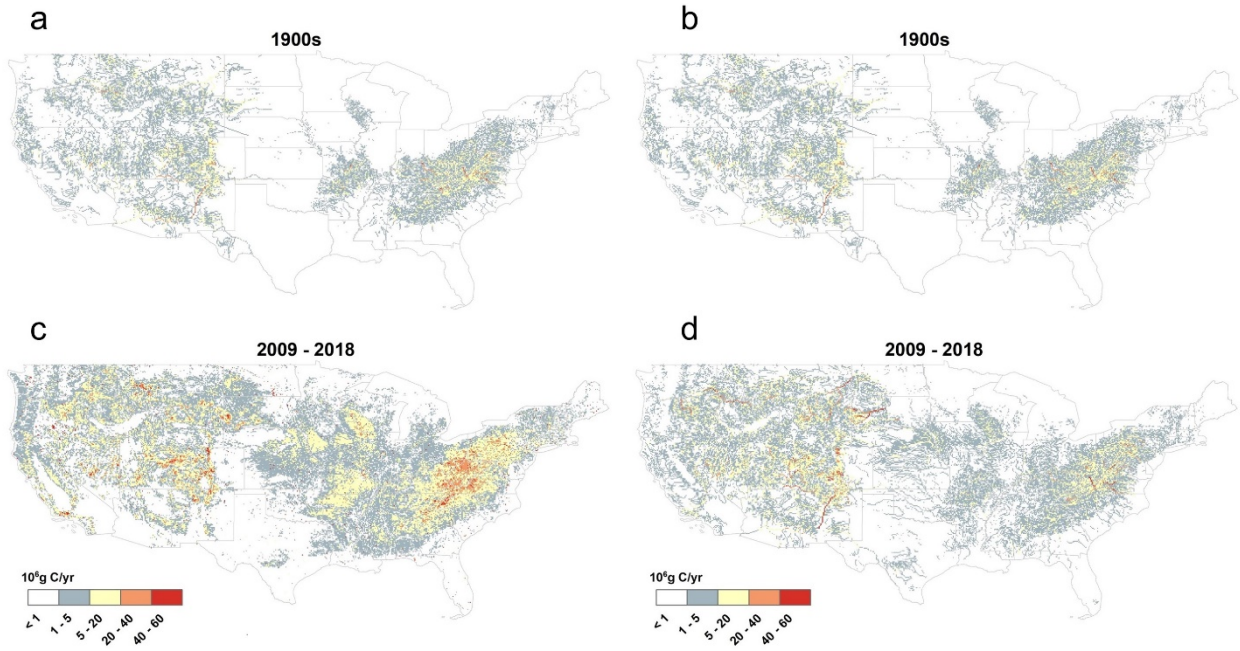

Figure 5-12. The spatial patterns of ebullitive CH_4 emissions. a,b. emission from small streams and rivers during the1900s. c,d. emission from small streams and rivers during 2009-2018.

The diffusive CH_4 emissions from rivers and streams over the CONUS increased from 1484.5 ± 233.4 Gg CH_4-C/yr in the 1900s to 1848.8 ± 286.3 Gg CH_4-C/yr in 2009-2018 (Figure 5-11.b). The diffusive CH_4 emissions from lakes over the CONUS increased from 853.29 ± 122.8 Gg CH_4-C/yr in the 1900s to 1115.9 ± 151.3 Gg CH_4-C/yr during 2009-2018 (Figure 5-11.c). The temporal pattern of diffusive CH_4 emission from streams and lakes had significant differences in two periods. One is 1900 to 1960, there was no statistically significant trend, in contrast, the diffusive CH_4 emission of stream and lakes increased significantly from 1960 to 2018 with the increasing rate of 11.7 Gg CH_4-C/yr and 7.77 Gg CH_4-C/yr, respectively (Figure 5-11.b.c). The ebullitive CH_4 emissions from rivers over the CONUS increased from 543.1 ± 25.7 Tg CH_4-C/yr in the 1900s to 737.2 ± 33.9 Tg CH_4-C/yr in 2009-2018. The ebullitive CH_4 emissions from lakes over the CONUS increased from 2970.7 ± 217.7 Tg CH_4-C/yr in the 1900s to 4095.9 ± 286.8 Tg CH_4-C/yr in 2009-2018. (Figure 5-12. b. c). The trend of ebullitive fluxes of streams and rivers had significant differences in three periods. From 1900 to 1915, no significant trend was found for streams and lakes. The ebullitive emissions of stream and lakes experienced large increases from 1945 to 1965 with the increasing rates of 12.71 Gg CH_4-C/yr and 66.65 Gg CH_4-C/yr, respectively. After 1965, the ebullitive emission of streams and lakes showed a slightly decreasing trend with the rate of 0.7 Gg CH_4-C/yr and 2.2 Gg CH_4-C/yr, respectively.

Similar to the riverine CO_2 emissions, the riverine CH_4 emissions of the eastern regions are much higher than that of the western regions (Figure 5-11, 5-12). The diffusive CH_4 emissions increased significantly in the southeast from the 1900s to 2009-2018 (Figure 5-11). However, the southwest did not show a significant increase in ebullitive CH_4 emissions. However, the ebullitive CH_4 emissions increased significantly in the corn-belt (Figure 5-12).

5.4.3 Factorial contribution of environmental factors to inland water CO_2 and CH_4 emissions.

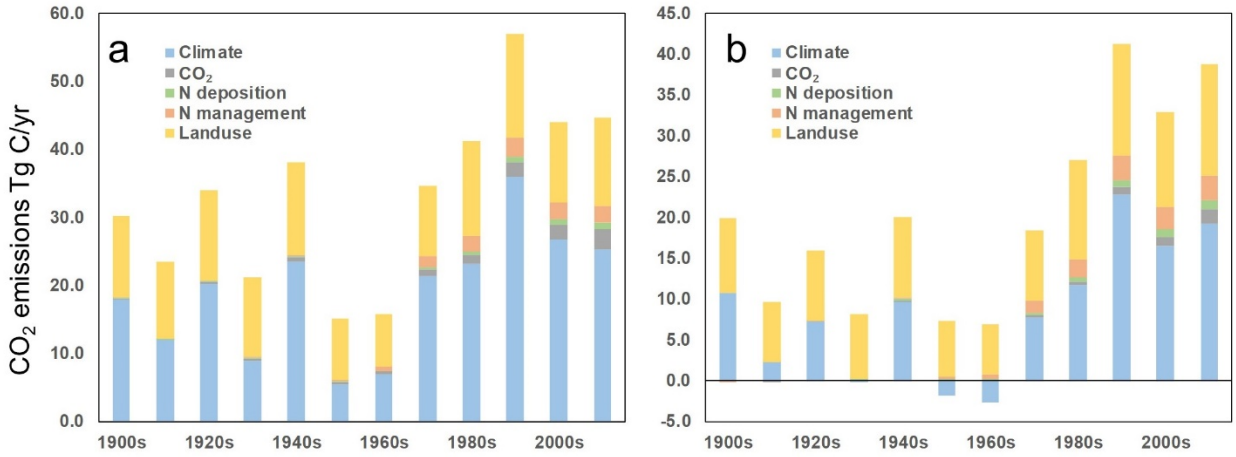

Figure 5-13. Contribution of climate, CO_2 effect, N deposition, N management and land-use change to CO_2 emissions from rivers (a) and lakes(b).

The attribution analysis revealed the contribution of environmental factors to the CO_2 emissions of rivers and lakes of CONUS from 1900 to 2018 (Figure 5-13). For both rivers and lakes, climate explained 40% - 60% of the variability in CO_2 degassing from 1900 to 2018. The long-term land-use conversion accounted for 30% - 40% of the increase in CO_2 degassing from rivers and lakes. Nitrogen inputs including nitrogen deposition, N fertilizer, and manure N applications, have a minor contribution to inland water CO_2 degassing by only explained ~10% of the changes in total (Figure 5-13).

Climate explained most of the changes in diffusive CH_4 emission from streams and lakes during 1900 - 2018. The elevated temperature and precipitation explained more than 70% of the changes in diffusive CH_4 emissions in streams and lakes (Figure 5-14. a, b). Land conversions only accounted for less than 20% of the changes in diffusive CH_4 emissions. The contribution of CO_2 fertilization to the change in CH_4 emissions from streams and lakes gradually reached to

17.3% and 12.5% during 2009-2018, respectively. For stream, N deposition and N management contributed 11% and 7.7 of the changes in diffusive CH_4 emissions. Similar to that of the streams, N deposition and N management contributed 9.5% and 6.1% of the increase in diffusive CH_4 emissions, respectively (Figure 5-14. a, b).

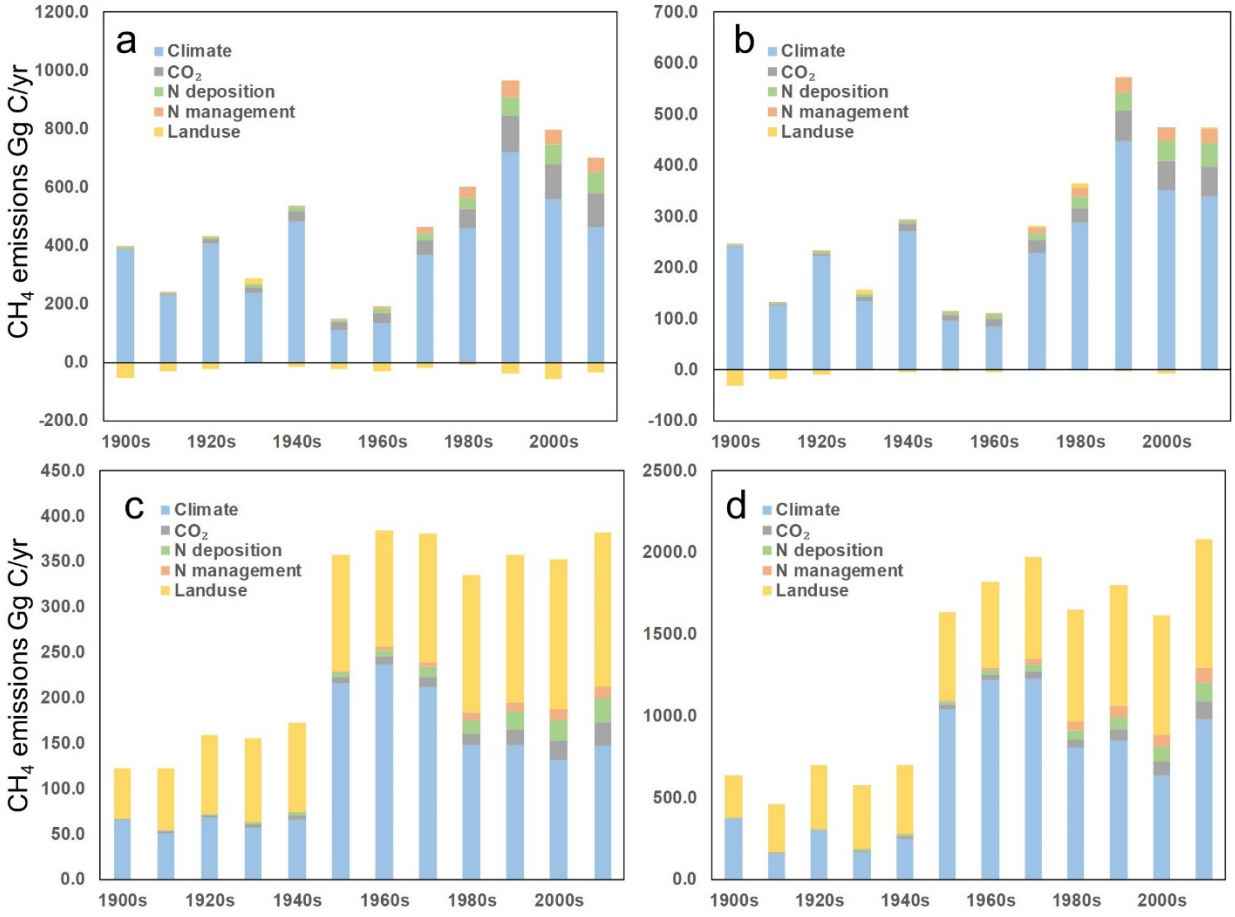

Figure 5-14.Contribution of climate, CO_2 effect, N deposition, N management and land-use change to diffusive CH_4 emissions from rivers (a) and lakes(b), and to ebullitive emissions from rivers (c) and lakes (d).

The contribution of climate to ebullitive CH_4 emissions is much lower than that of the diffusive counterparts. Although climate variables still explained most of the interannual variabilities, it

only accounted for 30% - 40% of the increase in ebullitive CH_4 emissions from streams and lakes (Figure 5-14. c, d). Land-use conversion explains 44.6% of the increase of ebullitive CH_4 emissions from streams, followed by Nitrogen deposition (5.6%), CO_2 (5.4%), and nitrogen management (4%), respectively. Similarly, Land-use conversion explains 38% of the increase of ebullitive CH_4 emissions from lakes, followed by Nitrogen deposition (7.1%), CO_2 (6.8%), and nitrogen management (3.3%), respectively (Figure 5-14. c, d).

5.5. Discussions

5.5.1 Compare with previous studies.

Our model provided the first estimates of inland water CO_2 and CH_4 emission by process-based model. Here, we compared the magnitudes of CO_2 and CH_4 emissions estimated by DLEM with the estimates from previous studies. The magnitude of our simulated CO_2 emissions from rivers and streams is 113.6 ± 16.9 Tg C/yr, which was in line with the result derived from a water quality data-based analysis (97 ± 32 Tg C/yr)by Butman & Raymond (2011). The magnitude of our estimated CO_2 emission from lakes and reservoirs (88.13± 13.5 Tg C/yr) is higher than that of estimates by (Butman et al., 2016)(16 (14.3–18.7) Tg C/yr. One possible reason for the higher lake CO_2 estimation in our modeling study might originate from different sources of water surface area inputs. The estimation by (Butman et al., 2016) is derived from the National Lakes Assessment (NLA) of the US Environmental Protection Agency (EPA), which only contains 1,028 lakes. The Hydrolakes data used in this study contains more than 10,000 lakes (include large lakes, small lakes, reservoirs), which has much larger water surface areas. Another potential reason for the higher estimation in our study is we do not consider the carbon uptake in the lentic system, due to the complexity of the model and difficulties in parameterization for a large scale (Kumar et al., 2008). Until now, none of the studies provides the estimate of inland

water CH_4 emission of CONUS to our best of knowledge. However, the ratio of global lake emissions (53.7 Tg C/yr) over riverine emissions (20.1 Tg C/yr) is 2.6 (Deemer et al., 2016), which is comparable to our estimated ratio (2.01) of lake CH_4 emissions (5.21 Tg C/yr) over riverine CH_4 emissions (2.58 Tg C/yr) from 2009 to 2018.

Our model could well address the relative role of small streams and large rivers in the riverine CO_2 and CH_4 emissions. Previous studies have suggested that the headwater stream released most of the CO_2 emissions (Butman and Raymond, 2011; Raymond et al., 2013). In our analysis, 88% of the riverine CO_2 gas released from 1^{st} -3^{rd} order streams (within 5 arc-min resolution grid cells), which is consistent with the data analysis-based study. A similar phenomenon has been found for N_2O gas emission from the headwater stream (Turner et al., 2015). In theory, significant CO_2, N_2O and CH_4 production in the hyporheic zone, which located at the interface between groundwater and surface water of the headwater zones (Clough et al., 2007; Holgerson and Raymond, 2016; Marzadri et al., 2014; Rasilo et al., 2017; Wohl et al., 2012). The hyporheic exchange between groundwater and surface water provides a favorable condition for the production of CH_4 and N_2O, due to the low oxygen level (Marzadri et al., 2017; Rulík et al., 2000). Until now, none of the previous study represent the high emission rate of CH_4 in the headwater stream, due to the lack of observations. Our modeled results highlighted importance of the small streams by contribute 75.6% and 75.1% of the total diffusive and ebullitive CH_4 emissions from rivers, which gives implications to the future filed work studies.

5.5.2 Factors control the emissions of CO_2 and CH_4 from inland waters.

Given the importance of anthropogenic effects and climate change on the magnitude and spatial pattern of carbon dynamics of the continental and global level, the contribution of environmental factors to the changes in CO_2 and CH_4 emissions from inland waters has been well investigated

in this study. It is certain that long-term changes in climate conditions such as elevated air temperature and precipitation would substantially promote the growth of plants (Pan et al., 2015, 2014; Tian et al., 2012, 2011). The increased growth of plants results in the accumulation of soil carbon pool through increasing litterfall (Vitousek and Howarth, 1991). Thus, a similar theory could be used to explain why increased N inputs would moderate the soil carbon and the associate riverine carbon fluxes and inland water CO_2, CH_4 emissions.

The contribution of land-use conversion to inland water CO_2 and ebullitive CH_4 emissions are much higher than that of the diffusive CH_4 emissions. That is because the indicators of dissolved CO_2, diffusive CH_4, and ebullitive CH_4 are DIC, DOC, and POC, respectively. The CONUS experienced massive land conversion from grassland to cropland (Figure 5-4, 5-5). The deforestation significantly increased the soil litter pool, which in turn increased soil respiration. Since most of the DIC loss from land is relevant to soil respiration (Hastie et al., 2019), DIC loading and the resulted CO_2 degassing increased significantly due to deforestation. However, the increased soil carbon pool only has limited contributions to the DOC loading, because the DOC loading only refers to the absorption and desorption of soil at a given depth (Andersson et al., 2000; Liu et al., 2016; Tian et al., 2015c). The POC loading to rivers is primarily sourced from soil erosions (Lal, 1995). DLEM calculated soil erosions by Modified Universal Soil Loss Equation (MUSLE) model (Williams and Berndt, 1977). Due to the high soil erosion rate of cropland, the POC loading increased substantially over the CONUS during the last century (Van Oost et al., 2007), which helps to explain the substantial contribution of land conversion to ebullitive CH_4 emissions (Figure 5-14.c.d).

It should be noted that nitrogen fluxes also regulate the CH_4 dynamics in aquatic systems. Overall, the nitrogen inputs contribute to the increase in CH_4 emissions (Figure 5-14), although

the contribution is small. That is because the increased nitrogen loading also prompted more CH_4 oxidation in waters (Chapra, 2008; Deutzmann et al., 2014), which substantially mitigates the positive effect of nitrogen induced carbon loading (Ren et al., 2015; Tian et al., 2015c).

5.5.3 Uncertainties

This study provides a first process-based modeling study of CH_4 dynamics in the land-aquatic continuum under the earth system modeling framework. However, the model structure, parameters as well as the input data would certainly induce significant uncertainties.

Our model still incorporated many empirical equations to simplify the processes in land and waters, although we calibrate the parameters to match the data, which implicitly contains the simplified biogeochemical processes. It should be noted that the gas exchange rates show considerable spatial heterogeneity by streams and lakes (Ulseth et al., 2019). Raymond et al. (2012) suggested eight ways to quantify the gas exchange rate of dissolved CO_2 from streams, which may induce significant uncertainties and require further investigations. We used empirical equations to estimate the gas exchange rate of CO_2 and CH_4 from lakes by using local wind speed (Bastviken et al., 2004; Lu et al., 2016). However, the empirical equation is validated in one site, but may not fit for all the lakes over the CONUS. Our model simplified the biogeochemical processes of CO_2 and CH_4 production in groundwater because none of the earth system models consider the lateral groundwater transport and the associated subsurface biogeochemical processes. Again, we do not consider the CO_2 uptake, which may undoubtedly induce large uncertainties in estimating CO_2 effluxes in the lentic water system (Battin et al., 2009; Maavara et al., 2017). Future research needs to consider the food chain of algae and microorganism activities for CO_2 and CH_4 dynamics (McGinnis et al., 2015). The parameters of the model also have large uncertainties. The previous study used to calibrate parameters to

represent the CH_4 production rate per cubic meter water. However, the volume of water itself is not a reliable indicator of CH_4 production. Thus, we used a simple ratio to represent the CH_4 production and oxidation obtained from field experiments (Deutzmann et al., 2014; Goñi and Thomas, 2000; McGinnis et al., 2015). However, the uncertainty range of the ratio is quite broad; more filed experiments need to be conducted in the future to guide the modeling work.

Model inputs also would induce large uncertainties. Our model does not explicitly model the dynamics of water pH. We generated static water pH data by interpolation long term observations collected from the USGS database. Water pH directly control the pCO_2 and the associated CO_2 emissions (Andersen, 2002), thus accurately predicting water pH is essential in quantifying CO_2 emissions. Additionally, it has been improved that the traditional methods to calculate pCO_2 largely overestimate CO_2 degassing in organic-rich freshwaters, thus accurately estimate organic matters and water pH may substantially improve the estimating of CO_2 evasions (Abril et al., 2015). Water pH also regulated the CH_4 production due to the microorganism activities, which has not been included in our current model. Except for water pH, the surface area of the water body also directly influences the total emissions. However, the surface areas are dynamic and remain large uncertain especially for the headwater streams (Allen et al., 2018). Although statistical-based methods have been developed to estimate the surface area of the small streams, the large measurement of headwater streams is still needed in the future to align with the improvement of remote sensing technology (Allen and Pavelsky, 2018).

5.6. Conclusion

In this study, we used a coupled modeling framework to address the biogeochemical processes relevant to CO_2 and CH_4 dynamics in the inland waters. We validated the lateral DOC, POC, and DIC fluxes of the river and CH_4 fluxes from streams across the CONUS. We found a significant

increase in CO_2 and CH_4 emissions from rivers and lakes due to climate change and human activities. It is worth noting that large uncertainties still exist in our modeling results due to the model structure and parameterizations as well as model inputs. To reduce the uncertainties, more reliable technology regarding modeling tools and data model integrations should be developed in the future.

Chapter 6: Increased riverine N_2O emission across the continental U.S.

Abstract: Emissions of nitrous oxide (N_2O) from the river networks constitute a poorly constrained term in the regional N_2O budget (Ciais et al., 2014; Tian et al., 2016). This N_2O component was previously estimated as indirect emissions from agricultural soils (Davidson and Kanter, 2014) despite that the magnitude of emissions is highly uncertain (Beaulieu et al., 2011; Hu et al., 2016; Kroeze et al., 2005; Kroeze and Seitzinger, 1998; Maavara et al., 2018; Reay et al., 2012; Seitzinger and Kroeze, 2000). Here, we present an improved model representation of nitrogen and N_2O processes at the land-ocean aquatic continuum (Regnier et al., 2013) constrained with a new ensemble of data products. The new model-data framework provides a quantification for how changes in nitrogen inputs (fertilizer, deposition, and manure), climate and atmospheric CO_2 concentration, and terrestrial processes have affected the N_2O emissions from the world's streams networks during the period of 1900-2016. The results show an increase of riverine N_2O emissions from 38.3 ± 6.2 Gg N_2O-N yr^{-1} in the 1900s to 60.5 ± 8.7 Gg N_2O-N yr^{-1} in 2009-2018 across the CONUS. The small rivers in headwater zones (lower than 4^{th} order streams) contributed up to 82.9% of riverine N_2O emissions over the CONUS. Nitrogen loads on headwater streams and groundwater from human activities, primarily agricultural nitrogen applications, play a significant role in the increase of the CONUS riverine N_2O emissions.

6.1 Introduction

During the last century, massive reactive nitrogen drained into aquatic ecosystems due to human activities, includes land conversion to cropland, extensive nitrogen fertilizer and manure applications, nitrogen deposition, and urban sewage release. Nitrous oxide (N_2O), a byproduct of nitrification and denitrification, has become the third important greenhouse gas because of its long lifetime in the atmosphere and high greenhouse effect (Davidson and Kanter, 2014).

Extensive studies have estimated N_2O emissions from inland waters as the product of dissolved inorganic nitrogen (DIN) by applying a lab-measured emission factor (Kroeze et al., 2005; Seitzinger and Kroeze, 2000). Emission factors (the ratio of N_2O emissions to riverine inorganic nitrogen at this moment) are determined from site-level field experiments or observations. Moreover, the measurements are usually of low-frequency. These spatial and temporal deficits of the EF method limit its use at a large spatial scale and a long time-scale, at which land and river conditions would show high heterogeneity. The difficulty can hinder this method in obtaining emission factors at various spatio-temporal scales. The wide range of emission factors results in considerable uncertainty in existing estimates of riverine N_2O emissions (Beaulieu et al., 2011; Hu et al., 2016; Kroeze et al., 2005; Kroeze and Seitzinger, 1998; Maavara et al., 2018; Reay et al., 2012; Seitzinger and Kroeze, 2000) from 0.03 to 2.0 Tg N_2O-N yr^{-1}. Using lab-measured emission factors also ignores the transport process of N_2O in aquatic ecosystems. In reality, the N_2O emission amount along the streamline could vary significantly, with small rivers releasing much more N_2O than high order streams due to the hyporheic exchange of water and nutrients between stream water and groundwater (Garnier et al., 2009; Turner et al., 2015).

To close the regional N_2O budget and properly attribute atmospheric changes to sources and sinks, it is important to better understand and quantify riverine nitrogen exports and associated

N_2O emissions through the land-ocean aquatic continuum. However, land and earth system models lack the representation of lateral fluxes and processes over continents and from continents to oceans (Ciais et al., 2008; Tian et al., 2018b). The most recent improvement in large-scale hydrology models considers the sub-grid routing processes (Li et al., 2013, 2015a) of small streams in large grid cells aiming to reduce the scale effect, which can be extended to simulate the physical and biogeochemical processes in small headwater streams.

Inspired by the recent new progress in hydrological modeling and field observations, we developed a process-based riverine N_2O model to simulate the N_2O concentration and emission from streams and rivers. We incorporated the riverine N_2O model into a scale adaptive water transport scheme, which fully coupled with a Dynamic Land Ecosystem Model (DLEM) (Tian et al., 2016; Yang et al., 2015c). Furthermore, we quantified the impacts of climate and human interaction on riverine N_2O effluxes across the continental U.S.

6.2. Methods and input data

Here we developed a riverine N_2O model within the framework of the Dynamic Land Ecosystem Model (Tian et al., 2015c) (DLEM) (Figure 6-1.a) by coupling a scale-adaptive hydrological scheme (Li et al., 2015a) and river biogeochemistry (Yang et al., 2015b) to simulate the riverine fluxes of water, carbon and nitrogen and the resulting emissions of greenhouse gases (GHGs). The model can effectively address the small stream processes by incorporating the sub-grid routing processes without conducting model simulation on fine resolution (Figure 6-1.b).

6.2.1 The DLEM model

The Dynamic Land Ecosystem Model (DLEM) is a fully distributed, process-based land surface model that couples the major land hydrological processes, plant physiology, soil biogeochemistry, and river- routing processes (Tian et al., 2015c) (Figure 6-1.b). The DLEM

explicitly simulates the carbon, nitrogen, and water fluxes between plants, soil, and atmosphere driven by climate, atmospheric CO_2, nitrogen deposition, land use and land cover, N fertilizer use, irrigation, and other management practices. Meanwhile, the surface and drainage runoff and nitrogen load from DLEM are used as the input of the aquatic model Yang et al. (2015). The simulated nitrogen loads include nitrate (NO_3^-), ammonium (NH_4^+), and dissolved organic nitrogen (DON).

The DLEM aquatic model calculates river routing and the biogeochemical processes in the aquatic ecosystems. The mineralization of DON to NH_4^+ is mainly controlled by water temperature, while NH_4^+ nitrification and NO_3^- denitrification are primarily regulated by water temperature and flow velocity. Detailed descriptions of DLEM aquatic biogeochemical processes could be found in Tian et al. (2015) and Yang et al. (2015). In this study, we improved the DLEM aquatic model through adopting a scale adaptive river routing approach, to quantify the physical and biogeochemical processes in small streams, which usually cannot be accounted in the majority of regional and global modeling research (Ciais et al., 2008; Tian et al., 2018b). Besides, a riverine N_2O model was developed for simulating N_2O emissions from river channels.

6.2.2 The scale adaptive river routing scheme

In this study, a scale adaptive water transport scheme, namely the Model for Scale Adaptive River Transport (MOSART) (Li et al., 2013, 2015a), has been coupled with DLEM. The water transport scheme (Figure 6-1.b) characterized the water transport processes within a grid cell into threefold: hillslope flow, subnetwork flow, and main channel flow. The hillslope flow represents the flowing course, which merges surface runoff and flows into subnetworks. The subnetwork flow, conventionally known as the 1^{st} – 3^{rd} order streams in the 0.5-degree cell, receives water from hillslope flow and subsurface runoff and drains into the main river channel of the gird unit.

Here, the lateral subsurface flow within a grid unit is lumped as the outflow from a groundwater pool to the local subnetworks with parameterized residence time (Costa and Foley, 1997; Liu et al., 2013). The main river channel receives water inputs from local subnetworks and upstream grid cells, and drainage into the downstream grid cells.

All three river routing processes were solved by using *Kinematic Wave Methods*, which require hydrograph datasets as input generated from the fine resolution topographic dataset (Li et al., 2015a). Thus, a hydrograph dataset was developed, including channel slope, width, length, roughness and bankfull depth for both small rivers and large rivers. The channel widths, lengths, and slopes of small rivers within the 0.5-degree grid cell were aggregated from the 15-arc Hydrosheds data (Li et al., 2013, 2015a). The same variables for the large river routing were derived from DDM30 0.5-degree grid dataset (Döll and Lehner, 2002). The Manning roughness coefficients maps of overland flow and channel flows were derived as a function of land-use type and channel depth (Getirana et al., 2012). Detailed information about the hydrological data can refer to (Li et al., 2015a) and Getirana et al. (2012).

6.2.3 Riverine N_2O model

A riverine N_2O module was developed based on the scale adaptive water transport scheme. Hillslope flow receives dissolved N_2O from the land surface (through surface runoff) and contributes to subnetwork flow. Here we assume N_2O concentration in the surface runoff to be equal to the atmospheric equilibrium N_2O concentration. The net fluxes of dissolved N_2O (including physical and biogeochemical processes) in the main channel (high-order streams) and subnetwork (small rivers) are estimated as:

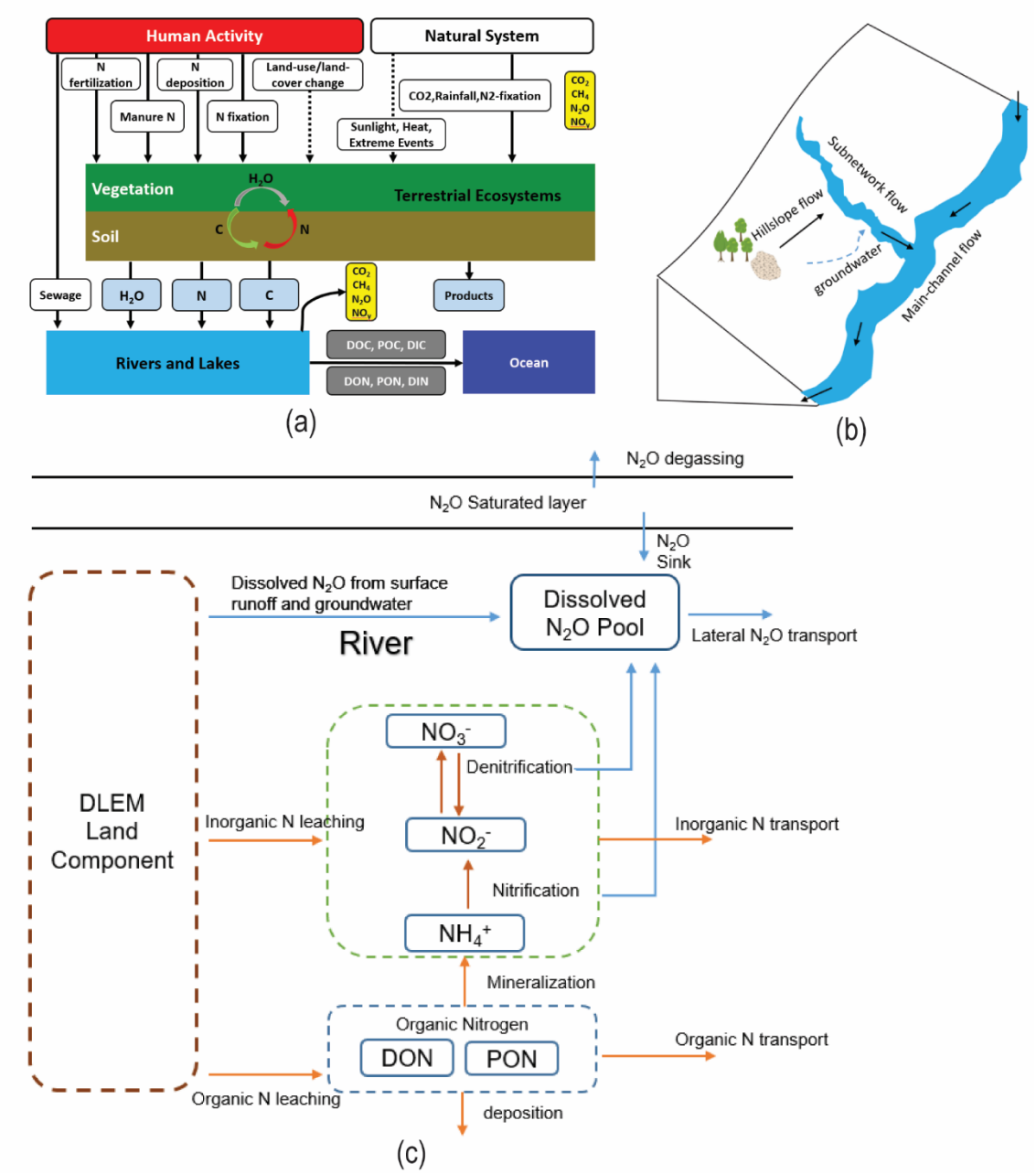

Figure 6-1. The framework of major biogeochemical and hydrological processes in the Dynamic Land Ecosystem Model (a) (Tian et al. 2015), which fully coupled with the conceptual model of the scale adaptive water transport module (b) and the riverine N2O model (c).

$$\frac{\Delta M_{N2O}}{\Delta t} = F_a + Y_{water} + D - R - E \quad (1)$$

where M_{N2O} is the total mass of dissolved N_2O in the main channel or subnetworks (gN), Δt is the time step, F_a is advective N_2O fluxes ($gN \cdot d^{-1}$), Y_{water} is the N_2O production within the water column ($gN \cdot d^{-1}$), D is the dissolved N_2O from rainfall to rivers (i.e. deposition) ($gN \cdot d^{-1}$) with an initial concentration equal to the atmospheric equilibrium N_2O concentration, R is the flux from N_2O reduction ($gN \cdot d^{-1}$) to nitrogen gas, and E is the riverine N_2O efflux ($gN \cdot d^{-1}$) through the air-water interface.

The advective N_2O flux through subnetwork flow considers contributions from both surface runoff and drainage and can be expressed as:

$$F_{a,sub} = Q_{hill}C_{hill} + Y_{g/h} - Q_{sub}C_{sub} \quad (2)$$

where Q_{hill}, and Q_{sub} are flow rates of hillslope flow, subnetwork flow ($m^3 \cdot s^{-1}$); C_{hill} , C_{sub} are concentrations (mg/L) of dissolved N_2O in hillslope flow (C_{hill} equals to the atmospheric equilibrium N_2O concentration), and subnetworks, respectively. DLEM model simulates soil biogeochemical processes of one crop type and four natural vegetation types nested in one grid cohort, and each plant function type has its soil carbon and nitrogen pools(Tian et al., 2012). The inorganic nitrogen leaching (i.e., NH_4^+ and NO_3^-) is the primary source for N_2O production in the groundwater and hyporheic zones(Quick et al., 2019). Thus, we parameterized the soil biogeochemistry associated with the groundwater N_2O production as a function of soil N availability and the local soil properties:

$$Y_{g/h} = \sum K_{g/h} \times Leach_{NO_3^-} \times Area_{veg} \quad (3)$$

where $Y_{g/h}$ is the dissolved N_2O production ($gN\ d^{-1}$) in groundwater and the hyporheic zone, $Leach_{NO_3^-}$ is the land nitrate leaching rate ($g\ N\ m^{-2}\ d^{-1}$) that varies with the plant function type (PFT; Gardner et al., 2016), and $Area_{veg}$ is the vegetation area (m^2) for each PFT. The

parameter $K_{g/h}$ represents the N_2O-N / NO_3^--N ratio and was calibrated for each PFT against observations, which fell in the ranges suggested by Jahangir et al., (2012) (Table 6-1).

The advective N_2O fluxes through the main channel can be described as:

$$F_{a,main} = \sum_{i=1}^{n} Q_{up,i}C_{up,i} + Q_{sub}C_{sub} - Q_{main}C_{main} \quad (4)$$

where Q_{up} and Q_{main} are the flow rates of upstream grid cells and the main channel in the current grid cell ($m^3 \cdot s^{-1}$), respectively. C_{up} and C_{main} are the associated dissolved N_2O concentrations (mg/L), respectively. Dissolved N_2O production in the water column was calculated from both nitrification and denitrification:

$$Y_{water} = R_{nitrif} \times k_{denitrif} + R_{denitrif} \times k_{nitrif} \quad (5)$$

where k_{nitrif} and $k_{denitrif}$ are the nitrogen removal rate ($gN \cdot d^{-1}$) through nitrification and denitrification. R_{nitrif} and $R_{denitrif}$ are the associated ratio of N_2O production through nitrification and denitrification(Beaulieu et al., 2011). The detailed description of riverine nitrification and denitrification processes in DLEM could be found in Yang et.al.(Yang et al., 2015a)

The nitrification or denitrification rate (k) can be estimated as:

$$k = \exp(\frac{-v}{\Delta d}) \quad (6)$$

where v is the settling velocity (d^{-1}) of NO_3^- or NH_4^+ through nitrification and denitrification respectively, and Δd is the hydraulic load (m) for rivers flow into the downstream grid cell. v can be simulated by a first-order kinetics equation(Yang et al., 2015a):

$$v = v_{ref} \times (Q_{10})^{\frac{T-T_S}{10}} \quad (7)$$

where v_{ref} is the settling velocity of NO_3^- or NH_4^+ at the reference temperature of 20 ˚C, Q_{10} is the change fraction of NO_3^- or NH_4^+ reaction rates at a temperature change of 10 ˚C and assigned 2.0 here, T is the water temperature (˚C), and T_s is the reference temperature (20 ˚C). Δd can be expressed as:

$$\Delta d = \frac{Q}{A_s} \tag{8}$$

where Q is water discharge (m/s), and A_s is the surface area of the waterbody. The reduction of N_2O in rivers is computed according to a first-order kinetics equation:

$$R = K_{reduction} \times M_{N2O} \tag{9}$$

where $K_{reduction}$ is the reduction rate ($m \cdot d^{-1}$) (the ratio of the parameter range could be found in Table 6-2), and M_{N2O} is the content of dissolved N_2O (g N) in the river channel. The Riverine N_2O emission or sink was estimated as:

$$E = K_{N2O} \times \left(C_{N2O} - C_{N2Oeq}\right) \times Area_{water} \tag{10}$$

where $Area_{water}$ is the water surface area (m^2) of rivers, which can be estimated based on channel geometry (Getirana et al., 2012; Li et al., 2015a; Raymond et al., 2013). C_{N2O} and C_{N2Oeq} are dissolved N_2O concentration (mg/L) and atmospheric equilibrium N_2O concentration(Sander, 2015) (mg/L), respectively. K_{N2O} ($m \cdot d^{-1}$) is the gas exchange rate (Fu et al., 2018). Here we use a newly developed method to calculate the channel width of small streams:

$$width = Q^{\frac{3}{5r+3}} \times (0.5\,A^{0.42})_i^{\frac{r-1}{r+0.6}} \times \left(8.1(9.8\,S)^{0.5}k^{-\frac{1}{6}}14^{-\frac{5}{3}}(1-\frac{1}{r+1})\right)^{-\frac{3}{5r+3}} \tag{11}$$

where Q is discharge (m/s), A is upstream area (ha), k is a bed roughness length scale, and r is shape parameter. More information could be found by Allen et al. (2018).

More information about the newly introduced parameters in the riverine N_2O module can be found in Table 6-2.

6.2.4 Study area and model input data

In this study, we developed a 5 arc-min resolution model input dataset of the Contiguous United States (CONUS) to drive the DLEM model. CONUS, known as U.S. 48, is the major component of the United States. The region spans 8,080,464.3 km^2 and supports 327.2 million people. Dominant plant function types in the CONUS include temperate evergreen needle-leaf and deciduous broadleaf evergreen shrubland, C3 grassland, temperate needle-leaf forest and deciduous shrubland as shown in Figure 6-2.

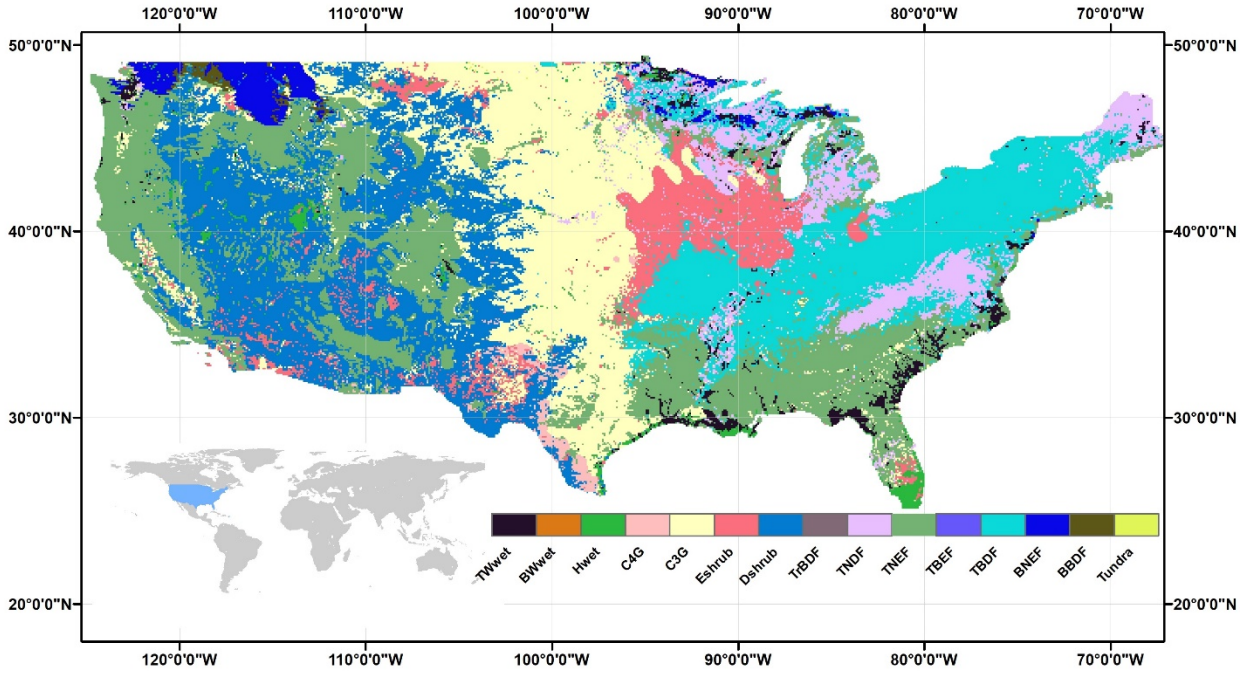

Figure 6-2. The major plant function types across the Contiguous United States (CONUS).

The model driving forces consist of land-use/land cover change, climate variables, atmospheric CO_2 and N_2O concentrations, atmospheric N deposition, nitrogen fertilizer, and manure nitrogen applications (Figure 6-3).

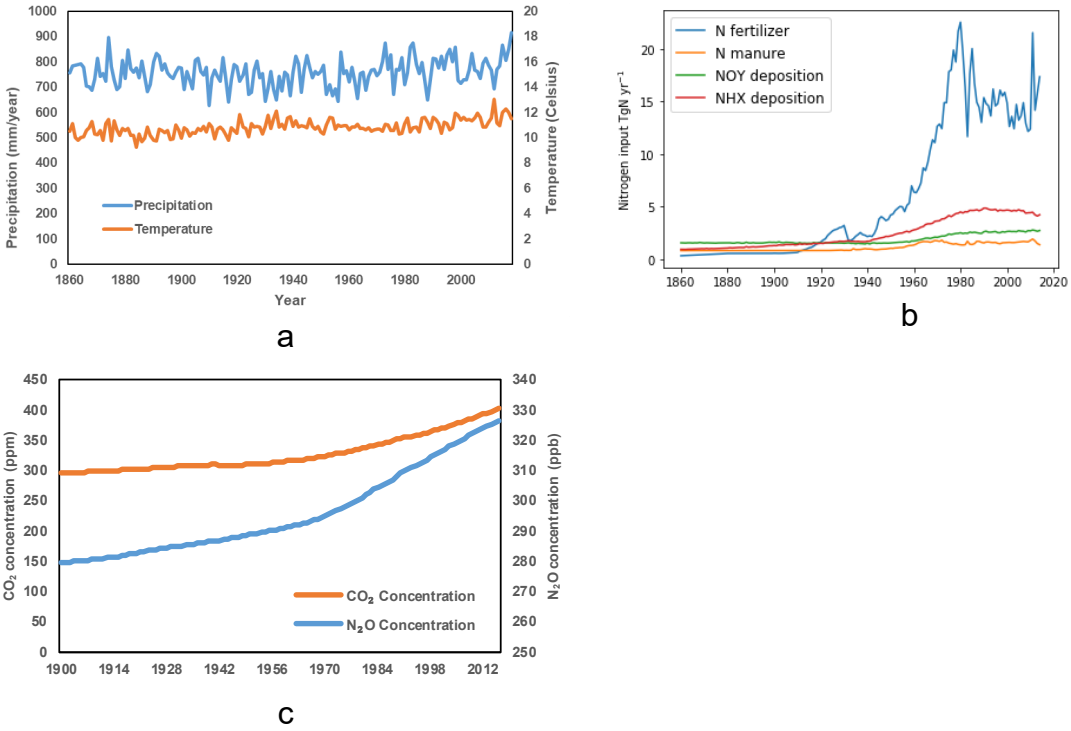

Figure 6-3. Model forcing for DLEM-N2O simulations. a. annual precipitation (mm) and temperature (°C) during 1860 -2018. b. nitrogen inputs (Tg N yr^{-1}) from 1860 to 2018. c. The atmospheric CO_2 (ppm) and N_2O concentrations (ppb) from 1900 to 2018.

The annual land-use/land cover change data were derived from a potential natural vegetation map (Synergetic Land Cover Product(Jung et al., 2006)) and a prescribed cropland area dataset from History Database of the Global Environment version 3.2 (HYDE 3.2: ftp://ftp.pbl.nl/hyde/). The daily climate variables (i.e., precipitation, mean temperature, maximum temperature, minimum temperature, and shortwave radiation) were obtained from the METADATA and CRU–NCEP dataset (https://vesg.ipsl.upmc.fr) for the time period 1900-2016. Annual atmospheric CO_2 concentration from 1900 to 2015 was obtained from the NOAA

GLOBALVIEW-CO_2 dataset (https://www.esrl.noaa.gov). Long-term atmospheric N_2O concentration was obtained from the AGAGE dataset (available at: https://agage.mit.edu/data/agage-data).

We obtained three spatially-explicit time-series datasets of agricultural N fertilizer use at a resolution of 5 arc-min from Lu and Tian (2017), which developed the datasets through spatializing IFA-based country-level N fertilizer consumption amount according to crop-specific N fertilizer application rates, distribution of crop types, and historical cropland distribution during 1900–2014. The total magnitude of fertilizer application as the major nitrogen input to agricultural land reached to 17.35 Tg N/year in 2018. N deposition dataset was obtained from Chemistry-Climate Model Initiative (CCMI) database. The N deposition increased continuously since 1860 with the value of NOX, and NOY reached 4.21 Tg N/year and 2.71 Tg N/year, respectively. The manure N data was obtained from Zhang et al. (2017).

The historical Gross Domestic Product (GDP) and population data obtained from the Inter-Sectoral Impact Model Intercomparison Project (ISIMIP: https://esg.pik-potsdam.de/search/isimip/) are used for estimating sewage N exports, using the method proposed by Van Drecht et al. (2009).

6.3 Simulations and validations:

To quantify the influences of natural and human activities on riverine N_2O emissions, the model was driven by multiple factors including climate (shortwave radiation, precipitation, air temperature, maximum temperature and minimum temperature), land use and land cover, and nitrogen inputs (fertilizer, deposition, manure and sewage) from 1900 to 2016 (Figure 6-3). The simulated river discharges and nitrate (NO_3^-), ammonium (NH_4^+), and dissolved organic nitrogen (DON) concentrations were calibrated using observations from selected large river basins across

the CONUS (Figure 6-7). The simulated groundwater dissolved N_2O concentration and riverine dissolved N_2O concentration agreed well with observations both spatially and temporally (Table 6-1; Figure 6-4). Moreover, factorial experiments (Figure 6-5.b) were conducted to attribute the contribution of each factor (i.e., climate, CO_2, fertilizer, manure, and N deposition) to riverine N_2O emissions (Table 6-3).

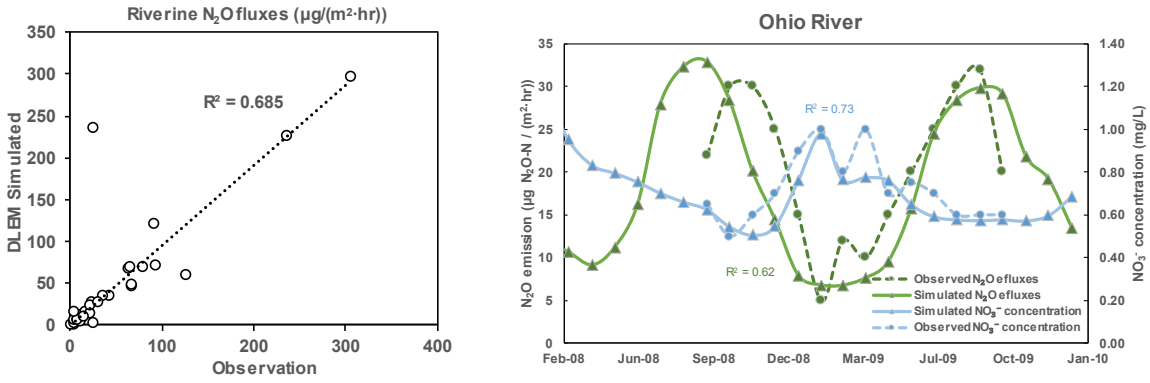

Figure 6-4. Validation N_2O fluxes across the CONUS.

6.4 Results and discussions:

We estimate that riverine N_2O emissions over the CONUS increased from 38.26 ± 6.23 Gg N_2O-N yr^{-1} in the 1900s to 60.53 ± 8.74 Gg N_2O-N yr^{-1} in 2016, at an average annual growth rate of 0.58 GgN_2O-N yr^{-1} (Figure 6-5. a). The increasing trend was not monotonic, and its evolution can be partitioned into the three periods of 1900-1960, 1960-2000, and 1997-2016, according to the piece-wise linear regression. During 1900-1960, no significant trend was found. During 1960-2000, the increasing growth rate accelerated to 1.75 Gg yr^{-1} due to the extensive use of N fertilizer, which contributed 85.8% of the riverine N_2O increase during the 1990s. However, riverine N_2O emissions started to decrease during 2000-2016 at a rate of 0.3 N_2O-N yr^{-1}, partially due to decreased N fertilizer (Figure 6-3.b) use as well as elevated CO_2-induced reduction in

N_2O emissions. The CO_2 fertilization effect promotes increased plant growth at higher CO_2 concentrations and therefore locks higher amounts of nitrogen into plant biomass.

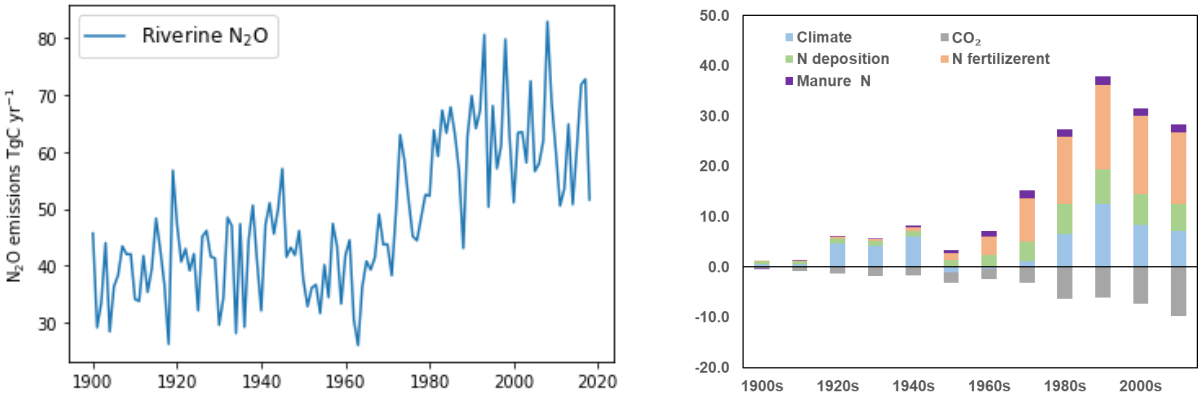

a b

Figure 6-5. The temporal pattern of riverine N_2O emissions (a) and the attribution analysis of environmental factors to the changes in riverine N_2O emissions over the CONUS(b).

The contribution of small rivers (lower than 3th order streams) dominated riverine N_2O emissions (Figure 6-6). For example, from 2009-2018, N_2O emissions from small rivers were 50.2 ± 8.1 Gg N_2O-N yr^{-1} whereas emissions from high-order streams only were 10.33 ± 1.81 Gg N_2O-N yr^{-1} (Figure 6-6). The groundwater processes combined the lateral groundwater transport from the soil root zone to streams and those in the hyporheic zone. The hyporheic zone is located beneath the stream bed and groundwater-stream repeat exchanges here. The groundwater processes played as the major N_2O source and produced, on average, 31.1 ± 6.6 Gg N_2O-N yr^{-1}, whereas the contemporary water column produced an average of 3.4 ± 1.8 Gg N_2O-N yr^{-1}. In contrast, for high-order streams water column dominated the N_2O production by generating on average 2.7 ± 0.5 Gg N_2O-N yr^{-1} (Figure 6-6). Nevertheless, it is noted that in part of high-latitude regions and arid regions, rivers acted as a sink for N_2O, which is consistent with the experimental evidence

(Beaulieu et al., 2011; Soued et al., 2016) (Figure 6-6).

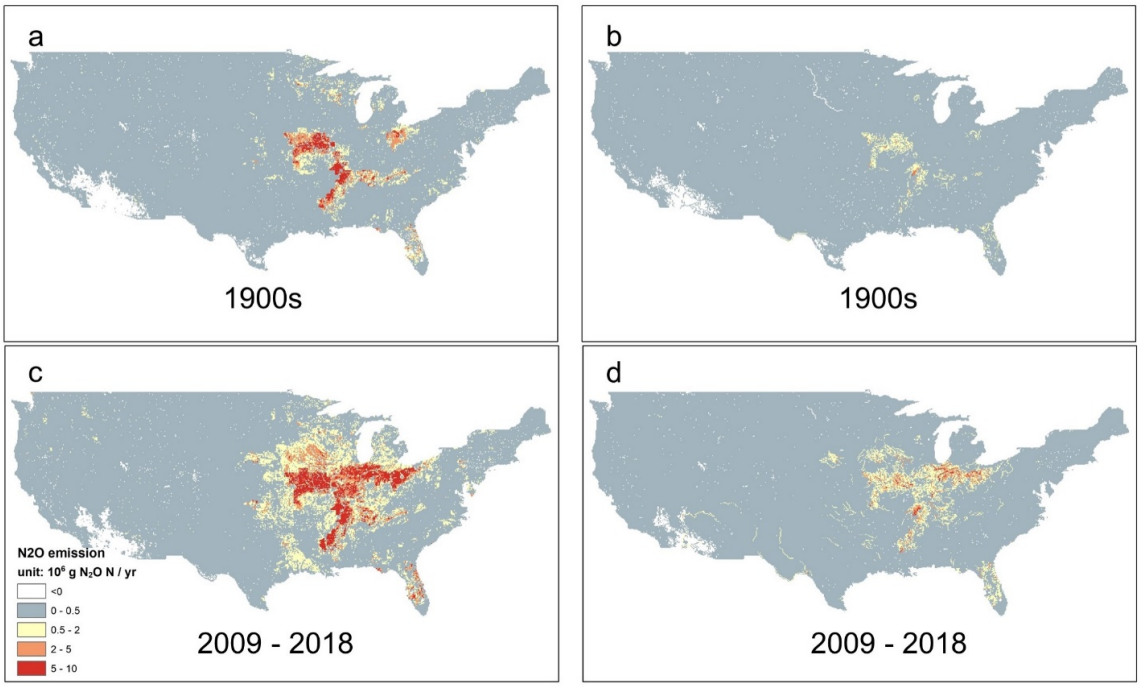

Figure 6-6. The riverine N_2O emissions of small streams (a, c) and rivers (b,d) during 1900s and 2008-2019.

Our approach is capable of estimating riverine N_2O emissions from both small streams and high-order rivers at fine spatial and temporal resolutions, thus overcoming the limitations of the emission factor approach. The results reveal the disproportionately large contribution of small rivers to riverine N_2O emissions, as hinted by several regional studies (Garnier et al., 2009; Turner et al., 2015). The hyporheic zone with large reactive surface area can facilitate N_2O production in small rivers. Compared to the high-order streams, small ones directly fed by hyporheic exchanges (Marzadri et al., 2017), have higher dissolved N_2O concentration, steeper channel slopes, and faster flow velocities, which contribute to higher gas exchange rates (Garnier et al., 2009). The dominant role of small headwater streams at the continental scale was not

recognized for a long time because they are not consistently gauged for discharge, and it is difficult to directly measure their surface area (Allen et al., 2018).

It is worth noting that the majority of dissolved N_2O in the water column was from N_2O-supersaturated groundwater, addressing the balance of N_2O emissions in excess of that produced via direct denitrification (Marzadri et al., 2017). This phenomenon could be explained by the long residence time (Marzadri et al., 2017) of subsurface transport, which provides enough time for denitrification to convert NO_3^- into N_2O and nitrogen gas. The long residence time induced a high rate of leached nitrogen accumulating in the groundwater pool and results in high N_2O concentration. Additionally, the low oxygen level (Rosamond et al., 2012) below the water table provides favorable conditions for the production of N_2O via denitrification process, which in turn produced more N_2O in groundwater. Our simulated results could well capture the reported N_2O sink in the high latitude and arid rivers (Rosamond et al., 2012) (Figure 6-6) because of the introduction of the N_2O consumption reaction in our riverine N_2O model. Additionally, the relatively low terrestrial-N inputs and the resulted low dissolved N_2O production in groundwater and surface water help explain the riverine N_2O sink in the high latitude and arid regions.

Anthropogenic N inputs and cropland expansions could explain the majority of the increase in the groundwater N_2O concentration (Jurado et al., 2017) and global riverine N_2O emissions. Among regions, the significant increase of riverine N_2O emissions in agricultural regions of the CONUS. since the 1960s (Figure 6-6) is due to the explosive growth in population, which boosts the demand for food and industrial supplies, and thus stimulates the heavy use of N-fertilizer and manure. For example. In contrast, the CO_2 fertilization effect is the primary reason for the decrease in riverine N_2O emissions since 2000 (Figure 6-5.b). The fertilization effect of CO_2 stimulates vegetation growth, and thus, more fixed N will enter the soil N pool as litterfall,

providing the substrate for production of NH_4^+ and NO_3^- through mineralization for production of NH_4^+ and NO_3^- through mineralization(Kanter et al., 2016). On the other hand, increased vegetation growth requires more uptake of NO_3^-.

Consequently, less NO_3^--N is exported into rivers, resulting in a decrease of N_2O production through denitrification (Beaulieu et al., 2011). Although the increase of reactive NH_4^+ provides more substance for nitrification, which benefits the production of N_2O, the simultaneously increased dissolved organic matter exported to aquatic systems can stimulate microbes to consume more available O_2, which in turn inhibits the nitrification process (Chapra, 2008). Therefore, the net effect of increased CO_2 fertilization on the riverine N_2O emissions could not be ascribed to one or two factors. Sewage-N inputs to rivers are one of the dominant sources for riverine N_2O production in urban regions (Beaulieu et al., 2010; Borges et al., 2015; Burgos et al., 2015), which however contribute only about 2.9% of the terrestrial-N exports to rivers at the global level(Lee et al., 2019), However, most of the megacities, where live more than half of the world's population, are distributed at the coastal zones (von Glasow et al., 2013). This effectively shortens the residence time of sewage-N in the riverine systems.

Our model unveils the spatio-temporal patterns of riverine N_2O emissions and the underlying governing factors of emissions. Our results on the asynchronously temporal changes in N_2O emissions and NO_3^- concentrations (Figure 6-4) in high-order streams suggest that it is not reasonable to use NO_3^- as an instantaneous predictor for riverine N_2O fluxes. We found that the temporal N_2O production was regulated by water temperature (Venkiteswaran et al., 2014), as well as the riverine NO_3^- content that might be significantly affected by the riverine transport with limited removal rates(Loken et al., 2018).

Our study highlights the importance of surface and subsurface processes in N_2O emissions from the world's river networks. We show that large N_2O emissions from headwater small streams have been ignored or underestimated in recent estimates of riverine N_2O emissions (Hu et al., 2016; Maavara et al., 2018). Also, applying a constant emission factor measured from headwater streams may lead to largely overestimated N_2O emissions from the rivers. To better estimate N_2O emissions from the riverine networks, models need to improve the representation of surface and subsurface hydrological and biogeochemical processes as well as the accuracy of driving data. In particular, model parameters were the largest source of uncertainty, followed by river surface area and nitrogen inputs. A rainfall event can increase the surface area of the first-order streams significantly, but the high flow velocities make surface area prediction difficult (Allen et al., 2018). Gas exchange rates also show large variations by streams which require further investigation (Ulseth et al., 2019). We simulated the N_2O production from nitrification and denitrification using a Q_{10} based empirical method, in which water temperature is the only determinant (the first-order mechanism). Although deficits exist in this method for explicitly accounting for other critical factors, such as carbon availability, microbe activity, and the level of dissolved oxygen, the parameterization of nitrification and denitrification rates at the reference temperature does implicitly consider impacts of other factors.

Moreover, the method is further validated by this study (Table 6-1) (Quick et al., 2019). Currently, the process-based subsurface hydrodynamic model requires variables such as thickness or extent of the hyporheic zone, hyporheic denitrification rate (Marzadri et al., 2017). However, these variables remain highly uncertain due to the lack of field measurements on a large scale. Therefore, the rigorous interaction between process-based modeling and field

experimentation will be essential to reduce the estimated uncertainty in the lateral N_2O emission for closing the continental N_2O budget.

Continental riverine N_2O emissions, as one sector of inland water systems (lake, reservoir, river, and estuary), account for about 6% of global anthropogenic N_2O emissions (Beaulieu et al., 2011). It should be noted that the increase in global riverine N_2O emissions (188.07% from the 1900s to 2009-2018) is much faster than that of soil N_2O emissions (58.73% from the 1860s to 2007-2016) (Tian et al., 2018b). The improved knowledge of the quantities, distribution, and hotspots of riverine N_2O emissions from this study can support the implementation of management strategies to increase crop nitrogen efficiency, thereby reducing nitrogen losses and their associated environmental impacts. Our study suggests that it is critical to reducing nitrogen loads into the headwater streams that are closer to human livelihood. All greenhouse gas emission pathways consistent with the goals of the Paris Climate Agreement require substantial and sustained reductions on N_2O emissions, which in turn require improved quantification, process attribution, and methodological transparencies.

Table 6-1. The collected annual mean riverine N_2O fluxes and concentrations for model calibration and validation.

Riverine N_2O emission				
Continent	***River Basin***	***Stream order***	***Emissions*** $\mu gN_2O\text{-}N \cdot m^{-2} \cdot hr^{-1}$	***Literature source***
North America	Hudson river, USA	5	8.30	(Cole and Caraco, 2001)(Cole and Caraco, 2001)
	Ohio river, USA	6	16.00	(Beaulieu et al., 2010a)(Beaulieu et al., 2010)
	Grand river, USA	1 ~ 4	90.00	(Venkiteswaran et al., 2014)(Venkiteswaran et al., 2014)
	Plate river, USA	7	63.00	(McMahon and Dennehy, 1999)(McMahon and Dennehy, 1999)
	Potomac river, USA	5	91.32	(McElroy et al., 1978)(McElroy et al., 1978)
	Neuse river, USA	1 ~ 4	64.00	(Stow et al., 2010)(Stow et al., 2005)
	NC (southern deciduous forest) , USA	1 ~ 4	41.67	(Beaulieu et al., 2010b)(Beaulieu et al., 2011)
	MI (northern deciduous forest) , USA	1 ~ 4	24.33	(Beaulieu et al., 2010b)(Beaulieu et al., 2011)
	MA (northern deciduous forest) , USA	1 ~ 4	65.73	(Beaulieu et al., 2010b)(Beaulieu et al., 2011)
	KS (tallgrass prairie) , USA	1 ~ 4	77.26	(Beaulieu et al., 2010b)(Beaulieu et al., 2011)
	WY (shrub steppe) , USA	1 ~ 4	2.36	(Beaulieu et al., 2010b)(Beaulieu et al., 2011)
	SW (desert) , USA	1 ~ 4	0.53	(Beaulieu et al., 2010b)(Beaulieu et al., 2011)
	PR (tropical forest) , USA	1 ~ 4	65.22	(Beaulieu et al., 2010b)(Beaulieu et al., 2011)
	OR (wet coniferous forest) , USA	1 ~ 4	3.78	(Beaulieu et al., 2010b)(Beaulieu et al., 2011)

Riverine dissolved N_2O concentration				
Continent	***River Basin***	***Stream order***	***Observation μgN_2O-N/L***	***Literature source***
North America	San Joaquin river, USA	6	0.905	(Hinshaw et al., 2012)(Hinshaw and Dahlgren, 2013)
	Ohio river, USA	6	1.1	(Beaulieu et al., 2010a)(Beaulieu et al., 2010)
Ground water dissolved N_2O concentration				
Continent	***River Basin***	***Observation μgN_2O-N/L***		***Literature source***
North America	Lake Creek, Oregon, USA	6.5−8.9		(Well et al., 2001, Jurado et al., 2017)(Well et al., 2001; Jurado et al., 2017)
	Bear Creek Watershed, Iowa, USA	10.2		(Kim et al., 2009, Jurado et al., 2011)(Kim et al., 2009; Jurado et al., 2017)
	Choptank watershed, USA	10.9		(Fox et al., 2014, Jurado et al., 2017)(Fox et al., 2014; Jurado et al., 2017)
	Narragansett Bay, Rhode Island, USA	2.5		(Clough et al., 2007, Jurado et al., 2017)(Clough et al., 2007; Jurado et al., 2017)

Table 6-2**.** Newly introduced parameters in the riverine N_2O module.

Parameter	Description	Calibrated value	Ranges	Unit	Reference
$K_{g/h}$	The ratio of groundwater N_2O production from NO_3^- leach rate	0.8% ~ 1.3%	0.33% ~ 1.63%	unitless	Introduced from Jahangir et al. (2012)(Jahangir et al., 2012) and calibrated for each plan function types
$R_{denitrif}$	The ratio of riverine N_2O production from riverine denitrification	1%	0.04-5.6%.	unitless	Introduced from Beaulieu et al. (2010)(Beaulieu et al., 2011)
R_{nitrif}	The ratio of riverine N_2O production from riverine nitrification	0.1%	0.04-5.6%.	unitless	Similar to denitrification N_2O production(Seitzinger and Kroeze, 2000)
$K_{reduction}$	N_2O consumption rate	0.012	0.0057~0.0344	1/d	*Introduced from Kolb et al. (2012)(Kolb and Horn, 2012) and convert from the areal N_2O consumption rate.

* Unit conversion: The areal N_2O consumption (−9.4 to −56.8 nmol m^{-2} h^{-1}) rate were obtained from Kolb et al. (2012). We assume the depth of the water column (bogs) as 6-m, the waterbody consumes N_2O to keep the dissolved N_2O concentration equals to the atmospheric equilibrium N_2O concentration (6.6 nmol/L). Thus, the N_2O consumption rate is converted as: -9.4(56.8) nmol m^{-2} h^{-1} × 24 hr / 6-m / 1000 / 6.6 nmol L^{-1} = 0.0057(0.0344) 1/d

Table 6-3. The experimental design for riverine N_2O emission simulations driven by natural and anthropogenic factors including climate, atmospheric carbon dioxide (CO_2), nitrogen deposition (NDEP), nitrogen fertilizer (NFER), and manure (NMAN).

	Climate	**CO_2**	**NDEP**	**NFER**	**NMAN**
Simulation 1	1901-2016	1900-2016	1900-2005	1900-2013	1900-2016
Simulation 2	1901-2016	1900-2016	1900-2005	1900-2013	1900
Simulation 3	1901-2016	1900-2016	1900-2005	1900	1900-2016
Simulation 4	1901-2016	1900-2016	1900	1900-2013	1900-2016
Simulation 5	1901-2016	1900	1900-2005	1900-2013	1900-2016
Simulation 6	1901	1900-2016	1900-2005	1900-2013	1900-2016

To attribute the contributions of each factors to riverine N_2O emissions, we designed a series of factorial experiments: **Simulation 1**: all-combined; **Simulation 2**: without manure input; **Simulation 3**: without N fertilizer; **Simulation 4**: without N deposition**; Simulation 5**: without CO_2, and **Simulation 6**: without climate.

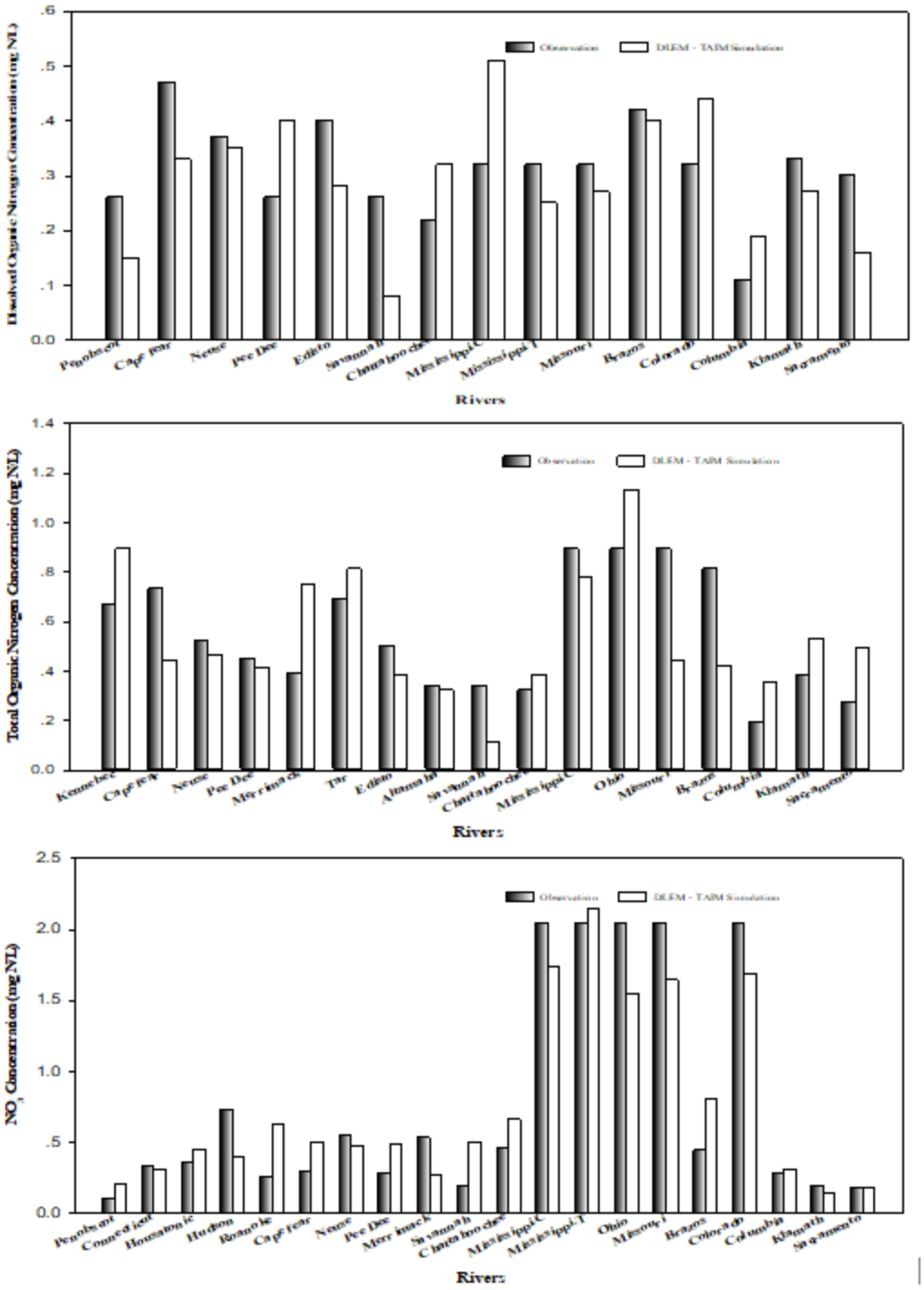

Figure 6-7. Validation of DLEM simulated nitrogen fluxes against USGS observations.

Chapter 7. Summary: The GHG budget of inland water ecosystems across the Conterminous United States

7.1. Summary and major conclusions

In this dissertation, the long-term CO_2, CH_4 and N_2O emissions from inland waters across the CONUS were investigated. A scale adaptive water transport scheme was coupled with the Dynamic land ecosystem model, with certain improvements on the aquatic biogeochemistry to represent the dynamics of CO_2, CH_4, and N_2O in the aquatic ecosystem. We named the newly developed modeling framework as Dynamic Land Ecosystem Model- Terrestrial Aquatic Interface Model (DLEM- TAIM). We developed the U.S hydrography data from high resolution hydrological corrected topographic data. We updated the model driving forces, including climate variables, land use conversions, and nitrogen fertilizer, manure nitrogen, and nitrogen depositions. Meanwhile, the contribution of environmental factors to the GHG emissions from inland water was quantified and analyzed through factorial analysis by the DLEM-TAIM. The major findings including:

(1). The inland water CO_2 emissions increased significantly since the preindustrial era (Figure 7-1. a). The magnitude of riverine CO_2 emission increased from 90.6Tg C/yr during the1900s to 113.6 Tg C/yr during 2009-2018. The magnitude of lake CO_2 emission increased from 64.9 Tg C/yr during the1900s to 88.13 Tg C/yr during 2009-2018. Specifically, from 1960 to 2018, the increasing rate of streams and lakes reached 0.56 Tg C/yr and 0.62 Tg C/yr, respectively. Small rivers dominate the inland water CO_2 emissions, with 88% of the riverine CO_2 released from the 1^{st}-3^{rd} order streams.

(2). The diffusive CH_4 emissions from rivers over the CONUS increased from 1484.5 ± 233.4 Gg CH_4-C yr^{-1} in the 1900s to 1848.8 ± 286.3 Gg CH_4-C yr^{-1} in 2009-2018. The ebullitive CH_4 emissions from rivers over the CONUS increased from 543.1 ± 25.7 Tg CH_4-C yr^{-1} in the 1900s to 737.2 ± 33.9 Tg CH_4-C yr^{-1} in 2009. The diffusive CH_4 emissions from lakes over the CONUS increased from 853.29 ± 122.8 Gg CH_4-C yr^{-1} in the 1900s to 1115.9 ± 151.3 Gg CH_4-C yr^{-1} during 2009-2018. The ebullitive CH_4 emissions from rivers over the CONUS increased from 2970.7 ± 217.7 Tg CH_4-C yr^{-1} in the 1900s to 4095.9 ± 286.8 Tg CH_4-C yr^{-1} in 2009. (Figure 7-1.c.d).

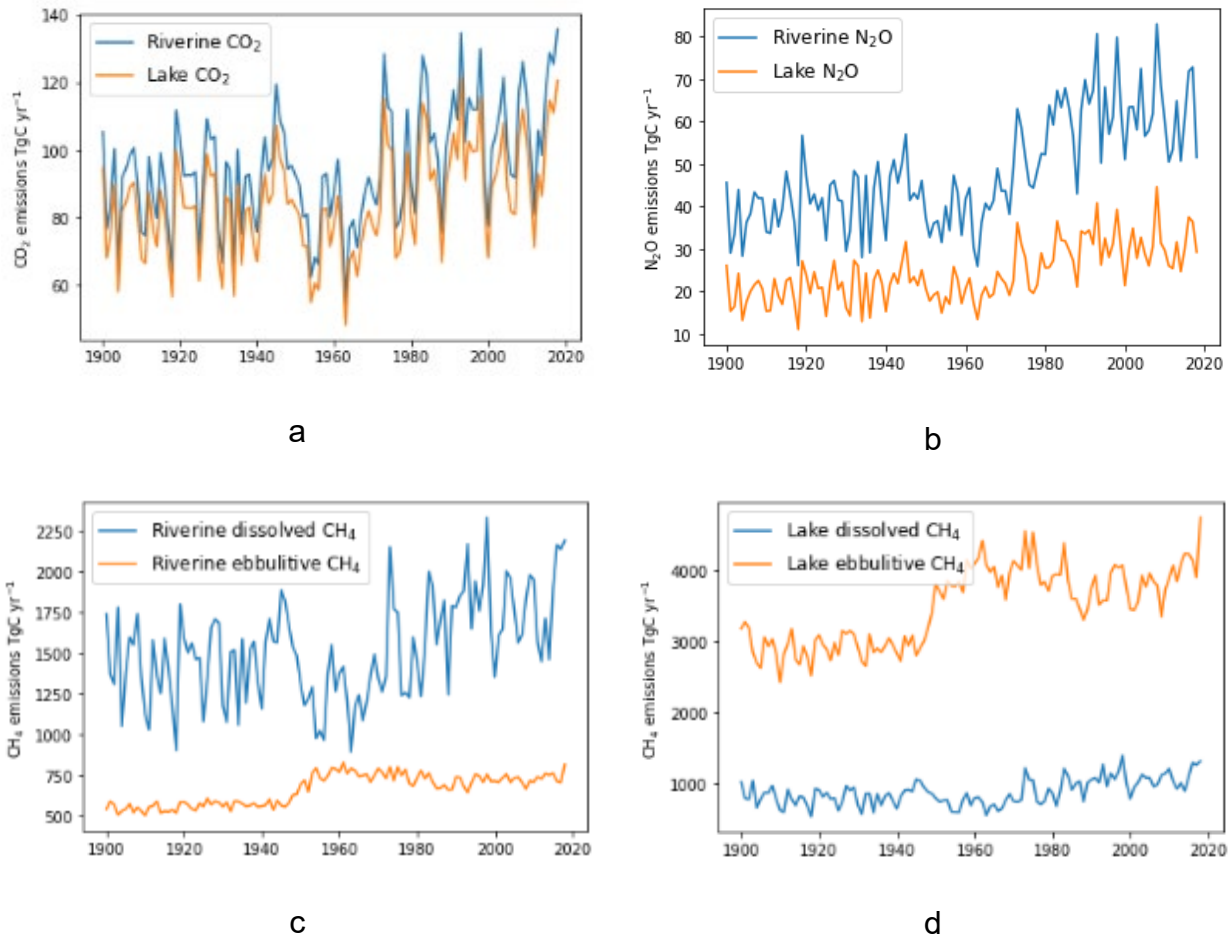

Figure 7-1. The GHG emissions from rivers and lakes over the from 1900 to 2018

(3). The riverine N_2O emissions over the CONUS increased from 38.3 ± 6.2 Gg N_2O-N yr^{-1} in the 1900s to 60.5 ± 8.7 Gg N_2O-N yr^{-1} in 2009(Figure 7-1. b). About 82.9% of riverine N_2O released from small rivers (1st-3rd stream orders) over the CONUS and most of the riverine N_2O is sourced from groundwater transport and hyporheic zone production.

7.2. The CO_2 equivalents and comparison to U.S. land carbon sinks

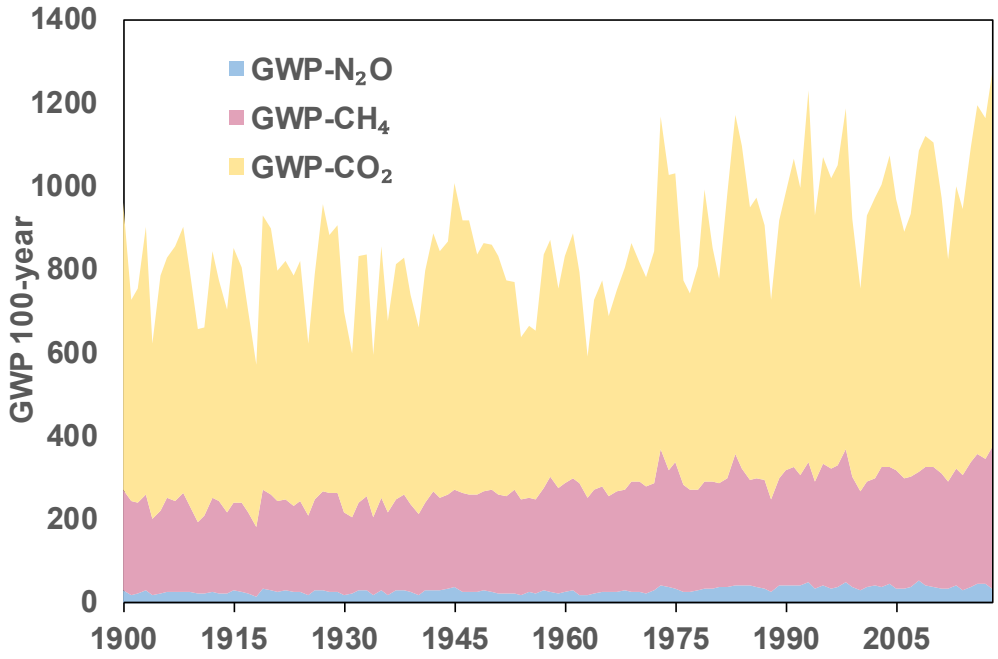

Figure 7-2. The Global Warming Potential (GWP 100-years) of the inland water CO_2, CH_4 and N_2O emissions over the CONUS.

From 2009 to 2018, the annual mean inland water GHGs emissions CO_2 equivalent reached 1.07 Pg CO_2 equiv. yr^{-1} (Figure 7-2). Our results suggested that the inland water CH_4 emission account for 68.1% the GWP, follow by CO_2 (28.4%) and N_2O (3.4%). (Here, we consider the GWP of CH_4 and N_2O are 28 and 265 times of CO_2, respectively). The terrestrial carbon sink of U.S. was estimated to range from 0.1 - 2 Pg-C/yr (which is 0.37 – 7.3 Pg CO_2 equiv. yr^{-1})

(Pacala et al., 2007). The inclusion of the inland water carbon loss and CH_4, N_2O could substantially revise the continental carbon and GHG budget.

7.3. The interaction between triple GHGs.

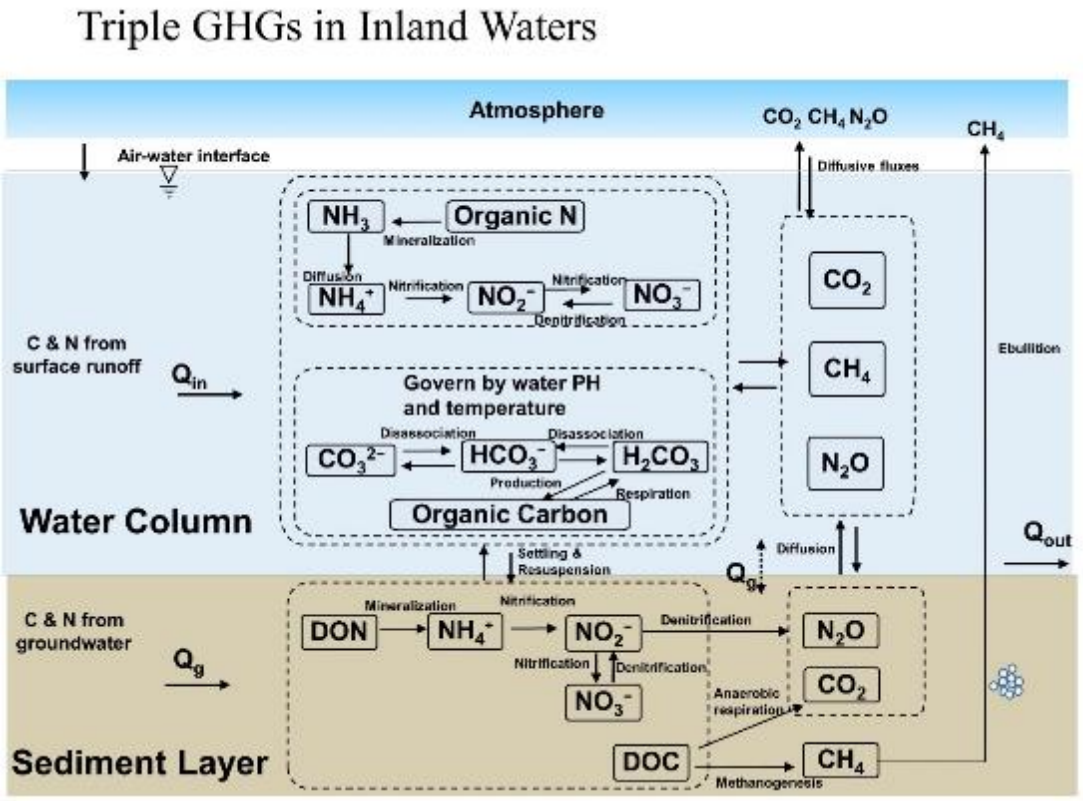

Figure 7-3. The general framework of GHG dynamics within the aquatic ecosystem.

It should be noted that the triple GHGs interact with each other in both terrestrial and aquatic ecosystems through C-N coupled dynamics (Figure 7-3). In the DLEM land model, carbon dynamics such as increased CO_2 and temperature promote the growth of the plant, and the associated nitrogen uptake could substantially reduce the N_2O emissions from terrestrial and aquatic systems. In the aquatic processes, the C-N nexus also regulates the interactions among the CO_2, CH_4, and N_2O. For instance, the CH_4 oxidation is positively correlated to the denitrification of NO_3^-. Our model still simplified the process and did not consider all the C-N

coupling in the terrestrial and aquatic systems. More processes could be considered in the future such as the carbon availability for microorganisms for N_2O production in waters.

7.4. Uncertainty and future study

Although our reconstructed model exhibited reliable estimates, there are still considerable uncertainties in the simulations of inland water GHG emissions throughout this dissertation. These uncertainties may be mainly due to the following three aspects of uncertainty: (1) input data (climate, land-use and remote sensing products, etc.) for driving the DLEM-TAIM, (2) model parameters, and (3) model structure and process representation. To quantify uncertainties in the simulated results, we will identify the most sensitive parameters and examine climate extremes and potential responses/feedbacks and consequent changes in the ecosystem, climate, and land use. The efficiency of the individual model and specific-module-induced uncertainty will be evaluated using graphical and standard statistical measures. We will quantify the uncertainty derived from the downscaling and upscaling algorithms and mismatch of required input data in each individual module, and the uncertainty induced by model fusion, coupling parameterization, interactive responses/feedbacks among the dependent systems in this study. Nevertheless, this dissertation is the first attempt to model the long-term GHG emissions from inland water driving by multiple environmental factors at the continental scales. This study provides insight knowledge to the global or regional carbon budget and the policy-relevant decision support. The processed based hydrological model and biogeochemistry model can be fully coupled with earth system models, thus the inter-comparison while coupling TAIM module with other earth system model could be one of the directions of future study.

Reference

Abril, G., Bouillon, S., Darchambeau, F., Teodoru, C.R., Marwick, T.R., Tamooh, F., Ochieng Omengo, F., Geeraert, N., Deirmendjian, L., Polsenaere, P., Borges, A.V., 2015. Technical Note: Large overestimation of pCO_2 calculated from pH and alkalinity in acidic, organic-rich freshwaters. Biogeosciences 12, 67–78. https://doi.org/10.5194/bg-12-67-2015

Allen, G.H., Pavelsky, T.M., 2018. Global extent of rivers and streams. Science 361, 585–588.

Allen, G.H., Pavelsky, T.M., Barefoot, E.A., Lamb, M.P., Butman, D., Tashie, A., Gleason, C.J., 2018. Similarity of stream width distributions across headwater systems. Nat. Commun. 9, 610.

Andersen, C.B., 2002. Understanding Carbonate Equilibria by Measuring Alkalinity in Experimental and Natural Systems. J. Geosci. Educ. 50, 389–403. https://doi.org/10.5408/1089-9995-50.4.389

Andersson, S., Nilsson, S.I., Saetre, P., 2000. Leaching of dissolved organic carbon (DOC) and dissolved organic nitrogen (DON) in mor humus as affected by temperature and pH. Soil Biol. Biochem. 32, 1–10.

Argerich, A., Haggerty, R., Johnson, S.L., Wondzell, S.M., Dosch, N., Corson-Rikert, H., Ashkenas, L.R., Pennington, R., Thomas, C.K., 2016. Comprehensive multiyear carbon budget of a temperate headwater stream: CARBON BUDGET OF A HEADWATER STREAM. J. Geophys. Res. Biogeosciences 121, 1306–1315. https://doi.org/10.1002/2015JG003050

Arismendi, I., Safeeq, M., Dunham, J.B., Johnson, S.L., 2014. Can air temperature be used to project influences of climate change on stream temperature? Environ. Res. Lett. 9, 084015.

Arnold, J.G., Moriasi, D.N., Gassman, P.W., Abbaspour, K.C., White, M.J., Srinivasan, R., Santhi, C., Harmel, R.D., Van Griensven, A., Van Liew, M.W., 2012. SWAT: Model use, calibration, and validation. Trans. ASABE 55, 1491–1508.

Asabere, S.B., Zeppenfeld, T., Nketia, K.A., Sauer, D., 2018. Urbanization leads to increases in pH, Carbonate and Soil Organic Matter Stocks of Arable Soils of Kumasi, Ghana (West Africa). Front. Environ. Sci. 6, 119.

Aufdenkampe, A.K., Mayorga, E., Raymond, P.A., Melack, J.M., Doney, S.C., Alin, S.R., Aalto, R.E., Yoo, K., 2011. Riverine coupling of biogeochemical cycles between land, oceans, and atmosphere. Front. Ecol. Environ. 9, 53–60.

Bastviken, D., Cole, J., Pace, M., Tranvik, L., 2004. Methane emissions from lakes: Dependence of lake characteristics, two regional assessments, and a global estimate. Glob. Biogeochem. Cycles 18.

Battin, T.J., Kaplan, L.A., Findlay, S., Hopkinson, C.S., Marti, E., Packman, A.I., Newbold, J.D., Sabater, F., 2008. Biophysical controls on organic carbon fluxes in fluvial networks. Nat. Geosci. 1, 95.

Battin, T.J., Luyssaert, S., Kaplan, L.A., Aufdenkampe, A.K., Richter, A., Tranvik, L.J., 2009. The boundless carbon cycle. Nat. Geosci. 2, 598.

Battin, T.J., Sloan, W.T., Kjelleberg, S., Daims, H., Head, I.M., Curtis, T.P., Eberl, L., 2007. Opinion: Microbial landscapes: new paths to biofilm research. Nat. Rev. Microbiol. 5, 76.

Bauer, J.E., Cai, W.-J., Raymond, P.A., Bianchi, T.S., Hopkinson, C.S., Regnier, P.A., 2013. The changing carbon cycle of the coastal ocean. Nature 504, 61.

Baulch, H.M., Dillon, P.J., Maranger, R., Schiff, S.L., 2011. Diffusive and ebullitive transport of methane and nitrous oxide from streams: Are bubble-mediated fluxes important? J. Geophys. Res. Biogeosciences 116.

Beaulieu, J.J., Shuster, W.D., Rebholz, J.A., 2010. Nitrous Oxide Emissions from a Large, Impounded River: The Ohio River. Environ. Sci. Technol. 44, 7527–7533. https://doi.org/10.1021/es1016735

Beaulieu, J.J., Tank, J.L., Hamilton, S.K., Wollheim, W.M., Hall, R.O., Mulholland, P.J., Peterson, B.J., Ashkenas, L.R., Cooper, L.W., Dahm, C.N., Dodds, W.K., Grimm, N.B., Johnson, S.L., McDowell, W.H., Poole, G.C., Valett, H.M., Arango, C.P., Bernot, M.J., Burgin, A.J., Crenshaw, C.L., Helton, A.M., Johnson, L.T., O'Brien, J.M., Potter, J.D., Sheibley, R.W., Sobota, D.J., Thomas, S.M., 2011. Nitrous oxide emission from denitrification in stream and river networks. Proc. Natl. Acad. Sci. 108, 214–219. https://doi.org/10.1073/pnas.1011464108

Beckman, N.D., Wohl, E., 2014. Carbon storage in mountainous headwater streams: The role of old-growth forest and logjams. Water Resour. Res. 50, 2376–2393.

Biemans, H., Haddeland, I., Kabat, P., Ludwig, F., Hutjes, R.W.A., Heinke, J., Von Bloh, W., Gerten, D., 2011. Impact of reservoirs on river discharge and irrigation water supply during the 20th century. Water Resour. Res. 47.

Bonan, G.B., Drewniak, B., Huang, M., Koven, C.D., Levis, S., Li, F., Riley, W.J., Subin, Z.M., Swenson, S.C., Thornton, P.E., 2013. Technical description of version 4.5 of the Community Land Model (CLM). NCAR Tech Note NCARTN-503 STR Natl.

Borges, A.V., Darchambeau, F., Teodoru, C.R., Marwick, T.R., Tamooh, F., Geeraert, N., Omengo, F.O., Guérin, F., Lambert, T., Morana, C., 2015. Globally significant greenhouse-gas emissions from African inland waters. Nat. Geosci. 8, 637.

Briggs, M.A., Lane, J.W., Snyder, C.D., White, E.A., Johnson, Z.C., Nelms, D.L., Hitt, N.P., 2018. Shallow bedrock limits groundwater seepage-based headwater climate refugia. Limnologica 68, 142–156.

Brown, G.W., 1969. Predicting temperatures of small streams. Water Resour. Res. 5, 68–75.

Brown, G.W., Krygier, J.T., 1970. Effects of clear-cutting on stream temperature. Water Resour. Res. 6, 1133–1139.

Buccola, N.L., Turner, D.F., Rounds, S.A., 2016. Water temperature effects from simulated dam operations and structures in the Middle Fork Willamette River, western Oregon. US Geological Survey.

Burgos, M., Sierra, A., Ortega, T., Forja, J.M., 2015. Anthropogenic effects on greenhouse gas (CH_4 and N_2O) emissions in the Guadalete River Estuary (SW Spain). Sci. Total Environ. 503, 179–189.

Burns, E.R., Zhu, Y., Zhan, H., Manga, M., Williams, C.F., Ingebritsen, S.E., Dunham, J.B., 2017. Thermal effect of climate change on groundwater-fed ecosystems. Water Resour. Res. 53, 3341–3351.

Butman, D., Raymond, P.A., 2011. Significant efflux of carbon dioxide from streams and rivers in the United States. Nat. Geosci. 4, 839.

Butman, D., Stackpoole, S., Stets, E., McDonald, C.P., Clow, D.W., Striegl, R.G., 2016. Aquatic carbon cycling in the conterminous United States and implications for terrestrial carbon accounting. Proc. Natl. Acad. Sci. 113, 58–63.

Cao, P., Lu, C.C., Yu, Z., 2018. Historical nitrogen fertilizer use in agricultural ecosystems of the contiguous United States during 1850–2015: application rate, timing, and fertilizer types. Earth Syst. Sci. Data Discuss. 10, 969.
Chapra, S.C., 2008. Surface water-quality modeling. Waveland press.
Chen, D., Hu, M., Guo, Y., Dahlgren, R.A., 2016. Changes in river water temperature between 1980 and 2012 in Yongan watershed, eastern China: Magnitude, drivers and models. J. Hydrol. 533, 191–199.
Chen, G., Fang, X., 2015a. Sensitivity analysis of flow and temperature distributions of density currents in a river-reservoir system under upstream releases with different durations. Water 7, 6244–6268.
Chen, G., Fang, X., 2015b. Accuracy of hourly water temperatures in rivers calculated from air temperatures. Water 7, 1068–1087.
Chen, G., Fang, X., Fan, H., 2016. Estimating hourly water temperatures in rivers using modified sine and sinusoidal wave functions. J. Hydrol. Eng. 21, 05016023.
Chen, G., Tian, H., Huang, C., Prior, S.A., Pan, S., 2013. Integrating a process-based ecosystem model with Landsat imagery to assess impacts of forest disturbance on terrestrial carbon dynamics: Case studies in Alabama and Mississippi. J. Geophys. Res. Biogeosciences 118, 1208–1224.
Chen, Y., Li, J., Wang, H., Qin, J., Dong, L., 2017. Large-watershed flood forecasting with high-resolution distributed hydrological model. Hydrol. Earth Syst. Sci. 21, 735–749.
Chow, V.T., 1964a. Handbook of applied hydrology. Section 8, 8–61.
Chow, V.T., 1964b. Handbook of applied hydrology.
Ciais, P., Borges, A.V., Abril, G., Meybeck, M., Folberth, G., Hauglustaine, D., Janssens, I.A., 2008. The impact of lateral carbon fluxes on the European carbon balance. Biogeosciences 5, 1259–1271.
Ciais, P., Sabine, C., Bala, G., Bopp, L., Brovkin, V., Canadell, J., Chhabra, A., DeFries, R., Galloway, J., Heimann, M., 2014. Carbon and other biogeochemical cycles, in: Climate Change 2013: The Physical Science Basis. Contribution of Working Group I to the Fifth Assessment Report of the Intergovernmental Panel on Climate Change. Cambridge University Press, pp. 465–570.
Claireaux, G., Webber, D.M., Lagardère, J.-P., Kerr, S.R., 2000. Influence of water temperature and oxygenation on the aerobic metabolic scope of Atlantic cod (Gadus morhua). J. Sea Res. 44, 257–265.
Clough, T.J., Addy, K., Kellogg, D.Q., Nowicki, B.L., Gold, A.J., Groffman, P.M., 2007. Dynamics of nitrous oxide in groundwater at the aquatic–terrestrial interface. Glob. Change Biol. 13, 1528–1537.
Coe, M.T., 1998. A linked global model of terrestrial hydrologic processes: Simulation of modern rivers, lakes, and wetlands. J. Geophys. Res. Atmospheres 103, 8885–8899. https://doi.org/10.1029/98JD00347
Colditz, R.R., Saldaña, G.L., Maeda, P., Espinoza, J.A., Tovar, C.M., Hernández, A.V., Benítez, C.Z., López, I.C., Ressl, R., 2012. Generation and analysis of the 2005 land cover map for Mexico using 250 m MODIS data. Remote Sens. Environ. 123, 541–552.
Cole, J.J., Caraco, N.F., 2001. Emissions of nitrous oxide (N_2O) from a tidal, freshwater river, the Hudson River, New York. Environ. Sci. Technol. 35, 991–996.
Cole, J.J., Prairie, Y.T., Caraco, N.F., McDowell, W.H., Tranvik, L.J., Striegl, R.G., Duarte, C.M., Kortelainen, P., Downing, J.A., Middelburg, J.J., 2007. Plumbing the global carbon

cycle: integrating inland waters into the terrestrial carbon budget. Ecosystems 10, 172–185.
Corson-Rikert, H.A., Wondzell, S.M., Haggerty, R., Santelmann, M.V., 2016. Carbon dynamics in the hyporheic zone of a headwater mountain stream in the Cascade Mountains, Oregon. Water Resour. Res. 52, 7556–7576.
Costa, M.H., Foley, J.A., 1997. Water balance of the Amazon Basin: Dependence on vegetation cover and canopy conductance. J. Geophys. Res. Atmospheres 102, 23973–23989.
Cover, M.R., de la Fuente, J.A., Resh, V.H., 2010. Catastrophic disturbances in headwater streams: the long-term ecological effects of debris flows and debris floods in the Klamath Mountains, northern California. Can. J. Fish. Aquat. Sci. 67, 1596–1610. https://doi.org/10.1139/F10-079
Daly, C., Halbleib, M., Smith, J.I., Gibson, W.P., Doggett, M.K., Taylor, G.H., Curtis, J., Pasteris, P.P., 2008. Physiographically sensitive mapping of climatological temperature and precipitation across the conterminous United States. Int. J. Climatol. 28, 2031–2064. https://doi.org/10.1002/joc.1688
Davidson, E.A., Kanter, D., 2014. Inventories and scenarios of nitrous oxide emissions. Environ. Res. Lett. 9, 105012. https://doi.org/10.1088/1748-9326/9/10/105012
Deemer, B.R., Harrison, J.A., Li, S., Beaulieu, J.J., DelSontro, T., Barros, N., Bezerra-Neto, J.F., Powers, S.M., dos Santos, M.A., Vonk, J.A., 2016. Greenhouse Gas Emissions from Reservoir Water Surfaces: A New Global Synthesis. BioScience 66, 949–964. https://doi.org/10.1093/biosci/biw117
Deutzmann, J.S., Stief, P., Brandes, J., Schink, B., 2014. Anaerobic methane oxidation coupled to denitrification is the dominant methane sink in a deep lake. Proc. Natl. Acad. Sci. 111, 18273–18278.
Dick, J.J., Tetzlaff, D., Birkel, C., Soulsby, C., 2015. Modelling landscape controls on dissolved organic carbon sources and fluxes to streams. Biogeochemistry 122, 361–374.
Dixon, R.K., Solomon, A.M., Brown, S., Houghton, R.A., Trexier, M.C., Wisniewski, J., 1994. Carbon pools and flux of global forest ecosystems. Science 263, 185–190.
Döll, P., Lehner, B., 2002. Validation of a new global 30-min drainage direction map. J. Hydrol. 258, 214–231. https://doi.org/10.1016/S0022-1694(01)00565-0
Drake, T.W., Raymond, P.A., Spencer, R.G.M., 2018. Terrestrial carbon inputs to inland waters: A current synthesis of estimates and uncertainty. Limnol. Oceanogr. Lett. 3, 132–142. https://doi.org/10.1002/lol2.10055
Earth Resources Observation And Science Center, 2017. Global Topographic 30 Arc-Second Hydrologic Digital Elevation Model 1 km. https://doi.org/10.5066/F77P8WN0
Fang, X., Stefan, H.G., 1998. Potential climate warming effects on ice covers of small lakes in the contiguous US. Cold Reg. Sci. Technol. 27, 119–140.
Fang, X., Stefan, H.G., 1995. Interaction between oxygen transfer mechanisms in lake models. J. Environ. Eng. 121, 447–454.
Ficklin, D.L., Barnhart, B.L., Knouft, J.H., Stewart, I.T., Maurer, E.P., Letsinger, S.L., Whittaker, G.W., 2014. Climate change and stream temperature projections in the Columbia River basin: habitat implications of spatial variation in hydrologic drivers. Hydrol. Earth Syst. Sci. 18, 4897–4912. https://doi.org/10.5194/hess-18-4897-2014
Ficklin, D.L., Luo, Y., Stewart, I.T., Maurer, E.P., 2012. Development and application of a hydroclimatological stream temperature model within the Soil and Water Assessment Tool. Water Resour. Res. 48.

Findlay, S., Strayer, D., Goumbala, C., Gould, K., 1993. Metabolism of streamwater dissolved organic carbon in the shallow hyporheic zone. Limnol. Oceanogr. 38, 1493–1499.
Findlay, S.E., 2005. Increased carbon transport in the Hudson River: unexpected consequence of nitrogen deposition? Front. Ecol. Environ. 3, 133–137.
Fox, R.J., Fisher, T.R., Gustafson, A.B., Jordan, T.E., Kana, T.M., Lang, M.W., 2014. Searching for the missing nitrogen: biogenic nitrogen gases in groundwater and streams. J. Agric. Sci. 152, 96–106. https://doi.org/10.1017/S0021859614000070
Fu, C., Lee, X., Griffis, T.J., Baker, J.M., Turner, P.A., 2018. A Modeling Study of Direct and Indirect N_2O Emissions From a Representative Catchment in the U.S. Corn Belt. Water Resour. Res. 54, 3632–3653. https://doi.org/10.1029/2017WR022108
Fung, I., John, J., Lerner, J., Matthews, E., Prather, M., Steele, L.P., Fraser, P.J., 1991. Three-dimensional model synthesis of the global methane cycle. J. Geophys. Res. Atmospheres 96, 13033–13065.
Gardner, J.R., Fisher, T.R., Jordan, T.E., Knee, K.L., 2016. Balancing watershed nitrogen budgets: accounting for biogenic gases in streams. Biogeochemistry 127, 231–253. https://doi.org/10.1007/s10533-015-0177-1
Garnier, J., Billen, G., Vilain, G., Martinez, A., Silvestre, M., Mounier, E., Toche, F., 2009. Nitrous oxide (N_2O) in the Seine river and basin: Observations and budgets. Agric. Ecosyst. Environ. 133, 223–233. https://doi.org/10.1016/j.agee.2009.04.024
Georghiades, A.S., 2003. Incorporating the Torrance and Sparrow Model of Reflectance in Uncalibrated Photometric Stereo., in: Iccv. p. 816.
Getirana, A.C.V., Boone, A., Yamazaki, D., Decharme, B., Papa, F., Mognard, N., 2012. The Hydrological Modeling and Analysis Platform (HyMAP): Evaluation in the Amazon Basin. J. Hydrometeorol. 13, 1641–1665. https://doi.org/10.1175/JHM-D-12-021.1
Goldewijk, K.K., 2001. Estimating global land use change over the past 300 years: the HYDE database. Glob. Biogeochem. Cycles 15, 417–433.
Goñi, M.A., Thomas, K.A., 2000. Sources and transformations of organic matter in surface soils and sediments from a tidal estuary (North Inlet, South Carolina, USA). Estuaries 23, 548–564.
Grant, S.B., Azizian, M., Cook, P., Boano, F., Rippy, M.A., 2018. Factoring stream turbulence into global assessments of nitrogen pollution. Science 359, 1266–1269. https://doi.org/10.1126/science.aap8074
Guo, S., Guo, J., Zhang, J., Chen, H., 2009. VIC distributed hydrological model to predict climate change impact in the Hanjiang basin. Sci. China Ser. E Technol. Sci. 52, 3234.
Haag, I., Luce, A., 2008. The integrated water balance and water temperature model LARSIM-WT. Hydrol. Process. Int. J. 22, 1046–1056.
Haddeland, I., Skaugen, T., Lettenmaier, D.P., 2006. Anthropogenic impacts on continental surface water fluxes. Geophys. Res. Lett. 33.
Hanasaki, N., Kanae, S., Oki, T., 2006. A reservoir operation scheme for global river routing models. J. Hydrol. 327, 22–41.
Harrison, J.A., Maranger, R.J., Alexander, R.B., Giblin, A.E., Jacinthe, P.-A., Mayorga, E., Seitzinger, S.P., Sobota, D.J., Wollheim, W.M., 2009. The regional and global significance of nitrogen removal in lakes and reservoirs. Biogeochemistry 93, 143–157.
Hassett, B., Palmer, M., Bernhardt, E., Smith, S., Carr, J., Hart, D., 2005. Restoring watersheds project by project: trends in Chesapeake Bay tributary restoration. Front. Ecol. Environ. 3, 259–267.

Hastie, A., Lauerwald, R., Ciais, P., Regnier, P., 2019. Aquatic carbon fluxes dampen the overall variation of net ecosystem productivity in the Amazon basin: An analysis of the interannual variability in the boundless carbon cycle. Glob. Change Biol.

He, Y., Wang, X., Chen, H., Yuan, X., Wu, N., Zhang, Y., Yue, J., Zhang, Q., Diao, Y., Zhou, L., 2017. Effect of watershed urbanization on N_2O emissions from the Chongqing metropolitan river network, China. Atmos. Environ. 171, 70–81.

Hinshaw, S.E., Dahlgren, R.A., 2013. Dissolved nitrous oxide concentrations and fluxes from the eutrophic San Joaquin River, California. Environ. Sci. Technol. 47, 1313–1322.

Hofmann, A.F., Soetaert, K., Middelburg, J.J., 2008. Present nitrogen and carbon dynamics in the Scheldt estuary using a novel 1-D model. Biogeosciences 5, 981–1006. https://doi.org/10.5194/bg-5-981-2008

Holgerson, M.A., Raymond, P.A., 2016. Large contribution to inland water CO_2 and CH_4 emissions from very small ponds. Nat. Geosci. 9, 222–226. https://doi.org/10.1038/ngeo2654

Homer, C., Dewitz, J., Yang, L., Jin, S., Danielson, P., Xian, G., Coulston, J., Herold, N., Wickham, J., Megown, K., 2015a. Completion of the 2011 National Land Cover Database for the conterminous United States–representing a decade of land cover change information. Photogramm. Eng. Remote Sens. 81, 345–354.

Homer, C., Dewitz, J., Yang, L., Jin, S., Danielson, P., Xian, G., Coulston, J., Herold, N., Wickham, J., Megown, K., 2015b. Completion of the 2011 National Land Cover Database for the conterminous United States–representing a decade of land cover change information. Photogramm. Eng. Remote Sens. 81, 345–354.

Hotchkiss, E.R., Hall Jr, R.O., Sponseller, R.A., Butman, D., Klaminder, J., Laudon, H., Rosvall, M., Karlsson, J., 2015. Sources of and processes controlling CO_2 emissions change with the size of streams and rivers. Nat. Geosci. 8, 696.

Houghton, R.A., 2010. How well do we know the flux of CO_2 from land-use change? Tellus B 62, 337–351.

Hu, M., Chen, D., Dahlgren, R.A., 2016. Modeling nitrous oxide emission from rivers: a global assessment. Glob. Change Biol. 22, 3566–3582. https://doi.org/10.1111/gcb.13351

Isaak, D.J., Luce, C.H., Rieman, B.E., Nagel, D.E., Peterson, E.E., Horan, D.L., Parkes, S., Chandler, G.L., 2010. Effects of climate change and wildfire on stream temperatures and salmonid thermal habitat in a mountain river network. Ecol. Appl. 20, 1350–1371.

Isaak, D.J., Wenger, S.J., Peterson, E.E., Ver Hoef, J.M., Nagel, D.E., Luce, C.H., Hostetler, S.W., Dunham, J.B., Roper, B.B., Wollrab, S.P., 2017. The NorWeST summer stream temperature model and scenarios for the western US: A crowd-sourced database and new geospatial tools foster a user community and predict broad climate warming of rivers and streams. Water Resour. Res. 53, 9181–9205.

Isaak, D.J., Young, M.K., Luce, C.H., Hostetler, S.W., Wenger, S.J., Peterson, E.E., Ver Hoef, J.M., Groce, M.C., Horan, D.L., Nagel, D.E., 2016a. Slow climate velocities of mountain streams portend their role as refugia for cold-water biodiversity. Proc. Natl. Acad. Sci. 113, 4374–4379.

Isaak, D.J., Young, M.K., Luce, C.H., Hostetler, S.W., Wenger, S.J., Peterson, E.E., Ver Hoef, J.M., Groce, M.C., Horan, D.L., Nagel, D.E., 2016b. Slow climate velocities of mountain streams portend their role as refugia for cold-water biodiversity. Proc. Natl. Acad. Sci. 113, 4374–4379.

Jahangir, M.M., Johnston, P., Khalil, M.I., Hennessy, D., Humphreys, J., Fenton, O., Richards, K.G., 2012. Groundwater: A pathway for terrestrial C and N losses and indirect greenhouse gas emissions. Agric. Ecosyst. Environ. 159, 40–48.
Jung, M., Henkel, K., Herold, M., Churkina, G., 2006. Exploiting synergies of global land cover products for carbon cycle modeling. Remote Sens. Environ. 101, 534–553. https://doi.org/10.1016/j.rse.2006.01.020
Jurado, A., Borges, A.V., Brouyère, S., 2017. Dynamics and emissions of N_2O in groundwater: A review. Sci. Total Environ. 584, 207–218.
Kalyanapu, A.J., Burian, S.J., McPherson, T.N., 2010. Effect of land use-based surface roughness on hydrologic model output. J. Spat. Hydrol. 9.
Kang, S., Kim, S., Oh, S., Lee, D., 2000. Predicting spatial and temporal patterns of soil temperature based on topography, surface cover and air temperature. For. Ecol. Manag. 136, 173–184.
Kanter, D.R., Zhang, X., Mauzerall, D.L., Malyshev, S., Shevliakova, E., 2016. The importance of climate change and nitrogen use efficiency for future nitrous oxide emissions from agriculture. Environ. Res. Lett. 11, 094003.
Keery, J., Binley, A., Crook, N., Smith, J.W., 2007. Temporal and spatial variability of groundwater–surface water fluxes: development and application of an analytical method using temperature time series. J. Hydrol. 336, 1–16.
Kim, D.-G., Isenhart, T.M., Parkin, T.B., Schultz, R.C., Loynachan, T.E., 2009. Nitrate and dissolved nitrous oxide in groundwater within cropped fields and riparian buffers. Biogeosciences Discuss. 6, 651–685. https://doi.org/10.5194/bgd-6-651-2009
King, J., Cambray, J.A., Impson, N.D., 1998. Linked effects of dam-released floods and water temperature on spawning of the Clanwilliam yellowfish Barbus capensis. Hydrobiologia 384, 245–265.
Kolb, S., Horn, M.A., 2012. Microbial CH_4 and N_2O consumption in acidic wetlands. Front. Microbiol. 3, 78.
Koontz, E.D., Steel, E.A., Olden, J.D., 2018. Stream thermal responses to wildfire in the Pacific Northwest. Freshw. Sci. 37, 731–746. https://doi.org/10.1086/700403
Kroeze, C., Dumont, E., Seitzinger, S.P., 2005. New estimates of global emissions of N_2O from rivers and estuaries. Environ. Sci. 2, 159–165. https://doi.org/10.1080/15693430500384671
Kroeze, C., Seitzinger, S.P., 1998. Nitrogen inputs to rivers, estuaries and continental shelves and related nitrous oxide emissions in 1990 and 2050: a global model. Nutr. Cycl. Agroecosystems 52, 195–212.
Kumar, S., Sterner, R.W., Finlay, J.C., 2008. Nitrogen and carbon uptake dynamics in Lake Superior. J. Geophys. Res. Biogeosciences 113.
Kurylyk, B.L., MacQuarrie, K.T.B., Caissie, D., McKenzie, J.M., 2015. Shallow groundwater thermal sensitivity to climate change and land cover disturbances: derivation of analytical expressions and implications for stream temperature modeling. Hydrol. Earth Syst. Sci. 19, 2469–2489. https://doi.org/10.5194/hess-19-2469-2015
Lal, R., 1995. Global soil erosion by water and carbon dynamics. Soils Glob. Change 131–142.
Laruelle, G.G., Goossens, N., Arndt, S., Cai, W.-J., Regnier, P., 2017. Air–water CO_2 evasion from US East Coast estuaries. Biogeosciences 14, 2441–2468. https://doi.org/10.5194/bg-14-2441-2017

Laruelle, G.G., Lauerwald, R., Rotschi, J., Raymond, P.A., Hartmann, J., Regnier, P., 2015. Seasonal response of air–water CO_2 exchange along the land–ocean aquatic continuum of the northeast North American coast. Biogeosciences 12, 1447–1458. https://doi.org/10.5194/bg-12-1447-2015

Laudon, H., Buttle, J., Carey, S.K., McDonnell, J., McGuire, K., Seibert, J., Shanley, J., Soulsby, C., Tetzlaff, D., 2012. Cross-regional prediction of long-term trajectory of stream water DOC response to climate change. Geophys. Res. Lett. 39.

Lauerwald, R., Laruelle, G.G., Hartmann, J., Ciais, P., Regnier, P.A., 2015. Spatial patterns in CO_2 evasion from the global river network. Glob. Biogeochem. Cycles 29, 534–554.

Leach, J.A., Moore, R.D., 2019. Empirical Stream Thermal Sensitivities May Underestimate Stream Temperature Response to Climate Warming. Water Resour. Res. 2018WR024236. https://doi.org/10.1029/2018WR024236

Lee, M., Shevliakova, E., Stock, C.A., Malyshev, S., Milly, P.C.D., 2019. Prominence of the tropics in the recent rise of global nitrogen pollution. Nat. Commun. 10, 1437. https://doi.org/10.1038/s41467-019-09468-4

Lehner, B., Liermann, C.R., Revenga, C., Vörösmarty, C., Fekete, B., Crouzet, P., Döll, P., Endejan, M., Frenken, K., Magome, J., 2011a. High-resolution mapping of the world's reservoirs and dams for sustainable river-flow management. Front. Ecol. Environ. 9, 494–502.

Lehner, B., Liermann, C.R., Revenga, C., Vörösmarty, C., Fekete, B., Crouzet, P., Döll, P., Endejan, M., Frenken, K., Magome, J., Nilsson, C., Robertson, J.C., Rödel, R., Sindorf, N., Wisser, D., 2011b. High-resolution mapping of the world's reservoirs and dams for sustainable river-flow management. Front. Ecol. Environ. 9, 494–502. https://doi.org/10.1890/100125

Li, H., Wigmosta, M.S., Wu, H., Huang, M., Ke, Y., Coleman, A.M., Leung, L.R., 2013. A Physically Based Runoff Routing Model for Land Surface and Earth System Models. J. Hydrometeorol. 14, 808–828. https://doi.org/10.1175/JHM-D-12-015.1

Li, H.-Y., Leung, L.R., Getirana, A., Huang, M., Wu, H., Xu, Y., Guo, J., Voisin, N., 2015a. Evaluating Global Streamflow Simulations by a Physically Based Routing Model Coupled with the Community Land Model. J. Hydrometeorol. 16, 948–971. https://doi.org/10.1175/JHM-D-14-0079.1

Li, H.-Y., Ruby Leung, L., Tesfa, T., Voisin, N., Hejazi, M., Liu, L., Liu, Y., Rice, J., Wu, H., Yang, X., 2015b. Modeling stream temperature in the Anthropocene: An earth system modeling approach: MODELING STREAM TEMPERATURE IN ESM. J. Adv. Model. Earth Syst. 7, 1661–1679. https://doi.org/10.1002/2015MS000471

Lindsay, J.B., 2016. The practice of DEM stream burning revisited. Earth Surf. Process. Landf. 41, 658–668.

Liu, J., Zhu, A.-X., Liu, Y., Zhu, T., Qin, C.-Z., 2014. A layered approach to parallel computing for spatially distributed hydrological modeling. Environ. Model. Softw. 51, 221–227.

Liu, M., Tian, H., Yang, Q., Yang, J., Song, X., Lohrenz, S.E., Cai, W.-J., 2013. Long-term trends in evapotranspiration and runoff over the drainage basins of the Gulf of Mexico during 1901-2008. Water Resour. Res. 49, 1988–2012. https://doi.org/10.1002/wrcr.20180

Liu, S., Raymond, P.A., 2018. Hydrologic controls on pCO_2 and CO_2 efflux in US streams and rivers. Limnol. Oceanogr. Lett. 3, 428–435.

Liu, Z., Dugan, B., Masiello, C.A., Barnes, R.T., Gallagher, M.E., Gonnermann, H., 2016. Impacts of biochar concentration and particle size on hydraulic conductivity and DOC leaching of biochar–sand mixtures. J. Hydrol. 533, 461–472.
Loken, L.C., Crawford, J.T., Dornblaser, M.M., Striegl, R.G., Houser, J.N., Turner, P.A., Stanley, E.H., 2018. Limited nitrate retention capacity in the Upper Mississippi River. Environ. Res. Lett. 13, 074030.
Lu, C., Tian, H., 2017. Global nitrogen and phosphorus fertilizer use for agriculture production in the past half century: shifted hot spots and nutrient imbalance. Earth Syst. Sci. Data 9, 181–192. https://doi.org/10.5194/essd-9-181-2017
Lu, X., Zhuang, Q., Liu, Y., Zhou, Y., Aghakouchak, A., 2016. A large-scale methane model by incorporating the surface water transport: Development of a Methane Model. J. Geophys. Res. Biogeosciences 121, 1657–1674. https://doi.org/10.1002/2016JG003321
Maavara, T., Lauerwald, R., Laruelle, G.G., Akbarzadeh, Z., Bouskill, N.J., Van Cappellen, P., Regnier, P., 2018. Nitrous oxide emissions from inland waters: Are IPCC estimates too high? Glob. Change Biol. https://doi.org/10.1111/gcb.14504
Maavara, T., Lauerwald, R., Regnier, P., Van Cappellen, P., 2017. Global perturbation of organic carbon cycling by river damming. Nat. Commun. 8, 15347.
Manabe, S., Wetherald, R.T., 1975. The effects of doubling the CO_2 concentration on the climate of a general circulation model. J. Atmospheric Sci. 32, 3–15.
Martí-Cardona, B., Prats, J., Niclòs, R., 2019. Enhancing the retrieval of stream surface temperature from Landsat data. Remote Sens. Environ. 224, 182–191. https://doi.org/10.1016/j.rse.2019.02.007
Marzadri, A., Dee, M.M., Tonina, D., Bellin, A., Tank, J.L., 2017. Role of surface and subsurface processes in scaling N_2O emissions along riverine networks. Proc. Natl. Acad. Sci. 201617454.
Marzadri, A., Tonina, D., Bellin, A., Tank, J.L., 2014. A hydrologic model demonstrates nitrous oxide emissions depend on streambed morphology. Geophys. Res. Lett. 41, 5484–5491. https://doi.org/10.1002/2014GL060732
McClain, M.E., Boyer, E.W., Dent, C.L., Gergel, S.E., Grimm, N.B., Groffman, P.M., Hart, S.C., Harvey, J.W., Johnston, C.A., Mayorga, E., McDowell, W.H., Pinay, G., 2003. Biogeochemical Hot Spots and Hot Moments at the Interface of Terrestrial and Aquatic Ecosystems. Ecosystems 6, 301–312.
McDonald, C.P., Stets, E.G., Striegl, R.G., Butman, D., 2013. Inorganic carbon loading as a primary driver of dissolved carbon dioxide concentrations in the lakes and reservoirs of the contiguous United States. Glob. Biogeochem. Cycles 27, 285–295.
McElroy, M.B., Elkins, J.W., Wofsy, S.C., Kolb, C.E., Duran, A.P., Kaplan, W.A., 1978. Production and release of N_2O from the Potomac Estuary 1. Limnol. Oceanogr. 23, 1168–1182.
McGinnis, D.F., Kirillin, G., Tang, K.W., Flury, S., Bodmer, P., Engelhardt, C., Casper, P., Grossart, H.-P., 2015. Enhancing surface methane fluxes from an oligotrophic lake: exploring the microbubble hypothesis. Environ. Sci. Technol. 49, 873–880.
McMahon, P.B., Dennehy, K.F., 1999. N_2O Emissions from a Nitrogen-Enriched River. Environ. Sci. Technol. 33, 21–25. https://doi.org/10.1021/es980645n
McQueen, D.J., Lean, D.R.S., 1987. Influence of water temperature and nitrogen to phosphorus ratios on the dominance of blue-green algae in Lake St. George, Ontario. Can. J. Fish. Aquat. Sci. 44, 598–604.

Menberg, K., Blum, P., Kurylyk, B.L., Bayer, P., 2014. Observed groundwater temperature response to recent climate change. Hydrol. Earth Syst. Sci. 18, 4453–4466. https://doi.org/10.5194/hess-18-4453-2014
Mengis, M., Gächter, R., Wehrli, B., 1996. Nitrous oxide emissions to the atmosphere from an artificially oxygenated lake. Limnol. Oceanogr. 41, 548–553.
Messager, M.L., Lehner, B., Grill, G., Nedeva, I., Schmitt, O., 2016. Estimating the volume and age of water stored in global lakes using a geo-statistical approach. Nat. Commun. 7, 13603. https://doi.org/10.1038/ncomms13603
Metz, B., Davidson, O., De Coninck, H., Loos, M., Meyer, L., 2005. IPCC special report on carbon dioxide capture and storage. Intergovernmental Panel on Climate Change, Geneva (Switzerland). Working ….
Mohseni, O., Stefan, H.G., Erickson, T.R., 1998. A nonlinear regression model for weekly stream temperatures. Water Resour. Res. 34, 2685–2692. https://doi.org/10.1029/98WR01877
Montzka, S.A., Dlugokencky, E.J., Butler, J.H., 2011. Non-CO 2 greenhouse gases and climate change. Nature 476, 43.
Nash, J.E., Sutcliffe, J.V., 1970. River flow forecasting through conceptual models part I — A discussion of principles. J. Hydrol. 10, 282–290. https://doi.org/10.1016/0022-1694(70)90255-6
Naylor, L.M., Schmidt, E.J., 1986. Agricultural use of wood ash as a fertilizer and liming material. TappiUnited States 69.
Nelson, K.C., Palmer, M.A., 2007. Stream temperature surges under urbanization and climate change: data, models, and responses 1. JAWRA J. Am. Water Resour. Assoc. 43, 440–452.
Nepstad, D.C., Stickler, C.M., Filho, B.S.-, Merry, F., 2008. Interactions among Amazon land use, forests and climate: prospects for a near-term forest tipping point. Philos. Trans. R. Soc. B Biol. Sci. 363, 1737–1746.
Noacco, V., Wagener, T., Worrall, F., Burt, T.P., Howden, N.J., 2017. Human impact on long-term organic carbon export to rivers. J. Geophys. Res. Biogeosciences 122, 947–965.
Oleson, K.W., Lawrence, D.M., Gordon, B., Flanner, M.G., Kluzek, E., Peter, J., Levis, S., Swenson, S.C., Thornton, E., Feddema, J., 2010. Technical description of version 4.0 of the Community Land Model (CLM).
Pacala, S., Birdsey, R.A., Bridgham, S.D., Conant, R.T., Davis, K., Hales, B., Houghton, R.A., Jenkins, J.C., Johnston, M., Marland, G., 2007. The North American carbon budget past and present. King AW Dilling Zimmerman GP Fairman DM Houghton RA Marland G Rose AZ Wilbanks TJ Eds First State Carbon Cycle Rep. SOCCR North Am. Carbon Budg. Implic. Glob. Carbon Cycle Natl. Ocean. Atmospheric Adm. Natl. Clim. Data Cent. Asheville NC 29-36 167-170.
Palmer, M., Ruhi, A., 2019. Linkages between flow regime, biota, and ecosystem processes: Implications for river restoration. Science 365, eaaw2087.
Pan, S., Tian, H., Dangal, S.R., Ouyang, Z., Lu, C., Yang, J., Tao, B., Ren, W., Banger, K., Yang, Q., 2015. Impacts of climate variability and extremes on global net primary production in the first decade of the 21st century. J. Geogr. Sci. 25, 1027–1044.
Pan, S., Tian, H., Dangal, S.R.S., Zhang, C., Yang, J., Tao, B., Ouyang, Z., Wang, X., Lu, C., Ren, W., Banger, K., Yang, Q., Zhang, B., Li, X., 2014. Complex Spatiotemporal Responses of Global Terrestrial Primary Production to Climate Change and Increasing

Atmospheric CO2 in the 21st Century. PLoS ONE 9, e112810. https://doi.org/10.1371/journal.pone.0112810
Pastor, J., Solin, J., Bridgham, S.D., Updegraff, K., Harth, C., Weishampel, P., Dewey, B., 2003. Global warming and the export of dissolved organic carbon from boreal peatlands. Oikos 100, 380–386.
Quick, A.M., Reeder, W.J., Farrell, T.B., Tonina, D., Feris, K.P., Benner, S.G., 2019. Nitrous oxide from streams and rivers: A review of primary biogeochemical pathways and environmental variables. Earth-Sci. Rev.
Rasilo, T., Hutchins, R.H.S., Ruiz-González, C., del Giorgio, P.A., 2017. Transport and transformation of soil-derived CO_2 , CH_4 and DOC sustain CO_2 supersaturation in small boreal streams. Sci. Total Environ. 579, 902–912. https://doi.org/10.1016/j.scitotenv.2016.10.187
Raymond, P.A., Cole, J.J., 2003. Increase in the export of alkalinity from North America's largest river. Science 301, 88–91.
Raymond, P.A., Hamilton, S.K., 2018. Anthropogenic influences on riverine fluxes of dissolved inorganic carbon to the oceans: Riverine fluxes of inorganic carbon to the oceans. Limnol. Oceanogr. Lett. 3, 143–155. https://doi.org/10.1002/lol2.10069
Raymond, P.A., Hartmann, J., Lauerwald, R., Sobek, S., McDonald, C., Hoover, M., Butman, D., Striegl, R., Mayorga, E., Humborg, C., Kortelainen, P., Dürr, H., Meybeck, M., Ciais, P., Guth, P., 2013. Global carbon dioxide emissions from inland waters. Nature 503, 355–359. https://doi.org/10.1038/nature12760
Raymond, P.A., Oh, N.-H., 2007. An empirical study of climatic controls on riverine C export from three major U.S. watersheds: CLIMATE AND RIVER C EXPORT. Glob. Biogeochem. Cycles 21, n/a-n/a. https://doi.org/10.1029/2006GB002783
Raymond, P.A., Zappa, C.J., Butman, D., Bott, T.L., Potter, J., Mulholland, P., Laursen, A.E., McDowell, W.H., Newbold, D., 2012. Scaling the gas transfer velocity and hydraulic geometry in streams and small rivers: Gas transfer velocity and hydraulic geometry. Limnol. Oceanogr. Fluids Environ. 2, 41–53. https://doi.org/10.1215/21573689-1597669
Reay, D.S., Davidson, E.A., Smith, K.A., Smith, P., Melillo, J.M., Dentener, F., Crutzen, P.J., 2012. Global agriculture and nitrous oxide emissions. Nat. Clim. Change 2, 410.
Regnier, P., Friedlingstein, P., Ciais, P., Mackenzie, F.T., Gruber, N., Janssens, I.A., Laruelle, G.G., Lauerwald, R., Luyssaert, S., Andersson, A.J., 2013. Anthropogenic perturbation of the carbon fluxes from land to ocean. Nat. Geosci. 6, 597.
Regnier, P., Lauerwald, R., Ciais, P., 2014. Carbon leakage through the terrestrial-aquatic interface: Implications for the anthropogenic CO_2 budget. Procedia Earth Planet. Sci. 10, 319–324.
Ren, W., Tian, H., Tao, B., Yang, J., Pan, S., Cai, W.-J., Lohrenz, S.E., He, R., Hopkinson, C.S., 2015. Large increase in dissolved inorganic carbon flux from the Mississippi River to Gulf of Mexico due to climatic and anthropogenic changes over the 21st century. J. Geophys. Res. Biogeosciences 120, 724–736. https://doi.org/10.1002/2014JG002761
Rice, K.C., Jastram, J.D., 2015. Rising air and stream-water temperatures in Chesapeake Bay region, USA. Clim. Change 128, 127–138.
Rosamond, M.S., Thuss, S.J., Schiff, S.L., 2012. Dependence of riverine nitrous oxide emissions on dissolved oxygen levels. Nat. Geosci. 5, 715–718. https://doi.org/10.1038/ngeo1556
Rulík, M., Čáp, L., Hlaváčová, E., 2000. Methane in the hyporheic zone of a small lowland stream (Sitka, Czech Republic). Limnologica 30, 359–366.

Runkel, R.L., Crawford, C.G., Cohn, T.A., 2004a. Load Estimator (LOADEST): A FORTRAN program for estimating constituent loads in streams and rivers.
Runkel, R.L., Crawford, C.G., Cohn, T.A., 2004b. Load Estimator (LOADEST): A FORTRAN program for estimating constituent loads in streams and rivers.
Sander, R., 2015. Compilation of Henry's law constants (version 4.0) for water as solvent. Atmospheric Chem. Phys. 15, 4399–4981. https://doi.org/10.5194/acp-15-4399-2015
Schindler, J.E., Krabbenhoft, D.P., 1998. The hyporheic zone as a source of dissolved organic carbon and carbon gases to a temperate forested stream. Biogeochemistry 43, 157–174.
Segura, C., Caldwell, P., Sun, G., McNulty, S., Zhang, Y., 2014. A model to predict stream water temperature across the conterminous USA. Hydrol. Process. 29, 2178–2195. https://doi.org/10.1002/hyp.10357
Seitzinger, S.P., Harrison, J.A., Dumont, E., Beusen, A.H.W., Bouwman, A.F., 2005. Sources and delivery of carbon, nitrogen, and phosphorus to the coastal zone: An overview of Global Nutrient Export from Watersheds (NEWS) models and their application: GLOBAL EXPORT OF C, N, AND P TO COASTAL SYSTEMS. Glob. Biogeochem. Cycles 19, n/a-n/a. https://doi.org/10.1029/2005GB002606
Seitzinger, S.P., Kroeze, C., 2000. Global distribution of N2O emissions from aquatic systems: natural emissions and anthropogenic effects 13.
Sharifi, A., Hantush, M.M., Kalin, L., 2016. Modeling Nitrogen and Carbon Dynamics in Wetland Soils and Water Using Mechanistic Wetland Model. J. Hydrol. Eng. 22, D4016002.
Snyder, C.D., Hitt, N.P., Young, J.A., 2015. Accounting for groundwater in stream fish thermal habitat responses to climate change. Ecol. Appl. 25, 1397–1419. https://doi.org/10.1890/14-1354.1
Soued, C., del Giorgio, P.A., Maranger, R., 2016. Nitrous oxide sinks and emissions in boreal aquatic networks in Québec. Nat. Geosci. 9, 116–120. https://doi.org/10.1038/ngeo2611
Stanley, E.H., Casson, N.J., Christel, S.T., Crawford, J.T., Loken, L.C., Oliver, S.K., 2016. The ecology of methane in streams and rivers: patterns, controls, and global significance. Ecol. Monogr. 86, 146–171. https://doi.org/10.1890/15-1027
Still, C.J., Berry, J.A., Collatz, G.J., DeFries, R.S., 2003. Global distribution of C3 and C4 vegetation: carbon cycle implications. Glob. Biogeochem. Cycles 17, 6-1-6–14.
Stow, C.A., Walker, J.T., Cardoch, L., Spence, P., Geron, C., 2005. N_2O emissions from streams in the Neuse River watershed, North Carolina. Environ. Sci. Technol. 39, 6999–7004.
Tao, B., Tian, H., Ren, W., Yang, J., Yang, Q., He, R., Cai, W., Lohrenz, S., 2014. Increasing Mississippi river discharge throughout the 21st century influenced by changes in climate, land use, and atmospheric CO_2. Geophys. Res. Lett. 41, 4978–4986. https://doi.org/10.1002/2014GL060361
Tarboton, D.G., 1997. A new method for the determination of flow directions and upslope areas in grid digital elevation models. Water Resour. Res. 33, 309–319.
Terrer, C., Vicca, S., Hungate, B.A., Phillips, R.P., Prentice, I.C., 2016. Mycorrhizal association as a primary control of the CO_2 fertilization effect. Science 353, 72–74.
Tesfa, T.K., Li, H.-Y., Leung, L.R., Huang, M., Ke, Y., Sun, Y., Liu, Y., 2014. A subbasin-based framework to represent land surface processes in an Earth system model. Geosci. Model Dev. 7, 947–963.
Thomann, R.V., Mueller, J.A., 1987. Principles of surface water quality modeling and control. Harper & Row Publishers.

Thornton, P.E., Rosenbloom, N.A., 2005. Ecosystem model spin-up: Estimating steady state conditions in a coupled terrestrial carbon and nitrogen cycle model. Ecol. Model. 189, 25–48. https://doi.org/10.1016/j.ecolmodel.2005.04.008

Thornton, P.E., Running, S.W., 1999. An improved algorithm for estimating incident daily solar radiation from measurements of temperature, humidity, and precipitation. Agric. For. Meteorol. 93, 211–228.

Tian, H., Chen, G., Zhang, C., Liu, M., Sun, G., Chappelka, A., Ren, W., Xu, X., Lu, C., Pan, S., Chen, H., Hui, D., McNulty, S., Lockaby, G., Vance, E., 2012. Century-Scale Responses of Ecosystem Carbon Storage and Flux to Multiple Environmental Changes in the Southern United States. Ecosystems 15, 674–694. https://doi.org/10.1007/s10021-012-9539-x

Tian, H., Lu, C., Chen, G., Xu, X., Liu, M., Ren, W., Tao, B., Sun, G., Pan, S., Liu, J., 2011. Climate and land use controls over terrestrial water use efficiency in monsoon Asia. Ecohydrology 4, 322–340. https://doi.org/10.1002/eco.216

Tian, H., Lu, C., Ciais, P., Michalak, A.M., Canadell, J.G., Saikawa, E., Huntzinger, D.N., Gurney, K.R., Sitch, S., Zhang, B., Yang, J., Bousquet, P., Bruhwiler, L., Chen, G., Dlugokencky, E., Friedlingstein, P., Melillo, J., Pan, S., Poulter, B., Prinn, R., Saunois, M., Schwalm, C.R., Wofsy, S.C., 2016. The terrestrial biosphere as a net source of greenhouse gases to the atmosphere. Nature 531, 225–228. https://doi.org/10.1038/nature16946

Tian, H., Ren, W., Yang, J., Tao, B., Cai, W.-J., Lohrenz, S.E., Hopkinson, C.S., Liu, M., Yang, Q., Lu, C., Zhang, B., Banger, K., Pan, S., He, R., Xue, Z., 2015a. Climate extremes dominating seasonal and interannual variations in carbon export from the Mississippi River Basin. Glob. Biogeochem. Cycles 29, 1333–1347. https://doi.org/10.1002/2014GB005068

Tian, H., Yang, J., Lu, C., Xu, R., Canadell, J.G., Jackson, R.B., Arneth, A., Chang, J., Chen, G., Ciais, P., Gerber, S., Ito, A., Huang, Y., Joos, F., Lienert, S., Messina, P., Olin, S., Pan, S., Peng, C., Saikawa, E., Thompson, R.L., Vuichard, N., Winiwarter, W., Zaehle, S., Zhang, B., Zhang, K., Zhu, Q., 2018a. The Global N2O Model Intercomparison Project. Bull. Am. Meteorol. Soc. 99, 1231–1251.

Tian, H., Yang, J., Xu, R., Lu, C., Canadell, J.G., Davidson, E.A., Jackson, R.B., Arneth, A., Chang, J., Ciais, P., Gerber, S., Ito, A., Joos, F., Lienert, S., Messina, P., Olin, S., Pan, S., Peng, C., Saikawa, E., Thompson, R.L., Vuichard, N., Winiwarter, W., Zaehle, S., Zhang, B., 2018b. Global soil nitrous oxide emissions since the preindustrial era estimated by an ensemble of terrestrial biosphere models: Magnitude, attribution, and uncertainty. Glob. Change Biol. https://doi.org/10.1111/gcb.14514

Tian, H., Yang, Q., Najjar, R.G., Ren, W., Friedrichs, M.A., Hopkinson, C.S., Pan, S., 2015b. Anthropogenic and climatic influences on carbon fluxes from eastern North America to the Atlantic Ocean: A process-based modeling study. J. Geophys. Res. Biogeosciences 120, 757–772.

Tian, H., Yang, Q., Najjar, R.G., Ren, W., Friedrichs, M.A.M., Hopkinson, C.S., Pan, S., 2015c. Anthropogenic and climatic influences on carbon fluxes from eastern North America to the Atlantic Ocean: A process-based modeling study. J. Geophys. Res. Biogeosciences 120, 757–772. https://doi.org/10.1002/2014JG002760

Trenberth, K.E., Shea, D.J., 2005. Relationships between precipitation and surface temperature. Geophys. Res. Lett. 32.

Trimmer, M., Grey, J., Heppell, C.M., Hildrew, A.G., Lansdown, K., Stahl, H., Yvon-Durocher, G., 2012. River bed carbon and nitrogen cycling: state of play and some new directions. Sci. Total Environ. 434, 143–158.
Triska, F.J., Duff, J.H., Avanzino, R.J., 1993. The role of water exchange between a stream channel and its hyporheic zone in nitrogen cycling at the terrestrial—aquatic interface, in: Nutrient Dynamics and Retention in Land/Water Ecotones of Lowland, Temperate Lakes and Rivers. Springer, pp. 167–184.
Turner, P.A., Griffis, T.J., Lee, X., Baker, J.M., Venterea, R.T., Wood, J.D., 2015. Indirect nitrous oxide emissions from streams within the US Corn Belt scale with stream order. Proc. Natl. Acad. Sci. 112, 9839–9843. https://doi.org/10.1073/pnas.1503598112
Ulseth, A.J., Hall, R.O., Canadell, M.B., Madinger, H.L., Niayifar, A., Battin, T.J., 2019. Distinct air–water gas exchange regimes in low-and high-energy streams. Nat. Geosci. 12, 259.
Van Drecht, G., Bouwman, A.F., Harrison, J., Knoop, J.M., 2009. Global nitrogen and phosphate in urban wastewater for the period 1970 to 2050. Glob. Biogeochem. Cycles 23.
Van Huissteden, J., Berrittella, C., Parmentier, F.J.W., Mi, Y., Maximov, T.C., Dolman, A.J., 2011. Methane emissions from permafrost thaw lakes limited by lake drainage. Nat. Clim. Change 1, 119.
Van Oost, K., Quine, T.A., Govers, G., De Gryze, S., Six, J., Harden, J.W., Ritchie, J.C., McCarty, G.W., Heckrath, G., Kosmas, C., 2007. The impact of agricultural soil erosion on the global carbon cycle. Science 318, 626–629.
Van Vliet, M.T., Ludwig, F., Kabat, P., 2013. Global streamflow and thermal habitats of freshwater fishes under climate change. Clim. Change 121, 739–754.
Van Vliet, M.T.H., Yearsley, J.R., Franssen, W.H.P., Ludwig, F., Haddeland, I., Lettenmaier, D.P., Kabat, P., 2012. Coupled daily streamflow and water temperature modelling in large river basins. Hydrol. Earth Syst. Sci. 16, 4303–4321.
Van Wijk, W.R., De Vries, D.A., 1963. Periodic temperature variations in a homogeneous soil. Phys. Plant Environ. 1, 103–143.
Varol, M., Li, S., 2017. Biotic and abiotic controls on CO_2 partial pressure and CO_2 emission in the Tigris River, Turkey. Chem. Geol. 449, 182–193. https://doi.org/10.1016/j.chemgeo.2016.12.003
Venkiteswaran, J.J., Rosamond, M.S., Schiff, S.L., 2014. Nonlinear response of riverine N2O fluxes to oxygen and temperature. Environ. Sci. Technol. 48, 1566–1573.
Vincent, L., Soille, P., 1991. Watersheds in digital spaces: an efficient algorithm based on immersion simulations. IEEE Trans. Pattern Anal. Mach. Intell. 583–598.
Vitousek, P.M., Howarth, R.W., 1991. Nitrogen limitation on land and in the sea: how can it occur? Biogeochemistry 13, 87–115.
von Glasow, R., Jickells, T.D., Baklanov, A., Carmichael, G.R., Church, T.M., Gallardo, L., Hughes, C., Kanakidou, M., Liss, P.S., Mee, L., Raine, R., Ramachandran, P., Ramesh, R., Sundseth, K., Tsunogai, U., Uematsu, M., Zhu, T., 2013. Megacities and Large Urban Agglomerations in the Coastal Zone: Interactions Between Atmosphere, Land, and Marine Ecosystems. AMBIO 42, 13–28. https://doi.org/10.1007/s13280-012-0343-9
Vörösmarty, C.J., Meybeck, M., Fekete, B., Sharma, K., Green, P., Syvitski, J.P., 2003. Anthropogenic sediment retention: major global impact from registered river impoundments. Glob. Planet. Change 39, 169–190.

Waisanen, P.J., Bliss, N.B., 2002. Changes in population and agricultural land in conterminous United States counties, 1790 to 1997. Glob. Biogeochem. Cycles 16.
Wanders, N., van Vliet, M.T., Wada, Y., Bierkens, M.F., van Beek, L.P., 2019. High-Resolution Global Water Temperature Modeling. Water Resour. Res. 55, 2760–2778.
Webb, B.W., Hannah, D.M., Moore, R.D., Brown, L.E., Nobilis, F., 2008. Recent advances in stream and river temperature research. Hydrol. Process. 22, 902–918. https://doi.org/10.1002/hyp.6994
Webb, J.R., Hayes, N.M., Simpson, G.L., Leavitt, P.R., Baulch, H.M., Finlay, K., 2019. Widespread nitrous oxide undersaturation in farm waterbodies creates an unexpected greenhouse gas sink. Proc. Natl. Acad. Sci. 116, 9814–9819.
Wehrly, K.E., Brenden, T.O., Wang, L., 2009. A Comparison of Statistical Approaches for Predicting Stream Temperatures Across Heterogeneous Landscapes. JAWRA J. Am. Water Resour. Assoc. 45, 986–997. https://doi.org/10.1111/j.1752-1688.2009.00341.x
Well, R., Augustin, J., Davis, J., Griffith, S.M., Meyer, K., Myrold, D.D., 2001. Production and transport of denitrification gases in shallow ground water. Nutr. Cycl. Agroecosystems 60, 65–75. https://doi.org/10.1023/A:1012659131811
Williams, J.R., Berndt, H.D., 1977. Sediment yield prediction based on watershed hydrology. Trans. ASAE 20, 1100–1104.
Wohl, E., Dwire, K., Sutfin, N., Polvi, L., Bazan, R., 2012. Mechanisms of carbon storage in mountainous headwater rivers. Nat. Commun. 3, 1263.
Wollheim, W.M., Vörösmarty, C.J., Bouwman, A.F., Green, P., Harrison, J., Linder, E., Peterson, B.J., Seitzinger, S.P., Syvitski, J.P., 2008. Global N removal by freshwater aquatic systems using a spatially distributed, within-basin approach. Glob. Biogeochem. Cycles 22.
Wu, H., Kimball, J.S., Elsner, M.M., Mantua, N., Adler, R.F., Stanford, J., 2012a. Projected climate change impacts on the hydrology and temperature of Pacific Northwest rivers. Water Resour. Res. 48.
Wu, H., Kimball, J.S., Li, H., Huang, M., Leung, L.R., Adler, R.F., 2012b. A new global river network database for macroscale hydrologic modeling: DATA AND ANALYSIS NOTE. Water Resour. Res. 48. https://doi.org/10.1029/2012WR012313
Wu, L.-C., Wei, C.-B., Yang, S.-S., Chang, T.-H., Pan, H.-W., Chung, Y.-C., 2007. Relationship between carbon dioxide/methane emissions and the water quality/sediment characteristics of Taiwan's main rivers. J. Air Waste Manag. Assoc. 57, 319–327.
Xu, X.F., Tian, H.Q., Zhang, C., Liu, M.L., Ren, W., Chen, G.S., Lu, C.Q., Bruhwiler, L., 2010. Attribution of spatial and temporal variations in terrestrial methane flux over North America. Biogeosciences 7, 3637–3655. https://doi.org/10.5194/bg-7-3637-2010
Yamazaki, D., Kanae, S., Kim, H., Oki, T., 2011. A physically based description of floodplain inundation dynamics in a global river routing model: floodplain inundation dynamics. Water Resour. Res. 47. https://doi.org/10.1029/2010WR009726
Yang, Q., Tian, H., Friedrichs, M.A., Hopkinson, C.S., Lu, C., Najjar, R.G., 2015a. Increased nitrogen export from eastern North America to the Atlantic Ocean due to climatic and anthropogenic changes during 1901–2008. J. Geophys. Res. Biogeosciences 120, 1046–1068.
Yang, Q., Tian, H., Friedrichs, M.A.M., Hopkinson, C.S., Lu, C., Najjar, R.G., 2015b. Increased nitrogen export from eastern North America to the Atlantic Ocean due to climatic and

anthropogenic changes during 1901-2008. J. Geophys. Res. Biogeosciences 120, 1046–1068. https://doi.org/10.1002/2014JG002763
Yang, Q., Tian, H., Friedrichs, M.A.M., Hopkinson, C.S., Lu, C., Najjar, R.G., 2015c. Increased nitrogen export from eastern North America to the Atlantic Ocean due to climatic and anthropogenic changes during 1901-2008: N EXPORT FROM EASTERN NORTH AMERICA. J. Geophys. Res. Biogeosciences 120, 1046–1068. https://doi.org/10.1002/2014JG002763
Yang, Q., Tian, H., Friedrichs, M.A.M., Liu, M., Li, X., Yang, J., 2015d. Hydrological Responses to Climate and Land-Use Changes along the North American East Coast: A 110-Year Historical Reconstruction. JAWRA J. Am. Water Resour. Assoc. 51, 47–67. https://doi.org/10.1111/jawr.12232
Yao, Y., Shi, X., 2015. Alternating scanning orders and combining algorithms to improve the efficiency of flow accumulation calculation. Int. J. Geogr. Inf. Sci. 29, 1214–1239.
Yao, Y., Tao, H., Shi, X., 2012. Multi-type sweeping for improving the efficiency of flow accumulation calculation, in: 2012 20th International Conference on Geoinformatics. IEEE, pp. 1–4.
Yearsley, J., 2012. A grid-based approach for simulating stream temperature. Water Resour. Res. 48.
Yearsley, J.R., Sun, N., Baptiste, M., Nijssen, B., 2019. Assessing the impacts of hydrologic and land use alterations on water temperature in the Farmington River basin in Connecticut. Hydrol. Earth Syst. Sci. 23, 4491–4508.
Yu, Z., Lu, C., 2018. Historical cropland expansion and abandonment in the continental US during 1850 to 2016. Glob. Ecol. Biogeogr. 27, 322–333.
Zhang, B., Tian, H., Lu, C., Dangal, S.R., Yang, J., Pan, S., 2017. Global manure nitrogen production and application in cropland during 1860–2014: a 5 arcmin gridded global dataset for Earth system modeling. Earth Syst. Sci. Data 9.
Zhang, W., Villarini, G., Vecchi, G.A., Smith, J.A., 2018. Urbanization exacerbated the rainfall and flooding caused by hurricane Harvey in Houston. Nature 563, 384.